DIN 71SD4268

EUV AND X-RAY SPECTROHELIOGRAPH FOR OSO-H

Dr. A.A. Sterk
F. Kieser
S. Peck
E. Knox

General Electric Co.
Space Division
P.O. Box 8555
Philadelphia, Pa. 19101

January 1972
Final Report

Prepared for

GODDARD SPACE FLIGHT CENTER
Greenbelt, Maryland 20771

1. REPORT NO.	2. GOVERNMENT ACCESSION NO.	3. RECIPIENT'S CATALOG NO.
4. TITLE AND SUBTITLE EUV AND X-RAY SPECTROHELIOGRAPH		5. REPORT DATE 20 January 1972 6. PERFORMING ORGANIZATION CODE 23991
7. AUTHOR(S) Sterk, A.; Kieser, F.; Peck, S.; Knox, E.		8. PERFORMING ORGANIZATION REPORT NO. DIN71SD4268
9. PERFORMING ORGANIZATION NAME AND ADDRESS Space Systems General Electric Co. Valley Forge, Pa.		10. WORK UNIT NO. 11. CONTRACT OR GRANT NO. NAS 5-11169 13. TYPE OF REPORT AND PERIOD COVERED Final Report
12. SPONSORING AGENCY NAME AND ADDRESS Goddard Space Flight Center Greenbelt, Maryland 20771		14. SPONSORING AGENCY CODE
15. SUPPLEMENTARY NOTES		

16. ABSTRACT: The General Electric Company, under contract to NASA/GSFC, provided an Extreme Ultraviolet and X-ray Spectroheliograph for Orbiting Solar Observatory - H. Work started on the instrument in mid 1968 and culminated in the launch of the instrument in September 1971.

The work performed under the contract and recorded in this report included the design of the instrument; the fabrication and qualification of the design; the refurbishment of the qualification unit; the calibration and acceptance test of the refurbished unit for flight; and the support provided to NASA/GSFC during the integration of the instrument into the spacecraft, spacecraft testing, and launch.

The principal investigator for the EUV and X-ray Spectroheliograph is Dr. Werner Neupert, Code 682 NASA/GSFC. The Technical Officer is Mr. Milton Kalet, Code 680, NASA/GSFC.

17. KEY WORDS (SELECTED BY AUTHOR(S))	18. DISTRIBUTION STATEMENT
EUV Spectroheliograph - 170 - 400Å X-ray Spectroheliograph - 1.7 - 16Å Hydrogen Alpha Spectroheliograph- 6563 Å X-ray Polarimeter (0.5Å)	Details of illustrations in this document may be better studied on microfiche

19. SECURITY CLASSIF. (OF THIS REPORT)	20. SECURITY CLASSIF. (OF THIS PAGE)	21. NO. OF PAGES	22. PRICE
Unclassified	Unclassified	204	12.25

TABLE OF CONTENTS

TABLE OF CONTENTS (Cont'd)

TABLE OF CONTENTS (Cont'd)

TABLE OF CONTENTS (Cont'd)

LIST OF ILLUSTRATIONS

LIST OF ILLUSTRATIONS (Cont'd)

LIST OF ILLUSTRATIONS (Cont'd)

LIST OF TABLES

SECTION 1
INTRODUCTION

1.1 PROGRAM SUMMARY

The General Electric Company, in conjunction with NASA/GSFC, designed, fabricated, tested, and calibrated a complex scientific instrument to be launched on OSO-H, the latest in the series of NASA's Orbiting Solar Observatories. This instrument consists of four spectroheliographs and an X-ray polarimeter. This instrument will be used to study solar radiation at selected wavelengths in the X-ray and extreme ultraviolet ranges, make observations at the H-Alpha wavelength, and measure the degree of polarization of X-ray emissions.

Work started in September 1968, under contract NAS5-11169. The program, as originally defined, contained two instruments: a prototype (qualification) model and a flight model. In May 1970, it was decided that it was in the best interest of the program to stop work on the fabrication and assembly of the flight unit and to refurbish the prototype model for flight. The instrument was qualified, refurbished, acceptance tested, and delivered to the spacecraft contractor for integration into OSO-H on April 30, 1971. Launch occurred on September 29, 1971. The successful satellite was renamed OSO-7.

Significant program events are shown in Figure 1-1.

1.2 ORGANIZATION OF REPORT

This report discusses the scientific and technical factors leading to the design of the instrument and reviews the results obtained in reducing the design to hardware. The report is separated into sections which will discuss each of the scientific experiments contained within the instrument separately. In each of the experiment sections (Sections 3 through 7), the report will address the experiment requirements, the design solution (which will include a discussion of each of the components in the experiment), alignment/calibration results and modes of operation of the experiments. Additional sections are provided to discuss

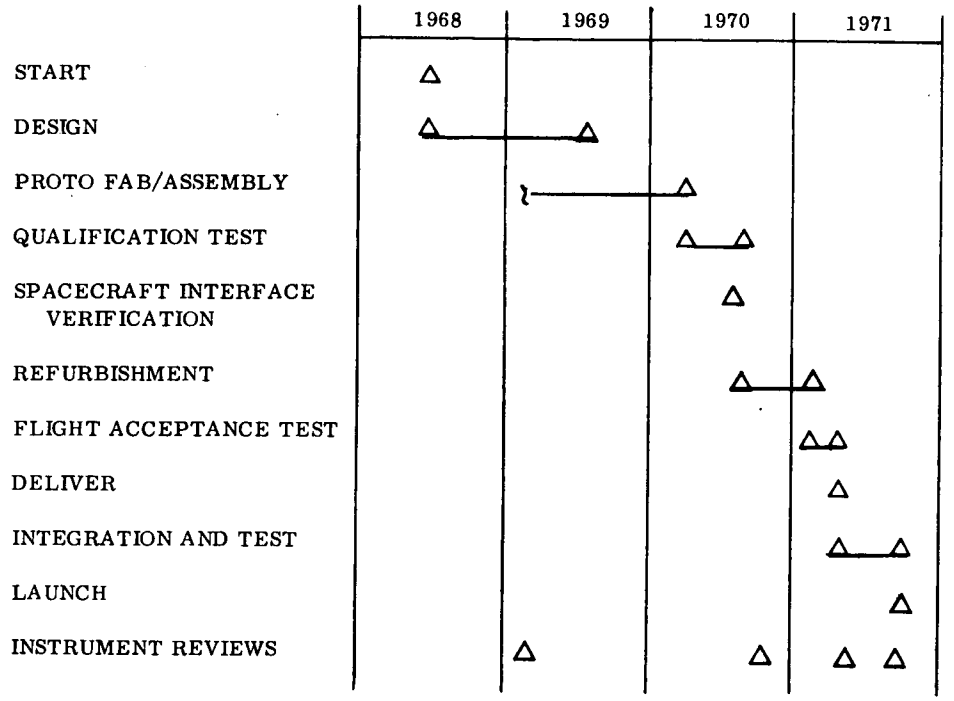

Figure 1-1. Major Program Milestones

subsystems/components which are not specifically identified as belonging to one of the experiments or, by usage are common to all experiments (i.e., low voltage power supply, motor drivers, etc.).

SECTION 2

INSTRUMENT DESCRIPTION

2.1 GENERAL

This section provides a brief description of the OSO-H X-ray and Extreme Ultraviolet Spectroheliograph. This instrument is the "right-hand" pointed instrument on the OSO-H spacecraft. Its position and relationship to the spacecraft and other scientific instruments is shown in Figure 2-1.

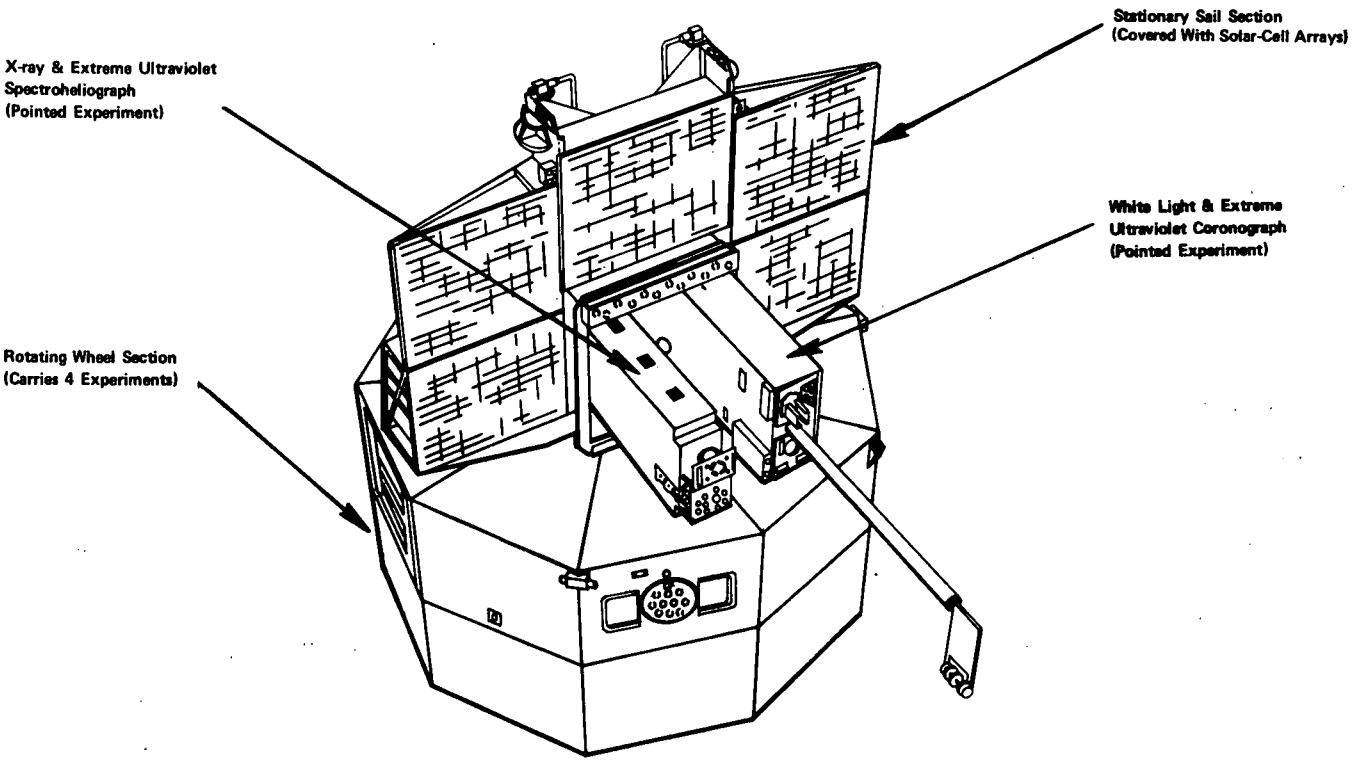

Figure 2-1. Orbiting Solar Observatory-H

The instrument consists of five separate scientific experiments. These experiments are as follows:

1. Extreme Ultraviolet (EUV) Spectroheliograph
2. H-Alpha Spectroheliograph
3. Longwave (LW) X-ray Spectroheliograph

4. Shortwave (SW) X-Ray Spectroheliograph

5. X-Ray Polarimeter

The locations of these five experiments within the instrument along with other instrument subsystems/components are shown in Figure 2-2. The instrument is defined by GE drawing 47R217399G1.

2.2 EUV SPECTROHELIOGRAPH

The EUV spectroheliograph is designed to obtain spectroheliograms in the EUV region between 170 and 400 Å. The experiment consists of a imaging system (Wolter Type II grazing incidence telescope), a variable aperture mechanism located at the focal plane of the telescope, a grating, and a carriage mechanism which scans the first order diffracted component from the grating; the scan being made along the spectrometer's focal curve. The variable aperture mechanism permits the selection of four different on-axis apertures and also provides the capability to scan the solar diameter when the instrument is center-sun pointing. The carriage mechanism contains three magnetic electron multipliers (MEM), a set of two selectable exit slits for each MEM, and associated drive motors and electronics. This arrangement permits three lines of radiation to be selected and observed at one time.

2.3 H-ALPHA SPECTROHELIOGRAPH

The H-Alpha experiment is designed to provide correlation between the visible light measurements and data obtained from the other four experiments. The experiment consists of the same imaging system, variable aperture, and grating as described in paragraph 2.4. In the case of the H-Alpha experiment, the zero-order diffracted component from the grating is deflected by mirrors through an entrance slit to a Ebert-Fastie spectrometer which selects the H-Alpha line. The radiation is directed through an exit slit and is transmitted to a red-sensitive photomultiplier. The analog output of the photomultiplier is converted to a digital output by an analog-to-digital converter.

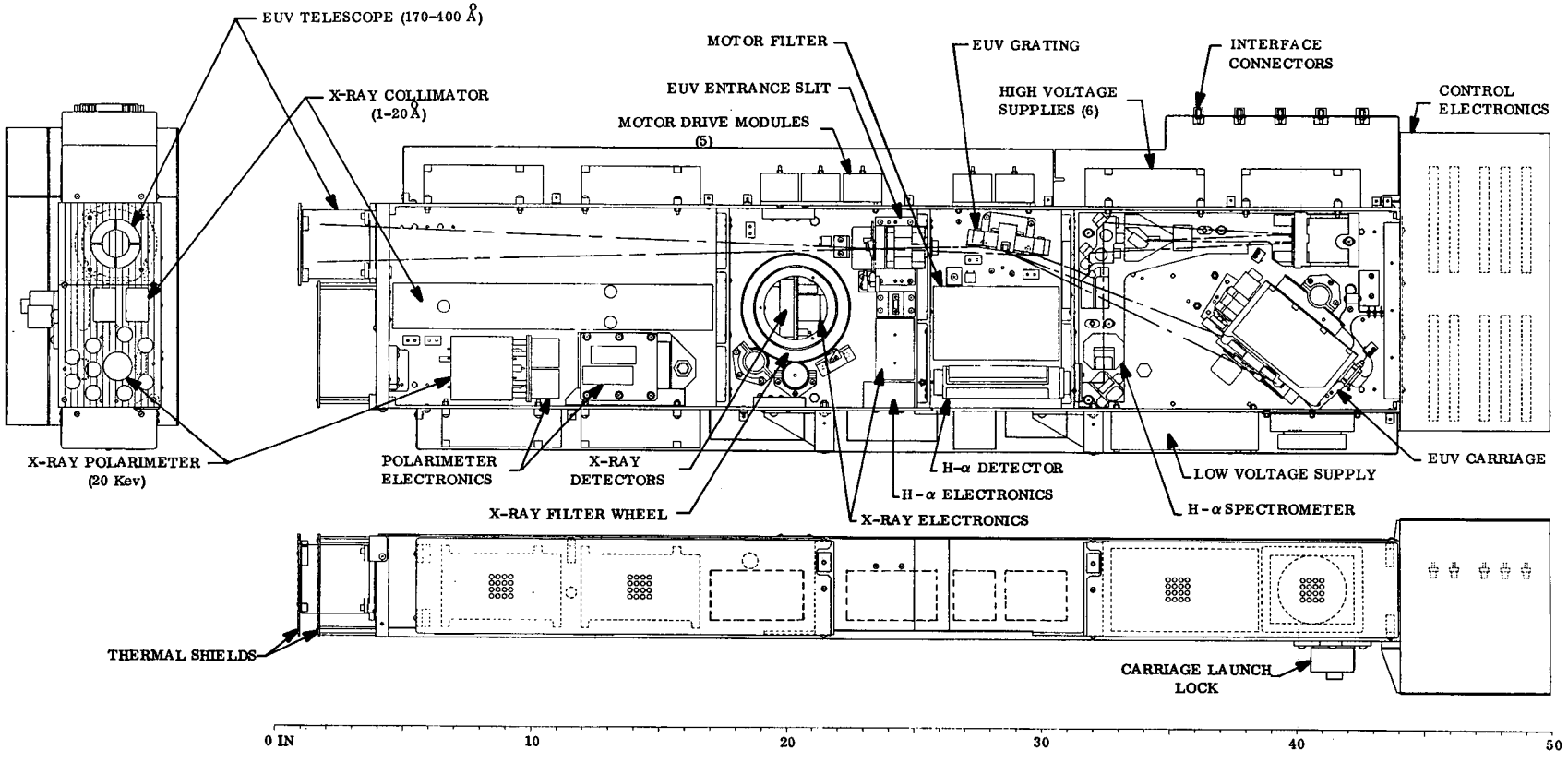

Figure 2-2. OSO-H Spectroheliograph

2.4 LONGWAVE X-RAY SPECTROHELIOGRAPH

The longwave X-ray experiment is designed to provide spectroheliograms in selected spectral bands between 7.9 Å and 16 Å. The experiment consists of a collimator, a filter wheel, a double chambered proportional counter, and associated electronics and drive motors. The filter wheel has 6 positions; five containing filter pairs and one "open" position which is used for calibration. Each filter pair consists of two side-by-side filters, each of which is common to only one of the two chambers of the proportional counters. With a filter pair placed in front of the proportional counter, it is possible to measure radiation in a very narrow spectral band by obtaining the difference in the outputs of the two proportional counter chambers. Filter-pairs are selectable by command.

2.5 SHORTWAVE X-RAY SPECTROHELIOGRAPH

The short wave X-ray experiment is designed to provide spectroheliograms in selected bands between 1.7 Å and 8 Å. Its description is the same as presented in paragraph 2.4 for the longwave X-ray spectroheliograph.

2.6 POLARIMETER EXPERIMENT

The polarimeter experiment is designed to measure the degree of polarization of flare emissions at 0.5 ± 0.2 Å. The experiment consists of a 6-chambered proportional counter surrounding a beryllium scattering block and associated electronics.

SECTION 3

EUV EXPERIMENT

3.1 REQUIREMENTS

The requirements for the EUV experiment are to provide spectroheliograms with a minimum spatial resolution of 10 x 20 arc-seconds. Other requirements are:

1. Resolutions of 20 x 20, 40 x 20, and 60 x 20 arc-sec.
2. An off-axis line scan of the sun with a resolution of 20 x 20 arc seconds.
3. Spectral range from 170 to 400 $\mathring{A}$
4. Three predetermined wavelengths in either of two groups are to be detected simultaneously
5. Spectral resolution of 1.8 $\mathring{A}$ at a base of a scanned line
6. Sensitivity should be 5×10^{-3} c-cm^{2}-ph^{-1}
7. Maximum allowable background noise is to be less than 120 counts/minute. Detector plateaus $\leqq$ 10%/100 volts
8. Life expectancy of the detector was tied to a maximum allowable integral pulse height resolution, defined as an allowable count rate change of $\leq$ 25% for a 10:1 change in threshold setting
9. Orbit stability was specified as less than 2% change in count rate for a 60-minute time period.
10. Maximum operating count rate was specified at 10^{5} cps.

3.2 DESIGN SOLUTION

3.2.1 EUV EXPERIMENT DESCRIPTION

The configuration selected for the EUV experiment consists of a focusing telescope, a variable geometry entrance aperture, grating, 2 sets of exit slits for each detector and three detectors (Magnetic Electron Multipliers). This arrangement is shown schematically in Figure 3-1.

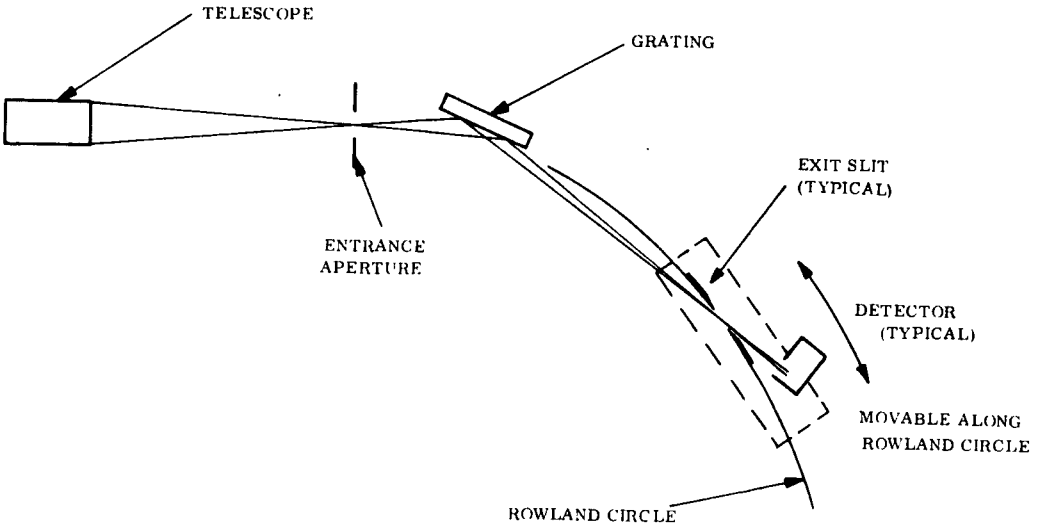

Figure 3-1. EUV Experiment Schematic

Spatial resolution is achieved with an EUV optical system consisting of the focusing telescope and the aperture which is located in the focal plane of the telescope. The telescope is a grazing incidence Wolter Type II system. This has the advantage of a short flange focal length. The optical focal length is 85 cm. The wavelength range is covered by scanning an assembly of three detectors along the Rowland circle. Simultaneous detection of up to three wavelengths is possible with three detectors. The detectors are windowless magnetic electron multipliers optimized for this wavelength range.

The detectors are operated in the pulse mode and output signals are digital from detector to telemetry. This assures high stability and large dynamic range, because indication is almost independent of gain. Output indication is pulse rate. For redundancy, there are two high voltage power supplies: one powering two detectors, the other powering the remaining detector.

A block diagram showing the signal processing from the detectors to telemetry is shown in Figure 3-2.

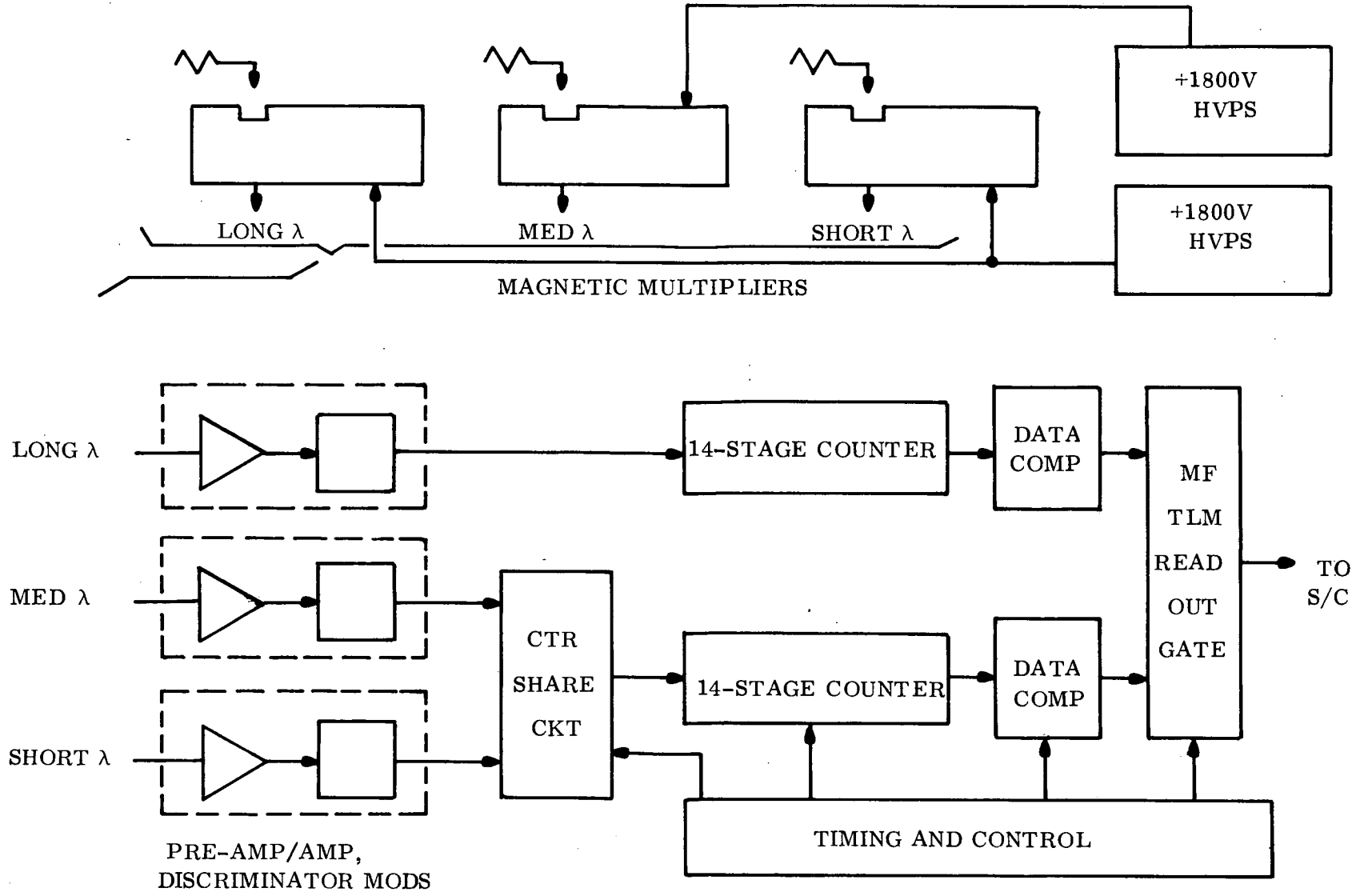

Figure 3-2. EUV Experiment Flow Diagram

3.2.2 COMPONENT DESCRIPTION

3.2.2.1 Telescope

General Characteristics. The telescope (Figure 3-3) projects an image of the sun on the entrance slit of the EUV spectrometer. The telescope is a grazing incidence Wolter Type II design to provide high efficiency in the EUV range of 170 Å to 400 Å. As shown in Figure 3-4, the design uses a paraboloid and hyperboloid element. Parallel incoming radiation strikes the paraboloidal reflector and is directed toward the focus F_1. The hyperboloidal reflector, confocal with the paraboloid, intercepts the rays and directs them toward the focus F_2 where the focal plane of the system is located.

The significant characteristics of the telescope are listed below:

1.	Collecting Area	11.0 cm^2	
2.	Effective Focal Length	85.56 cm	
3.	Flange Focal Length	50 $\pm$ 0.5 cm	
4.	f No.	18	
5.	Maximum Grazing Angle	13 degrees	
6.	Maximum Diameter	6.76 cm	(2.66 in.)
7.	Overall Length	9.09 cm	(3.58 in.)
8.	Weight	0.50 Kg	(1.1 lb)

The curvature of the focal plane as a function of the off axis angle of incoming radiation is shown in Figure 3-5.

The paraboloid conforms to the equation

$$Y^2 = 2PX + P^2$$

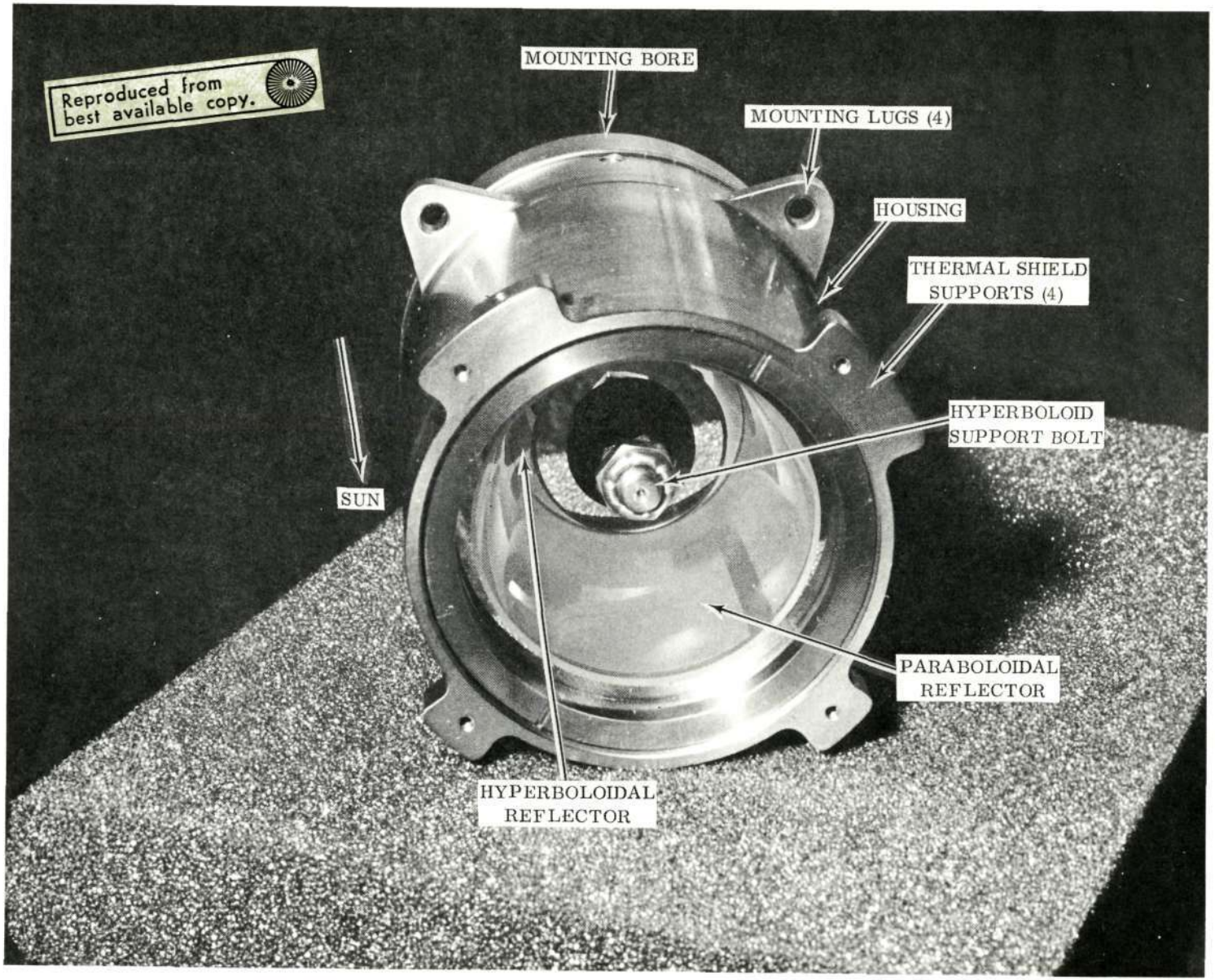

Figure 3-3. Telescope Assembly

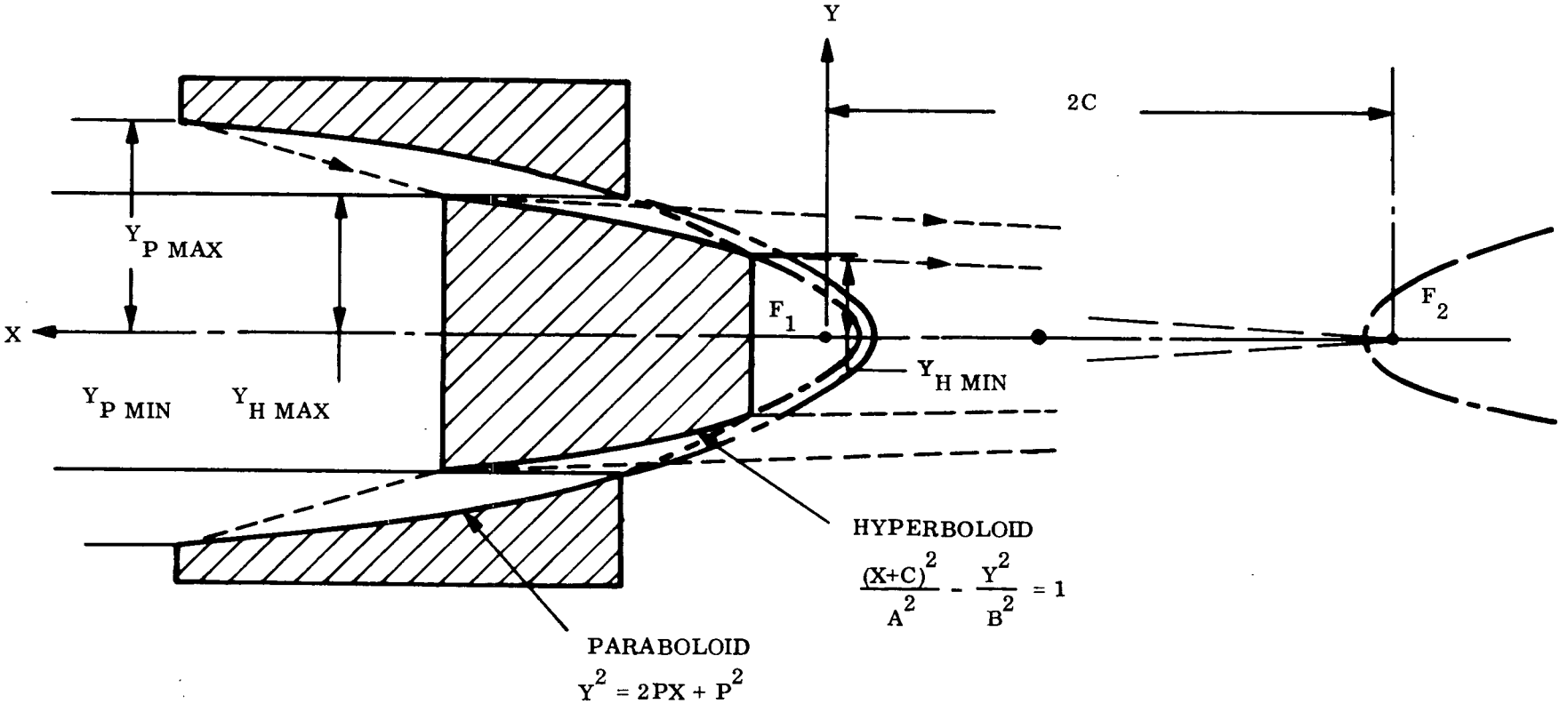

Figure 3-4. Telescope Design Showing Paraboloid and Hyperboloid

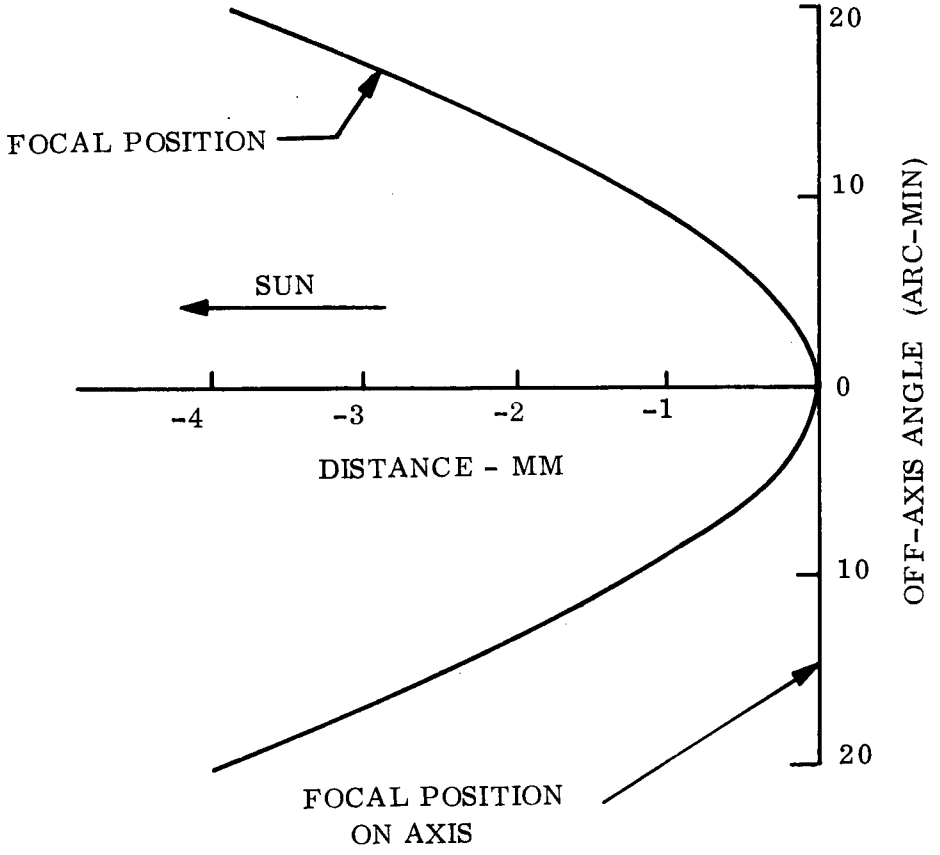

Figure 3-5. Curvature of Focal Plane as a Function of the Off-Axis Angle of Incoming Radiation

and the hyperboloid

$$\frac{(X+C)^2}{A^2} - \frac{Y^2}{B^2} = 1$$

The dimensions of both conics are on a common coordinate system originating at F_1. The significant parameters are listed below.

Paraboloid Parameters (cm)		Hyperboloidal Parameters (cm)	
P	= 0.33838	A	= 23.75758
Y	= 2.37663	B	= 2.11730
YP Min	= 1.46569	C	= 23.85174
XP Max	= 8.17669	YH Max	= 1.46569
XP Min	= 3.00511	YH Min	= 0.83780
Length of Section	5.17188	XH Max	= 5.04282
		XH Min	= 1.69815
		Length of Section	3.34467

Performance Requirements. The detail performance requirements of the telescope are contained in General Electric Specification SVS 7558. In summary, the telescope is required to have at 304 $\mathring{A}$ an efficiency of 20 percent and a resolution better than 10 arc-seconds on-axis and 20 arc-seconds up to 20 arc-minutes off-axis. In addition, utilizing a point source at infinity, whose geometrical size in the focal plane of the telescope is 0.00127 cm diameter and using visible light centered around the mercury green line, the amount of energy contained in a pinhole 0.01016 cm in diameter shall not be less than 64 percent of that contained within a pinhole 0.127 cm diameter. These requirements are to be met at ambient temperatures between 40 and 90°F and after being subjected to the vibration environments that the telescope will see when the instrument is vibrated at the qualification levels.

Design and Fabrication. The telescope design is shown in Figure 3-6. The hyperboloid and paraboloid elements and the spacer are fabricated from Ultra Low Expansion quartz

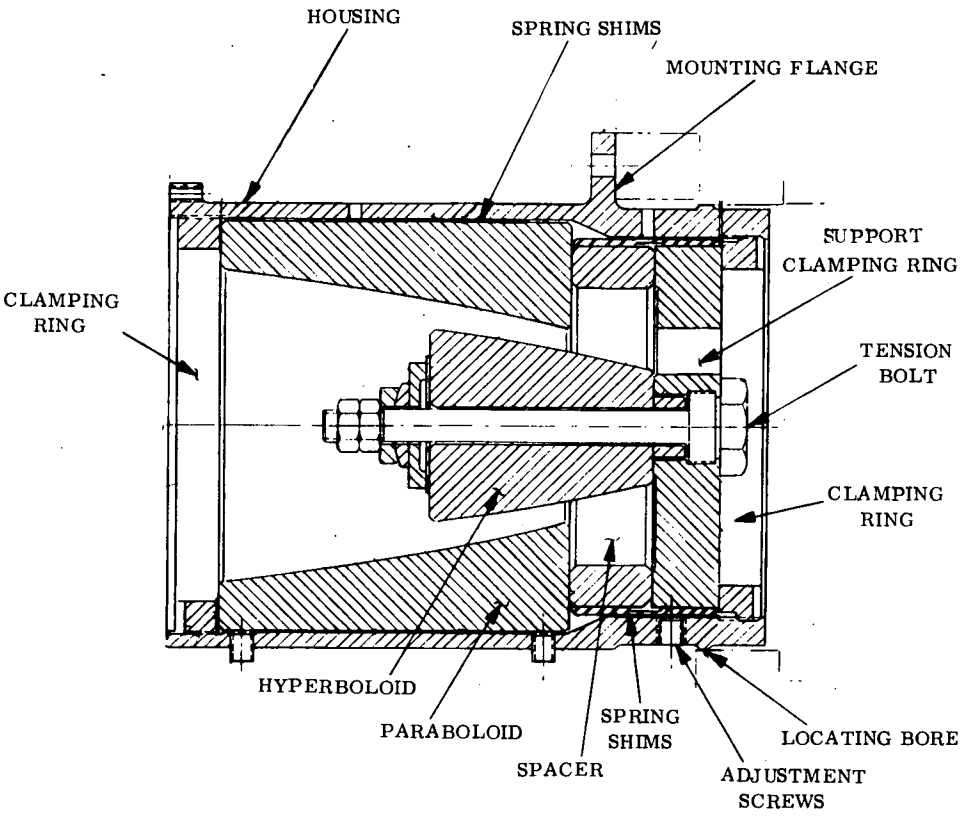

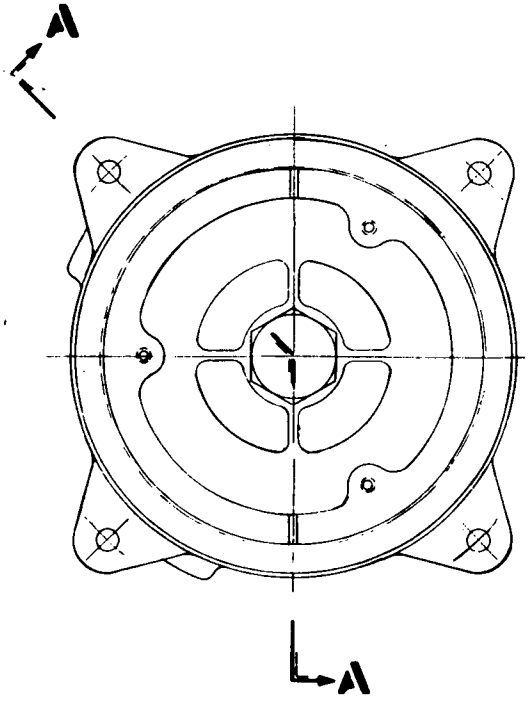

Figure 3-6. EUV Telescope

supplied by Corning Glass. The optical surfaces are not coated with a reflective coating because early testing indicated a single surface reflectivity of the bare quartz surface of 50 percent at 304 Å which was adequate to meet performance requirements. The telescope housing and hyperboloid support are fabricated from beryllium. The paraboloid is supported circumferentially in the housing by spring shims at its forward and aft ends. The hyperboloid is mounted to its support by a beryllium tension bolt. The hyperboloid support is restrained by circumferential spring shims and twelve set screws through the housing. The entire assembly is clamped in the housing by threaded rings at each end of the assembly. The axial spacing and tilt alignment of the hyperboloid to paraboloid is determined by the thickness and wedge angle of the quartz spacer between the hyperboloid support and the rear face of the paraboloid. The concentricity of the hyperboloid to the paraboloid is set by adjustment of the spring shims and set screws around the circumference of the hyperboloid support. Tilt alignment in the order of 2 arc-seconds, concentricity in the order of 12.7×10^{-5} cm and axial adjustment in the order of 25.4×10^{-5} cm is required to maintain high resolution of the telescope.

Initial prototype instrument vibration testing caused degradation of the telescope resolution. The degradation was due to a shift in concentricity between the hyperboloid and paraboloid. The corrective action was to stiffen the paraboloid support in the housing by replacing the mylar shims with spring shims previously described and by adding shims described above between the hyperboloid support and housing. The performance resulting from these design changes is subsequently described.

Testing. The energy distribution through a 0.01016 cm diameter pinhole in the focal plane as compared to a 0.127 cm diameter hole was measured on the initial telescope assemblies and found to be from 70 to 75 percent in visible light and 36 to 46 percent at 304Å.

The final assembly telescope testing after the design revisions, consisted of measurement of the tilt and concentricity alignment of the elements in the assembly, measurement of the resolution in visible light, vibration to qualification levels as amplified by the instrument structure, and final remeasurement of alignment and resolution.

The tilt and concentricity measurements were accomplished on the telescope measurement facility shown in Figure 3-7. By means of the autocollimator viewing the reflective surface on the front of the hyperboloid which is normal to the optical axis of the hyperboloid, the optical axis of the hyperboloid is established parallel to the axis of the rotary table. The concentricity between the forward and aft optical surfaces of the paraboloid is then a measure of the tilt of the paraboloid to the hyperboloid and the concentricity between the optical surface of the hyperboloid and the aft optical surface of the paraboloid is a measure of the concentricity of these two elements. The charts recording these measurements before and after vibration are shown in Figure 3-8. Within the accuracy of measurements ($\pm$ 10 x 10^{-6} inches and $\pm$ 1 arc-sec) no movement of the optical elements was detected. The results shown are for flight telescope (No. 3).

The resolution in visible light was measured as shown in Figure 3-9. The source was two illuminated 10 arc-second pinholes separated by a space of 10 arc-seconds. The distance from the telescope to the exit slit was varied in steps and the output of the photomultiplier was recorded on a strip chart for each focus position as the source was moved in a direction perpendicular to the exit slit. The magnitude of the dip between the peaks is a measure of the resolution. The focus adjustment for maximum dip was selected as the optimum focus for installation in the instrument. A typical resolution run is shown in Figure 3-10 and a plot to determine optimum focus is shown in Figure 3-11. All data presented is for the flight telescope (No. 3).

The vibration levels applied to the telescope are given in Figure 3-12. These levels are amplified levels as determined by instrumentation of the prototype instrument vibration test.

Since early telescope testing had established the degree of degradation of resolution from visible to EUV as being from about 75 to 30 percent, the final telescope was not tested in EUV as a component. EUV testing of resolution was done in the complete instrument during instrument calibration as discussed later.

Figure 3-7. Telescope Measurements Facility

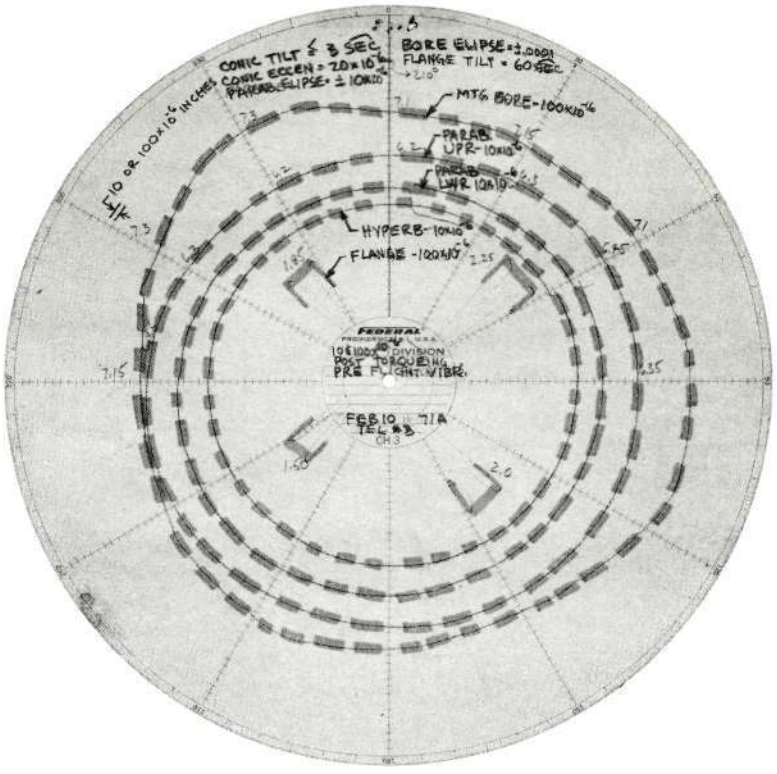

A. Pre-vibration

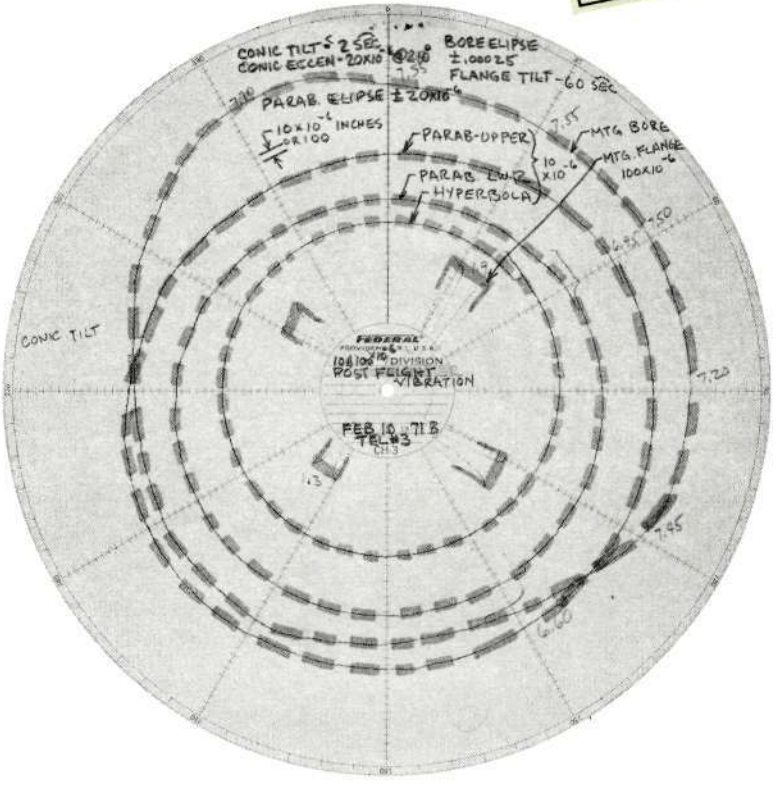

B. Post-Vibration

Figure 3-8. Telescope Measurements

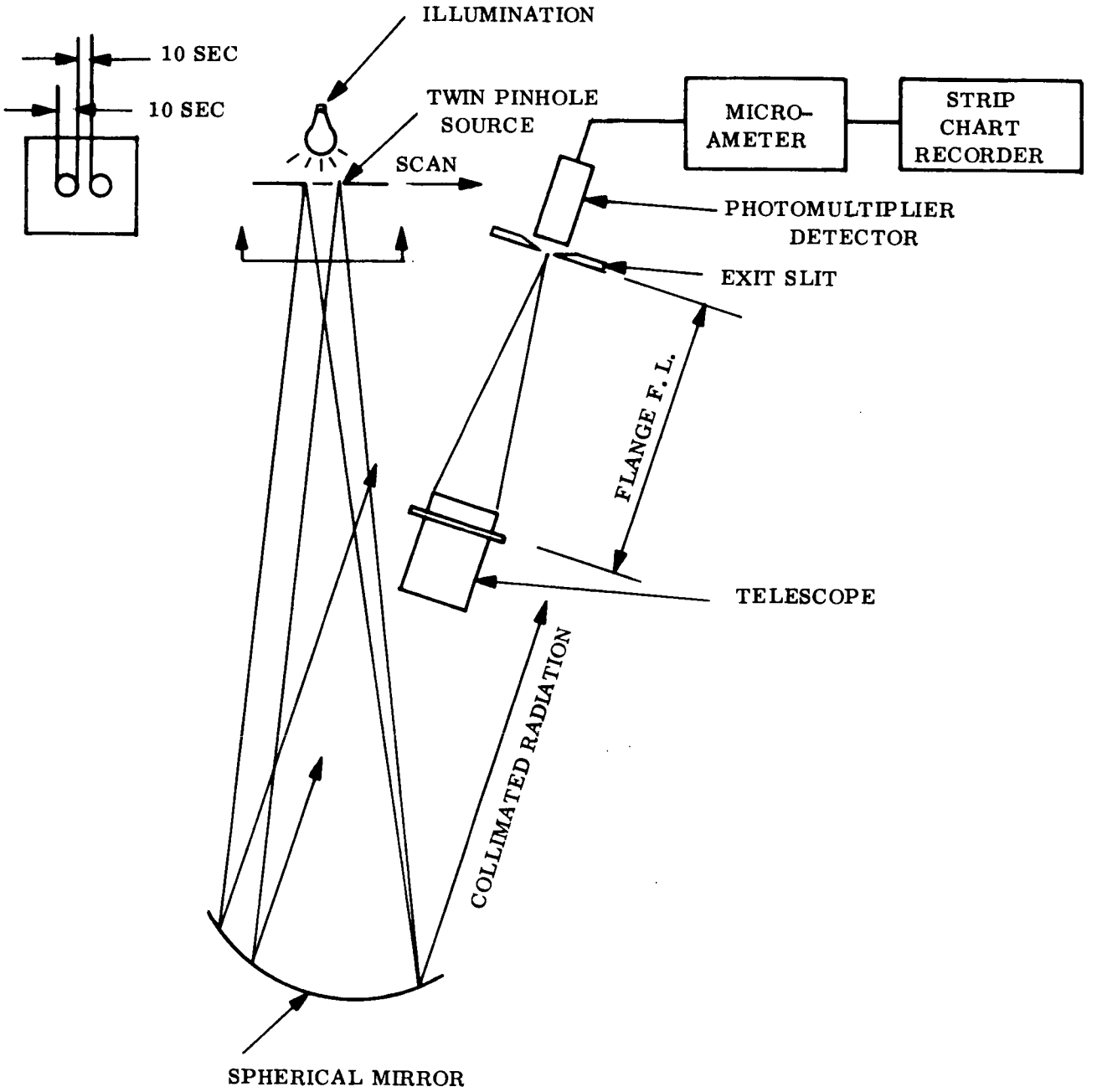

Figure 3-9. Telescope Resolution Measurement

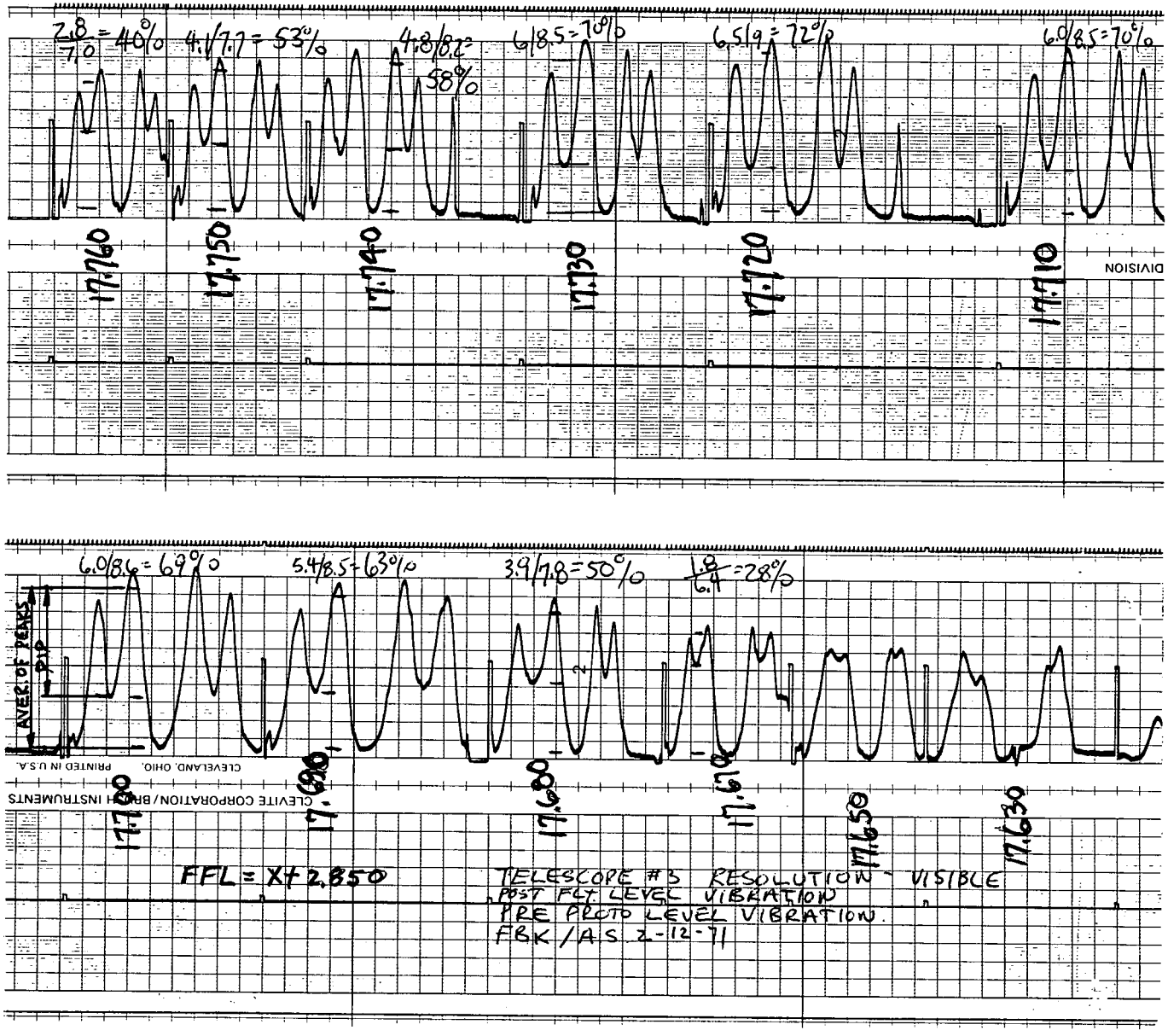

Figure 3-10. Telescope Resolution Data

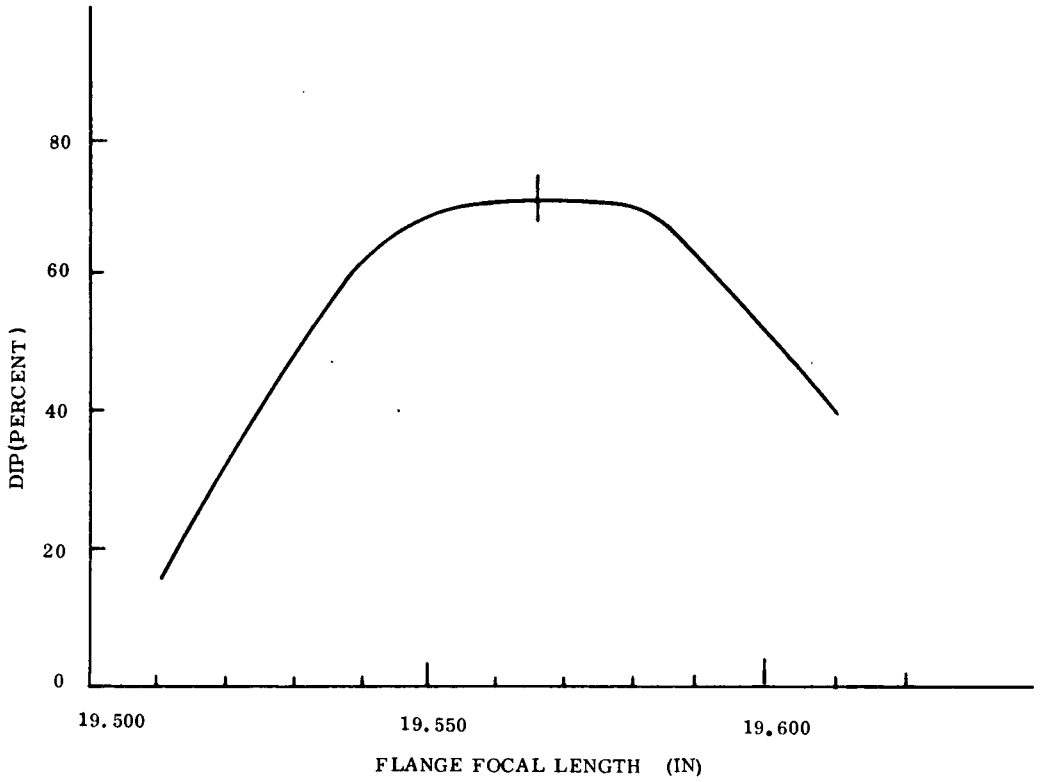

Figure 3-11. Telescope No. 3 Resolution in Visible Light Post-Flight Vibration

A special test was run on telescope No. 3 as reported in OSO-H-332 to determine if there was any shift of focus from visible to EUV. Test results showed no change so that the focus established by the visible test was used in the flight configuration.

3.2.2.2 Entrance Aperture

The entrance aperture as shown in Figure 3-13, located in the focal plane of the telescope, consists of a 20 arc-second wide fixed slit normal to the instrument base plate and a rotating slit assembly that limits the height of the fixed slit on the optical axis to 10, 20, 40 or 60 arc-seconds or scans across the solar disc along the fixed slit with a 20 arc-second aperture as a function of the rotary position. The rotating assembly is driven by a stepper motor and gear reduction unit. Two microswitches provide position indication of the rotary assembly and advance the position to a fixed reference position.

I SINUSOIDAL - SWEEP RATE 2 OCTAVES PER MINUTE

AXIS	FREQUENCY (Hz)	LEVEL (0 - peak g's)
X-X	5-800	3.3*
	800-900	10.0
	900-1000	16.6
	1000-1300	23.3
	1300-2000	13.3
Y-Y	5-150	3.3*
	150-220	10.0
	220-260	18.6
	260-1100	10.0
	1100-1400	23.3
	1400-2000	16.6
Z-Z	5-40	3.3
	40-70	12.0
	70-800	4.0
	800-900	8.0
	900-1000	12.0
	1000-1200	14.0
	1200-2000	4.0

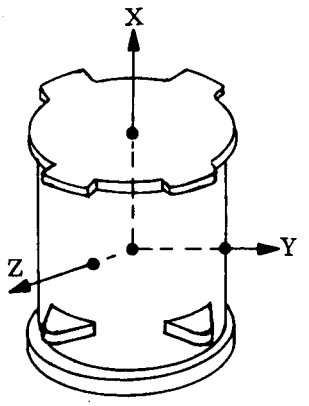

II RANDOM - DURATION 2 MINUTES PER AXIS

AXIS	FREQUENCY (Hz)	PSD LEVEL (g^2/Hz)	ACCELERATION (g-rms)
X-X	50-300	0.004-0.040**	18.6
	300-800	0.040	
	800-1000	0.040-0.666**	
	1000-1300	0.666	
	1300-2000	0.666-0.044**	
Y-Y	42-100	0.004-0.013**	24.7
	100-200	0.013-0.266**	
	200-1000	0.266	
	1000-1200	0.888	
	1200-2000	0.888-0.044**	
ZZ	50-300	0.004-0.040**	17.3
	300-1000	0.040-0.444**	
	1000-1200	0.444	
	1200-2000	0.444-0.044**	

*LIMITED TO 1/2 IN. D.A.
**INCREASING OR DECREASING AT A CONSTANT RATE.

Figure 3-12. Telescope Vibration Levels

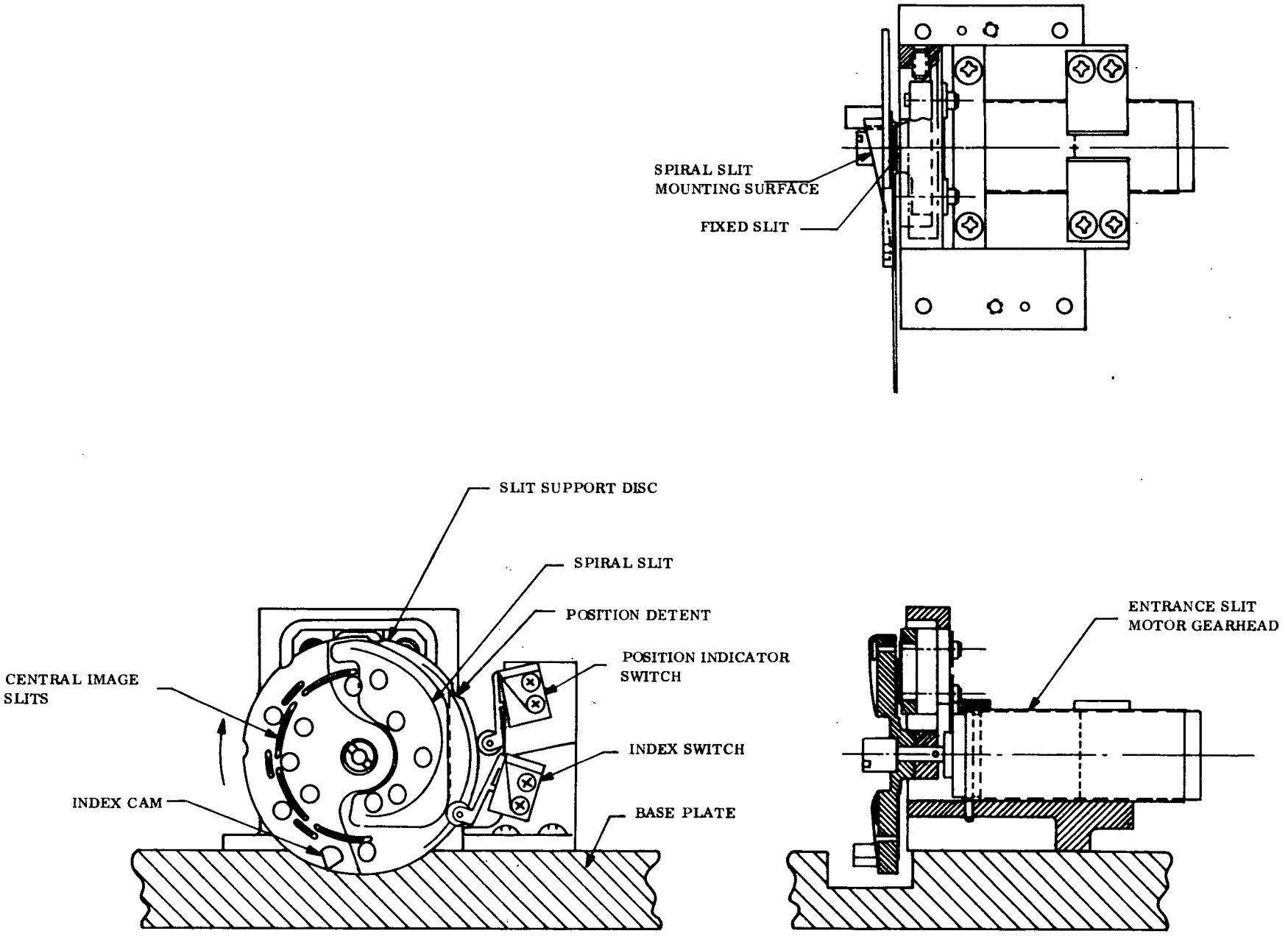

Figure 3-13. EUV Entrance Slit Assembly

Fixed Slit. The fixed slit is bonded to the entrance slit mounting base. The slit defined on GE drawing 47C217099, is fabricated by electroplating nickel on a 0.00762 cm thick electrolytic copper substrate to a thickness of 0.000762 cm around the desired slit configuration. The copper is then etched away in the area of the slit so that the desired slit configuration is formed by the nickel plating. This technique is used for all the slits in the instrument.

Rotating Slit Assembly. The rotating slit assembly (Ref. Drawing 47E217392) consists of the four central aperture slits and a single spiral slit. The central aperture slits are of constant radius from the center of rotation so as to always be on the optical centerline. They occupy approximately equal arc segments in 180 degrees of the disc. The blank space between the slits is bridged by a slit of larger radius so that a failure of the rotating slit drive cannot block the incoming radiation. One half of each slit segment is covered by a thin filter that attenuates the radiation by a factor of approximately 5.

The spiral slit occupies the remaining 180 degrees of the disc. The radial distance of the spiral varies such that the spiral scans the diameter of the solar disc as the slit is rotated. The face of the rotating disc, to which the spiral slit is mounted, is inclined to the plane normal to the axis of rotation of the disc such that as the disc rotates the axial position of the slit varies, being of longest focal length when the spiral slit is on the center of the solar disc and moving to a shorter focal length position as the spiral slit moves to either edge of the solar disc. In this way the slit approximates the optimum focal length of the telescope for off-axis radiation as shown in Figure 3-5. Slits are fabricated as previously described.

The motor step positions of each slit and filter from the reference is shown in Figure 4-7. The total entrance slit aperture area for each step position of the disc is, in general, proportional to the width of the rotating slit at that point. In the position of the bridges there will be a discontinuity of either greater or less area due to the specific detail of the overlap of the bridge slit with the main slit. Over the travel of the spiral slit, the area is slightly variable because the spiral edges form a trapezoided rather than a square entrance aperture and the shape of the trapezoid varies from one end of the spiral travel to the other. In addition, there are three small areas in which a narrow tie across the spiral slit is provided for structural integrity.

Motor Gearhead Assembly. The motor gearhead assembly consists of a 90 degree stepper motor with a reduction gear assembly attached to the output shaft of the motor. All five motors in the instrument are identical and the gear heads are similar varying in gear reduction ratio and size to suit the particular application. The characteristics of the motor are specified in GE Drawing 47D216200 and the gearheads on GE Drawing 47D216201.

The motors and gearheads use a solid film lubrication system which is Lubeco 905 applied in accordance with General Electric Specification 171A4567, except for the two motor bearings which utilize a Rulon C bearing cage. In addition, except for the filter wheel units, the motor gearhead is a sealed assembly to minimize loss of atmospheric pressure around the bearing surfaces as an additional protection to the lubrication system and to minimize the free backlash in the gearhead.

3.2.2.3 EUV Grating

The grating is curved with a 1 meter radius. The ruling constant is 1152 lines/mm and the blaze is optimized for the 170 to 400 $\mathring{A}$ band. Because the grating is wider than its optimum width, it was necessary to compensate for this by relocating the grating from its theoretical position. It was found that a position about 0.03 cm inside the Rowland circle gave best resolution. The grating movement allowed 3 degrees of freedom for grating alignment and no difficulties were experienced either in alignment or testing of the spectrometer. The grating efficiency was measured at 14 percent at 304 $\mathring{A}$.

3.2.2.4. EUV Detectors

All three EUV detectors are Bendix Magnetic Electron Multipliers (MEM's). Some of the requirements are as follows. The efficiency was originally specified at 5 percent. By measuring the total EUV system efficiency as well as the telescope and grating efficiency a detector efficiency of 3 percent is deduced. This should, however, not be of concern the total EUV subsystem efficiency is twice as high as specified.

The signal noise count was specified at 120 counts per minute; it was measured at 60 to 110 counts per minute as an average. The detector plateau was originally specified to 3%/100 volts, but this value could not be realized. A new limit of 10%/100 volts was then set. Actual measurements gave a value of 3-8%/100 volts.

Integral pulse height resolution was specified at an allowable count rate change of $\leq$ 25% for a 10:1 change in threshold setting. Measured results were values of 18 to 22 percent. Orbit stability was given as less than 2 percent in 60 minutes, it was measured at 0.5 to 1.0 percent on the average.

Count rate range was originally specified at 10^5 counts per second. While the detector itself will perform over this range, the characteristic of the electronics will cause saturation at lower values of count rates. Measured linearity data with an Fe^{55} source shows that saturation starts occurring at count rates above 2×10^4 cps.

3.2.2.5 EUV Sensor Electronics

The function of the EUV sensor electronics is to amplify, discriminate, and condition the output of the three magnetic electron multiplier (MEM) tubes which are used for EUV detectors. To accomplish this task each MEM is connected to an independent amplifier discriminator chain which is composed of a charge integrating preamplifier, a two stage linear voltage amplifier and a low level discriminator. A block diagram of the amplifier-discriminator chain is shown in Figure 3-14.

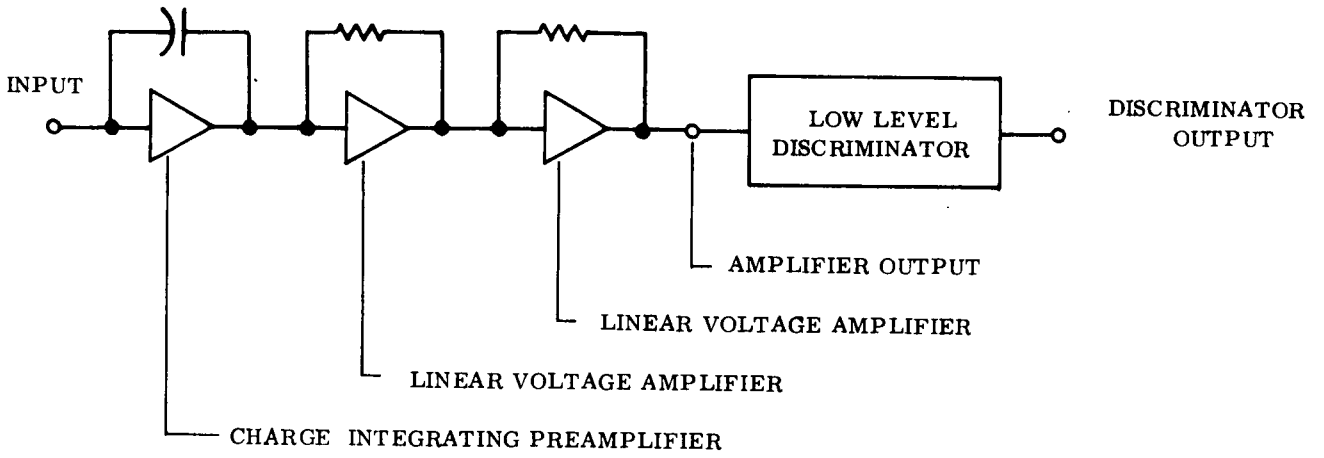

Figure 3-14. EUV Amplifier-Discriminator Chain

The amplifier chain amplifies 170 ηs current pulses of amplitudes ranging from 60 ηa to 3.6 μa to a level which can be discriminated (about 0.1v to 6.0v) with a resolution time of 2 μsec. Figure 3-16 shows the schematic for the charge integrating preamplifier and Figure 3-17 shows the schematic for the linear voltage amplifiers. A typical input-output waveform for the amplifier chain is shown in Figure 3-15.

The charge integrating preamplifier produces a voltage at its output which is proportional to the time integral of the input current. Such an amplifier minimizes the effect of stray input capacitance. The cascode input results in low noise and high gain. Each amplifier is a low noise video amplifier with high open loop gain, a closed loop gain of about 10 and a bandwidth of about 400 MHz. A large amount of negative feedback ensures the desired frequency response and excellent gain stability over extreme line voltage and temperature variations. It also ensures against gain changes due to component changes. A low operating power was achieved through the use of low leakage and low noise transistors with high beta and low operation currents.

Each amplifier output is discriminated by a low level threshold detector. The schematic is shown in Figure 3-18. This circuit utilizes a differential input stage followed by a two transistor output stage. Feedback is applied from the input to the reference input of the

INPUT WAVEFORM

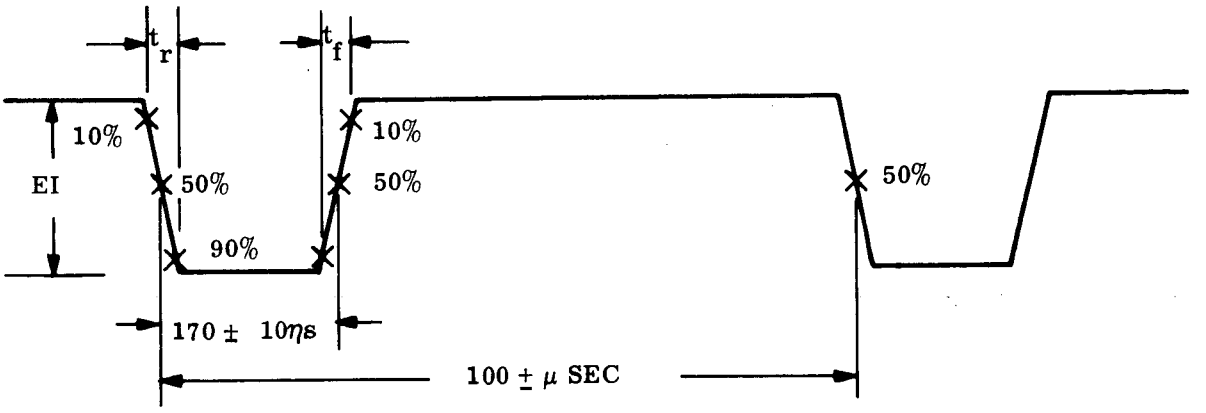

EI = 2.4 μa ± 0.1 μa

t_r ≤ 15 η sec

t_f ≤ 15 η sec

OUTPUT WAVEFORM

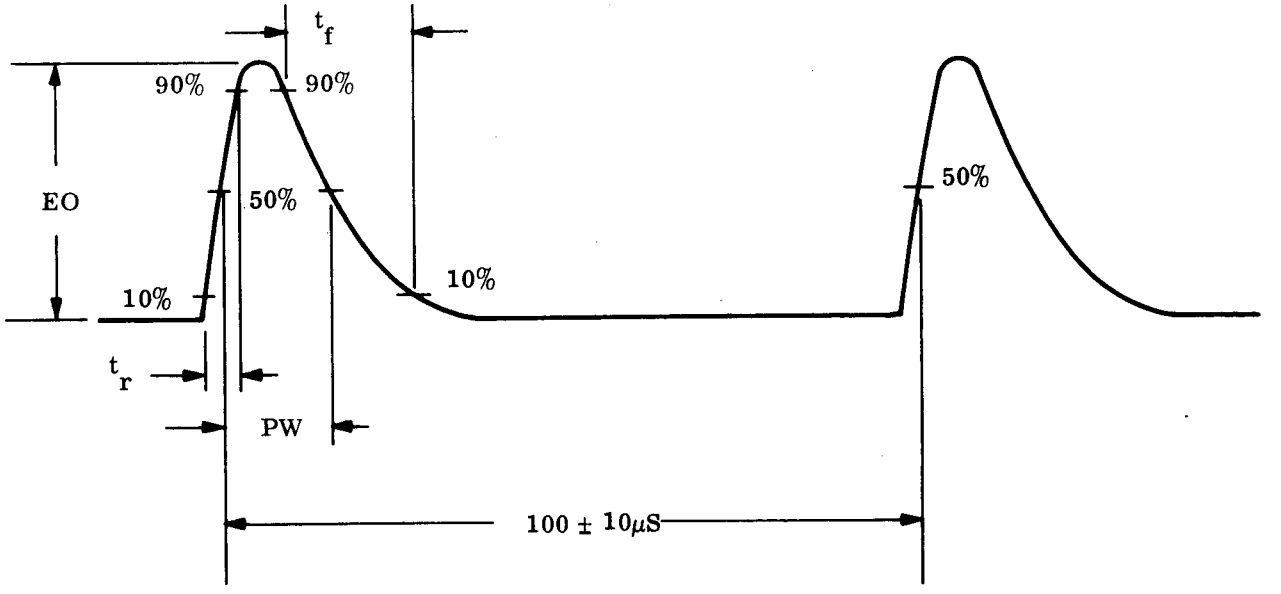

EO ≃ 4.0V

t_r ≤ 265 η sec

t_f ≤ 1.5 μ sec

PW ≤ 880 η sec

Figure 3-15. Typical Input-Output Waveforms

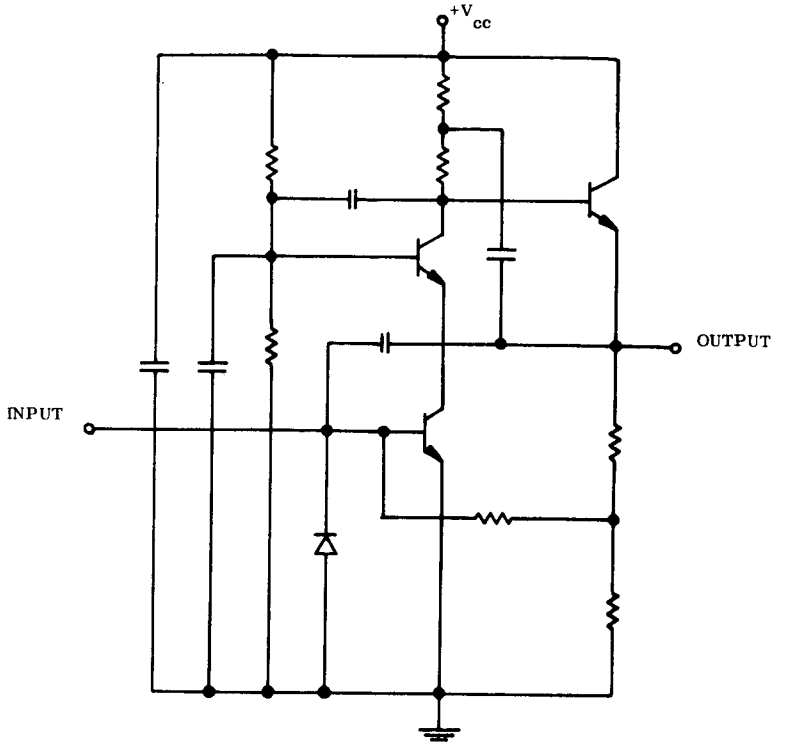

Figure 3-16. Charge Integrating Preamplifier

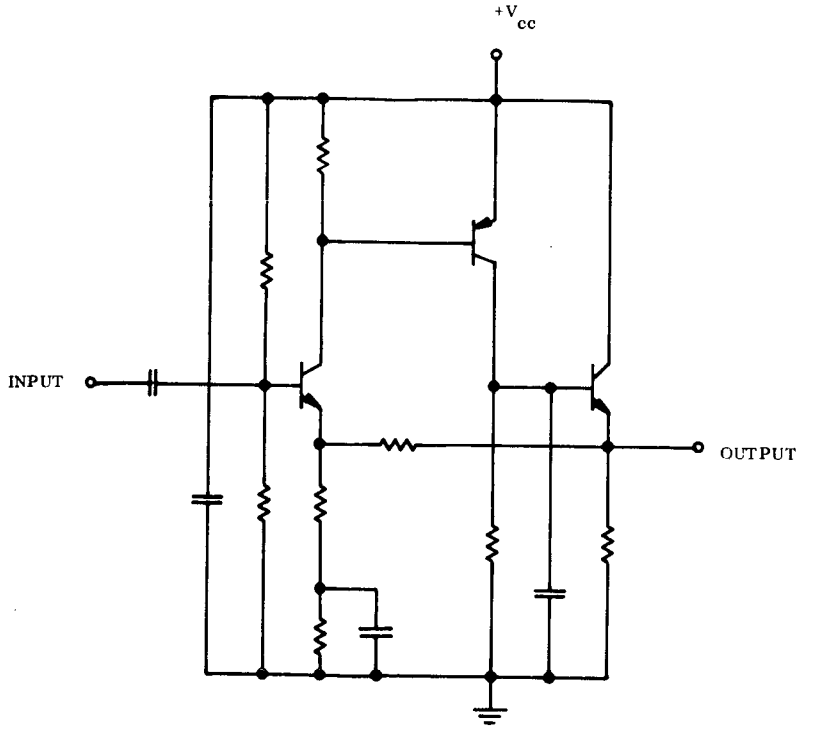

Figure 3-17. Linear Voltage Amplifier

differential amplifier. The feedback serves to control the output pulse width and thus ensures a fast recovery time.

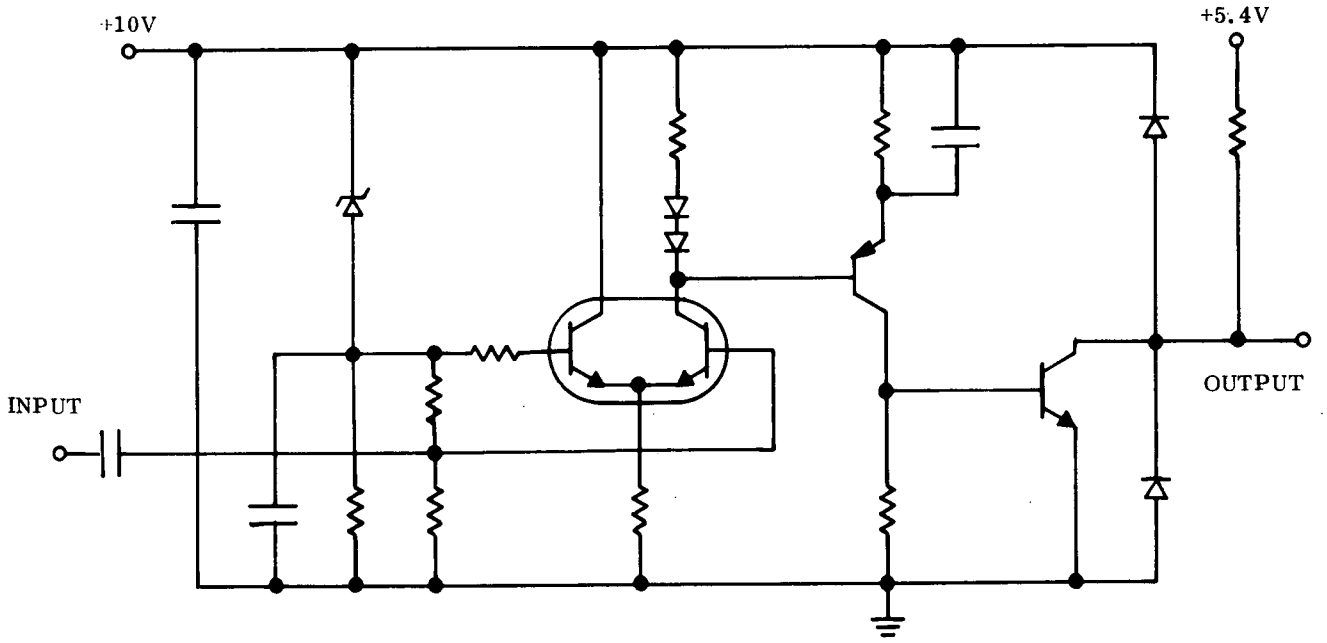

Figure 3-18. Low Level Threshold Detector (Discriminator)

The overall amplifier discriminator pair conform to or exceed the following requirements:

Input Charge Resolution	10^{-15} to 6×10^{-14} coul
Pulse-Pair Resolution Time	2 μ sec
Equivalent Input Noise	Less than 10^{-15} coul
Standby Power	Less than 15 mw
Discriminator Threshold	100 mV
Discriminator Output Pulse Width	Approx. 1μ sec
Discriminator Output Voltage for Logical "1"	2.5V
Discriminator Output Voltage for Logical "0"	0.5V

3.2.2.6 Data Processing Electronics

The data handling is accomplished by the use of series 54L Texas Instrument logic circuits.

In general, the output of a discriminator is coupled into a 14-stage counter through a detector selection circuit. The counter accumulates counts from the appropriate discriminator for 125 ms. The counter is disabled and the 14-bit word is compressed into an 8-bit word which is transmitted to the spacecraft. The counter is then cleared (reset to zero) and enabled again, thus starting the sequence again. The entire sequence takes 160 ms.

The data selection circuit is shown in Figure 3-19. Short and Medium EUV share a 14-stage counter (see Figure 3-20). The data selection circuit locks out the data from the discriminator not selected and couples the data from the desired discriminator into the counter. This circuit also performs the automatic data readout switching function at the end of raster in response to command XN-11 (GSFC RO UV AUTO). Since H-Alpha and long EUV have separate counters (H-Alpha has an 8-stage counter and Long EUV a 14-stage counter), the data from both detectors is always registered in their respective counters, but the signals from the points designated U and V enable the readout of the selected channel and disable the readout of channel not selected. Furthermore, this circuit is used to perform the enable/disable function for the counter shared by Short and Medium EUV in response to the appropriate timing function ($\overline{A + W}$).

Data compression is achieved by interrogating the 14-stage counter to locate the position of the most significant bit within the register. The interrogation is achieved by counting from the MSB toward the LSB until a "1" is encountered. A 4-stage ripple counter is used to register the location of the most significant "1". The contents of that counter are read out during the first four telemetry bit times in the appropriate word gate and the contents of the next four most significant bits in the 14-stage counter are read out during the last four telemetry bit times in that same word. The most significant bit in the data is read out first and the least significant bit is read out last.

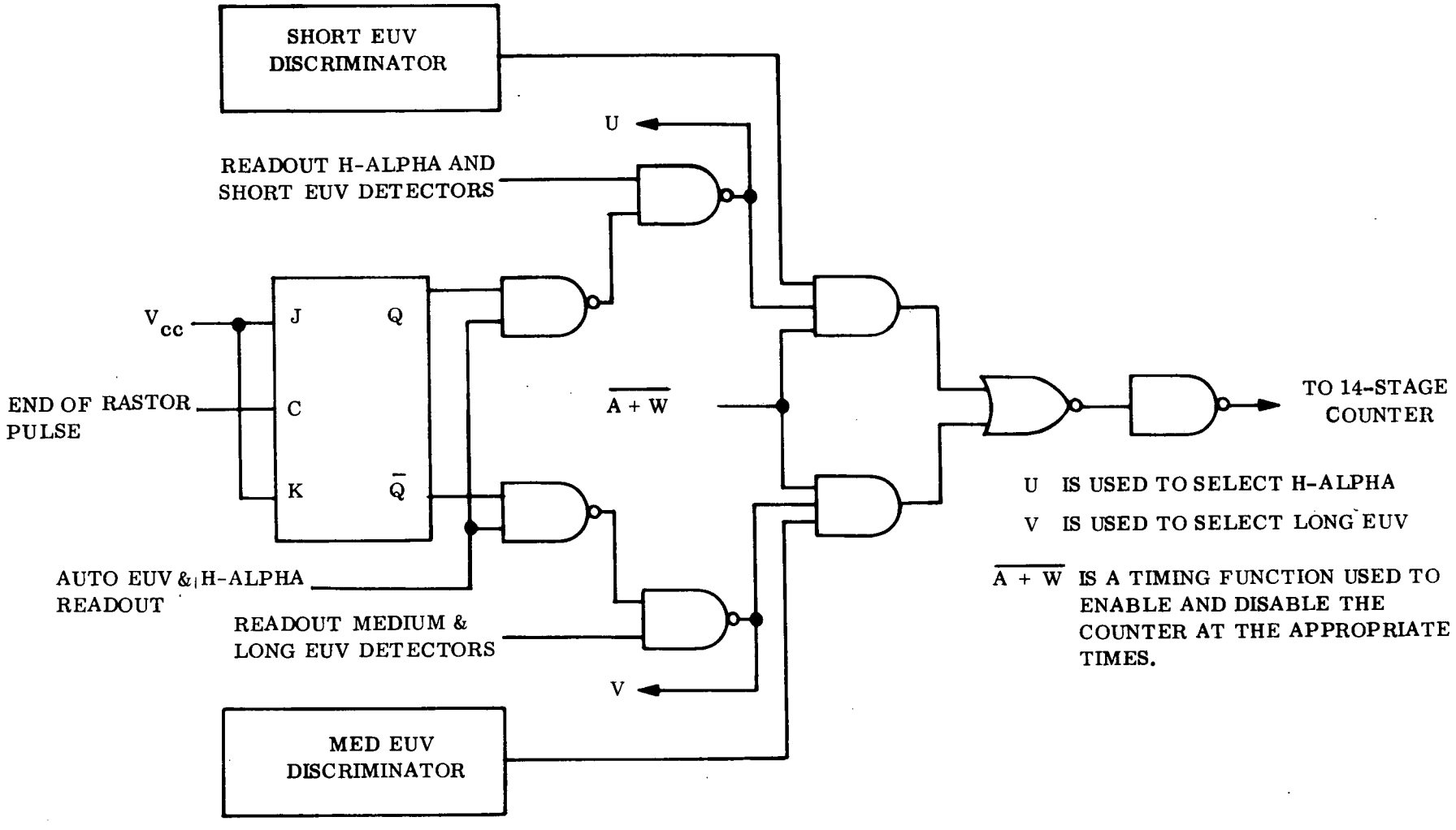

Figure 3-19. EUV Data Selection Circuit

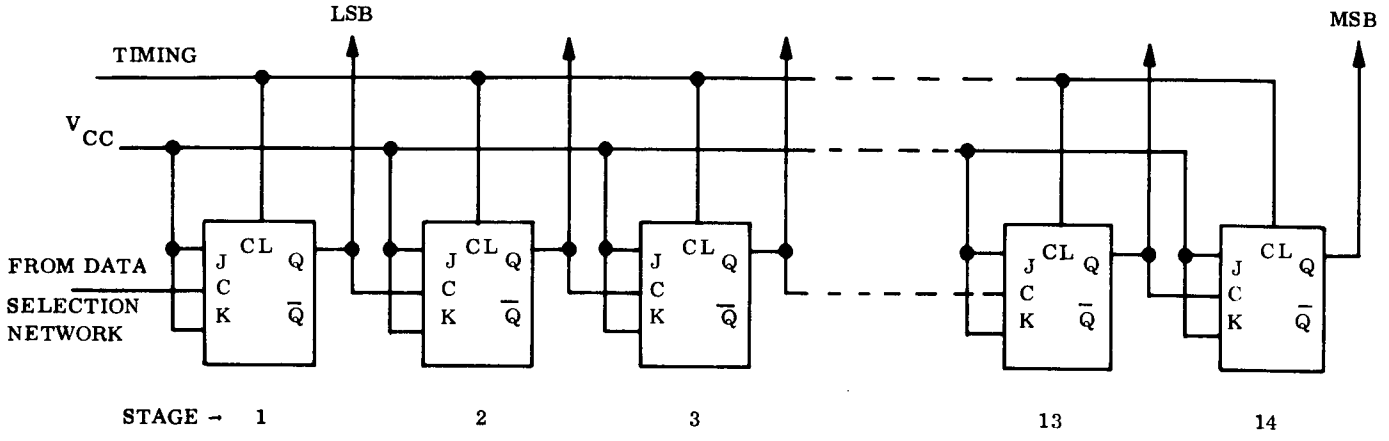

Figure 3-20. 14-Stage Counter

Data decompression is accomplished by reducing the telemetered 8-bit word into two 4-bit words and inserting the decimal equivalent of the two words into the following equation.

$$\text{Decompressed Data Value} = (B + 16)\ (2^{10-A}) \text{ where}$$

A is the decimal equivalent of the first 4-bit word

B is the decimal equivalent of the second 4-bit word

Example:

0 0 1 1 0 1 0 1		- 8-bit word
0 0 1 1	0 1 0 1	- 2 4-bit words

0 0 1 1 = 3 = A

0 1 0 1 = 5 = B

$$(5 + 16)\ (2^{10-3}) =$$

$$(21)\quad (2^{7}) \quad = 2688$$

As a result of the data compression a certain amount of data is lost. The possible error in the count actually appearing in the telemetered data is a function of the magnitude of the count. The following table defines the possible error as a function of the count.

Data Range	Maximum Possible Round Off Error
2 - 31	0
32 - 62	1
64 - 125	3
128 - 248	7
256 - 496	15
512 - 992	31
1024 - 1984	63
2048 - 3968	127
4096 - 7936	255
8192 - 15360	511
15872	∞

In addition, note that there is a count of 2 built into the EUV data accumulation logic.

Digital main frame (DMF) words 3 and 19 are used for H-Alpha or Medium EUV and DMF words 7 and 23 are used for Short EUV or Long EUV depending on which data is requested by command. Command XN-53 selects H-Alpha and Short EUV and Command XN-60 selects Medium EUV and Long EUV.

3.2.2.7 Housekeeping Electronics

Digital Subframe (DSF) word gates 2, 14, 26 and 38 are assigned to EUV Housekeeping. Each word is 8 bits in length and the bits are assigned the following functions:

TB1 Mask Position ("1" indicates B and "0" indicates A)

TB2 Direction of Spectral Scan ("1" indicates carriage will move or is moving toward the long wavelength end)

TB3 Spectral Scan - stopped or moving ("1" indicates moving)

TB4, TB5, TB6 } Spatial Scan Aperture Selected

	Code		
Aperture Selected	TB4	TB5	TB6
Slit Scan	0	0	0
10-Second Aperture	0	0	1
20-Second Aperture	0	1	0
40-Second Aperture	0	1	1
60-Second Aperture	1	0	0

TB7 Detectors Selected

"1" indicates H-Alpha and Short EUV
"0" indicates Long and Medium EUV

TB8 Spare

Each data bit is generated by a microswitch and/or a relay contact. The signals from the appropriate microswitches and/or relays are processed using series 54L logic. Each of the telemetry bits are generated in the following way.

1. TB1 - Two microswitches are used to generate TB1. When the mask is in position A, microswitch MS3 is actuated and MS3 remains actuated until the mask is commanded to change positions (TB1 = "0")

   Upon execution of Command XN-10, the mask moves until MS4 is actuated. TB1 changes to "1" and MS4 remains actuated until XN-10 is sent again.

2. TB2 - Four relays and two microswitches are used to generate TB2. When Command XN-23 is executed, Relay K3 is used to establish the direction of motion toward the long wavelength end and when the carriage reaches that end, microswitch MS5 is used to reverse the direction of motion. Similarly when Command XN-48 is executed, Relay K4 is used to establish the direction of motion toward the short wavelength end and when the carriage reaches that end, microswitch MS6 is used to reverse the direction of motion. When Command XN-20 is executed, Relay K6 is used to establish the next direction of motion toward the long wavelength end. Likewise, upon execution of XN-51, Relay K5 is used to establish the next direction of motion toward the short wavelength end.

3. TB3 - Relays K1, K2, K3 and K4 are used to generate a "1" in TB3 in response to Commands XN-15, XN-56, XN-23 and XN-48, respectively. Relays K5 and K6 are used to generate a "0" in TB3 in response to Commands XN-51 and XN-20, respectively. In addition the normally closed contacts of microswitches MS5 and MS6 are used to generate a "0" in TB3 after the execution of XN-23 and XN-48, respectively.

4. TB4, TB5 and TB6 - Microswitches MS7 and MS10 are used to generate TB4, TB5 and TB6. The signal from MS10 is used to clear a three-stage counter, thus setting TB4, TB5 and TB6 equal to zero. Each time MS7 is actuated the counter counts once. Since there are four detents which cause MS7 to be actuated before the wheel returns to the reference position, the counter counts to 4 before it is reset to zero by MS10.

5. TB7 - The signals from K29, K30 and K31 are used to generate TB7 in response to Commands XN-60, XN-53 and XN-11. XN-60 causes TB7 to be "0" and XN-53 causes TB7 to be "1". XN-11 enables an automatic switching function such that TB7 switches back and forth between "1" and "0" upon receipt of end of raster pulses.

In addition to the DSF housekeeping there are several housekeeping codes which appear in the DMF data. When the instrument receives either an end of line (EOL) or an end of raster (EOR) signal from the spacecraft, it locks a coded word into the DMF data. This effectively locks out the scientific data for that particular word gate. EOL or EOR codes are read out during Word Gates 3, 4, 7 and 8. When the carriage actuates either Microswitch MS5 or MS6 at the end of the spectral scan (EOSS), the signal from the microswitch is used to generate a coded word which is also locked into a DMF word. End of spectral scan is read out during Word Gates 19, 20, 23 and 24.

When any of the coded words are generated, they are read out in all four of the appropriate word gates during the main frame (320 ms). There is no mechanism which disallows the code from appearing in the scientific data; therefore, if the code does not appear in all four of the appropriate word gates during the main frame, it should not be interpreted as housekeeping but rather as scientific data.

The codes are as follows:

	TB1	TB2	TB3	TB4	TB5	TB6	TB7	TB8	Decimal* Value	Decompressed** Decimal Value
EOL	0	0	1	0	1	0	1	0	42	6656
EOR	0	1	1	0	1	1	1	1	111	496
EOSS	0	1	1	0	1	1	0	0	108	448

*The decimal value is the number which would be read out in the H-Alpha channel. It is a straight decimal equivalent of the binary word.

**The decompressed decimal value is the number which would be read out in the EUV or X-Ray channels.

In addition the EOR code is actually the binary sum of two coded words. The spacecraft sends two signals to the instrument at the end of raster and it is the sum of two coded words which is read out in the data as EOR. However, when the spacecraft is commanded into the raster mode, the spacecraft generates only one of the coded words until it finds the corner of the raster (starting point of the raster). This work wil be locked into Word Gates 3, 4, 7 and 8 until the spacecraft finds the corner and starts the raster and decodes to 69 in the H-Alpha channel and to 3144 in the EUV and X-ray channels.

3.2.2.8 Carriage Assembly

The carriage assembly shown in Figure 3-21 is a machined beryllium frame containing the three Bendix magnetic electron multiplier detectors, six spectrometer exit slits positioned on the spectrometer focal circle, the movable mask to select the desired group of three exit slits, the two microswitches for selecting the exit slit mask position, and the motor gearhead drive for the mask. The carriage is movable along the focal circle to cover the wavelength range of 170 Å to 400 Å in approximately 0.07 Å steps. At one unique position the six exit slits are aligned with six selected EUV lines, three of which can be viewed simultaneously by each of the three detectors as selected by positioning the mask. In Mask Position A, the 211.4 Å, 284.1 Å, and 335.2 Å lines are viewed. In mask position B, the 180.6 Å, 255.1 Å, and 303.8 Å lines are viewed. The wavelength range for each detector and each mask position is shown in Figure 3-22.

Carriage Drive. The carriage is supported on a track fixed to the instrument base and curved to the focal circle radius. A recirculating ball bearing with the balls riding in "V" groove races in the track and carriage provides low friction and stiff support for the carriage motion. The carriage is driven by a motor gearhead assembly fixed to the instrument baseplate with the output pinion driving a curved rack on the carriage. The gearhead ratio and the pinion size are such that for each 90-degree step of the motor, the carriage travels a linear distance of 0.0011 inch or approximately 0.07 Å. The control logic provides for three separate speeds of travel 6.25, 12.5, or 50 steps per second. At the long wave and

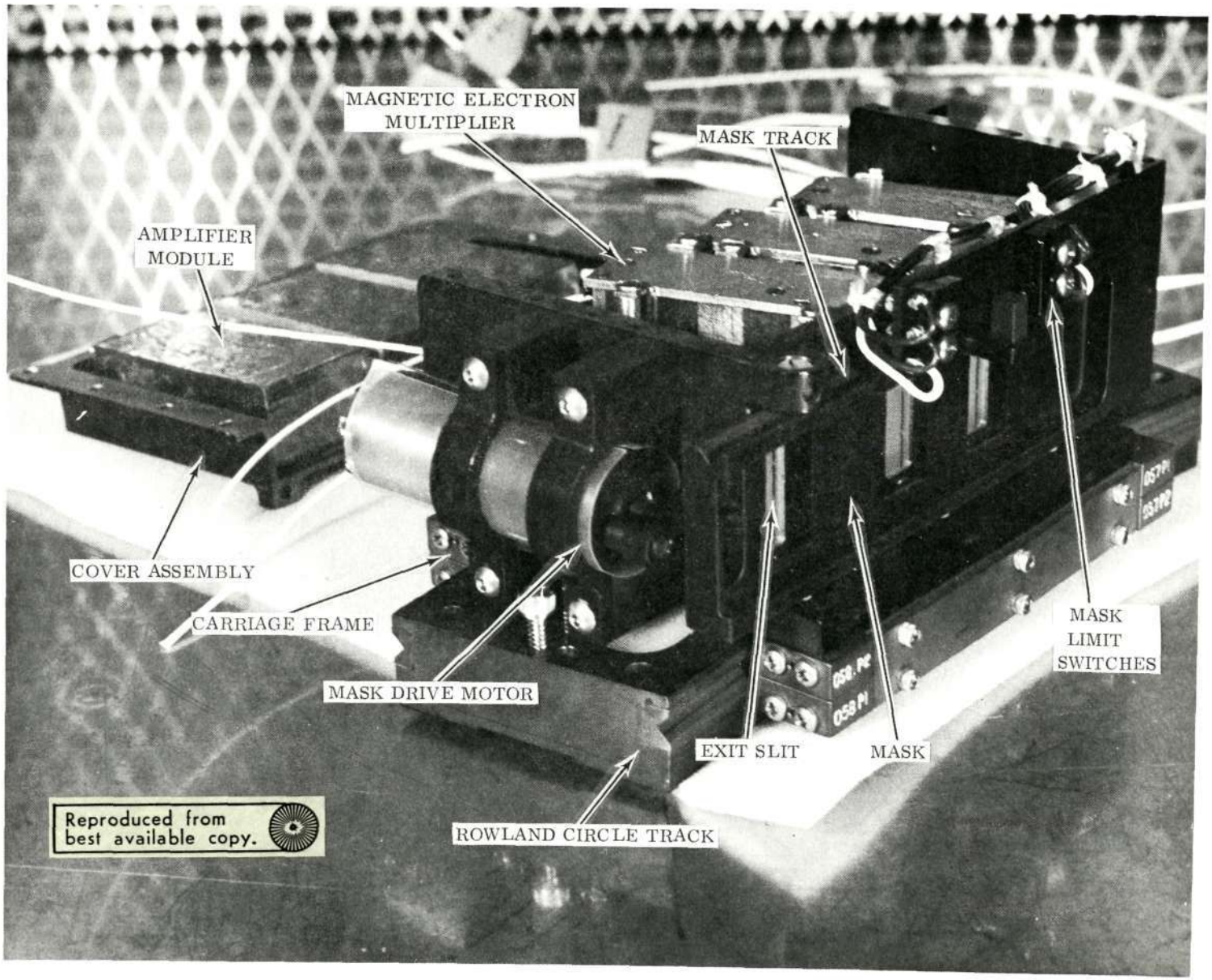

Figure 3-21. Carriage Assembly

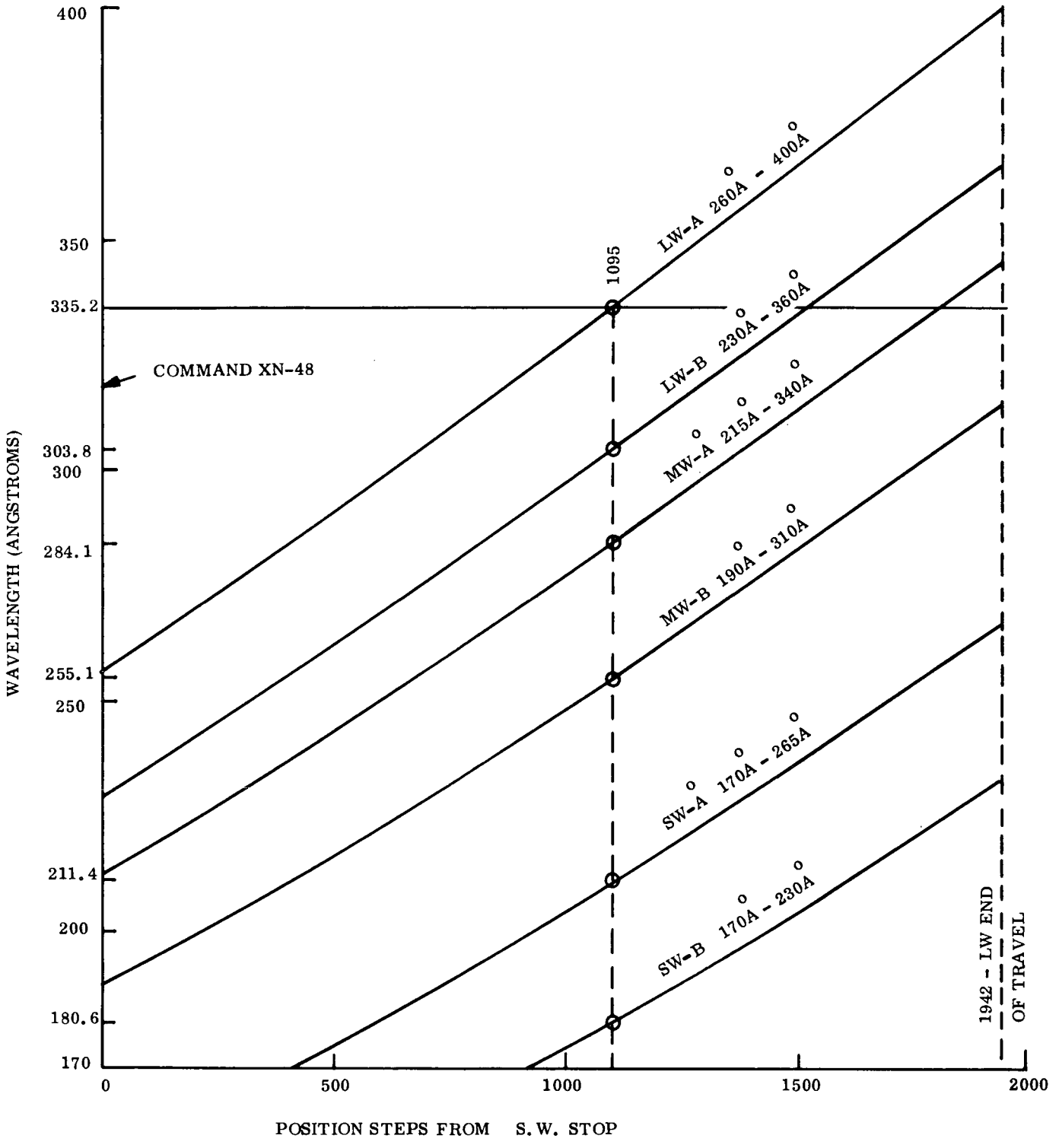

Figure 3-22. EUV Detectors Wavelength Range

short wave limit of its travel, the carriage actuates separate microswitches which give an indication to the control logic that the limit has been reached. The logic reverses the direction of travel and when so commanded, stops the travel.

The motor gearhead assembly, the rack and pinion, the carriage bearing races, and the ball return slots are lubricated with the same solid film lubricant process previously described in paragraph 3.2.2.2.

Exit Slit Assembly. The six exit slits are precisely positioned on a single exit slit foil by the plating and etching process described in paragraph 3.2.2.2. The foil is then mounted to a frame and the assembly is attached to the carriage. Particular care is taken in mounting the foil to the frame to maintain the slit leading and trailing edge in the same plane. Because of the shallow angle at which that the radiation passes through the slit, any out of plane condition of the two edges would appear to be a change in width of the slit, thus affecting the spectral resolution. The spacing between the six slits is accurately held so that the six selected spectral lines appear simultaneously at the same carriage position. Because slits are tangent to the Rowland circle, their width is such that the projected width, in a plane perpendicular to the incident radiation, is 85 μm. Spectral width measurements show that the effective width is uniform within 0.1 $\text{\AA}$ from slit to slit.

Exit Slit Mask and Drive. The exit slit mask is positioned immediately in front of the exit slits and travels in a "V" groove track parallel to the slit plane. At one end of its travel, it uncovers the three "A" position slits and at the other end, the three "B" position slits. The mask is driven by a motor gearhead through a crank attached to the gearhead output shaft. The travel of the mask is stopped by actuation of a microswitch at each end of its travel. The motor, gearhead and the "V" groove track are lubricated with the same solid film lubricant process previously described in paragraph 3.2.2.2.

3.2.2.9 Flexprints

The electrical connection between the instrument electrical system and the movable carriage is made through two flexprints. One flexprint contains the two high voltage conductors and the second contains 21 low voltage conductors. The conductors are etched copper ribbons between Kapton substrates and an external coating of Teflon. The thickness of the copper

conductors are 0.0027 inch for the low voltage flexprint and 0.0054 inch for the high voltage flexprint. The thickness of the Kapton is 0.002 inch in both cases.

The original thickness of the low voltage flexprint was 0.0054 inch. However, it was determined by life tests that this thickness was unsuitable for the bend configuration and flexing modes of the low voltage flexprint. The thickness was changed to 0.0027 inch and subsequent life tests show no failures after 43,000 cycles.

The high voltage flexprint with the 0.0054 inch thick conductors was life tested and withstood 41,000 cycles before failure. Forty-one thousand cycles represents a safety factor of approximately 4 based on the expected one-year operational mode of the instrument. This configuration was considered adequate and no change was made to the design.

3.2.2.10 Launch Lock

The launch lock is a pyrotechnic operated device which secures the movable carriage to the track during the application of the vibration and acceleration loads of the launch environment. The launch lock is fired upon command after orbit has been achieved and spacecraft separation has occurred.

The launch lock assembly is shown in Figure 3-23. The launch lock housing is mounted externally on the instrument base plate. A retractable pin projects through the base plate into a close fitting hole in the carriage assembly. The locking pin is loaded by a combination torsion and compression spring. The torsion holds the pin in the locked position in a detent in the housing. The pin is rotated against this torsion load and out of the detent by dual pyrotechnically actuated pistons. The compression in the spring then retracts the pin from the carriage. The dual pistons are provided for redundancy. Both pistons are actuated by the one firing command. Actuation of a single piston is adequate to release the locking mechanism.

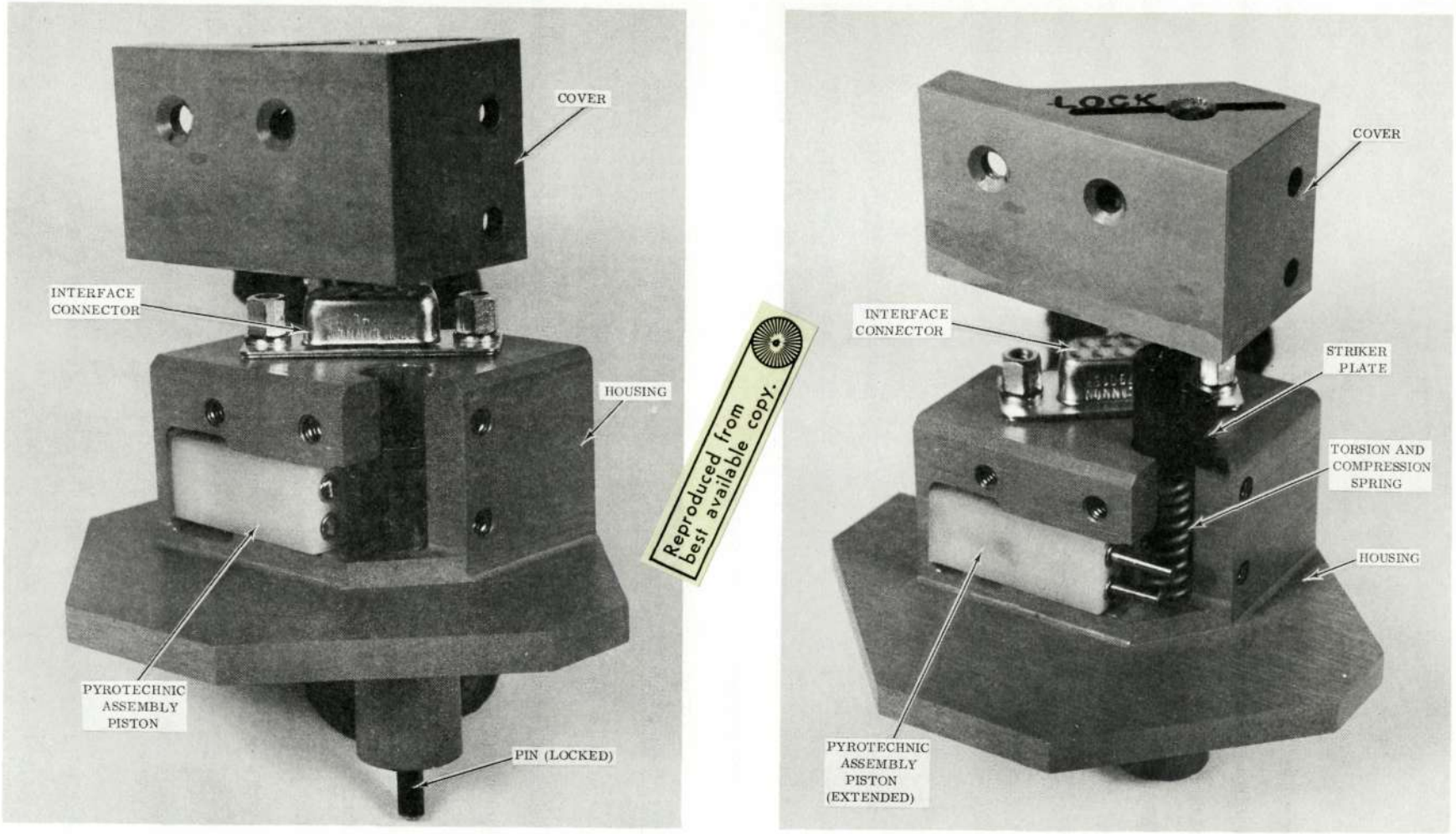

Locked Position

Retracted Position

Figure 3-23. Launch Lock Assembly

The pyrotechnic pistons are specified on General Electric Drawing 470217829. Each piston exerts a minimum force of 20 pounds and meets a 1 ampere no fire, 3-1/2 ampere all-fire requirement.

The launch lock assembly was subjected to an extensive series of development tests the results of which are contained in PIR OSO-H-043. Although no problems were encountered in this series of tests, the launch lock failed to release in the thermal-vacuum test at the spacecraft contractor after the spacecraft vibration test. The same launch lock had been fired successfully six times previously during instrument testing. Failure analysis revealed a binding of the locking pin due to peening of an edge on the housing diameter at the end of the piston stroke. Chamfering the edge corrected the problem.

3.2.2.11 Ion Traps

The openings to the instrument compartment which houses the EUV Magnetic Electron Multipliers are protected against charged particle penetration with ion traps. The ion traps consist of two charged grids. The outer grid is biased to -3 volts dc and the inner grid is biased to +19 volts dc with respect to chassis ground.

3.3 ALIGNMENT AND CALIBRATION

3.3.1 ALIGNMENT

The EUV subsystem alignment starts with the fabrication of the instrument base plate and the track and carriage assembly. The track is positioned on the base plate such that the mounting surface on the carriage for the exit slits is within 0.005 cm of the required radius of the 1/2 meter Rowland circle radius for all track positions. The entrance slit is at its proper position on the Rowland circle with a similar tolerance. The height of the entrance slit above the base plate is adjustable for later alignment with the X-ray subsystem. The bore for centering the telescope axis is machined into the front plate. Provision is made for adjusting the axial position and tilt of the telescope by means of a variable thickness spacer to suit the focal length of the individual telescope to be used.

The grating is adjustable in its radial distance from the center of the Rowland circle for optimum focus of the EUV lines on the exit slit. The tilt of the grating is adjustable to

place the EUV lines in the correct circumferential position on the Rowland circle and to align the EUV lines with the exit slit apertures. The grating adjustments are performed as the first step in the alignment procedure. Visible light was used to illuminate the entrance slit. The radial position of the grating was adjusted to 0.03 cm inside the Rowland circle and the tilt adjustments were made to bring the zero order image in alignment with an exit slit placed at the proper zero order position on the Rowland circle.

The telescope, entrance slit height, and X-ray collimator adjustments were made simultaneously to provide the required coalignment of the X-ray subsystem, EUV subsystem and eye block surfaces. The proper thickness spacer between the telescope and front plate was selected such that the optimum telescope focus in visible light as determined previously falls between the fixed and rotating entrance slits. Autocollimating surfaces normal to the optical axis are provided on both the telescope and collimator for alignment. The results of alignment measurements are shown in Figure 3-24. There appears to have been some slight drift of the alignment due to environments and time, but the alignments remained within the required accuracy.

COLLIMATOR ALIGNMENT RELATIVE TO TELESCOPE

		A2	EL	(ARC SECONDS)
3-11-71	PRE-VIBR AT GE	+10	-3	
3-13-71	POST VIBR AT GE	+ 5	+1	
7-20-71	POST VIBR AT BBRC	- 7	+7	

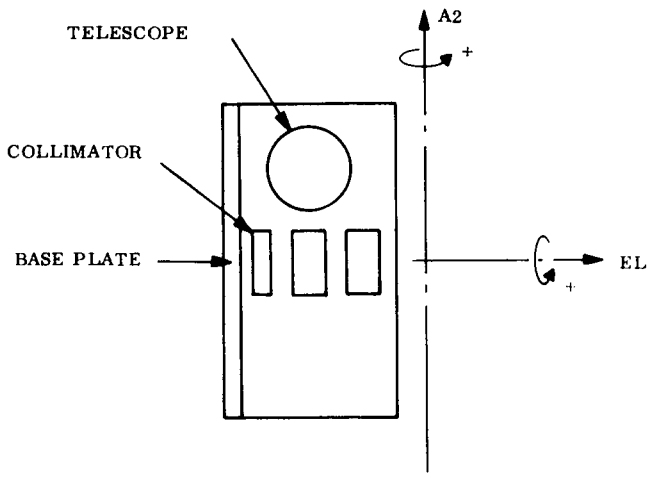

LOOKING AFT (FROM SUN)

Figure 3-24. Alignment Measurements Data

3.3.2.1 Absolute Calibration of EUV Sensitivity

Sensitivity of the EUV subsystem is defined as the ratio of the numerical readout to the incident EUV flux. Conventionally the readout is expressed in counts per second and the flux in photons-cm^{-2} sec^{-1}; sensitivity is then expressed in counts-cm^{2}-ph^{-1}.

In order to calibrate the spectroheliograph, the incident flux, measured in ph-cm^{-2}-sec^{-1} has to be determined.

The primary source of EUV radiation is a plasma generator of the hollow cathode type. The EUV output of such a source is not accurately known, either in intensity or in spectral composition, although the output remains constant over reasonable time intervals. The approach to standardize the source is to reference its output to a known detector.

Such a detector is a photodiode utilizing a tungsten photocathode. The photoelectric yield of tungsten has been measured by various authors (Samson, GCA Report 65-29-N). Measurements have also shown that the yield stays fairly constant with time.

The energy of photoelectrons is quite low and a small bias of $< 10V$ is adequate to assure complete collection efficiency of photoelectrons. The resulting current is directly proportional to the incident EUV flux.

Because the source emits more than one wavelength, the measured flux has to be monochromatized to the wavelength of interest - in the present case, 304 Å. This is accomplished with a grating. The efficiency of this grating has been established previously by independent means. Knowing the grating and photodiode efficiency, the flux radiated from the source can be determined if the effective source and detector areas are known.

The source area is given by a known pin-hole aperture, which has a 0.127 cm diameter. This corresponds to the effective area, if the monochromator-detector has a field-of-view which is larger than the source pin-hole. This condition is met in most cases. The monochromator-detector effective area is determined by the smaller of either the entrance or the exit slits.

The first step in the calibration procedure is then to measure the output of the source with the monochromator-photodiode combination.

Later on, a need for a detector more sensitive than the photodiode arises. The second step is then to substitute the photodiode with a Channel Electron Multiplier (CEM). By comparing the CEM output against the photodiode, with all other conditions remaining the same, the monochromator-CEM device serves as a secondary standard.

The third and last step is then apply the monochromator-CEM to measure the flux reflected from the collimating mirror. This gives the absolute value of flux applied to the instrument. It also gives the reflection efficiency of the collimating mirror.

Figure 3-25 shows the configuration of the set-up. Radiation from the source passes through entrance slit S_1, is diffracted by the grating and focuses on a photodiode. The grating has 1200 lines/mm, a radius of curvature of 1m and is blazed for 250 Å. The grating height is 0.321 cm and its width is 0.975 cm. The effective area of the monochromator is given

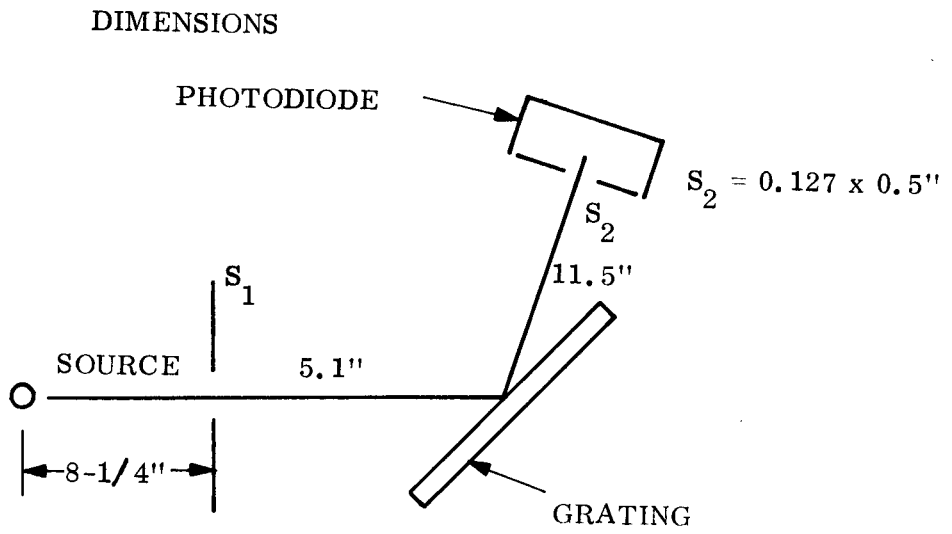

$$S_1 = 0.05 \times 1.265$$

$$= 0.064 \text{ cm}^2$$

Figure 3-25. Collimating Mirror Configuration

by the entrance slit width (0.05 cm) and the projected height (1.26 cm) of exit slit into plane of entrance slit (0.42 cm). The resultant area is 0.021 cm^2. The grating efficiency has been measured to 14 percent for 304 Å radiation. The photoelectric yield of tungsten has been determined independently as 6 percent.

The measured photodiode current is 6.5×10^{-12} amperes. This corresponds to 3.75×10^7 electrons-sec^{-1}. Taking the grating efficiency and photoelectric yield into consideration, a photon intensity of 4.5×10^9 ph-sec^{-1} is incident on the grating. The incident flux on the monochromator is then 2.1×10^{11} ph-cm^{-2}-sec^{-1}.

The photodiode is then replaced with CEM and an aperture of 50 μm diameter is placed in front of the CEM (see Figure 3-26). The effective area is now defined by the 50 μm pinhole and not the entrance slit. Transposing the pinhole dimensions into the plane of the entrance slit, we have to consider again that the grating is an image forming element in one plane only. In the focusing plane the effective entrance width is the same as the 50 μm pinhole. In the perpendicular plane the effective height is reduced to 16.8 μm, which is the ratio of distance of the pinhole to source to the distance of the entrance slit to source. The total effective area is then an ellipsoid with 660 μm^2 area. The CEM counting rate is measured to 12,060 cps which results in a CEM efficiency of 6.1 percent.

The flux incident on the collimating mirror is equal to the source flux measured previously reduced by the inverse square law. The previous measurement was made at 3.22 cm from the source, the mirror distance is 50.70 cm. The flux incident on the mirror is then $2.1 \times 10^{11} \times 4 \times 10^{-3} = 8.4 \times 10^8$ ph cm^{-2} sec^{-1}.

The monochromator is now applied to measure the collimated flux, see Figure 3-27. For this purpose the effective area of the CEM is increased, by removing the pinhole, to a slit 0.5 mm wide and 7 mm high. This area of 0.0350 cm^2 is equal to the effective area in the plane of the entrance slit on account of collimated beam conditions. The measured count rate is 94 cps, which by considering a 14 percent grating efficiency and a 6.1 percent CEM efficiency results in a collimated flux of 3.14×10^5 ph cm^{-2} sec^{-1}. The collimating mirror efficiency results to 3.2×10^{-4}.

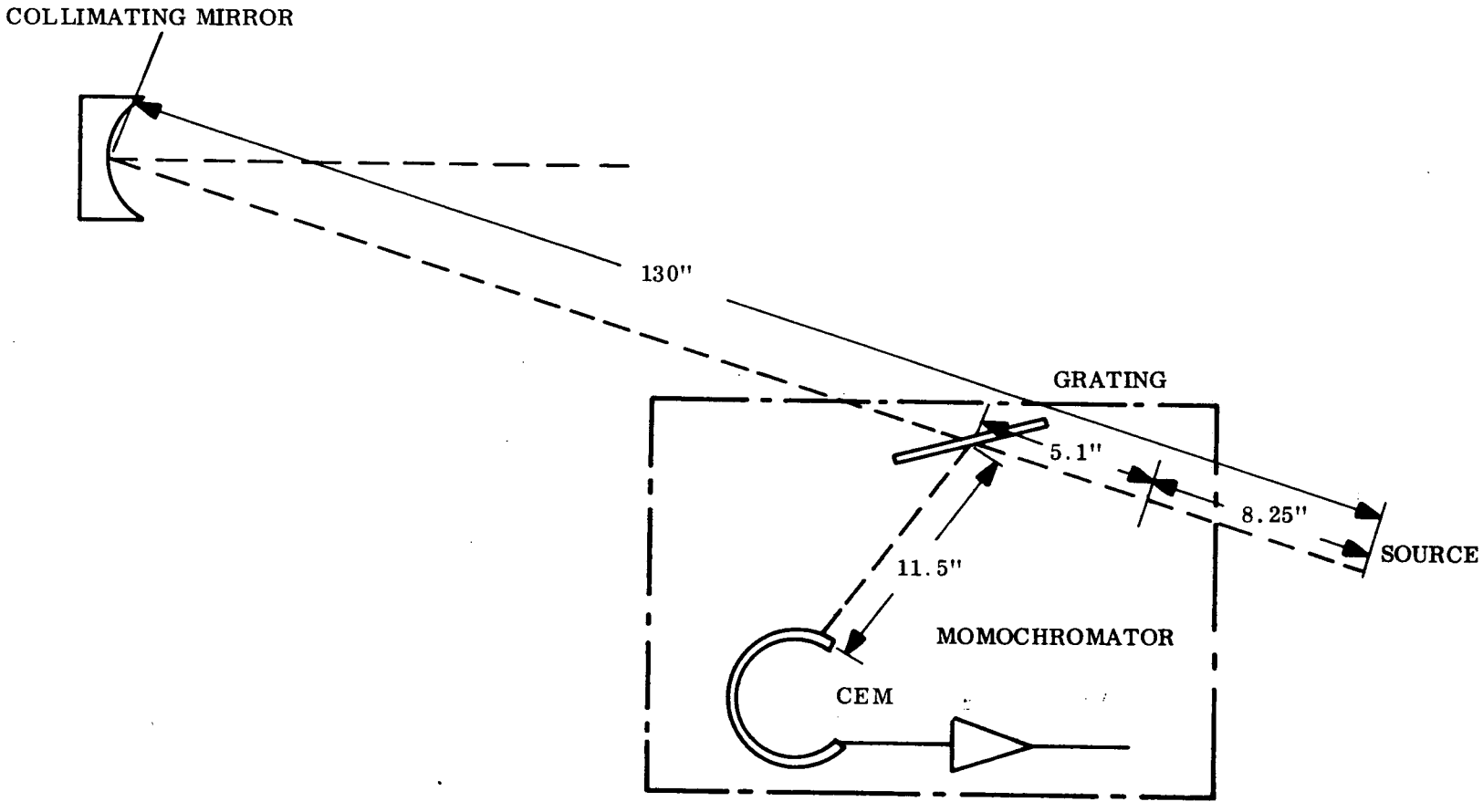

Figure 3-26. Calibration Assembly (CEM)

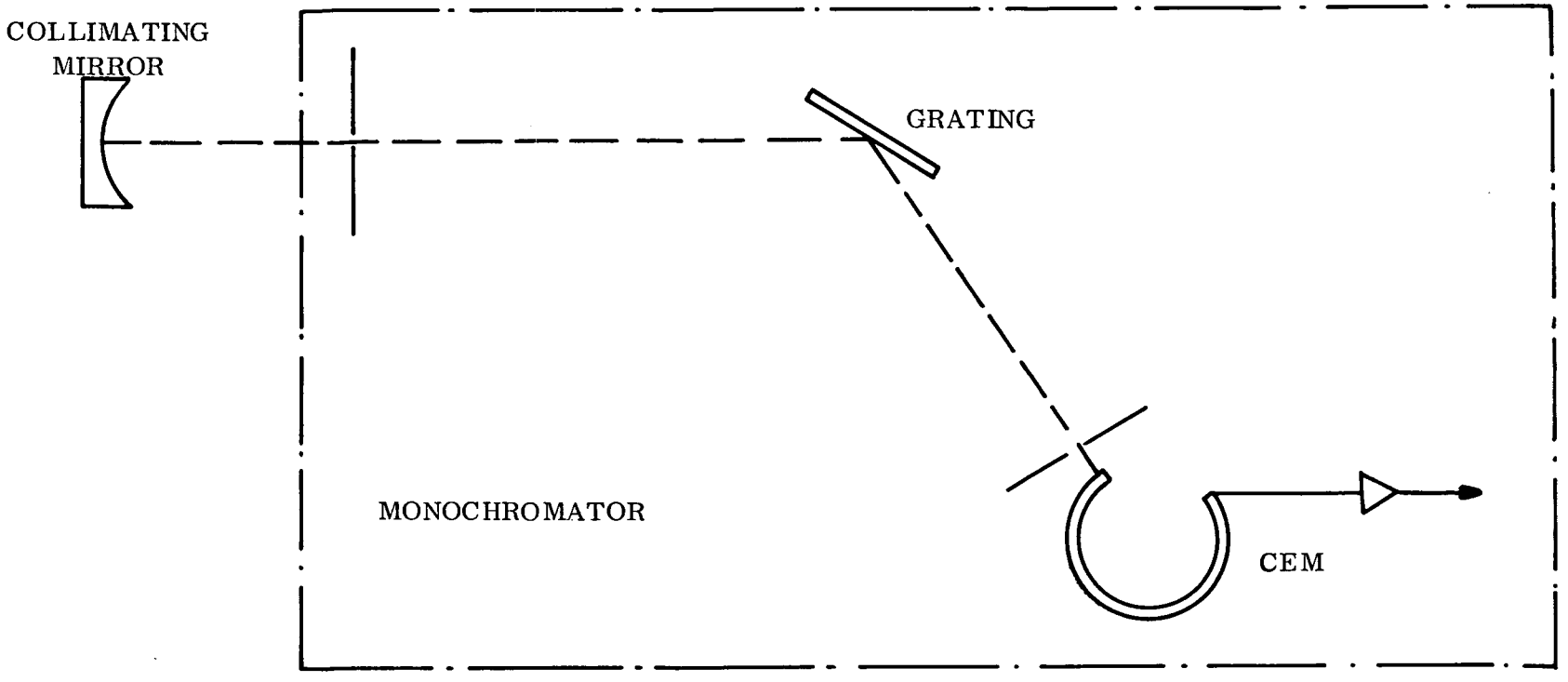

Figure 3-27. Monochromator

Finally, the efficiency of the spectroheliograph can be calculated. For the purpose of this calibration, a 20 x 60 arc-sec aperture is used in the spectroheliograph. The source is a 1.25 mm pinhole which corresponds to a 80 arc-sec diameter circular field of view. This corresponds to 5000 square arc-sec of which the instruments accept only 1200, or 24 percent.

The active part of the incoming flux is then $3.14 \times 10^5 \times 0.24 = 7.5 \times 10^4$ ph $cm^{-2} sec^{-1}$. With the instrument in the configuration shown in Figure 3-28, the output was 1080 counts in 1.28 seconds or 840 cps. It follows $840/7.5 \times 10^4 = 1.12 \times 10^{-2}$ c-cm^2-ph^{-1} as the instrumental sensitivity.

Or expressing it for the 11 cm^2 telescope aperture we get 10^{-3} c-ph^{-1} for efficiency. These values are about 2 times the original design goals. For a solar flux of 2×10^9 ph-cm^{-2}-sec^{-1} at the 304 Å line, and assuming a uniform brightness of the solar disc, and a 20 x 60 arc-sec aperture, the instrument readout will be 1×10^4 cps.

3.3.2.2 Resolution

The spectral resolution (FWHH) of the EUV experiment was measured as 0.86 Å which is in very close agreement with the calculated value of 0.9 Å for the entrance slit width of 85 μm.

There was one irregularity noticed. There is optical crosstalk between the long (LW) to medium (MW) wavelength detector. For the 304 Å line this crosstalk was 7 percent of the 304 Å response for the MW detector. A typical scan of the spectrometer is shown in Figure 3-29 which shows the position and width of five HeII lines in terms of motor steps for the MWA detector. One motor step is 0.07 Å on the average. Also to be noticed on this scan is the approximate 100:1 line to background ratio for the 304 Å line.

Spatial resolution of the EUV experiment was measured and determined to be better than 20 arc-seconds.

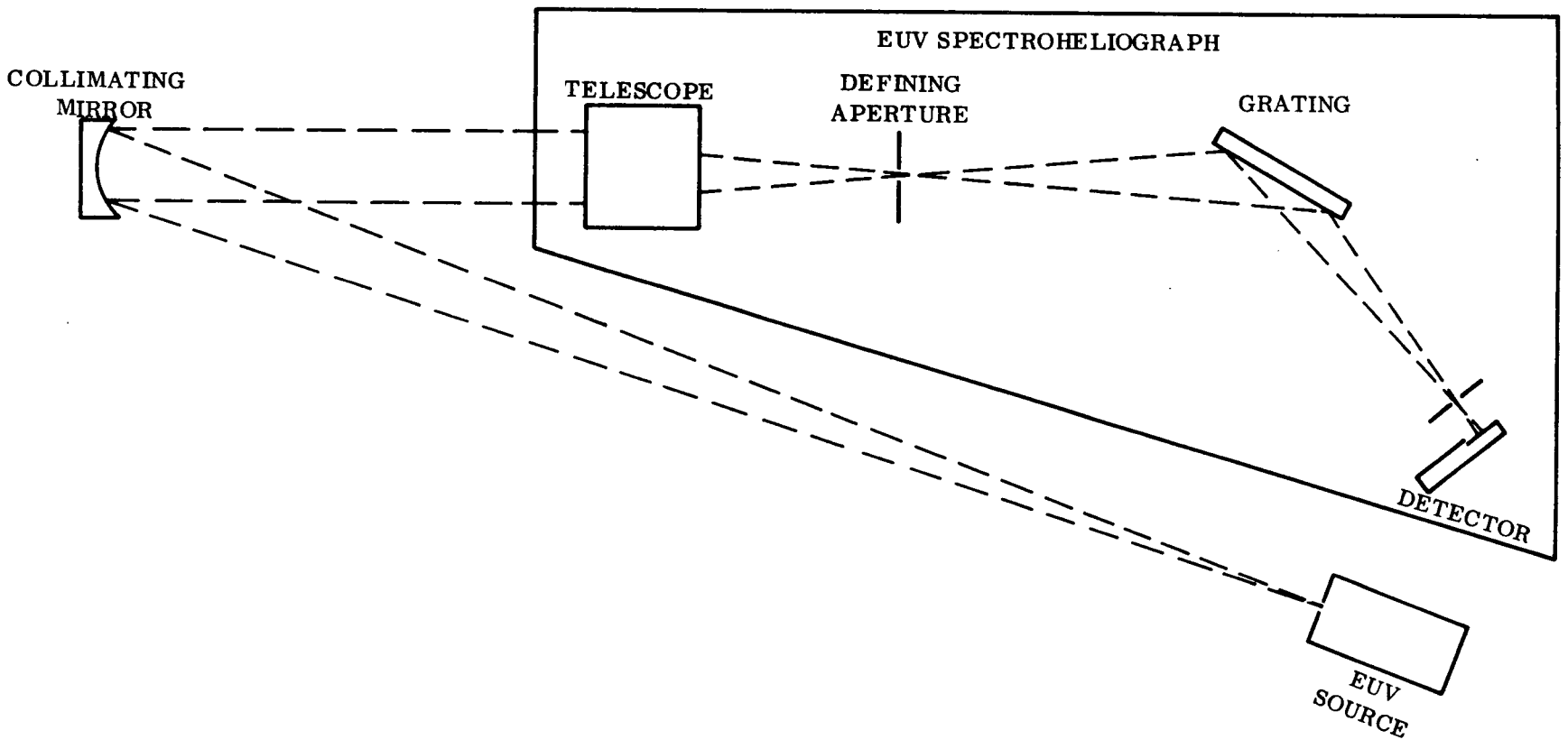

Figure 3-28. EUV Spectroheliograph

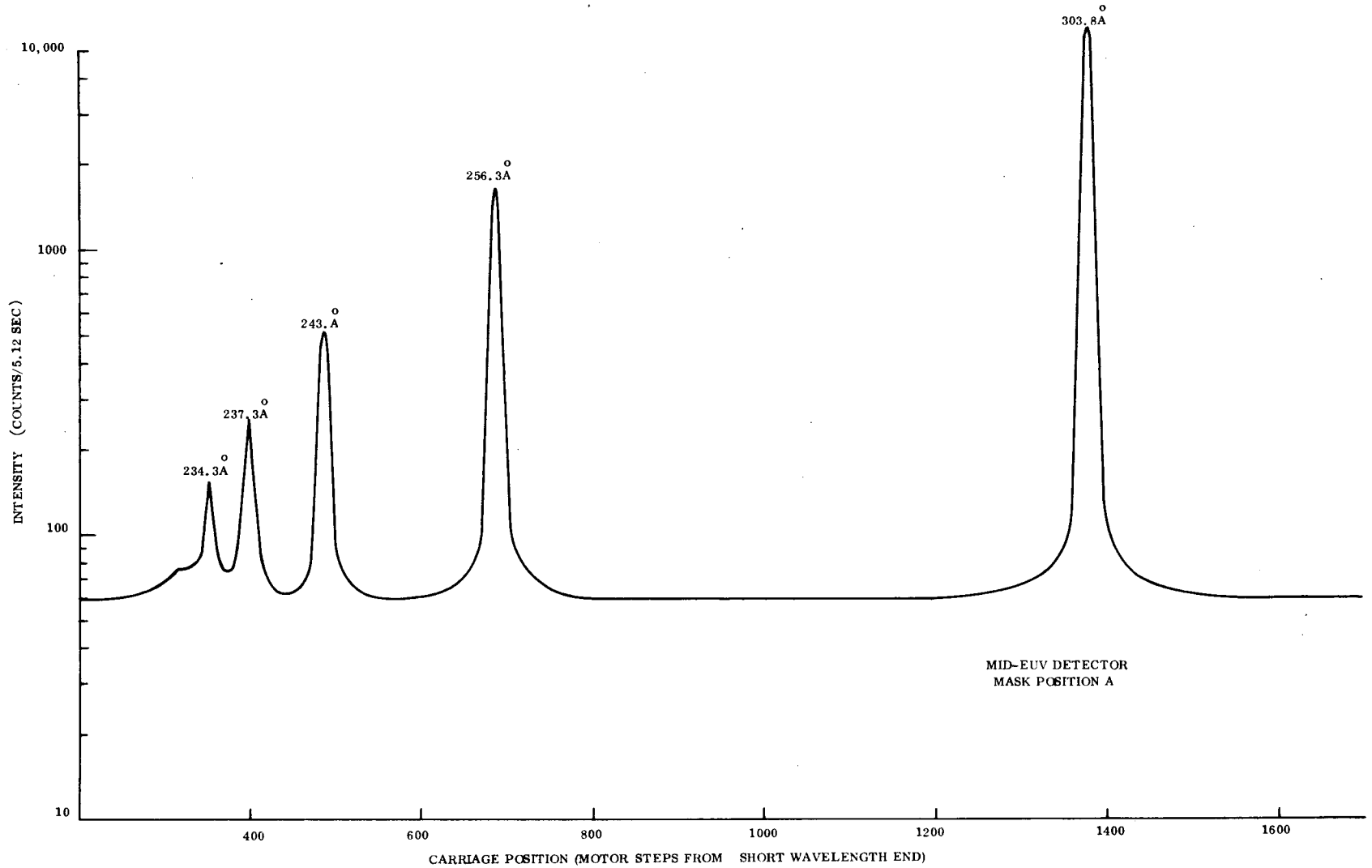

Figure 3-29. Spectrum of He II Series Lines Obtained with OSO-H Spectrometer

3.4 OPERATION

3.4.1 OPERATIONAL MODES

H-Alpha and short EUV data can be read out simultaneously or medium and long EVU data can be read out simultaneously.

The wavelength range for each of the EUV detectors is as shown below

	Mask A	Mask B
Short EUV	170 - 265Å	170 - 230Å
Medium EUV	215 - 340Å	190 - 310Å
Long EUV	260 - 400Å	230 - 360Å

In addition, the location of six spectral lines is well defined by the launch lock position which is at 1095 steps from the short wavelength end of the spectral scan (see Figure 3-30). These lines are as follows

	Mask A	Mask B
Short EUV	211.4Å	180.6Å
Medium EUV	284.1Å	255.1Å
Long EUV	335.2Å	303.8Å

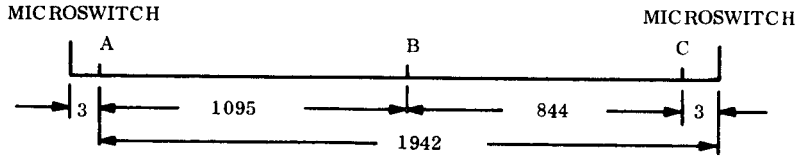

A = POSITION CARRIAGE STOPS AFTER IT IS SENT TO THE SHORT WAVELENGTH END USING XN-48

B = LAUNCH LOCK POSITION

C = POSITION CARRIAGE STOPS AFTER IT IS SENT TO THE LONG WAVELENGTH END USING XN-23

NOTE: LOCATION GIVEN IN MOTOR STEPS

Figure 3-30. Spectral Line Definition

There are other operational modes for the carriage, the mask and the aperture wheel. The varied modes may be derived from the next paragraph which discusses command definition and response.

3.4.2 COMMAND DEFINITION/RESPONSE

The following commands control the operation of the EUV Subsystem:

1. Data Selection Commands

   a. XN-53 (GSFC RO H-A and SUV) - Enables the readout of H-Alpha and short wavelength EUV and disables readout of medium and long wavelength EUV.

   b. XN-60 (GSFC RO MUX and LUV) - Enables the readout of medium and long wavelength EUV and disables readout of H-Alpha and short wavelength EUV.

   c. XN-11 (GSFC RO UV Auto) - Enables automatic readout switching at the end of each raster. Upon receipt of end of raster pulses from the spacecraft, the data readout switches back and forth between H-Alpha and short EUV and medium and long EUV.

      Note: (1) Either XN-53 or XN-60 will disable the automatic switching mode.
      (2) When the instrument has been left in the automatic switching mode the readout mode will also change at the night to day transition.

2. Carriage Operation Commands

   a. XN-15 (GSFC Spect Fast Scan) - Starts continuous scan of the grating spectrometer at 2 steps per readout (12.5 steps per second). The initial scan direction is determined by the last direction of motion.

   b. XN-56 (GSFC Spect Slow Scan) - Starts continuous scan of the grating spectrometer at 1 step per readout (6.25 steps per second). The initial scan direction is determined by the last direction of motion.

   c. XN-23 (GSFC Spect to LUV) - Advances the EUV detectors to the long wavelength end of the spectral scan at 50 steps per second. When the carriage activates the microswitch it reverses direction and steps off of the microswitch two or three steps and stops.

   d. XN-48 (GSFC Spect to SUV) - Advances the EUV detectors to the short wavelength end of the spectral scan at 50 steps per second. When the carriage actuates the microswitch, it reverses direction and steps off of the microswitch two or three steps and stops.

e. XN-20 (GSFC LUV Step/Stop Scan) - Advances the EUV detectors one step toward the long wavelength end of the spectrum and establishes the "last" direction of motion toward the long wavelength end. XN-20 will also stop the spectral scan when the carriage is traveling at 12.5 steps per second toward either end or when it is traveling at 6.25 steps per second toward either end and establishes the "last" direction of motion toward the long wavelength end. (Note: XN-20 will be ignored if it is sent when the carriage is moving toward the long wavelength end at 50 steps per second. However, it will stop the carriage when it is moving toward the short wavelength end at 50 steps per second and establish the "last" direction of motion toward the long wavelength end.)

f. XN-51 (GSFC SUV Step/Stop Scan) - Advances the EUV detectors one step toward the short wavelength end of the spectrum and establishes the "last" direction of motion toward the short wavelength end. XN-51 will also stop the spectral scan when the carriage is traveling at 12.5 steps per second toward either end or when it is traveling at 6.25 steps per second toward either end and establishes the "last" direction of motion toward the short wavelength end. (Note: XN-51 will be ignored if it is sent when the carriage is moving toward the short wavelength end at 50 steps per second. However, it will stop the carriage when it is moving toward the long wavelength end at 50 steps per second and establish the "last" direction of motion toward the short wavelength end.)

Note: At the night-to-day transition the direction of motion of the carriage will come up in a random state. That is, if the carriage was traveling toward or stopped toward the short or long wavelength end before night, the direction of motion after the night to day transition may be toward either end. This random state occurs because the logic associated with the direction of motion is switched off at night. However, the logic seems to have a preferred state which is toward the long wavelength end.

3. Mask Operation Commands

a. XN-10 (GSFC Switch Line SEL) - Changes the position of the grating spectroheliograph line selector (mask).

b. XN-61 (GSFC Line SEL Auto) - Enables the automatic switching of the mask position at the end of each raster. Upon the receipt of a raster pulse from the spacecraft the mask changes position. (Note: Command XN-10 disables the automatic switching mode).

Note: If the mask is in the automatic switching mode, it will also change positions at the night to day transition.

4. Aperture Wheel Operation Commands

a. XN-07 (GSFC Step Aptr Once) - Steps the aperture wheel one step.

b. XN-65 (GSFC Step Aptr Auto) - Initiates continuous rotation of the aperture wheel (grating spatial slit scan) at 6.25 steps per second.

c. XN-09 (GSFC Stop Aptr Auto) - Stops the continuous rotation of the aperture wheel.

d. XN-62 (GSFC Aptr to Ref) - Advances the aperture wheel to the reference position at 50 steps per second.

Note: The detents on the aperture wheel are in the following position with respect to the reference position.

Position	Steps from Ref	Time from Ref at 6.25 Steps/Sec
10 arc-sec	80 ± 1	12.8 sec
20 arc-sec	113 ± 2	18.08 sec
40 arc-sec	145 ± 2	23.20 sec
60 arc-sec	177 ± 2	28.32 sec
Reference	243	38.88

Note: If the aperture is in the continuous scan mode XN-09 should be sent to stop the wheel before XN-62 is sent to send the wheel to the reference position. If XN-09 is not sent before XN-62, it must be sent before the wheel will respond to either XN-07 or XN-65.

Note: Filters have been placed over part of each of the fixed apertures in order to extend the dynamic intensity range of the EUV subsystem. The approximate location of the centers of the filtered and unfiltered areas with respect to the reference position is as indicated below:

Aperture	Steps from Ref to Center of Slit	Time from Ref at 6.25 Steps/Sec
10 arc-sec unfiltered	75 ± 1	12.00
filtered	93 ± 1	14.88
20 arc-sec filtered	105 ± 1	16.80
unfiltered	120 ± 1	19.20
40 arc-sec unfiltered	140 ± 1	22.40
filtered	152 ± 1	24.32
60 arc-sec filtered	170 ± 1	27.20
unfiltered	182 ± 1	29.12

5. High Voltage Commands

a. XN-49 (GSFC SUV and LUV HV On) - Turns on the high voltage power supply which powers both the short and long wavelength EUV detectors.

b. XN-49 (GSFC SUV and LUV HV On)- Turns on the high voltage power supply which powers the medium wavelength detector.

c. XN-50 (GSFC EUV and H-A HV Off) - Turns off both EUV high voltage power supplies and the H-Alpha high voltage power supply simultaneuosly.

3.4.3 EFFECTS OF LOSS OF POWER

Power to the experiment can be interrupted in any one of three ways:

1. Only day power interrupted
2. Only orbit power interrupted
3. All power interrupted

The loss of day power only has no effect on the state of the instrument, except that all data is lost during the interrupt. The effect will be the same as the normal day-night-day transition.

If only the orbit power is interrupted the following effects will be noticed when the power is restored. All other states will remain the same assuming that no commands have been sent in the interim.

1. EUV Carriage - The direction of spectral scan may change.
2. EUV Mask - The mask may change positions.
3. Aperture Wheel - The wheel will return to the reference if it had been stopped prior to the loss of power. Otherwise it will continue to rotate.
4. High Voltage - Will remain on during orbit power interrupt, however, all data will be lost.

If all power to the experiment is interrupted the effect will be the same as if only the orbit power is interrupted with the exception that the high voltage power supplies will also turn off during the interrupt, but they will come back on when power is restored.

Note: In any case all data will be lost during the interrupt.

3.4.4 TELEMETRY

3.4.4.1 Scientific Data

In summary, the EUV data is read out during main frame word gates 3, 7, 19 and 23, but only two of the four channels can be read out simultaneously (H-Alpha and short EUV or medium and long EUV). The sample time is 125 ms and the sample frequency is 160 ms.

3.4.4.2 Housekeeping Data

EUV housekeeping is read out during DSF word gates 2, 14, 26 and 38. Thus, they are read out only once every 3.84 seconds and are, therefore, as much as 3.84 seconds out of sync with the actual state of the instrument. DSF data words are used to relay the following information:

1. Mask position
2. Direction of spectral scan (or direction of "next" spectral scan)
3. Spectrometer mode - scanning or stopped
4. Spatial scan aperture selected
5. Detectors Selected - H-Alpha and short EUV or medium and long EUV.

The end of line (EOL) and end of raster (EOR) housekeeping data are read out during DMF word gates 3, 4, 7 and 8. The end of spectral scan (EOSS) housekeeping data is read out during DMF word gates 19, 20, 23 and 24. Therefore, the DMF housekeeping data is less than 160 ms out of sync with the actual state of the instrument.

SECTION 4

H-ALPHA EXPERIMENT

4.1 REQUIREMENTS

The spatial resolution of the H-Alpha experiment is to be the same as specified for the EUV experiment. In addition, the following requirements are specified.

1.	Wavelength centering (vacuum)	6564.66 ± 0.1 Å
2.	Spectral bandpass	< 3Å
3.	Signal dynamic range (10 x 20 arc-sec aperture)	7:1
4.	Signal to noise ratio (10 x 20 arc-sec aperture)	20:1
5.	Orbit stability (60 min)	< 10% drift

4.2 DESIGN SOLUTION

4.2.1 H-ALPHA EXPERIMENT DESCRIPTION

The zero order from the EUV grating is used for the H-Alpha experiment. Using this approach the H-Alpha system is always aligned with the EUV system and therefore has the same spatial resolution. Adequate intensity is available for this purpose. Spectral resolution is achieved with an Ebert-Fastie spectrometer. Multiple orders are rejected by an interference filter. An RCA photomultiplier tube with an S-20 response is used for a sensor. The analog output of the photomultiplier is integrated and converted into a digital signal.

A schematic of the H-Alpha system is shown in Figure 4-2. An Electrical block diagram is shown in Figure 4-1.

4.2.2 COMPONENT DESCRIPTION

4.2.2.1 Telescope

The telescope is the same one used in the EUV experiment. Reference Paragraph 3.2.2.1.

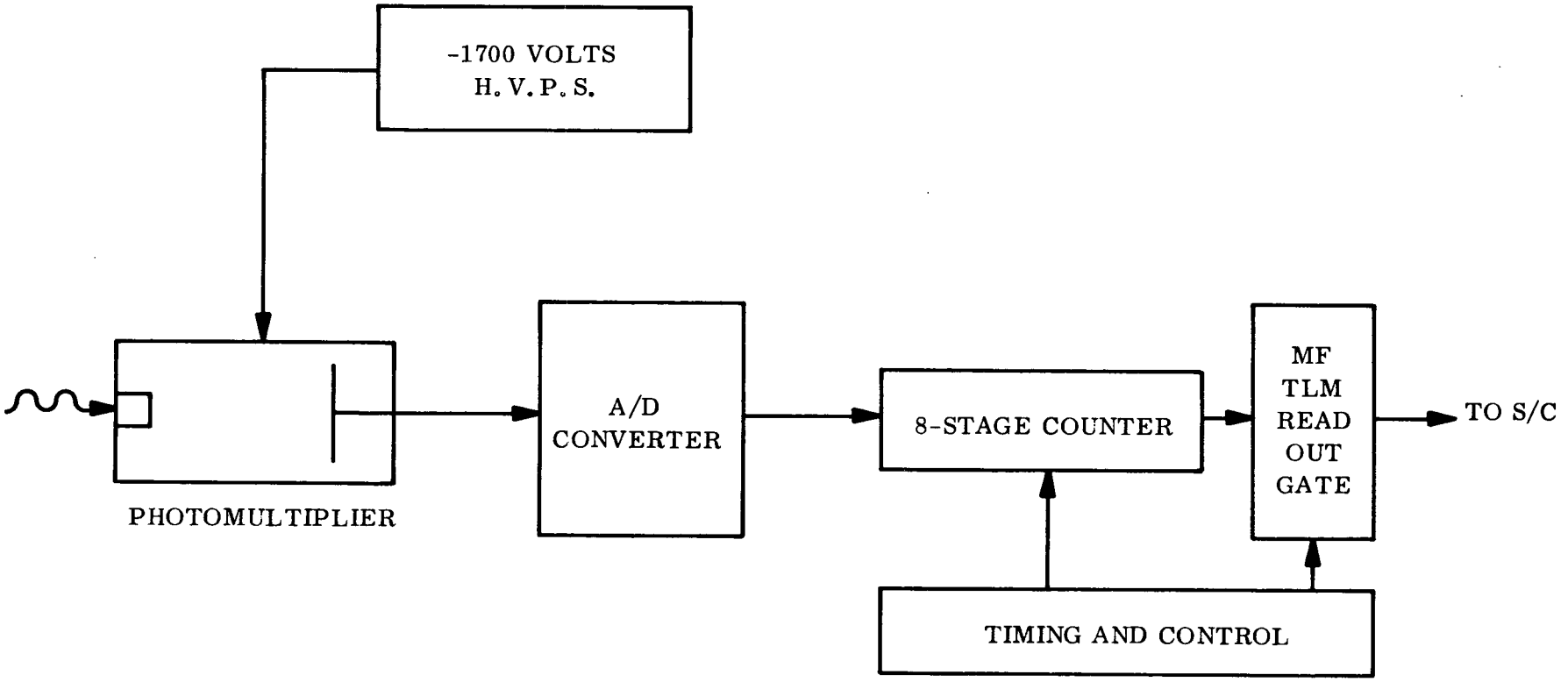

Figure 4-1. H-Alpha Experiment Block Diagram

4.2.2.2 Entrance Aperture

The entrance aperture is the same one used in the EUV experiment, Reference Paragraph 3.2.2.2.

4.2.2.3 Grating

Grating is the same one used in the EUV experiment. Reference Paragraph 3.2.2.3.

4.2.2.4 Optics

The H-Alpha optical subsystem utilizes an Ebert-Fastie spectrometer to give a bandpass of 1.0 Å of the H-α line centered about 6564.66 Å. A schematic of the optical path is shown in Figure 4-2 and the physical hardware is shown in Figure 4-3. All components are assembled on a base plate such that the subsystem can be assembled and preliminary adjustments made before installation in the instrument.

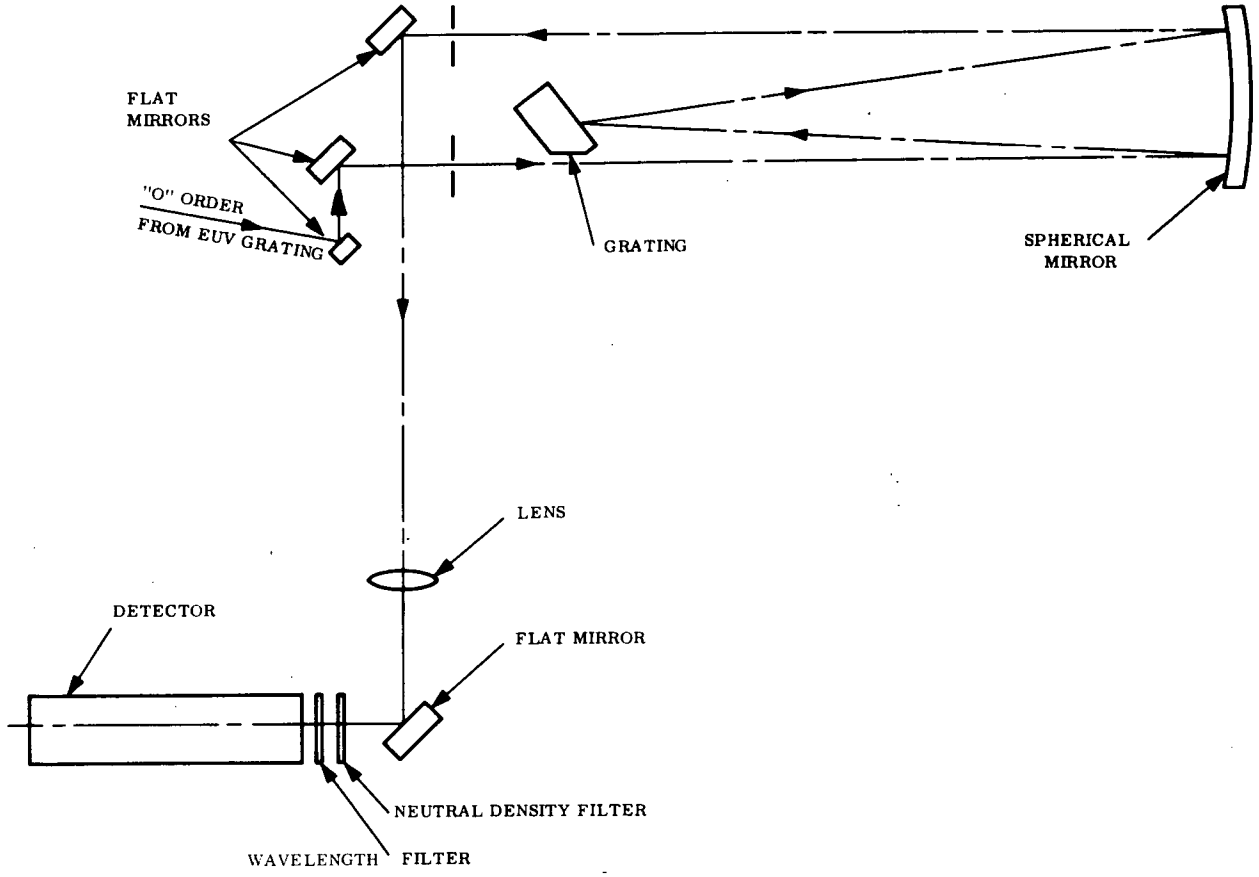

Figure 4-2. H-Alpha Spectrometer

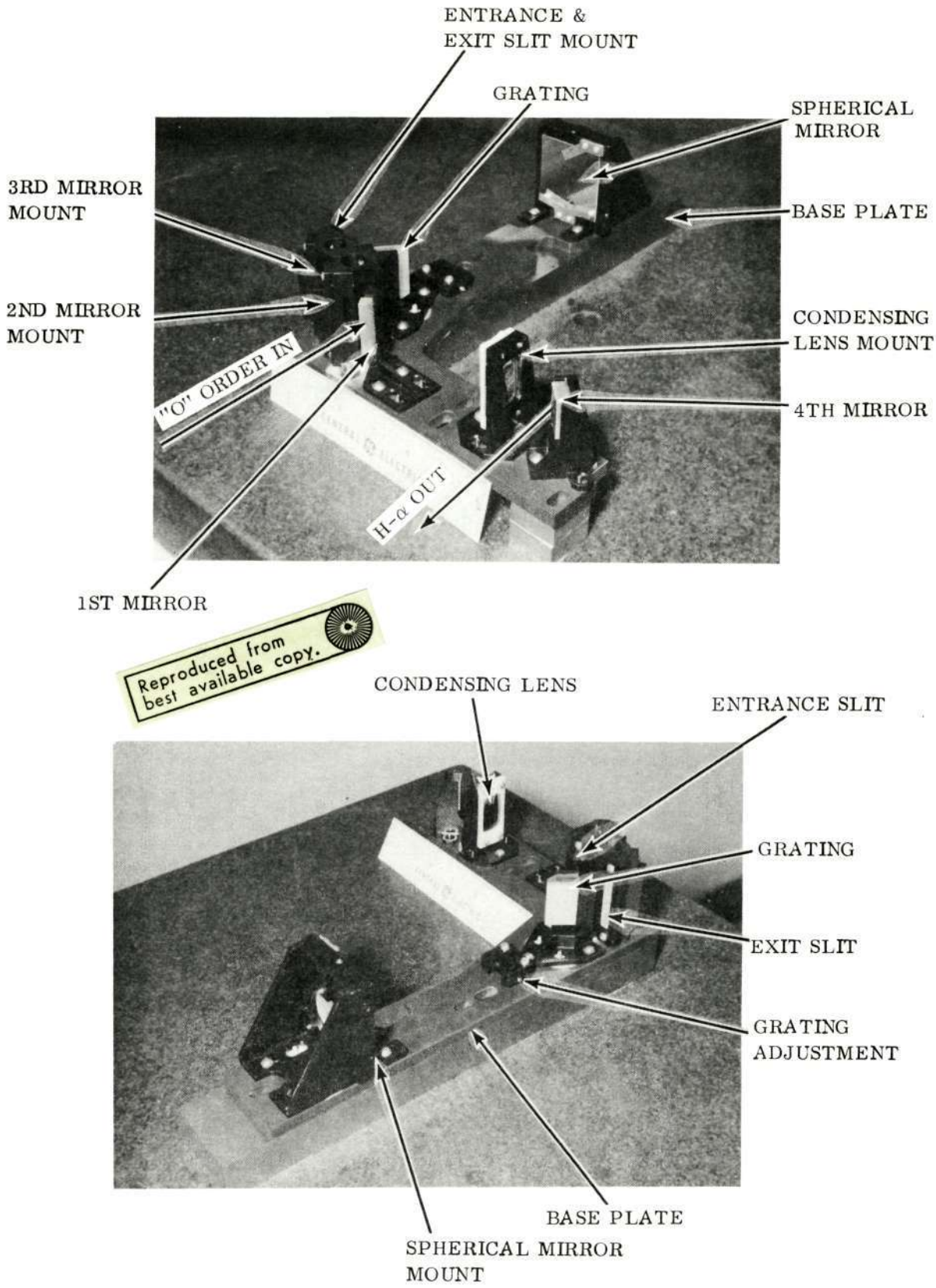

Figure 4-3. H-Alpha Spectrometer Assembly

The "O" order line from the main EUVgrating is intercepted by a flat mirror and reflected to focus on the spectrometer entrance slit by a second mirror. The radiation passing through the entrance slit is reflected from the spherical mirror to the H-Alpha grating. The diffracted energy from the grating is reflected from the spherical mirror to the spectrometer exit slit. The translational adjustment of the spherical mirror focuses the diffracted energy on the exit slit and the rotational adjustment of the grating selects the proper wavelength of radiation at the exit slit. From the exit slit, the H-Alpha line is reflected from a third flat mirror to a condensing lens and a final reflection from the fourth flat mirror directs the energy through a pair of filters to the photocathode detector. The first filter is a neutral density filter to adjust the intensity level at the detector and the second filter transmits energy only around the H-Alpha wavelength. In the flight configuration, no neutral density filter was used. Some physical parameters of the optical system are as follows:

1. Entrance Slit Width - 0.005334 cm
2. Exit Slit Width - 0.005334 cm
3. Spherical Mirror Radius - 35.04 cm
4. Grating Surface - 600 lines/mm (Flat)

The prototype instrument vibration test caused a shift in the wavelength centering of the spectrometer resulting from instability of the spherical mirror mount. Redesign of the mirror support system to stiffen the mounting corrected the problem. A slight chipping of the condenser lens also occurred which was corrected by additional cushioning of the lens in its mount.

4.2.2.5 Photomultiplier

An RCA multialkali, 10-Stage photomultipler tube is employed as a light sensor. This tube has a good response at the H-Alpha wavelength with quantum efficiency of 4 percent. Stability and ruggedness were considered in the selection. A neutral density filter was incorporated, but later removed for increased output.

4.2.2.6 H-Alpha Sensor Electronics

The H-Alpha sensor electronics is an analog to digital converter which measures the current output of the photomultiplier tube and converts it to a pulse rate.

The schematic is shown in Figure 4-4. Capacitor C1 integrates the current generated by the photomultiplier tube. As C1 charges, it decreases the voltage on the gate of Q2A. When the voltage on the gate of Q2A becomes sufficiently low Q3A turns off and Q3B turns on thus turning Q4, Q5 and Q6 on. When Q5 turns-on, it in turn turns on Q1 which discharges C1. Capacitor C7 ensures that Q3B turns on "hard" and that it stays on long enough for C1 to discharge. When C1 is discharged and C7 is charged Q2A turns on, thus turning Q3A on and transistors Q2B, Q3B, Q4, Q5, Q6 and Q1 off and the sequence is restarted.

The pulse rate is directly proportional to the average current since the voltage on C1 is determined by

$$V_{C1} = C \int i \, dt \cong C i_{AVE} \Delta t$$

where V_{C1} is the voltage on C1 which causes Q3A to turnoff and Q3B to turnon. If i_{AVE} increases Δt decreases and conversely.

The output of Q6 is buffered and coupled into an 8-stage counter.

4.2.2.7 Data Processing Electronics

The data handling is accomplished by the use of series 54L Texas Instrument logic circuits. The arrangement of the logic is shown in Figure 4-4. The output of the A/D converter is coupled into an 8-stage counter through a timing control circuit. The counter accumulates counts for 142.5 ms. The counter is then disabled and the 8-bit word is transmitted to the spacecraft. The counter is cleared (reset at zero) and enabled again, thus starting the sequence again. The entire sequence takes 160 ms. The logic configuration for the 8-stage counter is shown in Figure 4-5.

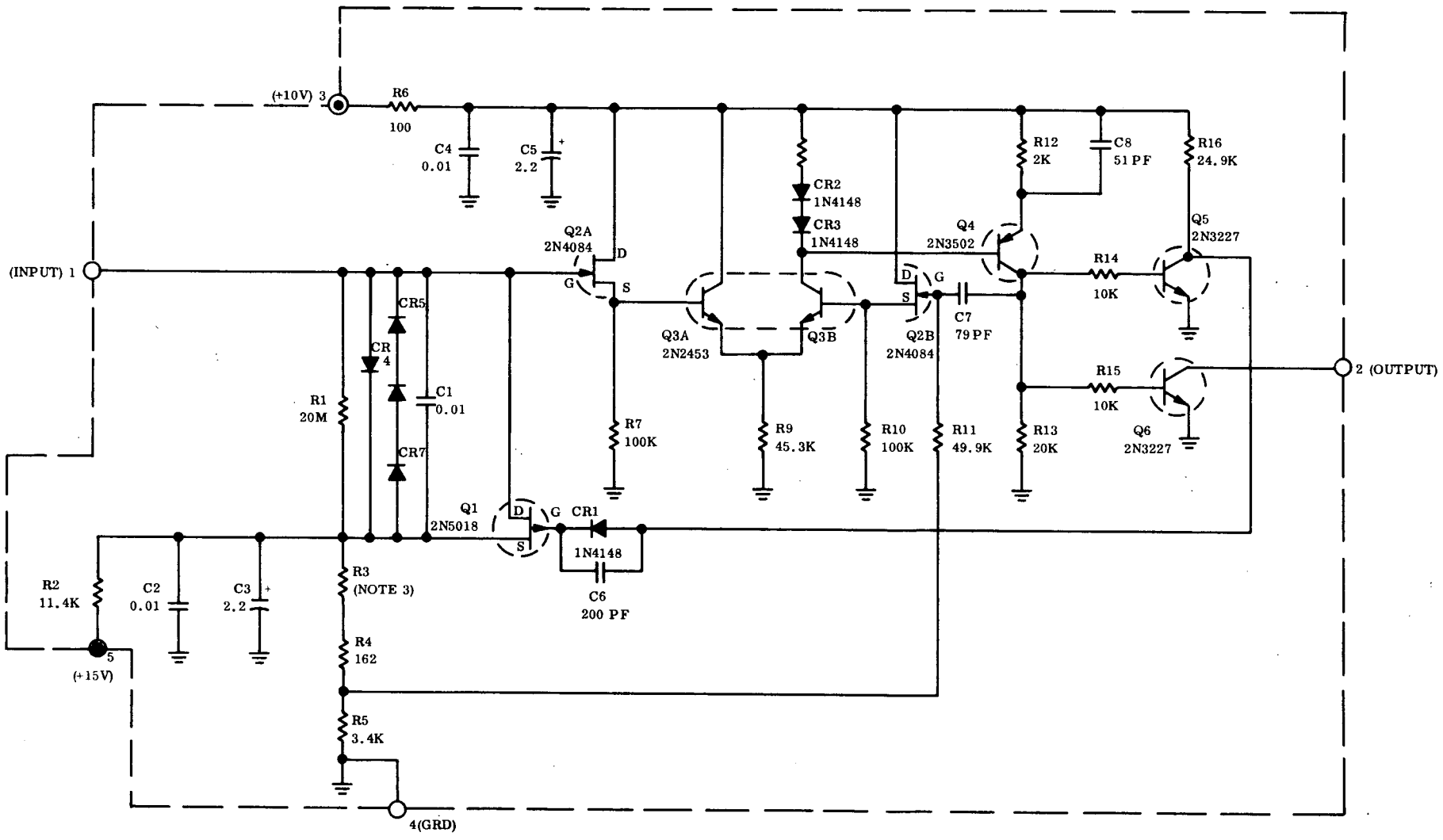

NOTE:

1. ALL RESISTORS IN OHMS AND ALL CAPACITORS IN MFD UNLESS OTHERWISE SPECIFIED.
2. DIODES - CR4, CR5, CR6 and CR7 are 1N4148
3. R3 MAY BE 1, 2, or 3 RESISTORS IN SERIES. TO BE SELECTED BY TEST

Figure 4-4. H-Alpha A/D Converter

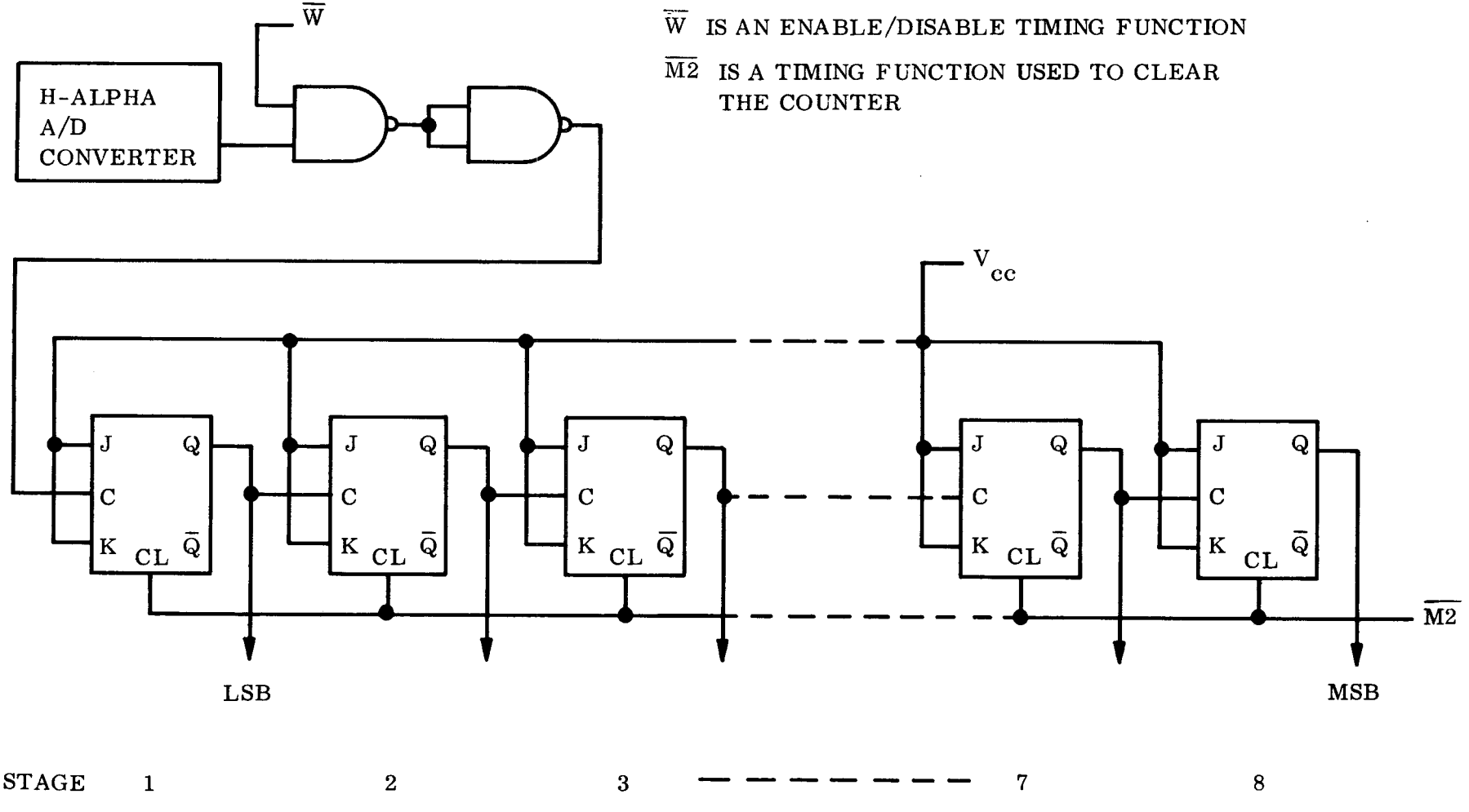

Figure 4-5. H-Alpha Data Accumulator (8-Stage Counter)

Since the counter only has eight stages the maximum count which can be readout is 255. If the A/D converter output is greater than 1790 pulses per second the counter overflows. However, since the most significant bit is latched once it becomes a "1", the counter does not start recounting from zero but rather from 128. The telemetered output thus is as shown in Figure 4-6 as a function of the pulse rate input for the 142.5 ms sample period.

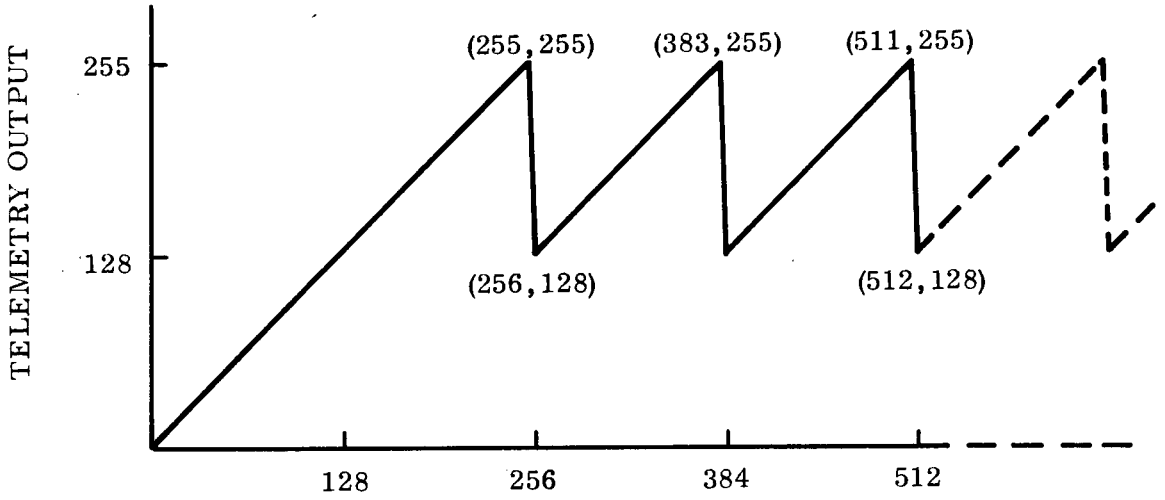

Figure 4-6. Telemetered Output

In addition, there is a built in count of one in the logic, therefore, the telemetered output should be 1 wherever the H-Alpha high voltage is turned off.

4.2.2.9 Housekeeping Electronics

The housekeeping for H-Alpha is the same as the housekeeping for EUV, except that only the information related to the aperature wheel, the detectors selected, and the DSF housekeeping (EOL and EOR) is pertinent to H-Alpha (telemetry bits TB4 through TB7). For a detailed description, reference paragraph 3.2.2.8.

4.3 ALIGNMENT AND CALIBRATION

4.3.1 ALIGNMENT

Wavelength centering was accomplished by tuning the H-Alpha spectrometer to a wavelength of 6564.66 $\mathring{A}$ which is the value for the H-Alpha line in vacuum. Because of a wavelength shift of 1.81 $\mathring{A}$ between air and vacuum a source of H-Alpha radiation could not be used for

alignment. Instead an auxiliary Jarrel-Ash spectrometer was used as a monochromator and the source was a tungsten filament lamp. The Jarrel-Ash was calibrated against a hydrogen lamp emitting H-Alpha.

Overall alignment of the experiment is accomplished by the alignment of the EUV telescope. Refer to paragraph 3.3.1 for alignment results.

4.3.2 CALIBRATION

Wavelength centering was accomplished to an accuracy of 0.14 Å. The sensitivity was first set against a standard tungsten filament lamp. The final sensitivity setting was done with the sun.

The sensitivity of the experiment was adjusted to provide approximately 150 counts per readout for a 75 percent sun. The full-scale signal-to-noise ratio is better than 25:1. Signal drift has been measured at less than 5 percent for 60 minutes.

4.4 OPERATION

4.4.1 OPERATIONAL MODES

The H-Alpha operational modes (internal to the experiment) are limited to viewing the sun through various openings in the aperture wheel. These modes are discussed in detail in paragraph 3.4.2 under Aperture Wheel Operation Commands.

In general, any one of four fixed aperture positions (10, 20, 40, 60 arc second slits - either filtered or unfiltered) can be selected or the aperture wheel can be commanded into an automatic scanning mode which gives a spatial scan in azimuth. Furthermore, it is possible to offset point from the spacecraft coordinates in azimuth by stopping the aperture wheel in the appropriate location on the spiral slit.

4.4.2 COMMAND DEFINITION AND RESPONSE

Command definition and response are as follows:

1. High Voltage Commands

   a. XN-31 (GSFC H-A HV On) - Turns on the high voltage power supply which powers the H-Alpha photomultiplier tube.

   b. XN-50 (GSFC EUV and H-A Off) - Turns off the H-A high voltage power supply and both of the EUV high voltage power supplies simultaneously.

   All of the commands related to data channel selection and to the aperture wheel operation are discussed in paragraph 3.4.2.

4.4.3 EFFECT OF LOSS OF POWER

Power to the experiment can be interrupted in any one of three ways:

1. Only day power interrupted
2. Only orbit power interrupted
3. All power interrupted

The loss of day power only has no effect on the state of the instrument, except that all data is lost during the interrupt. The effect is the same as the normal day-night-day transition.

If only the orbit power is interrupted, the only operational effect on the H-Alpha subsystem will be that the aperture wheel will return to the reference if it had been stopped prior to the loss of power; otherwise, it will continue to rotate when the power is restored. Also the high voltage power supply will remain on, but all data will be lost during the interrupt.

If all power to the experiment is interrupted the effect will be the same as if only the orbit power is interrupted with the exception that the high voltage power supplies will also turn off.

4.4.4 EFFECT OF FILTERS

In order to increase the dynamic range of the EUV subsystem, EUV filters were added to the aperture wheel over portions of each of the fixed slits. Due to the light weight and delicacy of the filters, they were attached to a wire mesh for support before installation. The wire mesh has a pronounced effect on the H-Alpha data. Figure 4-7, shows this effect.

4.4.5 TELEMETRY

4.4.5.1 Scientific Data

The H-Alpha data is read out during main frame word gates 3, 4, 19 and 23 only if Command XN-53 has been issued to select H-Alpha and short EUV data channels. The sample time is 142.5 ms and the sample rate is 160 ms.

4.4.5.2 Housekeeping Data

H-Alpha housekeeping data is read out during DSF word gates 2, 14, 26 and 38. Thus, they are read out only once every 3.84 seconds and are, therefore, as much as 3.84 seconds out of sync with the actual state of the instrument. DSF data words are used to relay the following information related to the H-Alpha subsystem:

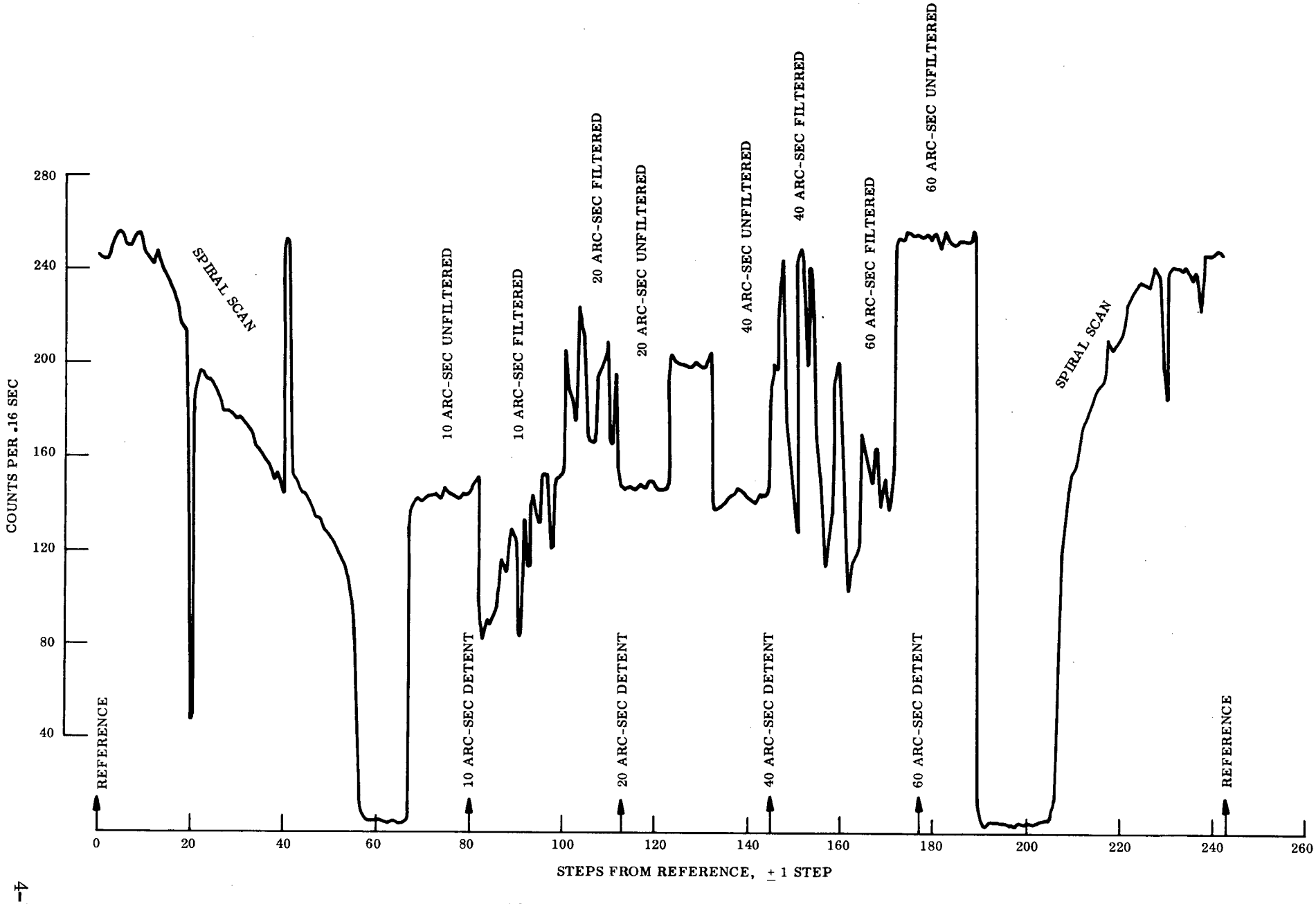

Figure 4-7. H-Alpha Sun Pointing Data: Aperture Wheel Scan No. 1

1. Aperture wheel position

2. Detectors selected - H-Alpha and short EUV or medium and long EUV

The end of line (EOL) and end of raster (EOR) housekeeping data are read out during DMF word gates 3, 4, 7 and 8. Therefore, the DMF housekeeping data is less than 160 ms out of sync with the actual state of the instrument.

SECTION 5

LONG WAVELENGTH X-RAY EXPERIMENT

5.1 REQUIREMENTS

The long wavelength (LW) X-ray experiment is designed to provide spectroheliograms in selected spectral bands between 8Å and 16Å. The field of view (spatial selectivity) is to be less than 20 x 20 arc-seconds. Other requirements are:

1.	Side lobe intensity (up to 40 arc-min)	< 0.1% of main lobe
2.	Coalignment with EUV experiment	< 10 arc-sec
3.	Collimator efficiency	≥ 12%
4.	Filter efficiency	≥ 40%
5.	Detector efficiency	≥ 0.25 counts/photon at 8Å
6.	Balance between filter-pairs	< 2%
7.	Spectral bands	10.19 - 12.13Å; 7.95 - 16Å; 14.50 - 15.90Å; 13.30 - 14.50Å; 7.95 - 9.51Å

5.2 DESIGN SOLUTION

5.2.1 LW X-RAY EXPERIMENT DESCRIPTION*

The LW X-ray experiment design consists of a collimator to provide the spatial selectivity and side lobe suppression, a set of five balanced filter-pairs (Ross Balanced Filter) to provide the spectral bands of interest, a double channel proportional counter, and associated electronics. The filter pairs are mounted on a 6-position filter wheel which is motor-driven so that each of the 5 filter pairs and an open position may be placed in front of the double-channel proportional counter by command. The channels in the detector are side-by-side (A&B) as are the filters (A&B) in each filter-pair; therefore, the output of each channel (A or B) is a function of the filter which is placed in front of the channel.

*Where elements of the (LW & SW) X-ray systems are alike, the description in this section applies to both systems.

One of the main design considerations is the degree of balance that can be maintained between channels. For this reason the collimator is one integral unit for both Channels A and B. This assures balance of area and optical axis. The filters are made oversize and the filter wheel indexing is not critical. Detector balance is enhanced by combining the detector halves into a common gas chamber. There is a common high voltage power supply for both Channels A and B.

The wavelength response of both channels is limited by the detector response and by the setting of the single channel Pulse Height Analyzer (PHA) associated with each detector.

The balance of the detector, as determined by the detector window and gas absorption path, does not change with wavelength. The relative setting of the PHA can and does however change between channels. Therefore, the balance between Channels A and B may depend on the wavelength distribution of the incident radiation. As a general rule the balance reading will only be significant if most of the radiation falls within the window of the PHA.

The LW X-ray experiment is shown schematically in Figure 5-1.

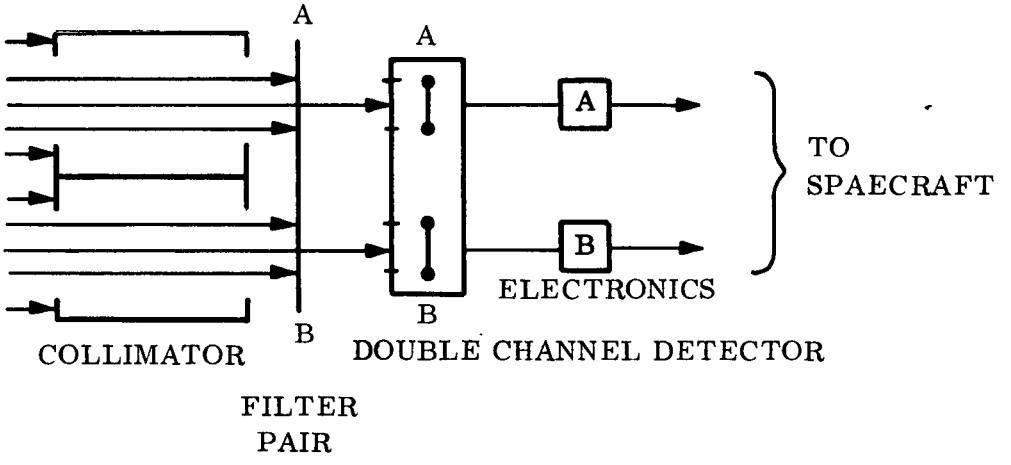

Figure 5-1. Long Wave X-ray Experiment Schematic

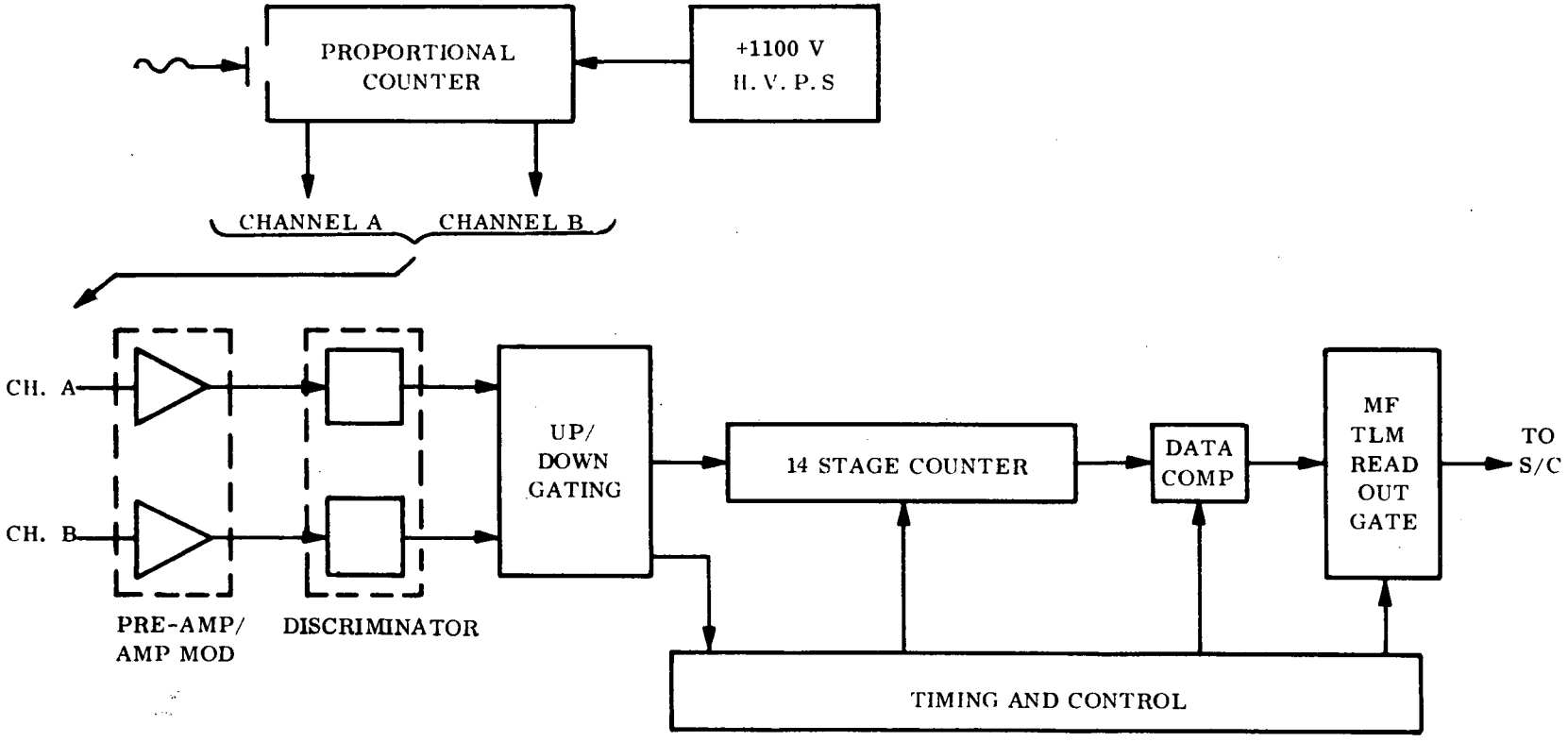

Figure 5-2. Long Wave X-ray Experiment Block Diagram

A block diagram showing the detector and electronics is presented in Figure 5-2.

5.2.2 COMPONENT DESCRIPTION

5.2.2.1 Collimator

The collimator as shown in Figure 5-3 restricts the field of view of the incoming energy to the X-ray subsystem. The collimator has two main apertures, the lower aperture for the long wave energy and the upper aperture for the short wave energy. The significant parameters of the collimator are given below.

1.	Wavelength Range (Å)	(SW) 1.75 - 8.0Å (LW) 8.0 - 16Å
2.	Spatial Resolution (FWHM) (Arc-Sec)	20 x 20
3.	Total Aperture (Each Section) (CM)	2.03 x 3.18
4.	Main Lobe Transmission (%)	12.0
5.	Side Lobe Transmission to 40 Arc-Min Off Axis (%)	< 0.1 of incident
6.	Effective Area (Each Section) (cm^2)	1.0
7.	Alignment - X-ray Axis to Ref. Surface (Arc-Sec)	$< \pm$ 5.0
8.	Size (CM)	4.52 x 7.62 x 31.75
9.	Weight (kg)	0.836

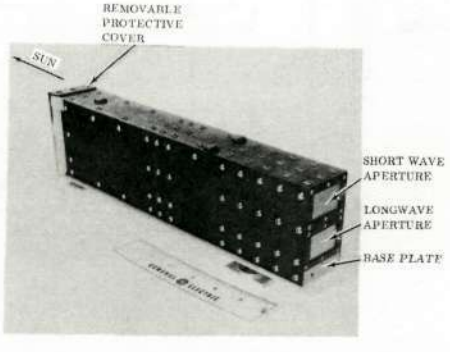

Figure 5-3. Collimator

Design. Collimation is achieved by mechanically blocking the field of view by a series of grids as shown in Figure 5-4. The two end grids determine the width of the main lobe, and the intermediate grids intercept the off-axis radiation. The number and placement of the grids as shown in Figure 5-4 are such that a minimum of two grids intercept the off axis radiation up to 40 arc-minutes. The grids are precision nickel plated arrays made by a process similar to the slit apertures previously described. All grids are made from the same master to minimize dimensional variations. The grids are gold coated with 3.5 micron thickness of gold to attenuate the off-axis radiation. The grids are precision assembled so that all holes are aligned to better than 0.0001 inch to maintain efficiency of transmission of the main lobe.

The structural elements of the collimator are fabricated from beryllium for light weight, high stiffness, and to match the thermal expansion characteristics of the instrument structure which also is beryllium.

The initial fabrication of the collimator utilized an array of eight intermediate grids and two end grids. X-ray testing revealed excessive off-axis transmission and a detailed analysis showed that there was an insufficient number of grids blocking the off-axis radiation at a few specific angular positions. To correct the problem, two additional grids were added in both the short wave and the long wave channels. In addition, two grids in the short wave channel were gold coated on both sides rather than on just one side as in all the other grids. These modifications brought the off-axis transmission below the maximum allowable value.

Testing. The collimator was tested for resolution, off-axis transmission, optical axis determination and efficiency before and after vibration. A transmission curve for the flight collimator is shown in Figure 5-5. All parameters were tested within the specified limits and there was no degradation of performance from the vibration environment.

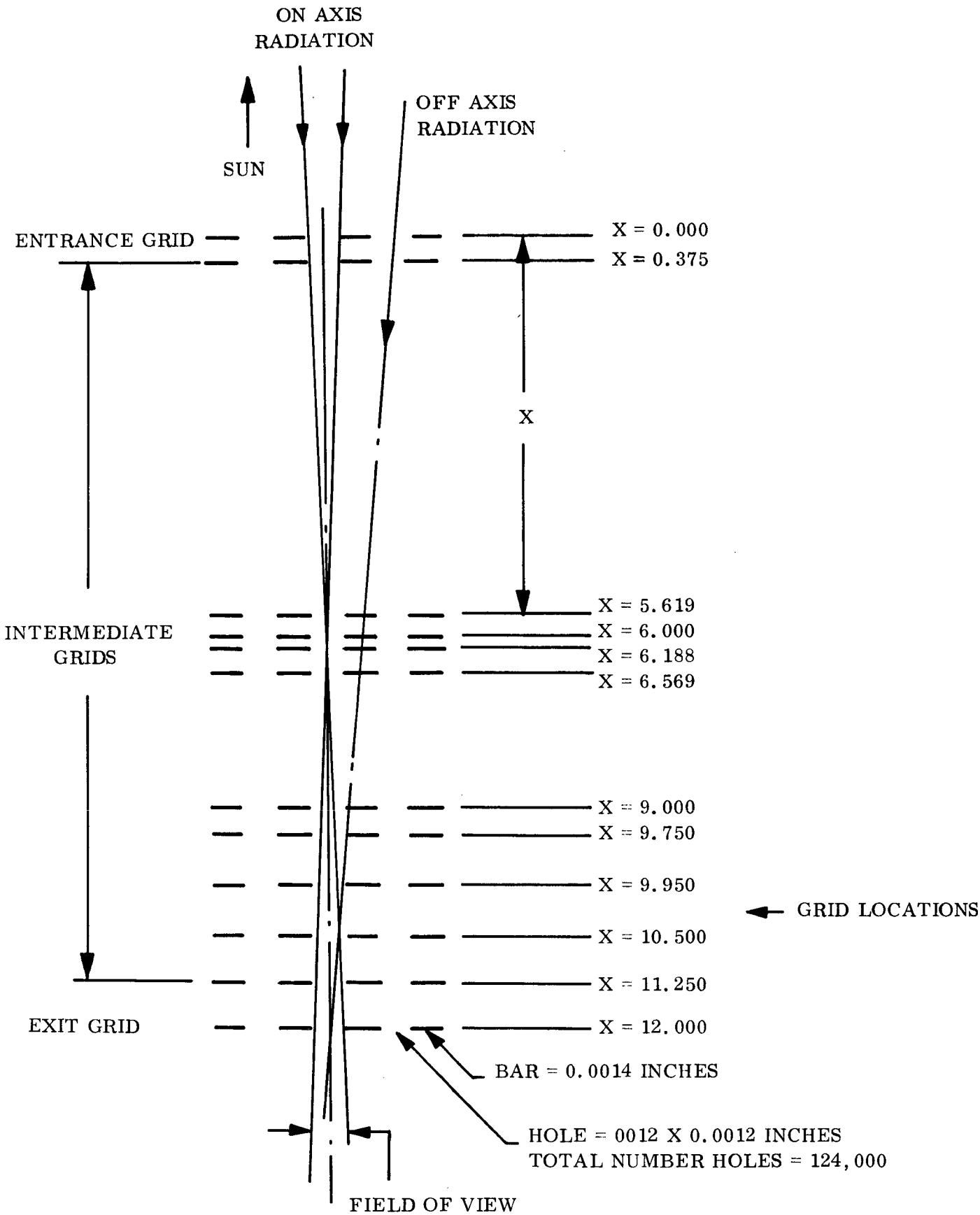

Figure 5-4. Collimator Grid Configuration

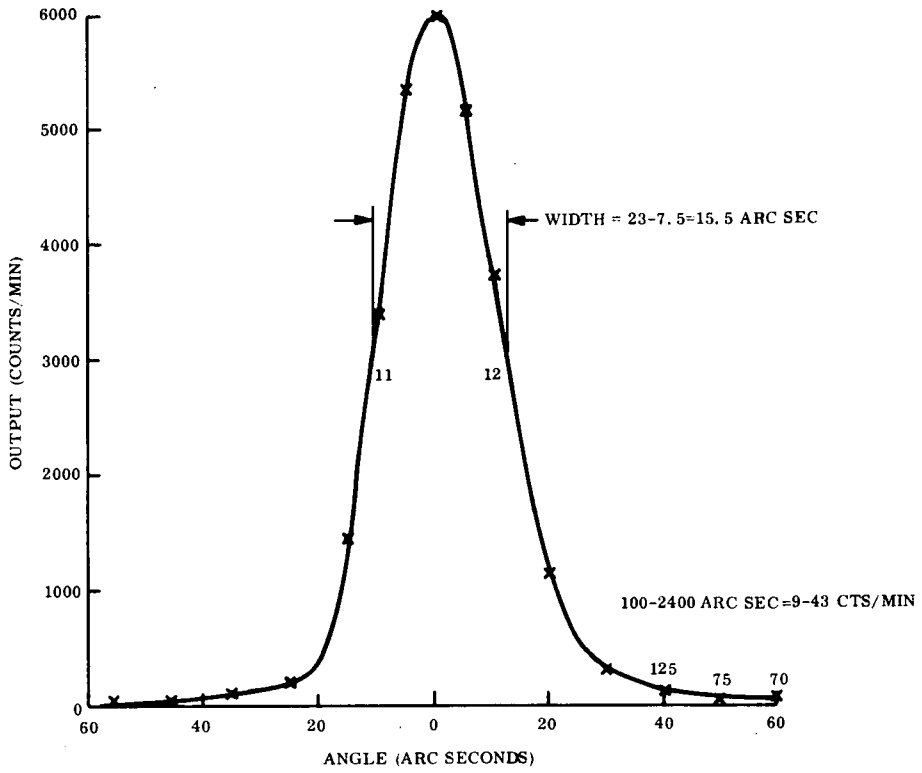

Figure 5-5. Collimator No. 1 Transmission

5.2.2.2 X-ray Sensors

The long and short wavelength X-ray sensors are identical in construction differing only in the entrance window and gas filling. The units consist of twin proportional counters housed in one envelope. Figure 5-6 is a schematic drawing of the sensors and Figures 5-7 and 5-8 are photographs of the long and short wavelength sensors, respectively. The actual constructional details of the sensors are listed in Table 5-1. It was important that each of the counters of each sensor have like characteristics. Therefore, each counter was exposed to the same gas composition and pressure, had equal chamber volumes and identical entrance windows.

Basic requirements for the proportional counters are as follows:

1.	Background	< 30 cpm
2.	Plateau Slope	3%/100 V
3.	Life	10^{10} counts

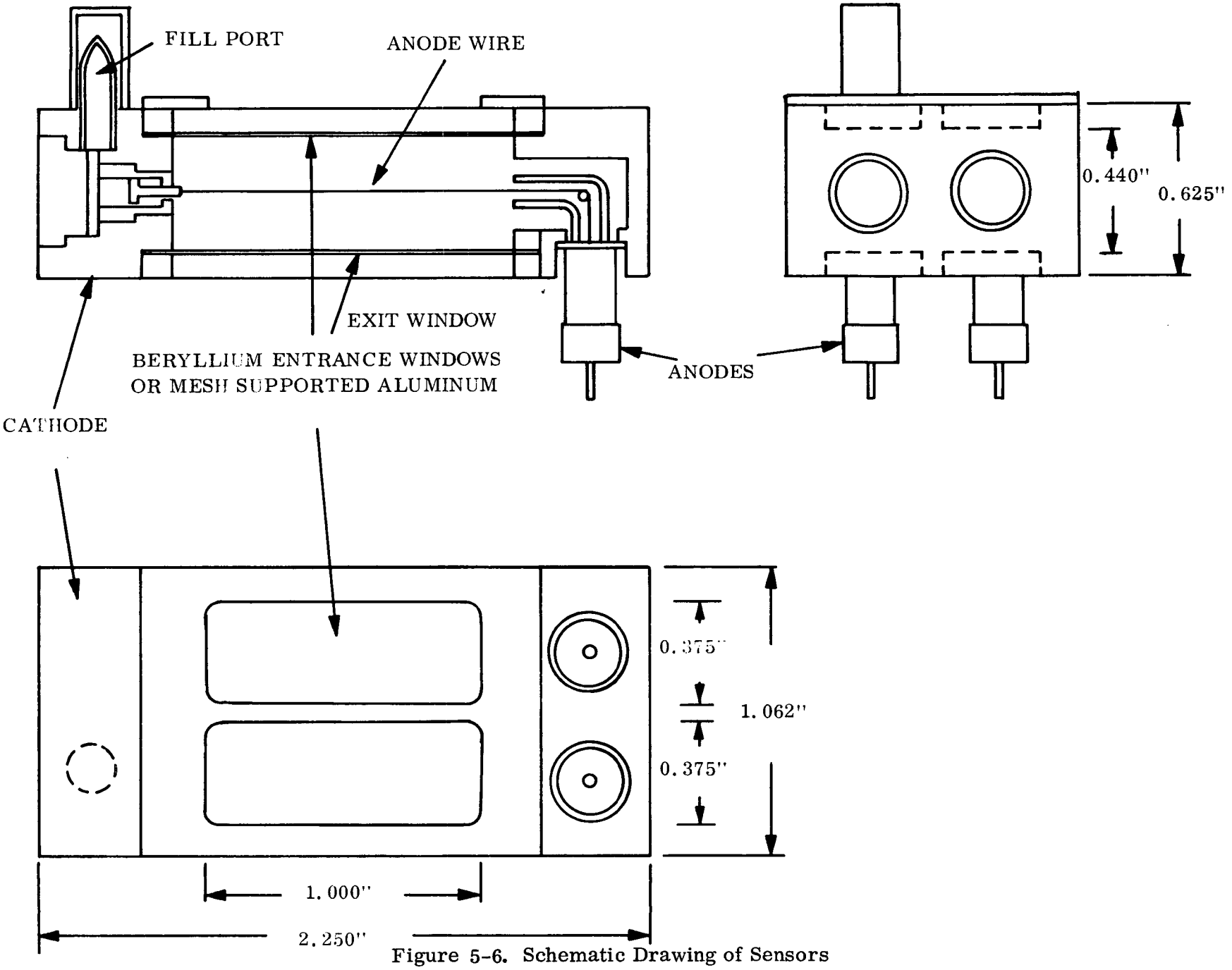

Figure 5-6. Schematic Drawing of Sensors

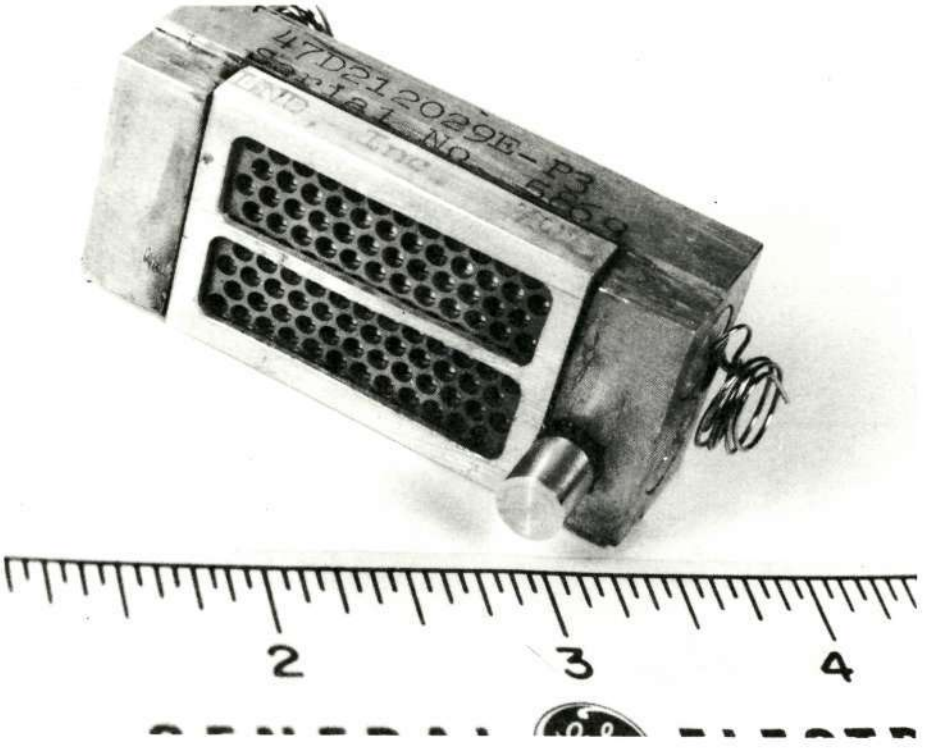

Figure 5-7. Long Wavelength Sensor

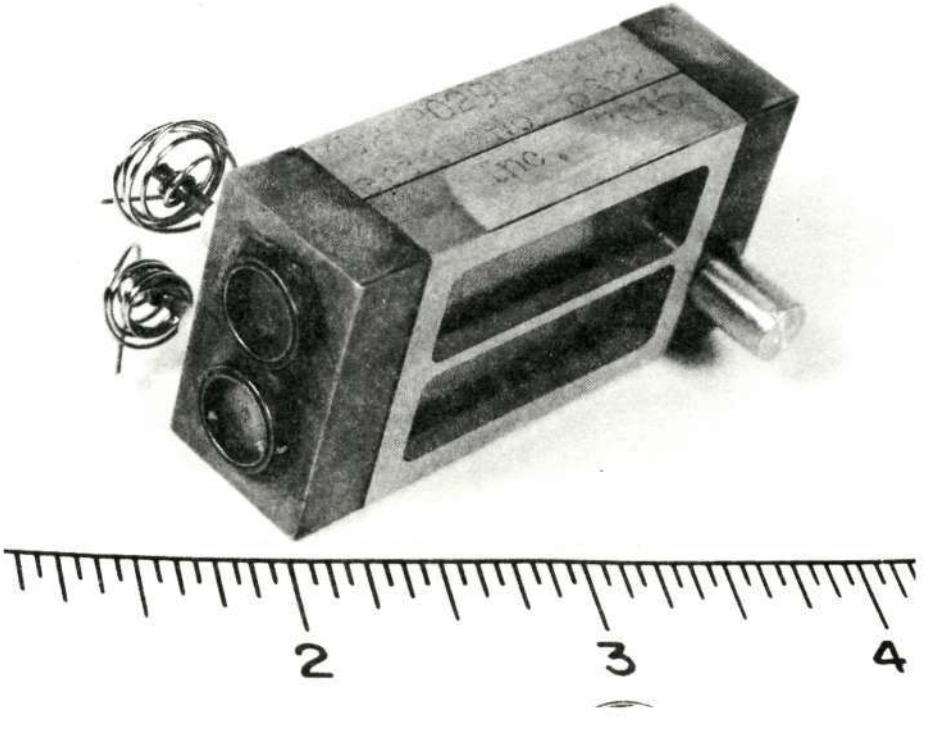

Figure 5-8. Short Wavelength Sensor

4.	Plateau Range	300 ± 100 V
5.	Resolution (Center of Window)	25% FWHM (2Å)
6.	Long Term Balance Between Two Sections	1%
7.	Orbit Stability	± 2%
8.	Count Rate Linearity Limit	10^5 cps

Table 5-1. The Proportional Counter Parameters

Sensor Identification	Wavelength Range (Å)	Dimensions (mm)	Gas Filling (1 Atm.)	Entrance Window	Exit Window	Anode Wire	Body Material
SW	1.5 - 8.0	25.0 Length*	90% X_e	Beryllium	Beryllium	Tungsten	Aluminum
		9.5 Width*	9% CO_2	12 mg/cm^2	37 mg/cm^2	25 microns	(Epoxy Seals)
		10.5 Height**	1% He				
LW	8.0 - 16.0	25.0 Length*	80% Ne	Aluminum	Gold Coating*** on back of counter wall.	Tungsten	Aluminum
		9.5 Width*	10% Ar	6 microns (Grid Support 60% Trans)		25 microns	(Epoxy Seals)
		10.5 Height**	9% CO_2 1% He				

*Window dimensions.
**Gas path dimensions.
***The gold coating reduces background counts because of hard X-ray fluorescence.

The outputs of each of the counters was connected to its own preamplifier and amplifier. The preamplifier is of the charge sensitivity type. The mulitplication factor of the sensors was adjusted to give a mean charge per pulse of 2×10^{-13} coulombs when exposed to 2Å and 8Å for the short and long wavelength sensors, respectively. This setting simplifies electronic design in terms of gain stability and still allows for good count rate linearity in excess of 10 kHz.

Because of the thickness of the windows and the attendant degradation/leakage problems, the LW X-ray sensors were periodically tested to measure the performance stability and establish life histories. All of the proportional counters procured on the program eventually showed signs of gain deterioration. Since attempts to rework some of the earlier units had not resulted in improved life, the decision was made to use for flight a proportional

counter which had been procured by NASA/GSFC and which had shown good stability over a long period. This GFE unit was installed following the flight acceptance test thermal-vacuum cycle.

The measured counting efficiencies for the LW and SW sensors as a function of wavelength and energy resolution are shown in Figures 5-9 and 5-10. Figure 5-9 was prepared from data taken on the flight SW sensor. Figure 5-10 was prepared from data taken on the LW sensor (S/N 2144) which was scheduled for flight. This sensor was replaced by a GFE sensor immediately before delivery.

5.2.2.3 Balanced Filters

The use of the balanced filter-pair method of X-ray energy isolation was chosen primarily because it yields high sensitivity while at the same time allowing adequate wavelength monochromatization. The method operates on the prinicple of measuring the count rate difference of two thin film filters made up of nearly adjacent elements. This differential count rate is proportional to the intensity of wavelength which lies in the wavelength passband formed by the absorption edges of the two filter materials. The flight balanced filter-pairs and their respective passband are given in Table 5-2.

Table 5-2. Balanced Filter Pairs

Long Wavelength		
Pair	λ	$\Delta\lambda$
Ni-Co (1)	14.50-15.90	1.40
Ge-Zn (2)	10.19-12.13	1.94
- (3)	-	-
Ni-Co (4)	14.50-15.90	1.40
Cu-Ni (5)	13.30-14.50	1.20
Al-Mg (6)	7.95- 9.51	1.56
Short Wavelength		
Fe-Mn (1)	1.74-1.90	0.16
Mn-Cr (2)	1.90-2.07	0.16
S-Al (3)	5.02-7.95	2.93
Fe-Mn (4)	1.74-1.90	0.16
Fe-Cr (5)	1.74-2.07	0.33
- (6)	-	-

Note: Number in parenthesis indicates filter wheel position

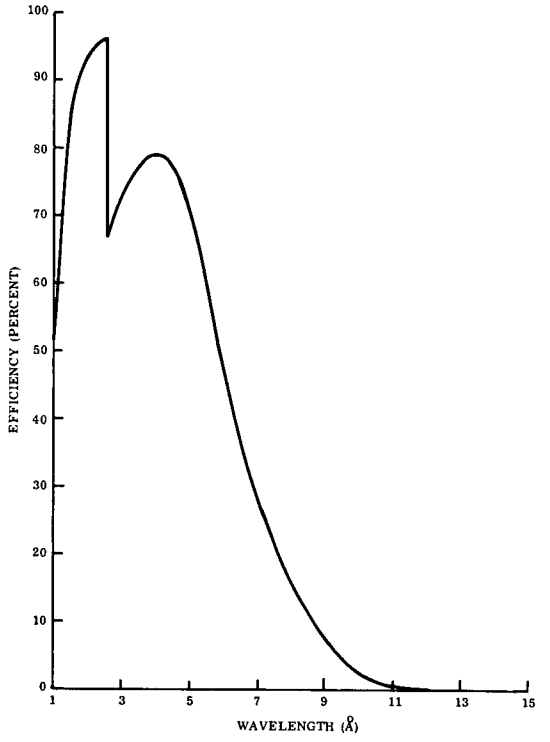

Figure 5-9. Efficiency of Short Wavelength Proportional Counter (Flight)

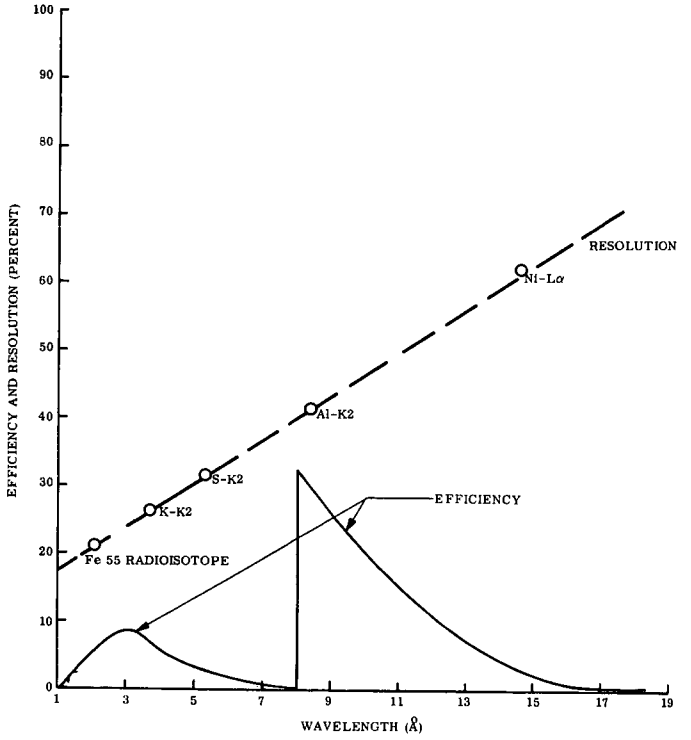

Figure 5-10. Efficiency and Resolution of Long Wavelength Proportional Counter (S/N 2144)

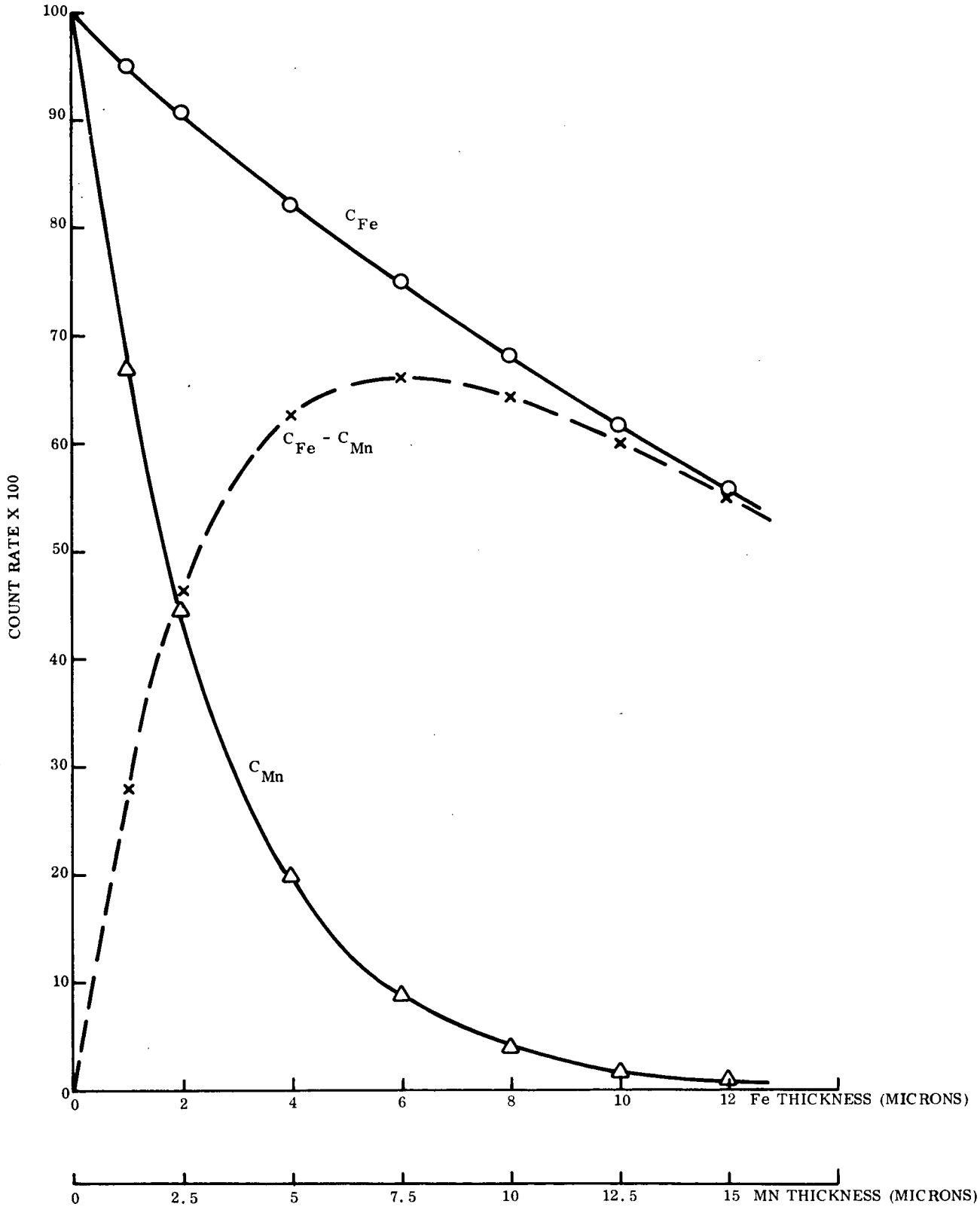

Figure 5-11. Transmitted Count Rate of Fe - Kα X-rays as a Function of Thickness of the (Fe-Mn) Filter-Pair (Dashed curve gives the differential count rate.)

Optimal Filter Material Thickness

The optimal thickness of any filter material to be used in a balanced pair arrangement is defined as that thickness that allows maximum differential transmission within the filter-pair passband or

$$I_t - I_a = \text{Max.} \tag{5-1}$$

where $I_t = I_o e^{-\mu_t x}$ and $I_a = I_o e^{-\mu_a x}$, the intensities transmitted through the "transmitting" and "absorbing" filters, respectively. To obtain a differential maximum then:

$$d(I_t)/dx - d(I_a)/dx = 0 \tag{5-2}$$

Making the substitution, performing the differentiation and simplifying, one obtains the quantity

$$x = \ell n\ (\mu_t/\mu_a)/\mu_t - \mu_a \text{ (cm)} \tag{5-3}$$

The transmitting filter thickness corresponding to the differential passband maximum count rate is a function of the absorption coefficient of the filter material within the passband and the absorption coefficient the material would have if extrapolated from the short wavelength side of the absorption edge. As an example, consider the filter-pair Fe-Mn from Table 5-2. The absorption coefficient for Fe at 1.82Å is,

$\mu_t = 485$ cm^{-1}* and the extrapolated coefficient is, $\mu_a = 4050$ cm^{-1}[8]. Substituting these values into Equation 5-3 one obtains,

$$x_{Fe} = 6 \text{ microns}$$

for maximum passband transmission. The thickness of the manganese filter is given by:

*Tables of X-Ray Mass Absorption Coefficients, J. Appl. Phys. 20, 1141, 1949.

$$x_{Mn} = \left[\mu_a \text{ (Fe)} / \mu \text{ (M}_n\text{)} \right] \quad x_{Fe} \text{ (at 1.82 Å)} \tag{5-4}$$

or

$$x_{Mn} = \left[\text{ 4050 cm}^{-1} / \text{3250 cm}^{-1} \right] \quad \text{6 microns} = \text{7.5 microns.}$$

The counting rate as a function of filter thickness is illustrated in Figure 5-11. The figure gives the detected counting rates of the Fe-Kα X-ray line as a function of the thickness of the iron and manganese filter pair. As the figure shows, the filter thickness that gives peak differential counting rates is predicted by Equation 5-3. Also, Figure 5-11 shows that the optimum filter thickness is quite a broad function. Thickness values between 4 and 10 microns can be used without seriously affecting the maximum differential count rate. These calculated filter thicknesses serve only as guide line values. The actual filter thickness can only be obtained through experimental balancing techniques.

Filter-Pair Balancing. The majority of the filter-pairs are made up by elements that are either adjacent or separated by one atomic number in the periodic table and, therefore their absorption edge discontinuities are identical (within 2 percent of each other). Balancing is achieved by proper filter thickness adjustment. However, there is one filter-pair (S-Al) whose absorption edge discontinuity differs by about 20 percent. To overcome this major unbalance it becomes necessary to compensate the transmitting filter of the pair; namely, sulphur, by the addition of an auxiliary filter which has no absorption edge within the wavelength region of interest. The transmission through the sulphur filter S plus this auxiliary filter x, will be made to just equal the transmission through the aluminum filter Al, or:

$$\left(\mu_{s_1} T_s + \mu_x T_x \right) / \left(\mu_{s_2} T_s + \mu_x T_x \right) = \mu_{a\ell_1} / \mu_{a\ell_2} * \tag{5-5}$$

Where the μ's are the absorption coefficients and the T's are the filter thicknesses. The suffix 1 refers to that coefficient on the short wavelength side of the absorption edge and

*The Encyclopedia of X-rays and Gamma Rays, G. L. Clark, Ed., Reinhold Publishing Co., N.Y., 1963, p. 391.

2 to that on the long wavelength side. The auxiliary filter thickness is then given by:

$$T_x = T_s \left(\mu_{s_1}/\mu_{s_2} - \mu_{a\ell_1}/\mu_{a\ell_2}\right) \mu_{s_2}/\left(\mu_{a\ell_1}/\mu_{a\ell_2} - 1\right) \mu_x \qquad (5\text{-}6)$$

Where T_s is determined from Equation 5-3.

Let us consider the case of the S-Al filter-pair, from Reference 1 and Equation 5-3 then,

$$\left.\begin{aligned} \mu_{s_1} &= 4850\ \text{cm}^{-1} \\ \mu_{s_2} &= 460\ \text{cm}^{-1} \end{aligned}\right\} \text{ at } 5\text{Å}$$

$$\left.\begin{aligned} \mu_{a\ell_1} &= 12600\ \text{cm}^{-1} \\ \mu_{a\ell_2} &= 970\ \text{cm}^{-1} \end{aligned}\right\} \text{ at } 8\text{Å}$$

$$T_s = 2.7 \text{ microns determined at } 6.5\ \text{Å}.$$

Formvar was used for the auxiliary filter material, and from tabulated data $\mu_x = 269\ \text{cm}^{-1}$ at 5Å. Substituting the above quantities into Equation 5-6 and performing the required operation yields,

$$T_x = 0.95 \text{ micron.}$$

The thickness of the aluminum filter will be given from Equation 5-4 by,

$$T_{a\ell} = \left(\mu_s + \mu_x/\mu_{a\ell}\right) T_s + x \text{ at } 6.5\ \text{Å or,}$$

$$T_{a\ell} = (9800 + 580/7200)\ 3.65 = 5.25 \text{ microns.}$$

5.2.2.4 Sensor Electronics

The purpose of the X-ray sensor electronics is to amplify, discriminate and condition the output of the dual chambered proportional counter. The output from each chamber of the

proportional counter is separately amplified and discriminated. The outputs of the discriminators are appropriately called Channel A and Channel B, respectively.

The amplifiers used to amplify the output signals of the proportional counters are the same as the amplifier use in the EUV subsystem. For a detailed description reference paragraph 3.2.2.6.

However, the discriminators differ from the one used in the EUV subsystem in that a window discriminator is required. To accomplish this function, a low level threshold detector, a high level threshold detector, a ramp generator, and an output threshold detector are employed in the configuration shown in Figure 5-12. When the signal from the amplifier is of sufficient magnitude to trigger the low level threshold, the output of the low level discriminator starts a ramp generator. If the amplifier output signal does not reach the high level threshold, the ramp generator triggers the output threshold detector. However, if the signal exceeds the upper threshold, the output of the high level threshold detector inhibits the ramp generator before it triggers the output threshold detector. Therefore, only signals which fall between the upper and lower thresholdd produce an output which is counted by the logic. Figure 5-13 shows the typical waveforms for the operation of the window discriminator for (1) the case when the amplifier signal exceeds the lower threshold but not the upper threshold, and (2) the case where the signal exceed both thresholds.

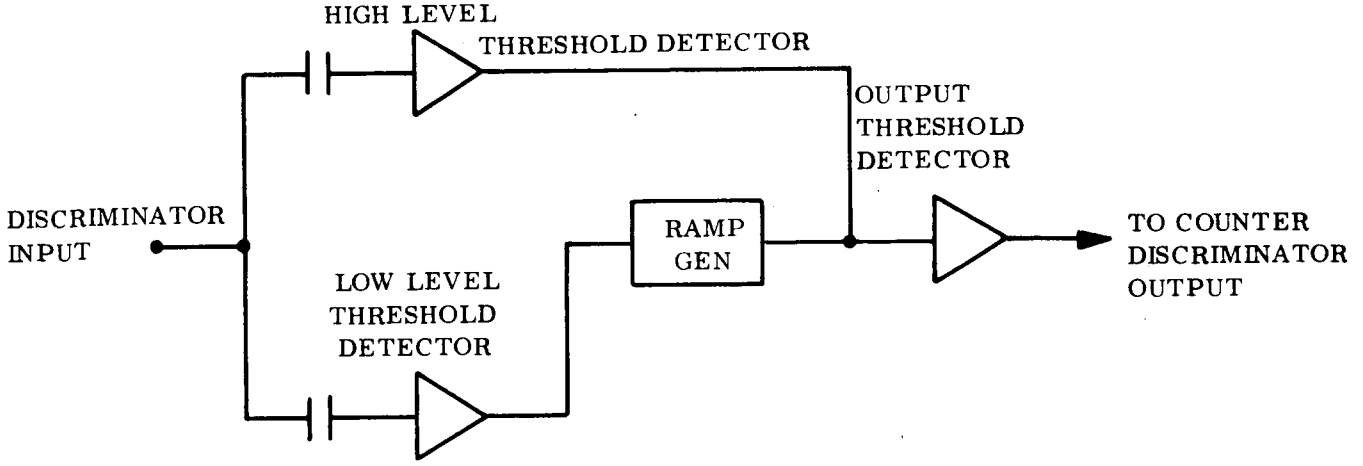

Figure 5-12. Block Diagram of Window Discriminator

The low level threshold discriminator and the output threshold discriminator are discussed in paragraph 3.2.2.6.

The high level threshold discriminator is identical in operation to the low level threshold discriminator. Its design is the same except for the reference for the differential amplifier. The schematic is shown in Figure 5-14.

The schematic of the ramp generator which provides the necessary time delay between the output of the low level detector and the triggering of the output discriminator to ensure that the amplifier output signal does not exceed the upper threshold is shown in Figure 5-15.

5.2.2.5 Data Processing Electronics

The outputs of Channel A discriminator and Channel B discriminator are coupled into a counter circuit through a mode selection network. There are three possible modes which can be selected. The operator can select data from Channel A only, from Channel B only, or he can select a mode which yields the difference (A-B) between the two channels. The data handling is performed using 54L series Texas Instrument logic circuits, and the arrangement of the logic is shown on Drawing No. 47C217126. The data mode selection logic is shown in Figure 5-16.

A 13 Stage up-down counter (Figure 5-17) with a prescaler is employed to do the data accumulation. In response to the appropriate command, the counter can be gated to accumulate counts from Channel A only or from Channel B only. In either of these cases, it performs like the 14-Stage counters used in the EUV data handling logic. Also it can be commanded to accumulated the difference between Channel A and Channel B. In this mode, the counter utilizes its up-down capability. When the counter receives a pulse from Channel A, it counts "up" one (adds one count) and when it receives a pulse from Channel B it counts "down" one (subtracts one count). Regardless of the mode, the counter accumulates counts for 146.25 ms. The counter is then disabled and the 13 most significant bits of the 14-bit word are compressed into an 8-bit word which is then transmitted to the spacecraft. The counter is then cleared (reset to zero) and enabled again, thus, starting the sequence again. The entire sequence takes 160 ms.

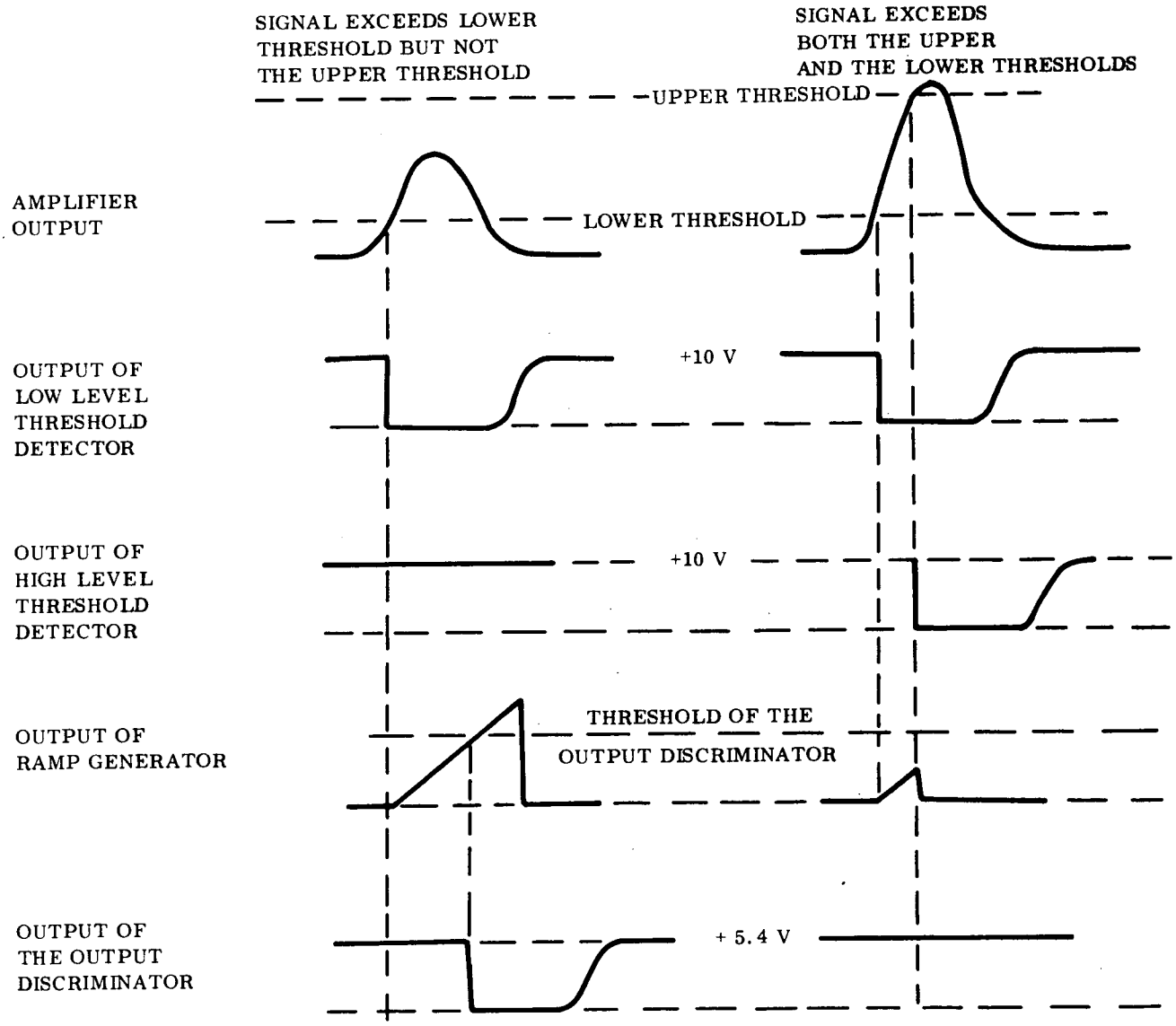

Figure 5-13. Typical Waveforms Characteristic of the Window Threshold Detector

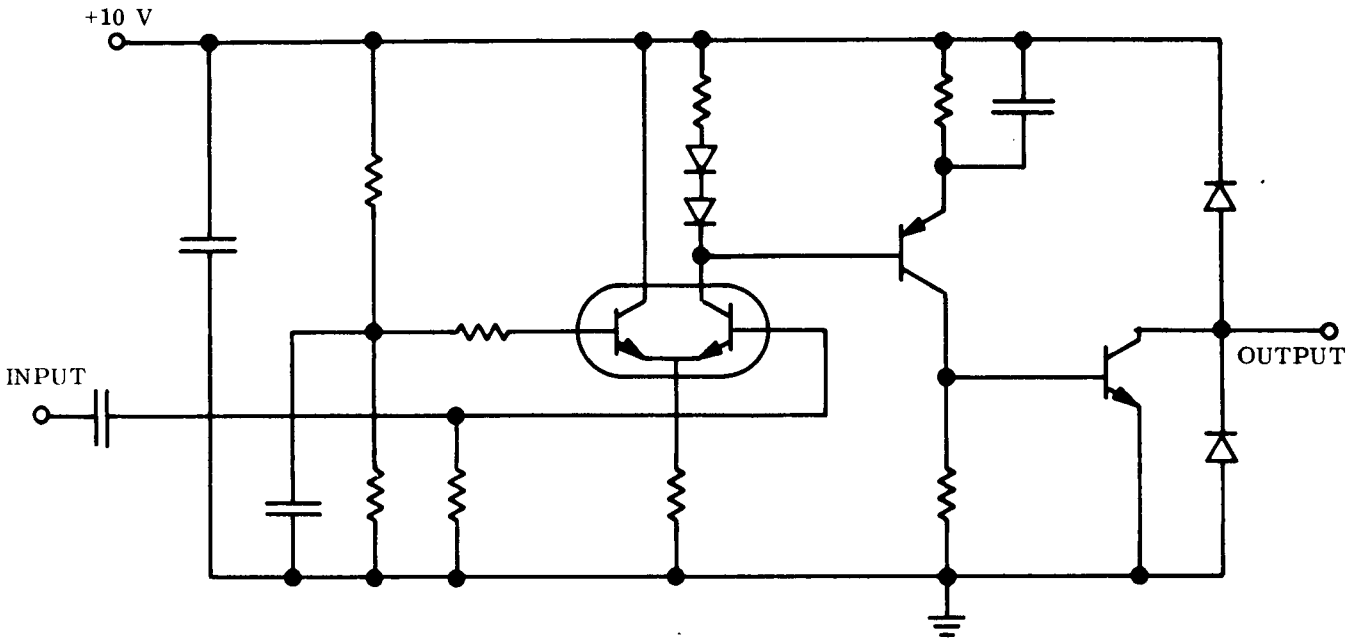

Figure 5-14. High Level Threshold Detector (Discriminator)

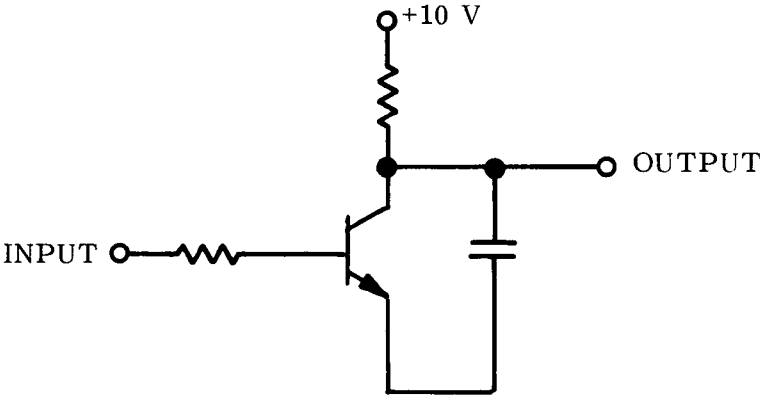

Figure 5-15. Ramp Generator

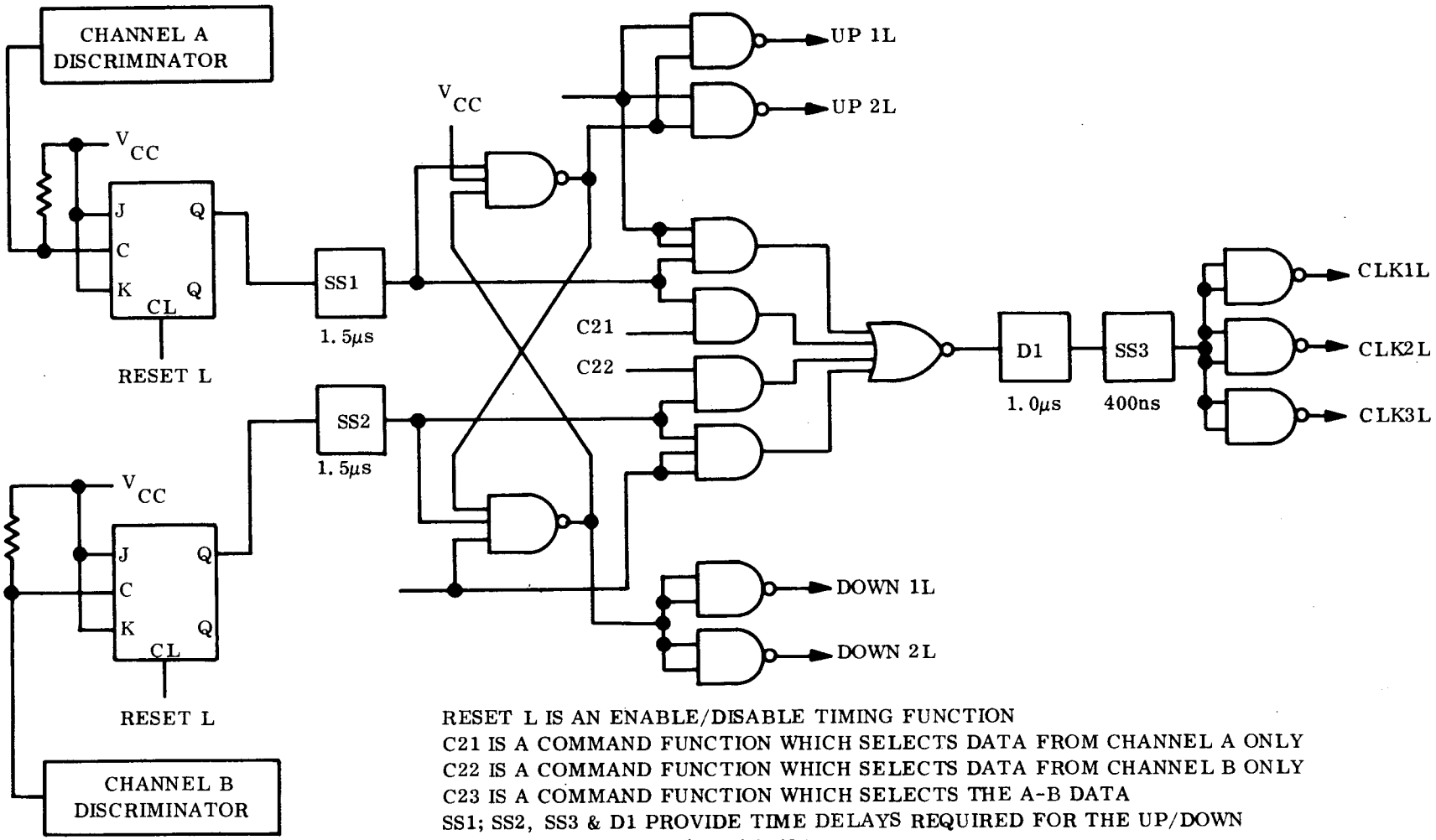

Figure 5-16. Long X-ray Data Mode Selection Logic

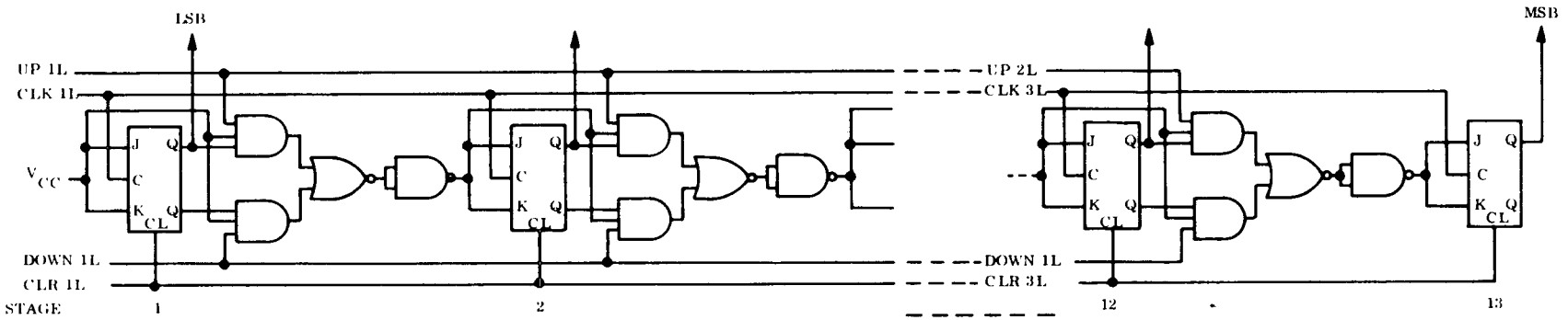

UP 1L, UP 2L - SET-UP SIGNAL GENERATED BY THE DATA MODE SELECTION CIRCUIT WHICH PROGRAMS THE COUNTER TO INCREASE THE COUNT IN THE REGISTER BY ONE ON THE NEXT CLK 1L PULSE

DOWN 1L, DOWN 2L - SET-UP SIGNAL GENERATED BY THE DATA MODE SELECTION CIRCUIT WHICH PROGRAMS THE COUNTER TO DECREASE THE COUNT IN THE REGISTER BY ONE ON THE NEXT CLK 1L PULSE

CLK 1L, CLK 2L, CLK 3L - "CLOCK" PULSE USED TO REGISTER THE COUNTS

CLR 1L, CLR 2L, CLR 3L - TIMING FUNCTION USED TO CLEAR THE COUNTER

Figure 5-17. Long X-ray 13-Stage Up/Down Counter

X-Ray Data Compression. The X-ray data compression logic is identical to that used in the EUV subsystem; i.e., the X-ray and the EUV experiments time share the same data compression logic. However, several differences exist in the telemetered data.

The data compression logic only compresses the contents of the 13 most significant bits into 8 bits. The content of the least significant bit (LSB) which is located in the prescaler is not read out; therefore, no odd numbers will appear in the decoded X-ray data. Note that the 8-bit compressed word is decoded in the same manner as the EUV word because there is in fact a 14-Stage counter (13-Stage up-down counter plus a prescaler) used to accumulate the data. Furthermore, because of the prescaler the maximum possible round-off error in X-ray differs slightly from that in EUV. A difference exists only in the 2 to 30 data range. The maximum possible round-off error in this range in X-ray is one (1) whereas in EUV it is zero (0). For a detailed description of data compression, see paragraph 3.2.2.7.

Note that the up-down counter cannot count negative; therefore, if the A-B mode is selected and B is greater than A the telemetered data will read 15872. This number is simply the maximum number which can be telemetered to the spacecraft and it is used as a code in the A-B mode to indicate that B was greater than A for that data accumulation period.

The long X-ray data is transmitted to the spacecraft during DMF word gates 4 and 20.

5.2.2.6 Housekeeping Electronics

X-ray housekeeping is broken down into two categories: X-ray channel selection and X-ray filter wheel position. The last 4 telemetry bits of DSF words 4, 16 and 28 are used to indicate the data channel selections, and DSF words 8, 20, 32 and 44 are used to indicate the filter wheel positions. The telemetry bits in these words are assigned the functions illustrated in Tables 5-3 and 5-4.

Each data bit is generated by a microswitch or a combination of relay contacts. The signals from the appropriate microswitches and relays are processed using series 54L Texas Instrument logic circuits. The logic configuration is shown on drawing No. 47C217R6. In general, each of the telemetry bits are generated in the following manner.

Table 5-3. Data Format for X-ray Channel Selections

Telemetry Bits in DSF Words 4, 16 and 28		TB5	TB6	TB7	TB8
Short X-ray Channel	A only	0	1	---	---
Short X-ray Channel	B only	1	0	---	---
Short X-ray Channel	A-B	1	1	---	---
Long X-ray Channel	A only	---	---	0	1
Long X-ray Channel	B only	---	---	1	0
Long X-ray Channel	A-B	---	---	1	1

Table 5-4. Data Format for X-ray Filter Wheel Position

Telemetry Bits in DSF Words 8, 20, 32, 44	Long X-ray Filter Wheel Position			Short X-ray Filter Wheel Position			Spare Bits	
Position	TB1	TB2	TB3	TB4	TB5	TB6	TB7	TBA
1	0	0	1	0	0	1	-	-
2	0	1	0	0	1	0	-	-
3	0	1	1	0	1	1	-	-
4	1	0	0	1	0	0	-	-
5	1	0	1	1	0	1	-	-
6	1	1	0	1	1	0	-	-

1. Telemetry Bits in DSF Words 4, 16 and 28

   a. TB5 and TB6. The short X-ray housekeeping logic senses the state of three relays (K17, K18 and K19) to determine which short X-ray data selection command was sent last and thus what data channel is being read out (A, B or A-B).

   b. TB7 and TB8. The long X-ray housekeeping logic senses the state of three relays (K20, K21 and K22) to determine which long X-ray data selection command was sent last and thus what data channel is being read out (A, B or A-B).

2. Telemetry Bits in DSF Words 8, 20, 32 and 44

   a. TB1, TB2 and TB3. The signals from microwswitches MS1 and MS8 are used to indicate the position of the long X-ray filter wheel. There are six equally spaced detents on the wheel. In addition, half way between the two detents which correspond to Positions 6 and 1 there is a reference microswitch. The signal from the reference microswitch (MS1) is used to clear a three-Stage counter and each time MS8 is actuated the counter counts once. Since there are six detents which cause MS8 to be acuated before the wheel passes through the reference, the counter counts to 6 before it is reset to zero by MSI. Note that the filter wheel does not stop turning when it reaches the reference microswitch, but rather continues on until it reaches the next detent (detent corresponding to Position 1).

   b. TB4, TB5 and TB6. The position indication for the short X-ray filter wheel is generated in the same manner as that for the long X-ray filter wheel, except that microswitch MS2 is the reference microswitch and MS9 is used to step the counter.

Note that any time the orbit power to the instrument has been off, both filter wheels will lose their reference and the wheels must be advanced past the reference position before the housekeeping will be in sync with the actual filter wheel positions. Therefore, it is possible for the housekeeping to read 7 or 0 before the wheels pass through the reference for the first time. It is also possible for the housekeeping to read 1 for two consecutive positions. For instance, if the logic randomly comes up (when the power is applied) reading 4 when the wheel is really in Position 1, then as the wheel advances from position to position the housekeeping will read 4-5-6-7-0-1-1-2-3-4-5-6-1-2-.

In addition to the DSF housekeeping data there are three housekeeping codes which appear in the DMF data. These codes indicate End of Line (EOL) End of Raster (EOR) and End of Spectral Scan (EOSS). Each of these codes and the manner in which they are generated is discussed in detail in paragraph 3.2.2.8. Note that although only the EOL and EOR codes are pertinent to X-ray the EOSS also appears in the X-ray data.

5.2.2.7 Filter Wheel Assembly

The filter wheel assembly, shown in Figure 5-18, contains the long wave and short wave filter wheels which rotate independently about a common pedestal, to insert wavelength

selective filters in the X-ray path. Each wheel has provision for mounting six such filter pairs. The X-ray proportional counters and their associated electronic amplifiers are mounted internally within the pedestal.

The filter wheel rotates on a large diameter thin race bearing. A large ring gear is attached to the wheel.

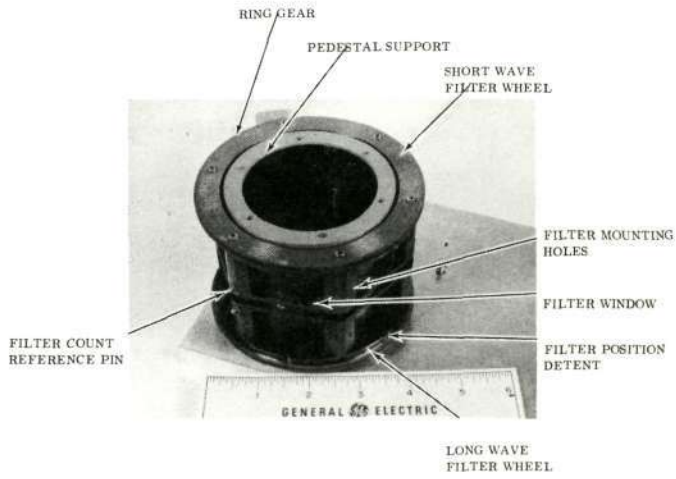

Figure 5-18. Filter Wheel Assembly

Each wheel is driven independently through its ring gear by a separate motor gearhead similar to the other motor gearheads in the instrument. The rotation of the wheels is controlled by two microswitches for each wheel. One microswitch engages the detents when the filter is fully in front of the proportional counter. It provides an input to the control logic to stop the wheel in this position and to advance the filter position count. The second switch is actuated once each complete revolution by a pin projecting from the wheel. This actuation resets the telemetered filter position count.

Each wheel also contains a radioactive source which comes into view of the detector once each revolution of the wheel. The source provides a calibration level for the system.

The filter wheel bearings, ring gear and gearhead output pinion are lubricated with the same solid film lubricant described previously. The gearheads for the filter wheel drives, unlike the other gearheads, are not sealed by an O-ring on the output shaft since backlash in this system is not critical. The elimination of this O-ring provides additional torque margin in the drive system resulting in greater reliability than would be available if the O-ring were used.

5.3 ALIGNMENT AND CALIBRATION

5.3.1 ALIGNMENT

Alignment of the LW and SW X-ray experiments is accomplished by aligning the collimator relative to the EUV telescope. Refer to paragraph 3.3.1 for alignment results.

5.3.2 CALIBRATION

The spectral selectivity depends on the degree of balance of the filter pair as well as the characteristics of other components affecting the received spectral distribution. Examples of this are shown in Figure 5-19. Shown are the percentage transmissivity values of three typical filter pairs; namely, Al-Mg; Ge-Zn and Ni-Co. The total response shown is determined by the individual filter pair response as modified by the detector Al window response.

Consider the Al-Mg filter case. The plot shows the balanced filter pair response as the shaded area. The detector window which is also Al attenuates the filter pair response by the dotted line. Otherwise it acts as an additional broadband filter providing discrimination against radiation outside the filter-pair window, mainly at the longer wavelengths. The situation is different and less favorable for the Ni-Co filter. Here the Al detector window attenuates the wavelengths within the Ni-Co passband. At the same time wavelengths in the 7.95 to 11Å region are much less attenuated. Therefore it is very important that the Ni-Co filter pair be well balanced in the 7.95 to 11Å region. For example, a 2 percent unbalance of the filter pair at 8Å would appear as a 16 percent imbalance realtive to a signal falling within the passband. The Ge-Zn filter pair is an intermediate case as far as the influence of the Al window goes. It is proposed that the spectral purity of the filter pair response be checked by comparing the responses of different pairs for different spectral distributions on the sun. In this way, the discriminating characteristics of the pairs can be checked.

The absolute efficiency for the 5 filter pairs positions can now be calculated by considering the collimator efficiency of 12 percent, collimator area of 3.2 cm^2 per channel (A or B), detector and actual filter pair efficiency. Table 5-5 lists filter pairs identification,

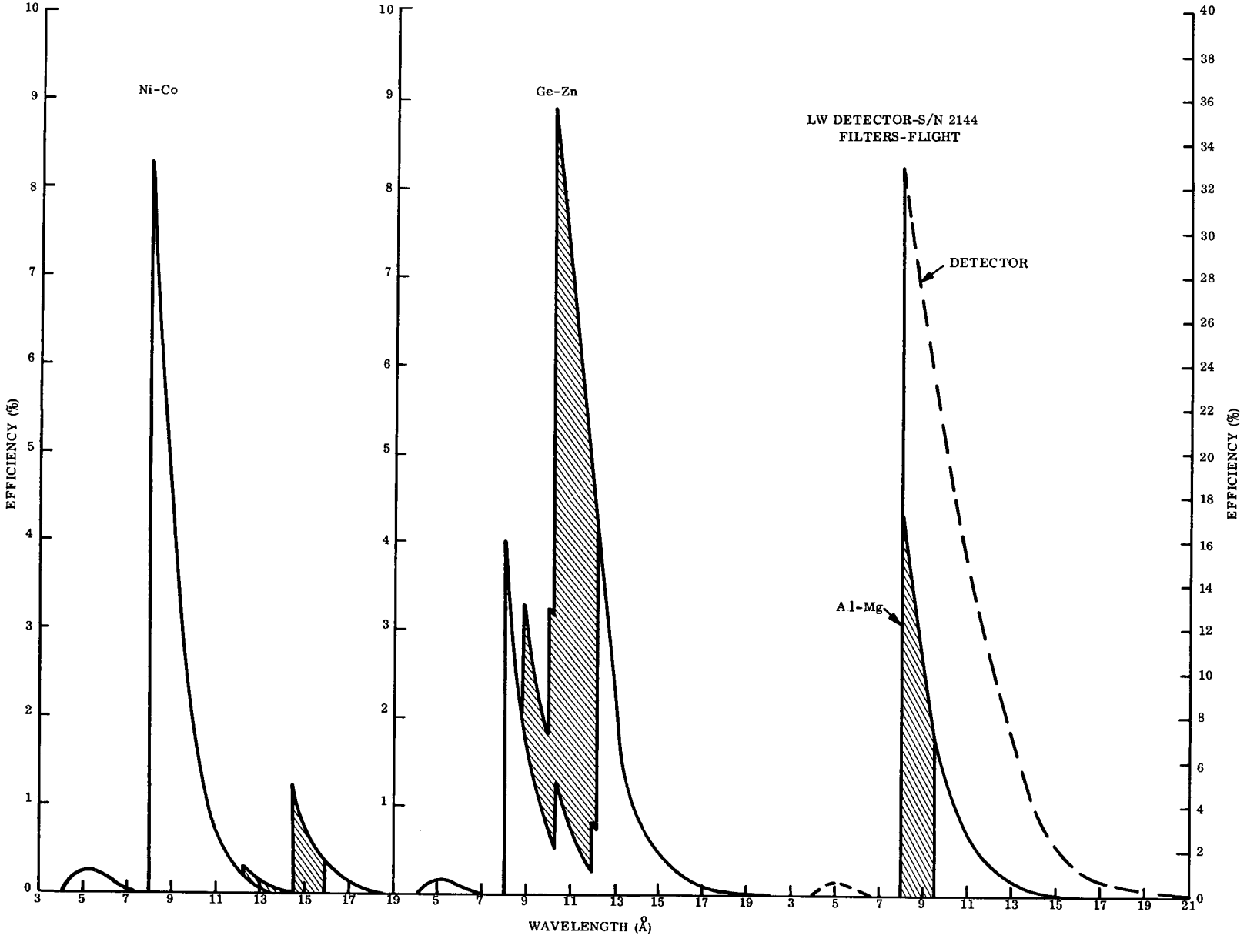

Figure 5-19. Efficiency versus Wavelength

efficiencies and wavelengths at which efficiency was measured. These values take the window support structure of the GFE long wavelength detector into account. Calculated detector efficiencies were also used.

Table 5-5. Listing of Efficiency Measurements (Flight Filter Pairs)

F/W Position	Serial No.	Type	λ_o Å	Sensitivity ($c\text{-}ph^{-1}\text{-}cm^2$)
1	5L	Ni-Co	14.6	3.5×10^{-3}
2	7L	Ge-Zn	10.45	2.6×10^{-2}
3	(no filters)			
4	8L	Ni-Co	14.6	3.75×10^{-3}
5	9L	Cu-Ni	13.36	8.1×10^{-3}
6	4L	Al-Mg	8.34	4.6×10^{-2}

If an efficiency (or sensitivity) at any other wavelength, within the band, is desired it can be obtained by referring to the curves in Figure 5-20 and applying the appropriate scale factor. It can also be calculated to an adequate accuracy with the relation

$$\frac{u}{\rho} = 1.11 \lambda^{2.77}$$

which gives the mass absorption coefficient for Al as a function of wavelength (in Å$_o$).

Filter pairs for the Short Wave (SW) system are tabulated below. (Flight Filter Pairs)

F/W Position	Serial No.	Type	Filter Pair Efficiency		Detector Efficiency	Sensitivity ($c\text{-}ph^{-1}\text{-}cm^2$)
			Low	High		
1	1S	Fe-Mn	0.60	0.64	0.95	0.23
2	2S	Mn-Cr	0.64	0.57	0.95	0.22
3	8S	S -Al	0.39 at 6.15	---	0.5	0.75
4	3S	Fe-Mn	0.64	0.62	0.95	0.23
5	5S	Fe-Cr	0.67	0.61	0.95	0.24
6	(no filters)					

Except for the S-Al pair, relative passbands are small. Because transmission is mainly governed by filters (and not the detector) efficiencies across the band are reasonably constant. Efficiency of the S-Al pair is plotted in Figure 5-20 and numerical values for any wavelength can be obtained from the Figure 5-20.

Figure 5-21 shows the measured plateau curves for Channels A and B of the LW detector. An operating voltage of 1125 V was selected. The Fe55 sources used in measuring these curves falls outside the nominal operating range and is situated somewhat outside the plateau. Because of a peculiarity in Channel A (double pulsing for large pulses) a change in gain of either A or B can easily be detected by observing increases or decreases in count rates with the instrument's built-in Fe55 source over a given period of time.

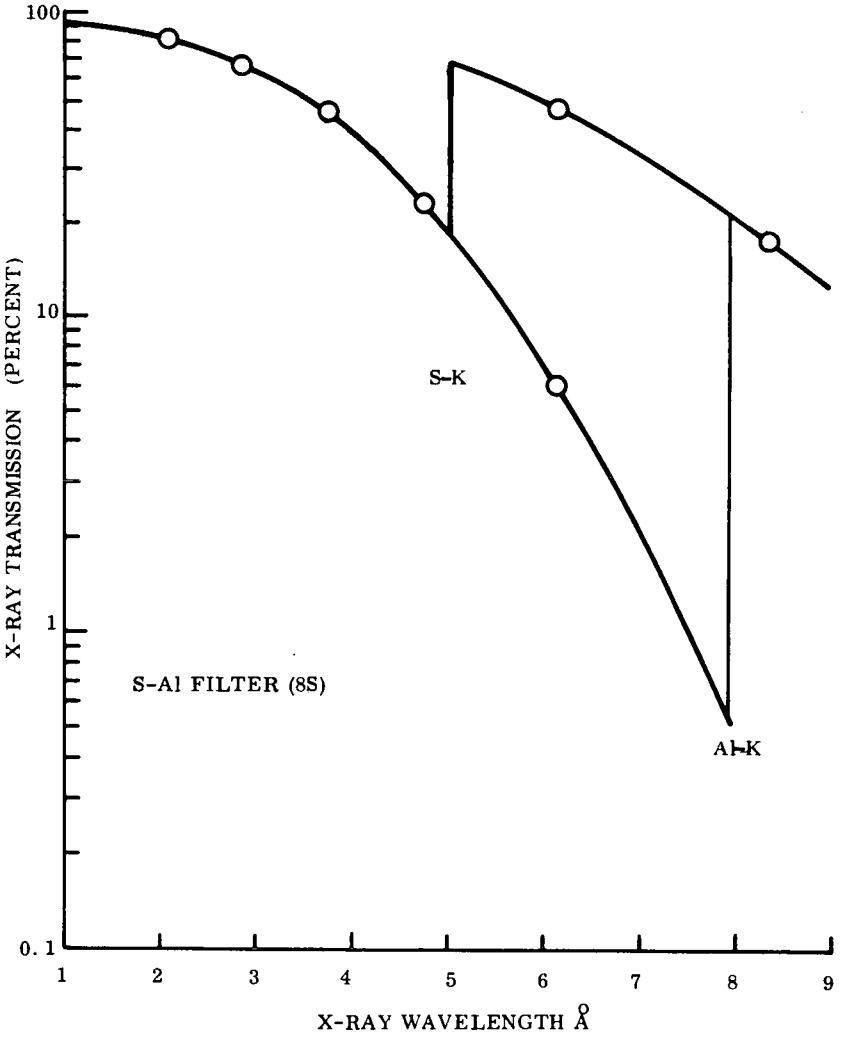

Figure 5-20. S-Al Passband Efficiency

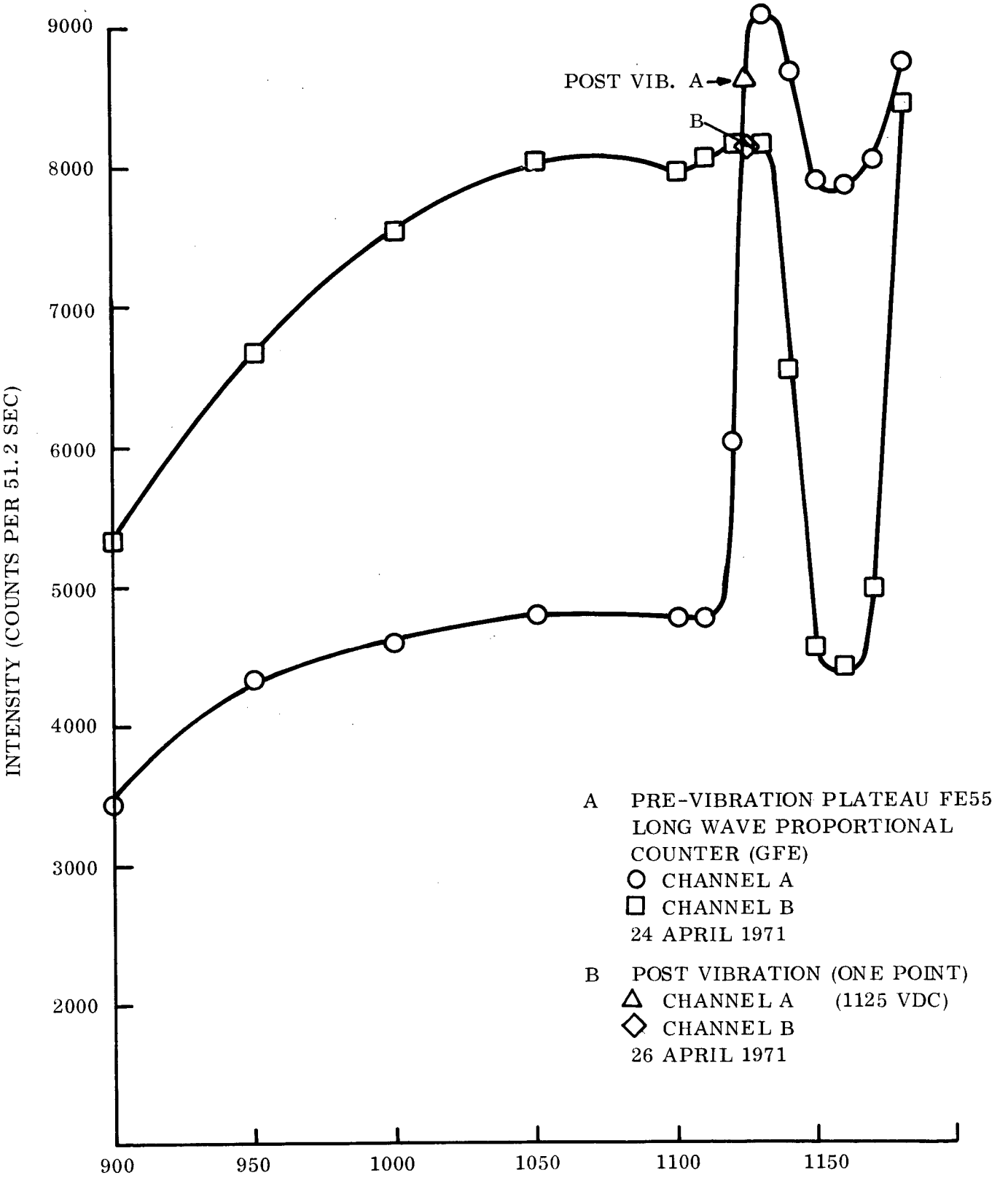

Figure 5-21. Long Wavelength X-ray Subsystem Test (Fe 55)

Both X-ray systems were subjected to a balance test, also called an X-ray end-to-end test. The purpose of this was to determine the degree of balance, and if necessary, to take corrective action.

The short wave subsystem was exposed to the continuum of a tungsten target X-ray tube operated at 15 kV and 40 ma. Balance was measured by scanning the collimator aperture with a pencil-shaped beam. Integration of the response over the whole surface gave an unbalance of 5 percent with B higher than A. A masking wire was added to the B reducing the effective area by 8 percent. Balance measurements on the long wavelength section were much more difficult. The final measurements were made at BBRC using a GFE generator. On the basis of these measurements a wire was added to section LWB masking 6 percent of its area.

In summary the LW & SW X-ray systems have adequate wavelength coverage in selected bands within the wavelength range between 1.76 and 15.9Å; a field of view which is less than 20 arc-seconds with adequate side lobe suppressions; co-alignment with the EUV system within 10 arc-sec; and filter balance that is better than 2 percent for substantially all the wavelengths.

The sensitivity of the SW X-ray system exceeds specification requirements. However, the sensitivity of the LW X-ray system is below the original expected level. This condition was due primarily, to window losses in the proportional counter.

5.4 OPERATION

5.4.1 OPERATIONAL MODES

The operational modes which can be selected can be placed into two independent catagories: channel selection and filter wheel operational modes. It is possible to read out data from Channel A only, Channel B only, or the difference between Channel A and Channel B (A-B). Simultaneously, it is possible to operate the filter wheel in any one of three basic modes. The wheel can be single-stepped to any one of six positions in order to place the desired filter pair in front of the proportional counter. This mode is a static mode in that the wheel remains in the selected position unless commanded to change positions. In addition, there are two dynamic modes for the filter wheel which can be selected. Both are continuously rotating modes. In one case, the wheel rotates 60 degrees (one position) at the end of each raster and in the other case the wheel rotates 60 degrees every 5.12 seconds. Note that in either mode of operation it takes the wheel about one (1) second to rotate 60 degrees.

5.4.2 COMMAND DEFINITION AND RESPONSE

The following commands control the operation of the long X-ray subsystem:

1. Data Channel Selection Commands

   a. XN-19 (GSFC LXR A Only) - Enables the readout of the long X-ray Channel A only.

   b. XN-52 (GSFC LXR B Only) - Enables the readout of the long X-ray Channel B only.

   c. XN-21 (GSFC LXR A-B) - Enables the readout of the difference between the long X-ray Channel A and Channel B (A-B).

2. Long X-Ray Filter Wheel Operation Commands

   a. XN-58 (GSFC Step LXR FW) - Advances the long X-ray filter wheel one step (60^{o}). It also disables both Command XN-03 and Command XP-69.

b. XN-03 (GSFC Step LXR/SXR FW's Auto) - Enables the automatic advancing mode for both the long and short X-ray filter wheels. In this mode both of the wheels advance one position (60^{o}) every 5.12 seconds. The start of the advance of the long X-ray filter wheel is syncronized to word gate 4 in DMF's 4, 20 and 36 and the start of the advance of the short X-ray filter wheel is syncronized to word gate 2 in DMF's 4, 20 and 36.

Note: XN-58 or XN-08 will disable this mode of operation. However, if XN-58 is sent to disable this mode, then the long X-ray filter wheel may advance either 1 or 2 steps before stopping and the short X-ray filter wheel may advance either 0 or 1 steps before stopping; and if XN-08 is send to disable this mode, then the short X-ray filter wheel may advance either 1 or 2 steps before stopping and the long X-ray filter wheel may advance either 0 or 1 step before stopping. The uncertainty in the number of stops results from the uncertainty in the timing between the automatic advance and the issuance of the disabling command. If it is desired to keep the wheels in the same relative location to each other, then both XN-58 and XN-08 should be sent.

Furthermore, if either wheel takes two steps before stopping, it may appear that the wheel skipped a position since the housekeeping is read out only once every 3.84 seconds and the wheel will have taken two steps within that time period.

c. XP-69 (GSFC LXR FW Auto) - Enables the long X-ray filter wheel automatic advancing mode. In this mode the long X-ray filter wheel advances one position (60^{o}) upon the receipt of an end of raster (EOR) pulse from the spacecraft.

Note: XN-58 disables this mode and in the process advances the long X-ray filter wheel one step (60^{o}).

Also if the filter wheel is in this mode at the night-to-day transition, the long X-ray filter wheel will advance one step at the transition whether or not the spacecraft is in the raster mode.

3. High Voltage Commands

a. XN-18 (GSFC LXR HV ON) - Turns on the high voltage power supply which powers the long X-ray proportional counter.

b. XN-05 (GSFC Polar and XR HV OFF) - Turns off both long and short X-ray high voltage power supplies and the polarimeter high voltage power supply simultaneously.

5.4.3 EFFECTS OF LOSS OF POWER

Power to the experiment can be interrupted in any one of these ways:

1. Only day power interrupted
2. Only orbit power interrupted
3. All power interrupted.

The loss of day power only has no effect on the state of the instrument except that the data is lost during the interrupt. The effect will be the same as the normal day-night-day transition.

If only the orbit power is interrupted the following effects will be noticed when the power is restored. All other states will remain the same assuming that no commands have been sent in the interim.

1. X-Ray Filter Wheel Position - Either or both filter wheels may advance one position when power is restored.
2. X-Ray Filter Wheel Housekeeping - The filter wheel position housekeeping will no longer be in sync with the actual position of the wheels and it will remain out of sync until the wheel has passed by the reference microswitch.
3. High Voltage - Will remain on during orbit power interrupt. However, all data will be lost.

   If all power to the experiment is interrupted the effect will be the same as if only the orbit power is interrupted with the exception that the high voltage power supplies will also turn off during the interrupt, but they will come back on when power is restored.

   Note: In any case all data will be lost during the interrupt.

5.4.4 TELEMETRY

5.4.4.1 Scientific Data

In summary, the long X-ray data is readout during main frame word gates 4 and 20. Data can be readout from Channel A only, from channel B only, or the difference between channel A and channel B (A-B). The sample time is 146.25 ms and the sample frequency is 160 ms.

5.4.4.2 Housekeeping Data

Telemetry Bits 5, 6, 7 and 8 in DSF Words 4, 16 and 28 are used to indicate the data channels selected on both long and short X-ray. This data is therefore readout three times in each main frame.

DSF Words 8, 20, 32 and 44 are used to relay the position of both of the filter wheel positions. Thus, the filter wheel positions are readout only once every 3.84 seconds and are, therefore, as much as 3.84 seconds out of sync with the actual state of the instrument.

The end of line (EOL) and the end of raster (EOR) housekeeping data are readout during DMF word gates 3, 4, 7 and 8. The end of spectral scan (EOSS) housekeeping data is also readout in the X-ray data channels although it is not pertinent to the X-ray subsystem. The EOSS code is readout during DMF Words 19, 20, 23 and 24. The DMF housekeeping is less than 160 ms out of sync with the actual state of the instrument.

C-3

SECTION 6

SHORT WAVELENGTH X-RAY EXPERIMENT

6.1 REQUIREMENTS

The requirements for the short wavelength (SW) X-ray experiment are the same as defined for the LW X-ray experiment (see paragraph 5.1), except for the spectral bands. The spectral bands of interest for the SW X-ray experiment are as follows:

1. 1.74 - 1.90 Å
2. 1.90 - 2.07 Å
3. 5.02 - 7.95 Å
4. 1.74 - 2.07 Å
5. 1.70 - 8.00 Å

6.2 DESIGN SOLUTION

6.2.1 SHORT WAVELENGTH X-RAY EXPERIMENT DESCRIPTION

The SW X-ray experiment is basically the same as the LW X-ray experiment, except for the selection of the spectral bands of interest and the construction of the sensor (refer to Paragraph 5.2.1).

A block diagram showing the sensor and electronics is shown in Figure 6-1. The schematic of the experiment is the same as shown in Figure 5-1 for the LW X-ray experiment.

6.2.2.1 Collimator

The collimator for the short and long wavelength X-ray experiments are almost identical. Refer to paragraph 5.2.2.1 for a detailed description.

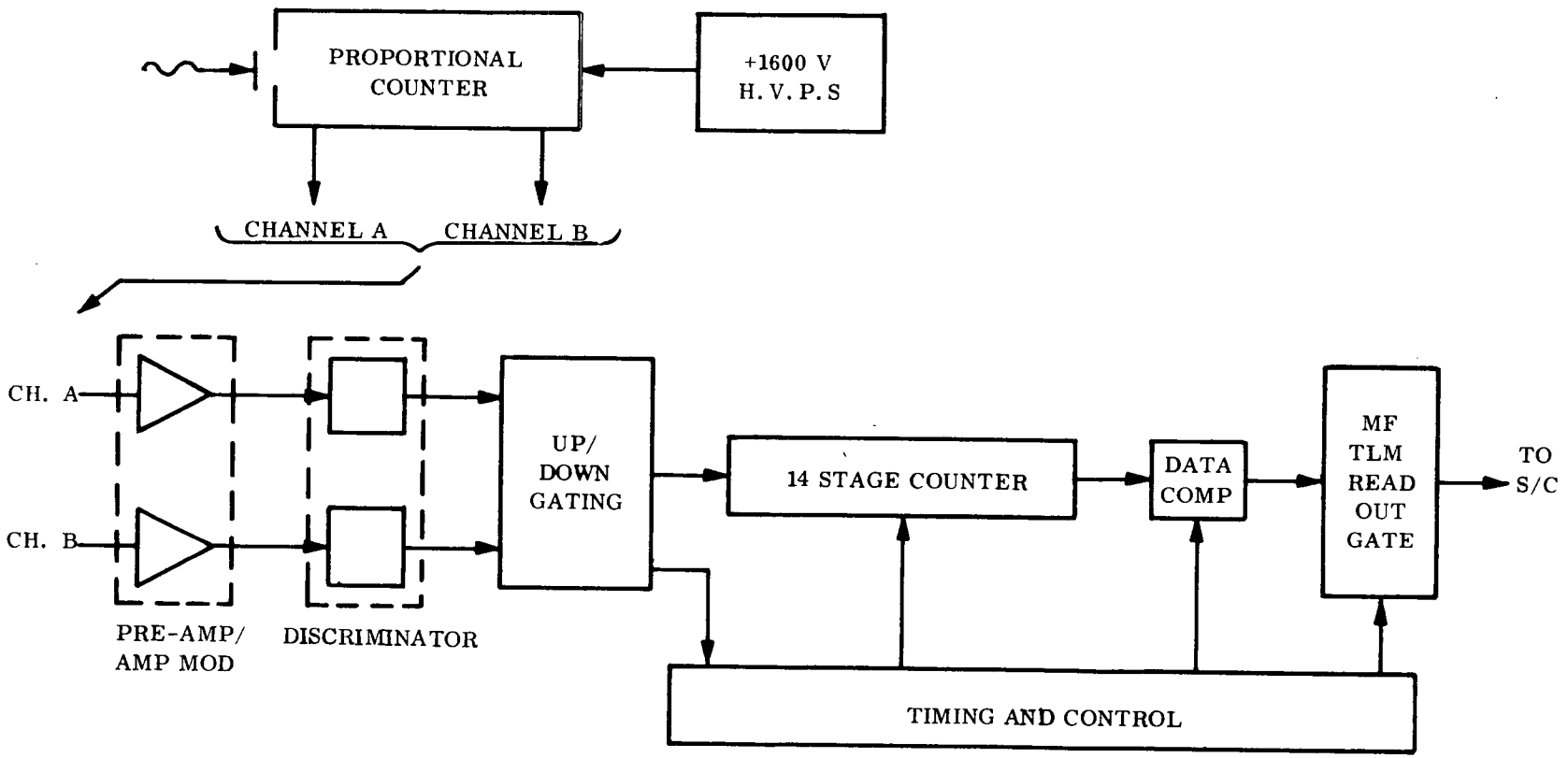

Figure 6-1. Short Wave X-ray Experiment Flow Diagram

6.2.2.2 Short Wavelength X-ray Sensor

The description of the short wavelength X-ray sensor is included in the description of the long wavelength X-ray sensor. Refer to paragraph 5.2.2.2.

6.2.2.3 Short Wavelength Balanced Filters

The description of the short wavelength balanced filters are included in the description of the long wavelength balanced filters. Refer to paragraph 5.2.2.3.

6.2.2.4 Sensor Electronics

The sensor electronics for the short X-ray subsystem are identical to those in the long X-ray subsystem, reference paragraph 5.2.2.4 for a detailed description.

6.2.2.5 Data Processing Electronics

The data processing electronics for the short X-ray are identical to those in the long X-ray subsystem, except that the short X-ray data is readout during DMF words 8 and 24. Reference paragraph 5.2.2.5 for a detailed description.

6.2.2.6 Housekeeping Electronics

Short and long X-ray housekeeping electronics are identical. Refer to paragraph 5.2.2.6 for a detailed description of the X-ray housekeeping electronics.

6.3 ALIGNMENT AND CALIBRATION

6.3.1 ALIGNMENT

Alignment of the LW and SW X-ray experiments is accomplished by aligning the collimator to the EUV telescope. Refer to paragraph 3.3.1 for alignment results.

6.3.2 CALIBRATION

Calibration of the SW X-ray experiment is discussed in paragraph 5.3.2.

6.4 OPERATION

6.4.1 OPERATIONAL MODES

The operational modes for the short X-ray are identical to those of the long X-ray. Paragraph 5.4.1 discusses these modes in detail.

6.4.2 COMMAND DEFINITION AND RESPONSE

The following commands control the operation of the short X-ray subsystem.

1. Data Channel Selection Commands

   a. XN-64 (GSFC SXR A Only) - Enables the readout of the short X-ray Channel A only

   b. XN-35 (GSFC SXR B Only) - Enables the readout of the short X-ray Channel B only

   c. XN-36 (GSFC SXR A-B) - Enables the readout of the difference between the short X-ray Channel A and Channel B (A-B).

2. Short X-ray Filter Wheel Operation Commands

   a. XN-08 (GSFC Step SXR FW) - Advances the short X-ray filter wheel one step (60^{o}). It also disables both Command XN-03 and Command XP-68

   b. XN-03 (GSFC Step LXR/SXR FW's Auto) - Reference paragraph 5.4.2 for a detailed description of the definition and response to this command.

   c. XP-68 (GSFC SXR FW Auto) - Enables the short X-ray filter wheel automatic advancing mode. In this mode the short X-ray filter wheel advances one position (60^{o}) upon the receipt of an end of raster (EOR) pulse from the spacecraft.

      Note: XN-08 disables this mode and in the process advances the short X-ray filter wheel one step (60^{o})

      Also if the filter wheel is in this mode at the night-to-day transition, the short X-ray filter wheel will advance one step at the transition whether or not the spacecraft is in the raster mode.

3. High Voltage Commands

a. XN-32 (GSFC SXR HV On) - Turns on the high voltage power supply which powers the short X-ray proportional counter.

b. XN-05 (GSFC Polar and XR HV Off) - Turns off both X-ray high voltage power supplies and the polarimeter high voltage power supply simultaneously.

6.4.3 EFFECT OF LOSS OF POWER

Reference paragrph 5.4.3 for a discussion of the effects of loss of power on the X-ray subsystem.

6.4.4 TELEMETRY

6.4.4.1 Scientific Data

The short X-ray data is readout during main frame words 8 and 24. Data can be readout from Channel A only, from Channel B only, or the difference between Channel A and Channel B (A-B). The sample time is 146.25 ms and the sample frequency is 160 ms.

6.4.4.2 Housekeeping Data

Reference paragraph 5.4.4.2 for a description of the X-ray housekeeping data.

SECTION 7

POLARIMETER

7.1 REQUIREMENTS

The purpose of this experiment is to measure linear polarization at predetermined wavelength bands. From the original specified options of 0.5 ± 0.2 Å, 1.39 ± 0.02 Å, or $1.67 + 0.02 - 0.000$Å; the 0.5 ± 2 region was selected. From the originally suggested approaches, the scattering method was selected. It was felt that the originally specified area of 10-25 mm^2 was too small. The area of the polarimeter was increased to 4 cm^2. The cosmic-ray background response was held to < 150 cpm per channel and, assuming a minimum usable signal of 500 cpm per channel, the minimum required input flux can be calculated. With a measured sensitivity of 0.466 c-cm^{-2} -ph^{-1} per channel, which is a good average value for the passband, a solar flux 18 ph-cm^{-2} -sec^{-1} is required. Additional requirements were: linearity with a range from 0 to 275 cps, which is the telemetry saturation value; balance between the three channels within 5 percent; and long-term stability corresponding to a maximum allowable change in counting rate of $\pm$ 3.5 percent for 60 minutes.

Requirements for the detector were established as: (1) plateau range of 300 ± 100 V (2) plateau slope of 3%/100 V and (3) energy resolution of 30 percent FWHM with a Cd^{109} source.

7.2 DESIGN SOLUTION

The measurement of all properties of X-ray quanta requires that they interact with a substance. For the keV X-ray energy range, several interaction processes can occur. However, only scattering will be considered here since this is the process that will be used to detect polarization. If a beam of X-rays polarized such that all quanta electric vectors oscillate in the same direction is allowed to impinge on a scattering medium, then the X-ray quanta will be preferentially scattered in a plane perpendicular to the incident beam and normal to the electric vector. Therefore, if two detectors were placed orthogonally around the scatterer, one detector will always read a high count rate while the other reads low.

Let us now consider those requirements that an efficient scatterer must necessarily fulfill. As is known, the mass attenuation coefficient is composed of the sum of the coefficients for scattering (σ_s) and photoelectric absorption (σ_a), for the keV X-ray energy range. In order that an instrument based on scattering be highly efficient requires that (σ_s) be as large as possible compared to (σ_a). Since (σ_s) increases only slightly with atomic number, while (σ_a) increases rapidly, the use of light elements as scatterers is indicated. Ease with which a particular substance can be handled and manufactured must also be considered. A list of important parameters for the selection of a scatterer are given in Table 7-1.

Table 7-1. Scattering Material Parameters

Substance	Density	$\sigma_s / \sigma_s + \sigma_a$						$x_{90\%}$*	$x_{67\%}$**
	gm/cm^3	Wavelength A^o						cm	cm
		0.2	0.4	0.5	0.6	0.8	1.0		
Lithium	0.534	1.00	0.97	0.92	0.87	0.69	0.52	24.0	4.20
Beryllium	1.850	1.00	0.95	0.81	0.71	0.47	0.32	55.9	1.06
Boron	2.340	0.97	0.90	0.76	0.63	0.39	0.24	3.4	0.67
Carbon (Graphite)	2.250	0.94	0.73	0.56	0.42	0.24	0.14	3.0	0.51
Polyethylene	0.950	0.99	0.77	0.59	0.44	0.25	0.15	7.7	1.40
Magnesium	1.740	0.60	0.25	0.12	0.07	0.04	0.02	0.8	0.15

*Thickness for 90 percent absorption at 0.5A^o (determines the material length).
**Thickness for 67 percent transmission at 0.5A^o (determines the material radius).

A comparison of scatterers can be made by plotting the ratio of the photon scattering to attenuation coefficients multiplied by the ratio of the thickness for 67 percent transmission ($x_{67\%}$) to the square root of the 90 percent absorption thickness $(x_{90\%})^{1/2}$, as a function of atomic number. Figure 7-1 shows this plot for various X-ray wavelengths.

A measure of effective sensor sensitivity can be obtained by establishing the ratio of the sensors net signal response to the magnitude of the statistical fluctuations of the background. The signal response is proportional to the sensor area while the background response is

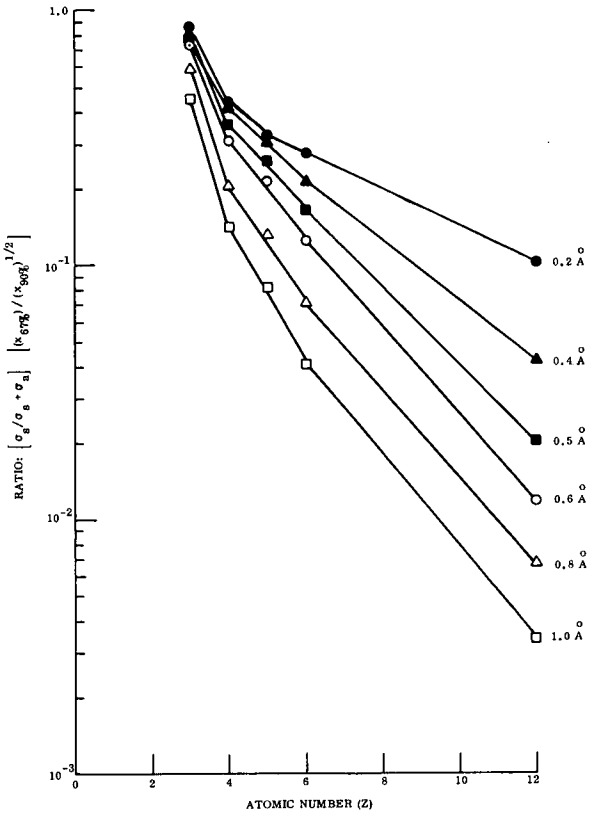

Figure 7-1. Material Scattering Parameter as a Function of Atomic Number for Various X-ray Wavelength

proportional to the sensor volume. Substituting these quantities into the above ratio and simplifing yields the quantity $[(x67\%)/(x90\%)^{1/2}]$.

Beryllium was chosen as the scattering media for this polarimeter. The choice was made based on the information contained in Figure 7-1, coupled with the relatively large size and weight of the instrumentation required for a lithium scatterer and its handling difficulties.

7.2.1 POLARIMETER

The polarimeter is composed of a scattering block surrounded by six proportional counters as shown in the diagram of Figure 7-2. Each of the six proportional counters is separated electrically from every other counter by ground planes. Constructional details of the unit are listed in Table 7-2. The polarimeter is so constructed such that if a beam of X-ray quanta, a fraction of which is polarized, is incident on the scatterer parallel to the pointing axis, the resulting scattered polarized quanta will be emitted preferentially in a plane per-

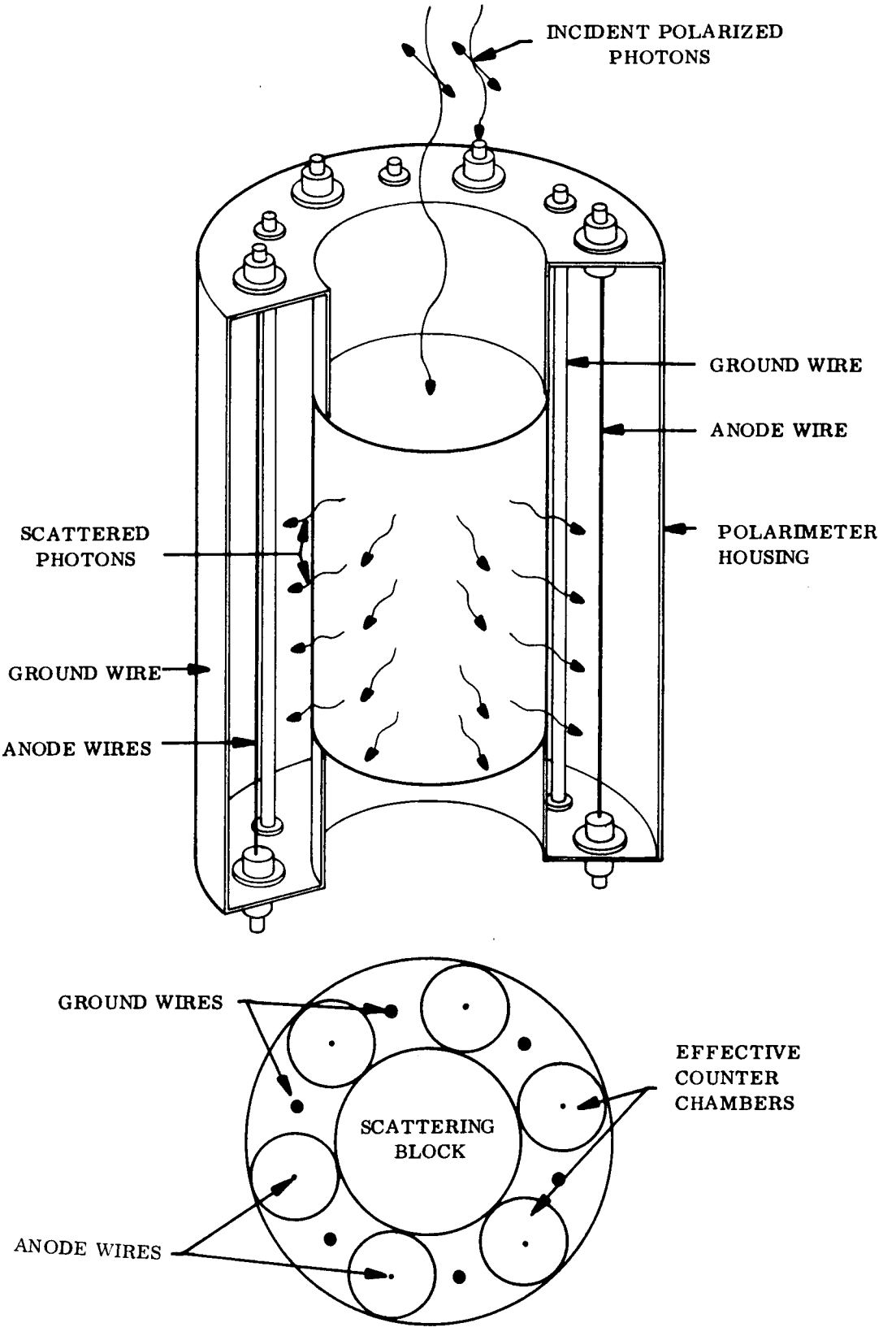

Figure 7-2. Diagram of Polarimeter

pendicular to the pointing axis and normal to the electric vector. Using six independent counters operated in adjacent pairs, there will always be counter combinations with maximum and minimum count rates regardless of the relative plane polarization. As an example, referring to Figure 7-2, Anodes 1 and 4 will have a maximum count rate while Anodes 2 and 5, and 3 and 6 will have minimum rates. Therefore, the differential magnitude of the quanta detected by each anode pair will give a quantative measure of the fractional polarization of the incident X-ray beam. In addition, the direction of the plane of polarization can also be ascertained.

Table 7-2. Constructional Parameters

Wavelength Range:	0.15- 0.85Å
Shape:	Cylindrical
Diameter:	3.0 inches (7.62 cm)
Length:	5.0 inches (12.7 cm)
Gas filling:	90% Xenon, 9% CO_2, 1% Helium
Gas Pressure:	3 atmospheres
Scatterer Material:	Beryllium
Scatterer Shape:	Cylindrical
Diameter:	0.875 inch (2.22 cm)
Length:	3.0 inches (7.62 cm)

7.3 CALIBRATION

X-ray bremsstrahlung from an X-ray tube with a beam divergence of 3 degrees was scattered from a thin graphite scatterer placed at an angle of 45 degrees to the beam. The resultant scattered quanta collimated to 0.5 degree impinged on the polarimeter which was axially mounted on a rotating table. The scattering angle was maintained at 90 $\pm$ 2 degrees to the beam from the X-ray tube to ensure nearly a 100 percent polarized beam. The counting rate from each polarimeter channel was then recorded as a function of rotation angle. The results are shown in Figure 7-3.

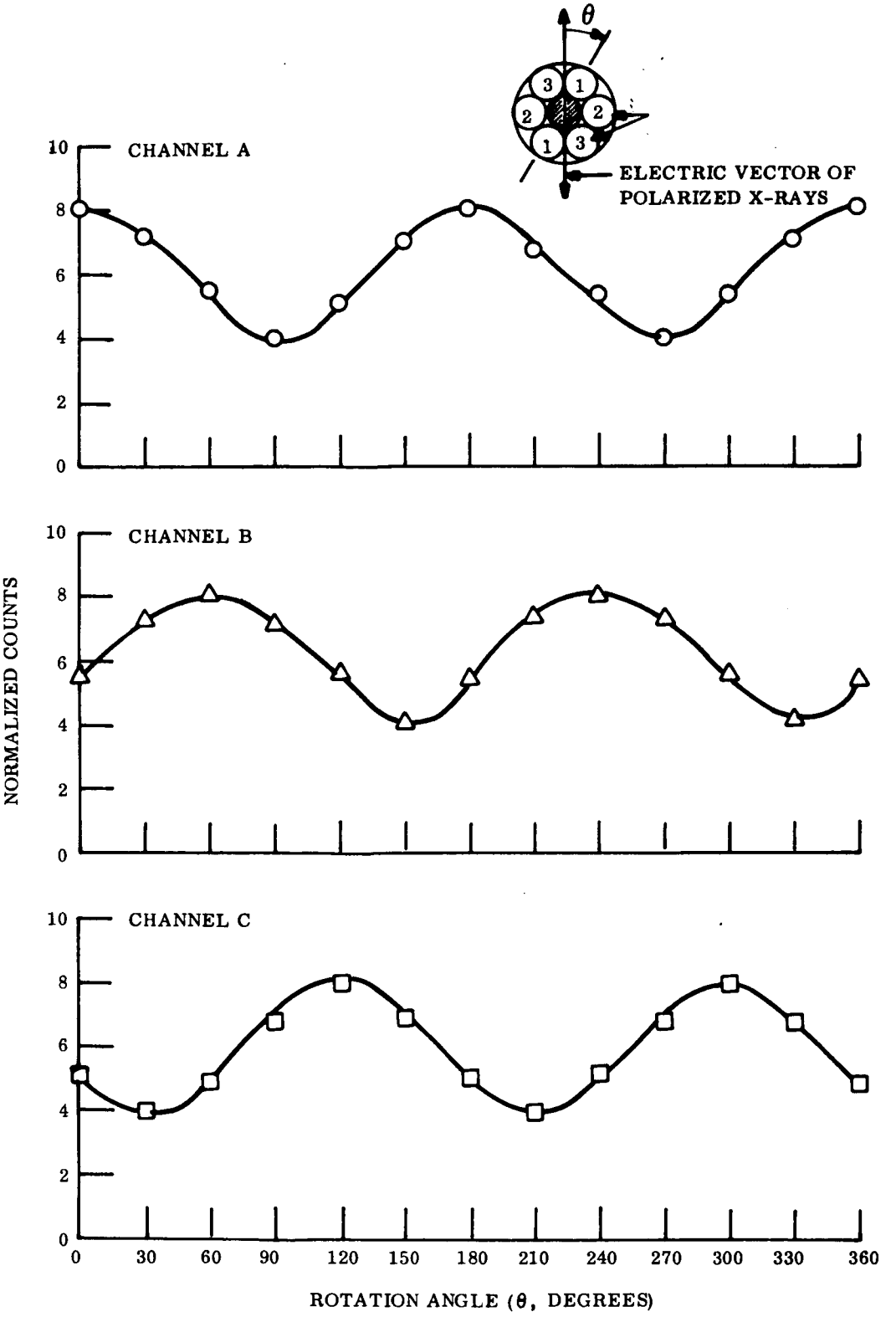

Figure 7-3. Counting Rate Variations for Each Counter Channel of the Polarimeter as the Polarimeter is Rotated with Respect to a Beam of 100 Percent Polarized X-rays

Figure 7-4, shows a graph of the counting efficiency of the apparatus as a function of wavelength of the incident photons for each polarimeter channel. Efficiency is defined as the ratio of recorded counts to the number of incident monochromatic photons. The remainder of the polarimeter test and calibration data are given in Table 7-3.

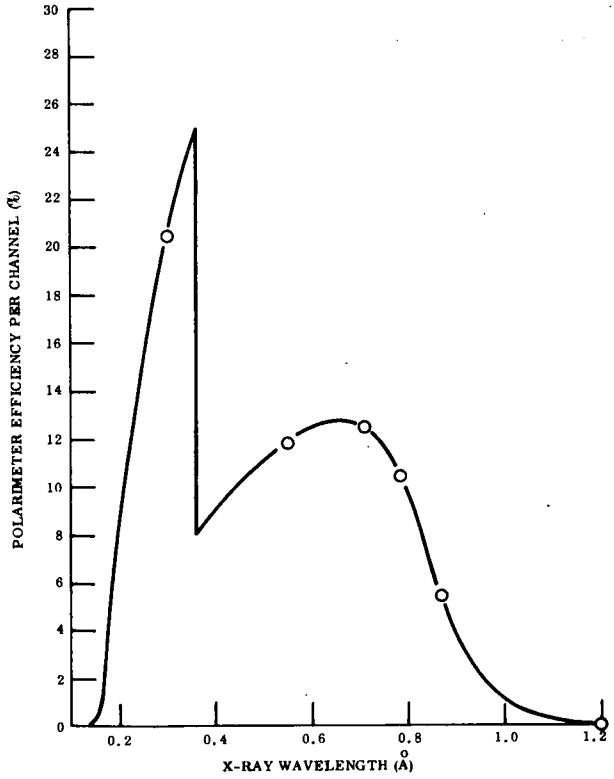

Figure 7-4. Polarimeter Detection Efficiency (Measured and Calculated) as a Function of X-ray Wavelength for Each Channel

7.3.1 DATA REDUCTION

A beam of partially polarized X-rays incident on the polarimeter can be regarded as two completely polarized beams whose planes of polarization are orthogonal. Then by definition polarization is:

$$P = (N_a - N_b) / (N_a + N_b) \quad (1)$$

where N_a and N_b are the X-ray fluxes whose electric vectors are aligned orthogonally.

The number of counts given by any one polarimeter detector in the plane of orientation corresponding to a maximum is given by:

$$C_1 = N_a k_1 + N_b k_2 \tag{2}$$

and that corresponding to a minimum is given by:

$$C_2 = N_a k_2 + N_b k_1 \tag{3}$$

Table 7-3. Polarimeter Operational Parameters

Wavelength Range	0.15-0.85A°
Sensitivity	as counts-cm^2/photon-channel
Polarization Sensitivity Modulation Ratio	2:1
Counting Plateau Range	300 ± 100 volts
Counting Plateau Slope	3%/100 volts
Energy Resolution	25% FWHM at Cd-109
Gain Stability	< 2% Drift/60 minutes
Channel Balance	< 5% Difference Maximum-to-Minimum
Count Rate Linearity	<2% change from true to 1 KHz rate
Background Count Rate	< 50/counts/minute-channel
Operating Temperature Range	+50°C to -20°C
Calibration	In-flight X-ray
Intensity Range	0-275 cps

where k_1 is the instrument efficiency for maximum sensitivity orientation and k_2 is the efficiency for minimum. Solving (2) and (3) for N_a and N_b and substituting into (1) yields:

$$P = (k_1 + k_2/k_1 - k_2)\ (C_1 - C_2/C_1 + C_2) \tag{4}$$

Polarization is then determined from the instrument constants and the detector maximum and minimum count rates. The instrument k-values can be established experimentally by measuring C_1 and C_2 for a 100 percent polarized X-ray beam. Based on the test results for this particular polarimeter then

$$(k_1 + k_2/k_1 - k_2) = 3 \tag{5}$$

The present polarimeter is not designed for rotation in the X-ray beam. As a result, true maximum and/or minimum count rates cannot be obtained. Therefore, polarization of the incident X-ray beam must be ascertained from the counting rates of all three channels. Table 7-4, shows the possible polarimeter reading combinations as a function of X-ray polarization angle, assuming a 15 degree maximum differential readibility. From Table 7-4, then, polarization measurements will be made based on the conditions listed in the table.
Conditions 1, 5, 9, and 13:

$$P = 3\ (C_A - C_L)/C_A \tag{6}$$

Conditions 3, 7, and 11:

$$P = 3\ (C_H - C_A)/C_A \tag{7}$$

Conditions 2, 4, 6, 8, 10, and 12:

$$P = 1.73\ (C_H - C_L)\ C_A \tag{8}$$

Where C_H is the high count rate, C_L is low rate and C_A is the average rate.

The principal limitations of accurately measuring X-ray polarizations with this polarimeter will be dependent on the minimum count rate above background and the instrument counting statistics.

Table 7-4. Polarimeter Reading Combinations

Condition No.	Polarization Angle	Channel No.		Channel No.		Channel No.
1	0^{o}	1	=	2	>	3
2	15^{o}	2	>	1	>	3
3	30^{o}	1	=	3	<	2
4	45^{o}	2	>	3	>	1
5	60^{o}	2	=	3	>	1
6	75^{o}	3	>	2	>	1
7	90^{o}	1	=	2	<	3
8	105^{o}	3	>	1	>	2
9	120^{o}	1	=	3	>	2
10	135^{o}	1	>	3	>	2
11	150^{o}	2	=	3	<	1
12	165^{o}	1	>	2	>	3
13	180^{o}	Same as 0^{o}				

7.4 OPERATION

7.4.1 OPERATION MODES

The polarimeter has only two operational modes (on or off) and there is no housekeeping that is relevant to the operation of the polarimeter.

7.4.2 COMMAND DEFINITION AND RESPONSE

These are as follows:

1. XN-22 (GSFC Polar HV On) - Turns on the high voltage power supply that powers all six of the proportional counters in the polarimeter.

2. XN-05 (GSFC Polar and XR HV Off) - Turns off both X-ray high voltage power supplies and the polarimeter high voltage power supply simultaneously.

7.4.3 TELEMETRY

7.4.3.1 Scientific Data

The polarimeter data is readout only once every main frame during the DSF words in paragraph 7.2.2.3. The sample time is 15.048 seconds and the sample frequency is 15.36 seconds.

SECTION 8

POWER SUBSYSTEM

8.1 LOW VOLTAGE POWER SUPPLY

The function of the low voltage power supply is to condition the spacecraft raw bus and provide the three discrete low voltages required by the electronics. It is required to operate within specification over a temperature range of $-20^{o}C$ to $+50^{o}C$ and input voltage variations from 16 v to 22 v. The output design requirements were as shown Table 8-1.

Table 8-1. Output Design Requirements

Output Voltages		+10 V ± 0.5 V +5.4 V ± 0.3 V -3.0 V ± 0.5 V
*Maximum Output Noise	+10 V Line +5.4 V Line -3.0 V Line	500 mv P. T. P. 500 mv P. T. P. 500 mv P. T. P.
Load Requirements	+10 V Line +5.4 V Line -3.0 V Line	30 to 35 ma 300 to 500 ma None
In addition, the low voltage power supply is required to provide dc isolation between the spacecraft power ground and the instrument signal ground and provide short circuit protection on the -3.0 v line.		
*Note: Since there is additional filtering down stream of the L. V. P. S., the noise requirements at the power supply output were relaxed from the origional spec requirements which were 50 mv P. T. P.		

The basic conversion circuit is a free running Jensen oscillator. The dc input voltage is chopped into a square wave, transformed to the desired voltage level, rectified back to dc, and filtered to remove commutation noise. Transformer coupling provides dc isolation and allows the electronics signal ground to be isolated from the spacecraft power ground.

The spacecraft bus is preregulated to prevent raw bus variations from affecting the electronics. The raw bus is filtered to protect the electronics from raw bus noise and to

protect the raw bus from the commutation noise. Figure 8-1 is a block diagram of the low voltage power supply.

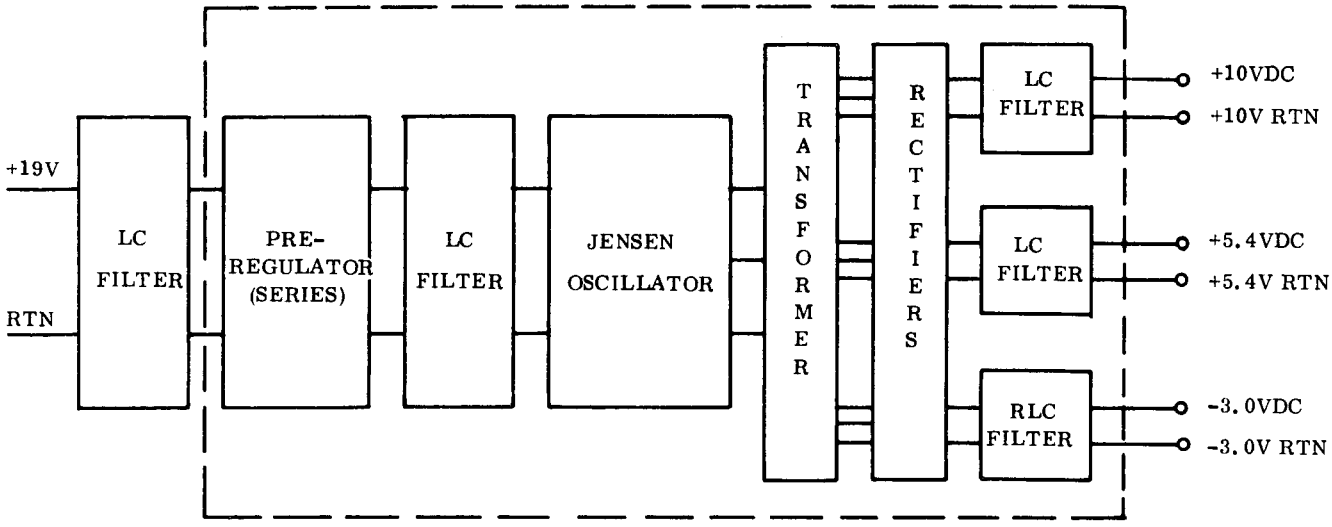

Figure 8-1. Low Voltage Power Supply Block Diagram

All of the circuitry (except the input filter) is packaged in a single chassis, and interfaces with the spacecraft bus and the instrument electronics by hard wiring to stand-off terminals on the chassis. The electronic components were packaged in cordwood modules in order to maintain the overall size of the supply at a minimum.

Four major considerations (size, weight, efficiency, reliability) were involved in the design of the low voltage power supply over and above the design requirements listed in Table 8-1. In order to develop an optimum design, tradeoffs were made between the above four considerations. The following selections were made:

1. A Jensen oscillator was selected rather than a Royer type oscillator. Although it is slightly more complex, the Jensen oscillator is inherently quieter and therefore requires less filtering.

2. Boost, buck and boost-buck type regulators were considered, but were discarded in favor of a series type regulator. Although the series regulator is less efficient, it is far less complex and therefore more reliable and smaller to package. Furthermore, since the magnitude of the power consumption is small, the series regulator is better in a weight verses efficiency tradeoff.

3. The cordwood module packaging design was selected rather than using printed circuits. While although printed circuits are easier to trouble-shoot, modify and repair, they require a larger overall volume, and space was at a premium in the original instrument specification.

4. Passive filters were selected rather than active filters because they are more efficient, less complex, and more reliable.

During the course of the program two significant problems arose. These were (1) excessive conducted noise and (2) unstable operation at orbit night loads. The noise problem was associated with the packaging of the power supply. The cordwood module packaging design greatly modified the circuit performance because of the addition of many extraneous parasitic parameters. The breadboard model of the supply was much quieter and slightly more efficient than the cordwood module version. As a result additional filtering was required to remove the additional noise.

During spacecraft testing, it was observed that the power supply was causing a low frequency oscillation (220 Hz) on the orbit bus during some of the orbit nights. This problem was caused by the addition of a requirement that certain logic circuits remain powered during orbit night (see paragraph 8.4). As a result, the power supply was required to operate at approximately 40 percent of its design load during this interval.

Detailed investigation of this condition on the flight spare unit indicated that when the load on the supply was reduced to a critical point the supply generated the observed oscillation. It was determined that there were no problems associated with this operating mode that would cause any malfunction of the experiment or any abnormal stress in any circuit. But because this condition coupled a large amount of noise back onto the spacecraft bus and because it was not determined how stable this condition was, it was decided to make a change to the power supply which eliminated this condition. A detailed description of the irregular operating condition and the design change can be found in PIR No. 1J86-0SO-869.

8.2 SURGE SUPPRESSORS

During prototype EMI testing it became apparent that an additional circuit was required to limit the inrush current when the instrument is turned on in order to meet the specified limit of one ampere maximum. Two GFE surge suppressors were supplied and one was inserted into the day bus power line and the other into the orbit bus power line.

The schematic is shown in Figure 8-2. This circuit limits the inrush current by inserting a relatively high impedance in series with the power line and then sequentially reducing the impedance to virtually zero. Initially, the current is limited by R1. A short time later determined by the time constant R1C1, Transistor Q1 turns on SCR 1 and thus reduces the line impedance to the parallel combination of R1 and R4. Similarly, at a time determined by R5C2 transistor Q2 and SCR 2 turn on; thus, the current to the instrument is now only limited by R7. Finally, at a time determined by R8C3 transistors Q3 and Q4 turn on at which time relay K1 switches and the series impedance is reduced to the impedance of L1 and the relay contacts.

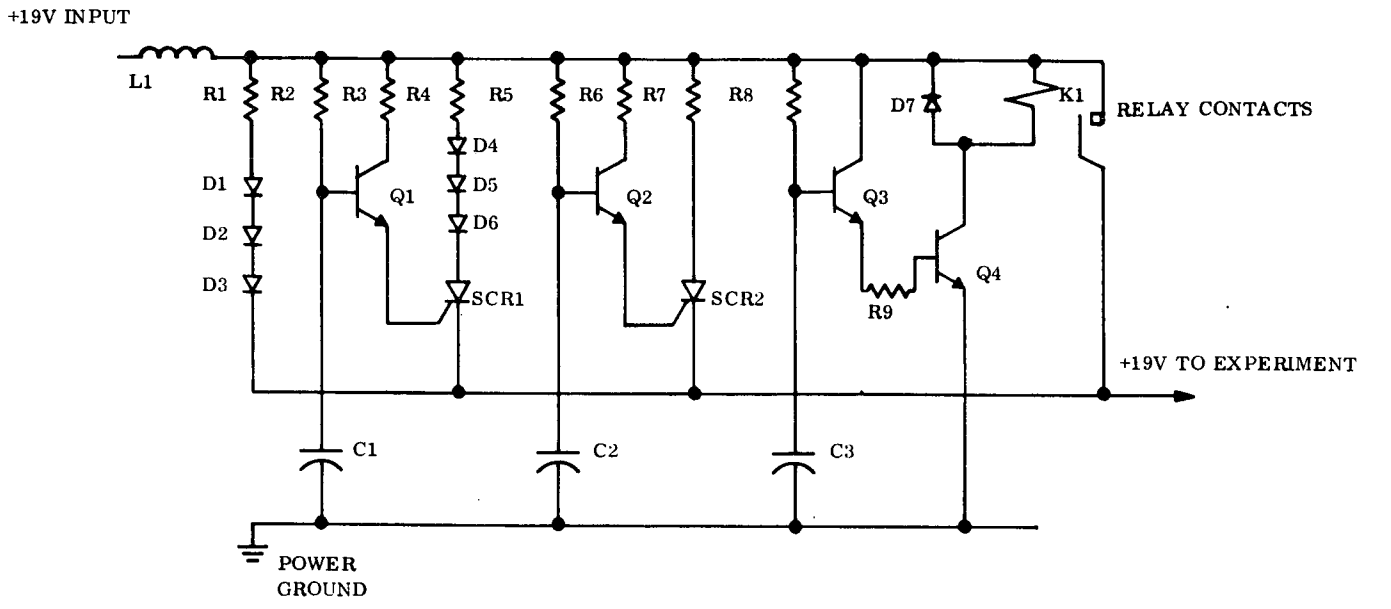

Figure 8-2. GFE Surge Suppressor

The surge suppressor is required since the input to the instrument is capacitive. The suppressor simply controls the charge rate of the capacitor.

8.3 EMI CONTROL

As mentioned in paragraph 8.1, the packaged version of the low voltage power supply exhibited considerably different noise characteristics from the breadboard version. It was decided that it would be easier and less expensive to design and build additional filtering for all of the power lines than it would be to repackage and/or redesign the L. V. P. S.

Additional filtering was added to the +10 v and +5.4 v lines in order to reduce the noise content within the instrument. Additional filtering was also added to the input power line and each of the ground lines at the interface in order to reduce the noise reflected back to the spacecraft. The additional filtering reduced the noise levels to a acceptable level.

Figure 8-3. shows the configuration of the added filtering.

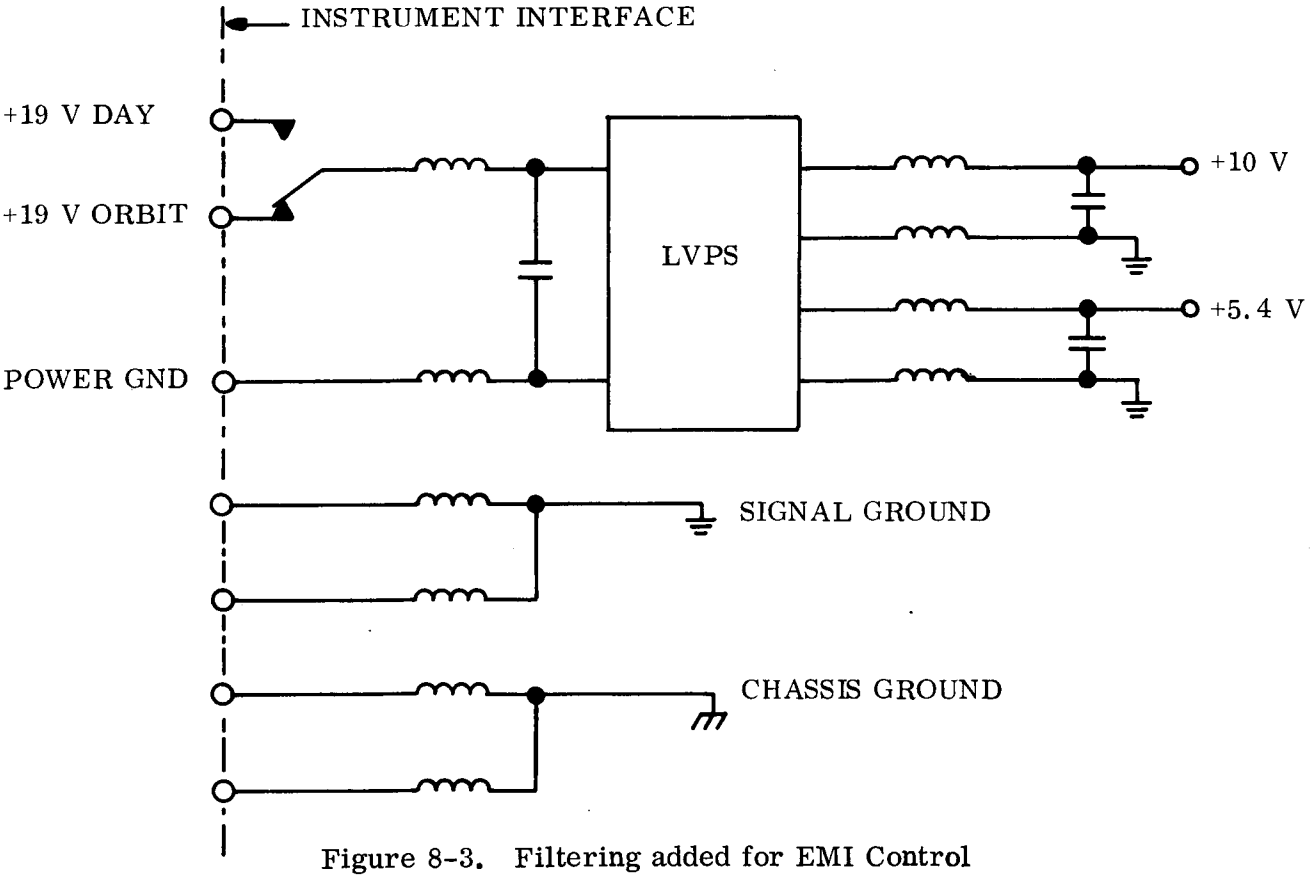

Figure 8-3. Filtering added for EMI Control

8.4 POWER SWITCHING

During the open-bench test it was determined that each time the instrument power was turned on several things happened in a random fashion. Depending on which state the logic assumed when it was initially powered, the mask may have changed states and the filter wheels may have advanced one step. In addition, the aperture wheel always returned to the reference and the filter wheel position housekeeping read a random position until the filter wheels advanced through the reference. This set of random states meant that in order to collect data in an orderly fashion, many commands would have to be sent to the instrument after each dawn. This was obviously an unacceptable condition.

To correct this operational problem, the circuitry was revised to provide continuous power to certain appropriate portions of the experiment logic. Three relays and an automatic relay driver were used to accomplish this task. The relay driver senses the voltage on the day power bus. When the bus is turned "on" (dawn), the automatic relay driver generates a pulse which latches the relays in the day mode, and when the day power bus is turned "off" (dusk) the automatic relay driver generates a pulse which latches the relays in the night mode. The relay configuration and a block diagram for the relay driver are shown in Figure 8-4. Note that each of the relays is a 2 PDT magnetic latch and that the contacts of the relays are protected against current surges by limiting resistors. At night the power to the sensor electronics and the power to most of the experiment logic is turned off. Only the logic required to maintain references and positions is powered at night via the +5.4 v continuous bus. This requires that the low voltage power supply remain on continuously, and that at night the load on the supply is greatly reduced. Since the power supply was not originally designed to operate at this low load condition, this caused an additional problem which is discussed in paragraph 8.1.

The schematic for the relay driver is shown on NASA Goddard drawing No. SK70-069. it was designed and built by Goddard and supplied as GFE.

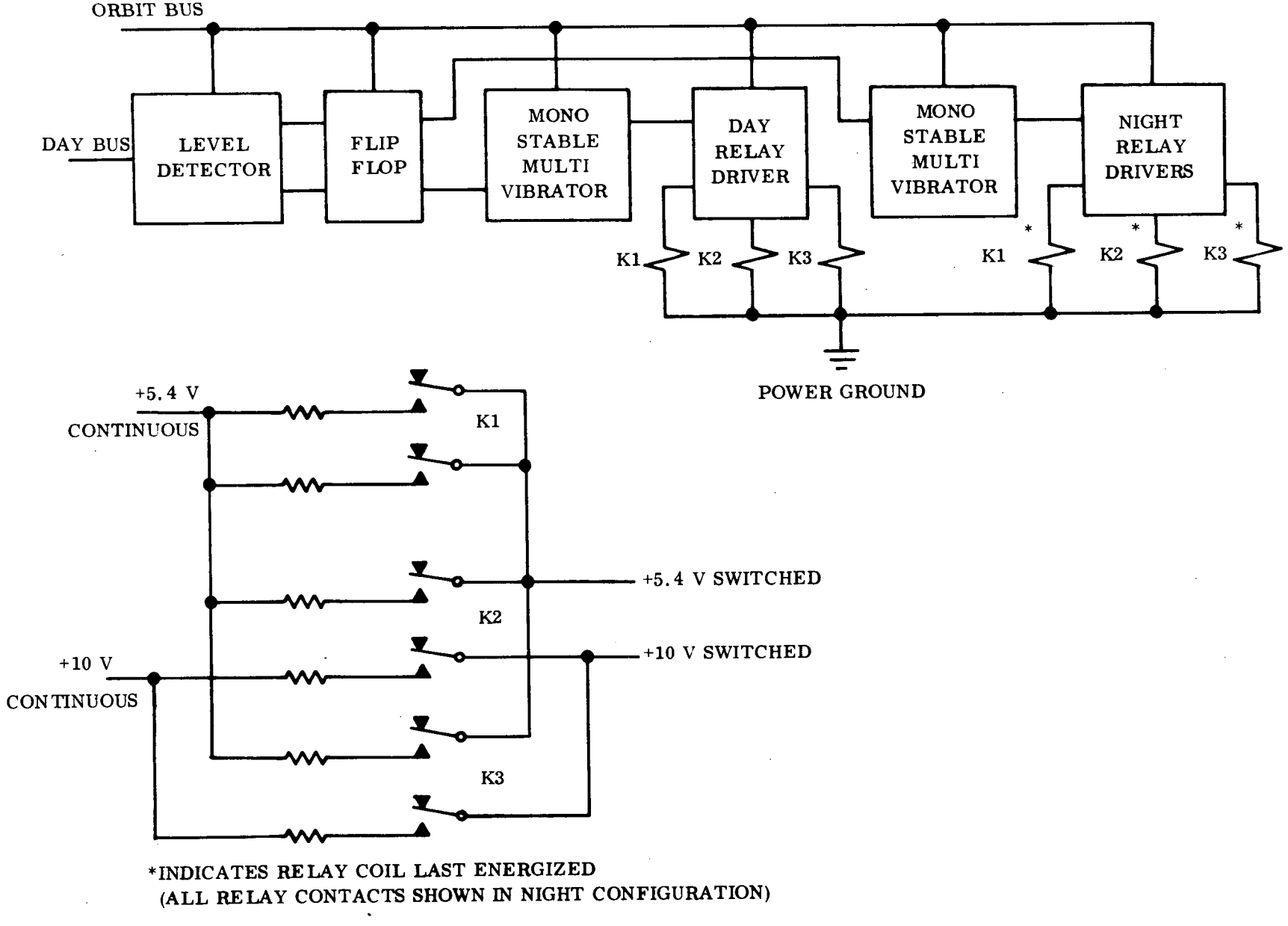

Figure 8-4. Relay Configuration and Relay Driver Block Diagram

The following commands effect the day-night operation of the experiment.

1. XN-70 (GSFC LV to LCH Pwr) - Enables the "normal" operating mode of the experiment. That is after XN-70 is sent the experiment will maintain continuous power on all of the logic circuits required to maintain the references and positions. It will also automatically switch to the night mode at dusk and the day mode at down.

2. XN-06 (GSFC LV to Day Pwr) - Enables the emergency mode of operation. In this mode all of the experiment power is turned off at night and the experiment must be commanded every orbit to regain reference positions and to reestablish the desired state of the instrument. This mode should only be used in the event that the automatic relay driver fails to either turn the power off at night or on at dawn.

   Note: That whenever XN-70 is sent the experiment will switch to the night mode (it will resume normal operation at the next dawn). Therefore, if all of the power to the experiment has been off it is necessary to send the Operational Mode Command (XN-70) before the power on command (SL-60) in order to turn the instrument on in the day mode.

8.5 MOTOR POWER CONDITIONING

Each of the five stepper motors has four windings and each winding has an impedance of 100 ohms. In order to step the motor 90 degrees, the appropriate winding must be powered by a minimum of 13 volts for about 15 ms. The fastest stepping rate employed in the instrument is 50 steps per second. In order to supply the required power to the motors and simultaneously to limit the amount of noise feedback onto the power bus a power conditioning/filtering circuit is required. Figure 8-5 shows the schematic for the motor power conditioning circuit (active filter).

In order to keep the power used by each of the motors at a minimum and thus prevent the motor from overheating, the +19 volt power bus is first regulated down to +14 volts by a series regulator. The output of the regulator is then filtered by a passive LC filter. The passive filter and regulator combination are designed such that under worst-case conditions, the motors will receive a minimum of 13 volts and the noise reflected back on the power bus will be within the specified limit. The operational concept is simply that the initial burst of energy required by the motor is supplied almost entirely by the passive filter.

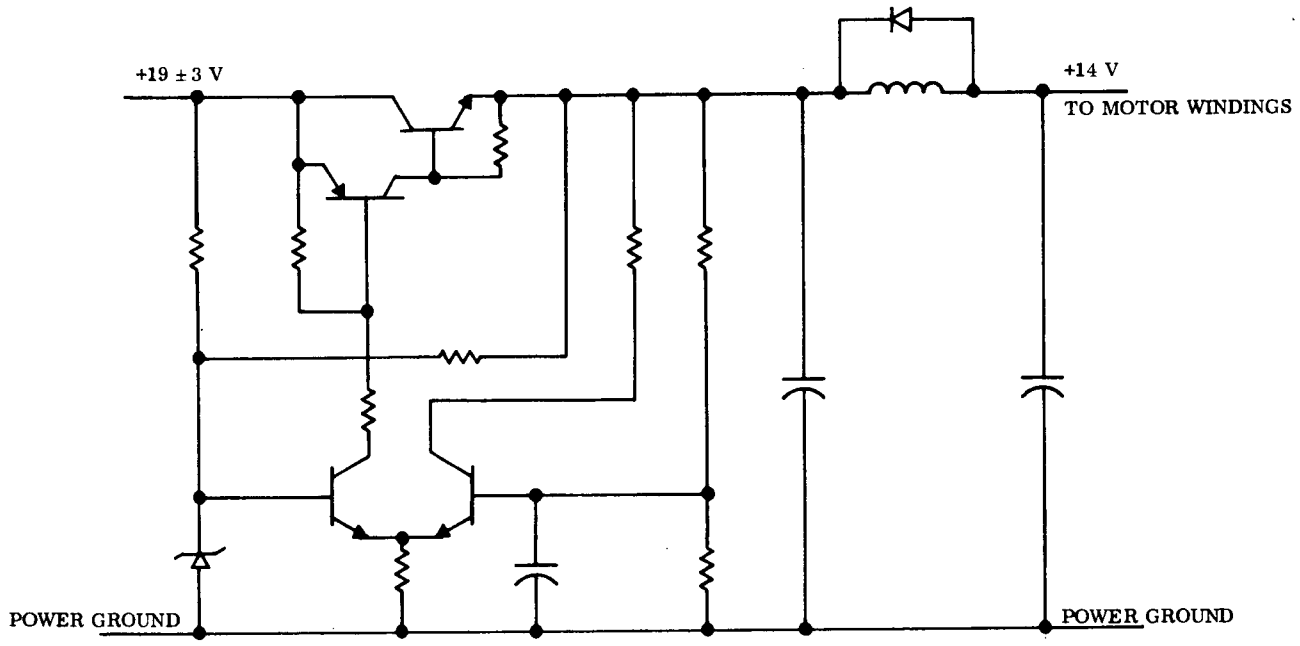

Figure 8-5. Motor Power Conditioning

The regulator turns on and off gradually to meet the load requirement and recharge the filter. In this manner the rate of change of the current demand on the power line is reduced to an acceptable level as determined by the "noise" requirements on the power line. Note that it is the rate of change in the current (di/dt) that produces the noise on the bus. This circuit controls the di/dt, thus controlling the amount of "noise" which is coupled back onto the power line while still meeting the large di/dt requirement of the motor.

8.6 HIGH VOLTAGE POWER SUPPLIES

The high voltage power supplies are employed by the instrument to provide the necessary high voltage potentials to the seven detectors. These supplies are broken down into five types (A, B, C, D and E). Each detector is powered by the type indicated as follows:

Detector	Type
Polarimeter	A
H-Alpha	B
Short X-ray	C
Long X-Ray	D
Long and Short EUV	E
Medium EUV	E

Note that the long and short EUV detectors share one type E supply.

All of the supplies were designed, built and tested by the Time Zero Corporation in accordance with GE Specification 7561.

Figure 8-6 shows the block diagram for the high voltage power supplies. The spacecraft raw bus is preregulated to approximately 14 volts in order to eliminate bus variations. The output of the preregulator is used to power an oscillator which provides the timing signal for the chopper driver. Power reaches the transformer through a buffer which is used to adjust the input voltage to the transformer. The chopper driver impresses a square wave voltage waveform on the primary of the transformer which transforms the primary voltage established by the buffer to the appropriate levels on the two dc isolated secondaries. One of the secondaries provides a feedback signal to the reference and error amplifier which in turn provides a signal to the buffer. The buffer adjusts the primary voltage and in this manner provides the required output regulation. The other secondary output is connected to a voltage multiplier which boosts the voltage to the appropriate selected level. The high voltage is then filtered to remove commutation noise. The output voltage is selectable over the range indicated below (for each supply type) by selection of resistor R6 which is external to the appropriate supply.

The supplies operate within the specifications listed for each type in Table 8-2.

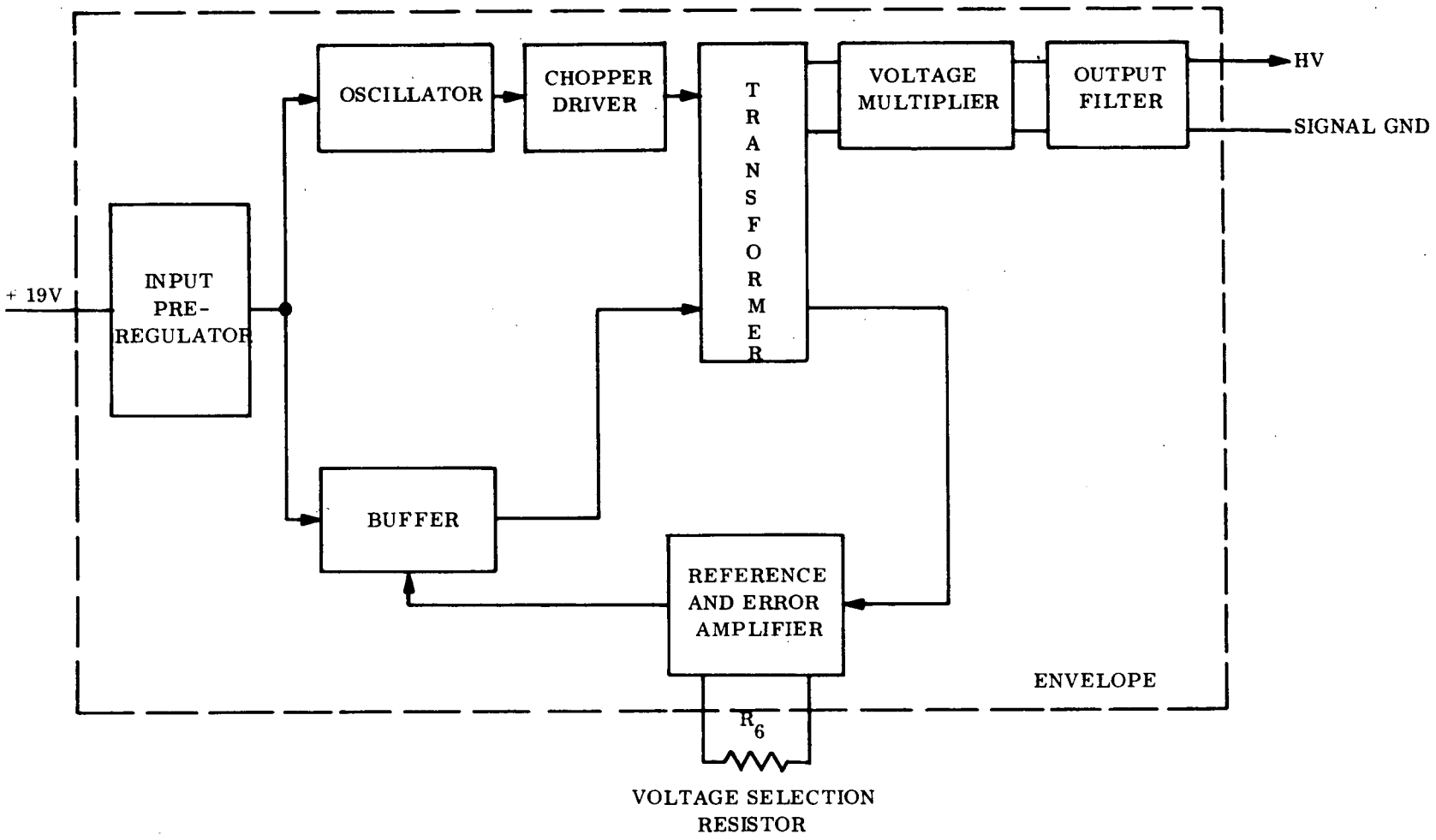

Figure 8-6. High Voltage Power Supply Block Diagram

Table 8-2. High Voltage Supply Specifications

	Type A	Type B	Type C	Type D	Type E
Output Voltage (VDC)					
Minimum	2300	-1500	1400	950	1550
Nominal	2600	-1700	1600	1100	1850
Maximum	2900	-1900	1800	1250	2050
Load Current (μA)					
Minimum	0	0	0	0	35
Maximum	5	25	5	3	110
Output Ripple (%)					
Broad Band	0.003	0.003	0.002	0.002	0.01
Regulation (%)					
vs Line & Temperature (0 to + 25°C)	0.32	0.25	0.375	0.25	0.65
vs Load (Min to Max Load at 25°C)	0.15	0.75	0.20	0.30	1.70

In addition, each supply was designed with short circuit protection such that any partial or complete output short does not cause any degradation to the supply. Furthermore, when the output is shorted the input current does not exceed three times the normal operating current.

In the final instrument configuration the following voltages were selected to power the indicated detectors:

Detector	Selected Voltage
Polarimeter	2650
H-Alpha	-1680 V
Short X-ray	1500
Long X-ray	1125
Short and Long EUV	1600
Medium EUV	1600*

*Note that the actual voltage applied to the medium wavelength EUV detector is 1500 volts. Since the Type E supply used for this detector has a minimum output voltage of 1550V, a

2 M ohm resistor was connected in series with the high voltage line. The detector draws about 50μ amps of current, therefore; the voltage across the series resistor is about 100V and the voltage on the detector is 1500 V.

8.7 STEPPER MOTOR DRIVERS

The stepping motor drivers are required to switch power to the appropriate motor windings in response to a signal from the motor control logic. The motor drivers must also provide dc isolation between signal and power grounds, since the motor control logic power is returned to signal ground and the motor drive power is referenced to power ground.

Figure 8-7 shows the block diagram for a motor driver. The motor drive control logic supplied a 50 kHz signal to the appropriate phase input. The signal is amplified and used to drive the isolation transformer. The transformer output signal is rectified and filtered to a dc signal which is used to trigger the power switch. The control logic sequentially controls the phase to be energized thus causing the motor to turn in the desired direction.

An additional feature of the circuit is that it requires little standby power.

In order to achieve minimum size each motor driver was packaged in a single cordwood module. Since all of the motors are identical, only one circuit design was required and thus the modular design allows for 100 percent interchangibility.

8.8 STEPPER MOTOR CONTROL ELECTRONICS

The start, stop, direction and speed control of the stepper motors is performed by the use of series 54L Texas Instrument logic circuits. The logic processes the signals from the spacecraft (EOR) and the signals from the appropriate microswitches and relays in order to control the motors. The logic configuration is shown on drawing 47C217126. Each motor has its own motor control logic and there are four separate pairs of outputs from each control section. Each pair of outputs is connected to the appropriate phase input on the appropriate stepper motor drive electronics (reference paragraph 8.7 for a description of the motor driver). The output stage of the motor drive control logic is shown in Figure

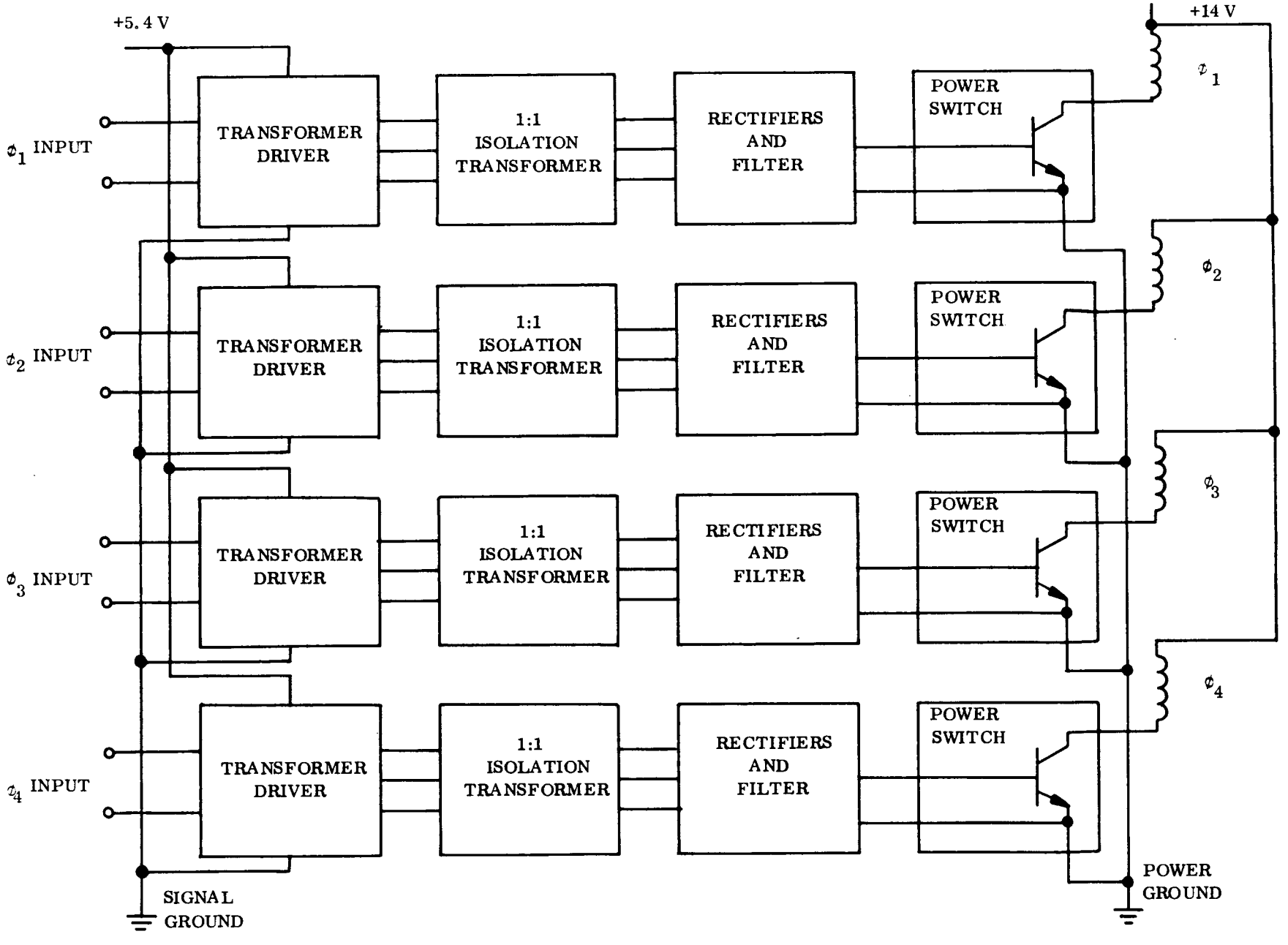

Figure 8-7. Block Diagram of Stepping Motor Driver

8-8. When all of the control signals to any phase are "1's" the output of that phase circuit is a 50 kHz signal and the outputs of the other phases are dc levels. The 50 kHz signal is used by the motor driver to power the appropriate winding on the motor. By controlling the sequencing of the phases the motor control logic determines the direction of motor rotation and by controlling the duty cycle it controls the speed of rotation. Figure 8-9 shows the phase pulsing sequence for both forward and reverse motion (clockwise and counter-clockwise rotation of the motor). Note that the pulsing sequence is the same no matter what the stepping rate is. Figure 8-10 shows the motor power duty cycle for the four stepping speeds employed by the five motors in the experiment. It also shows during which word gate times the actual stepping occurs. In addition, the aperture wheel motor and the carriage drive motor can be single stepped. In order to perform this function the control logic remembers which winding was last energized and energizes the next winding in the sequence upon command.

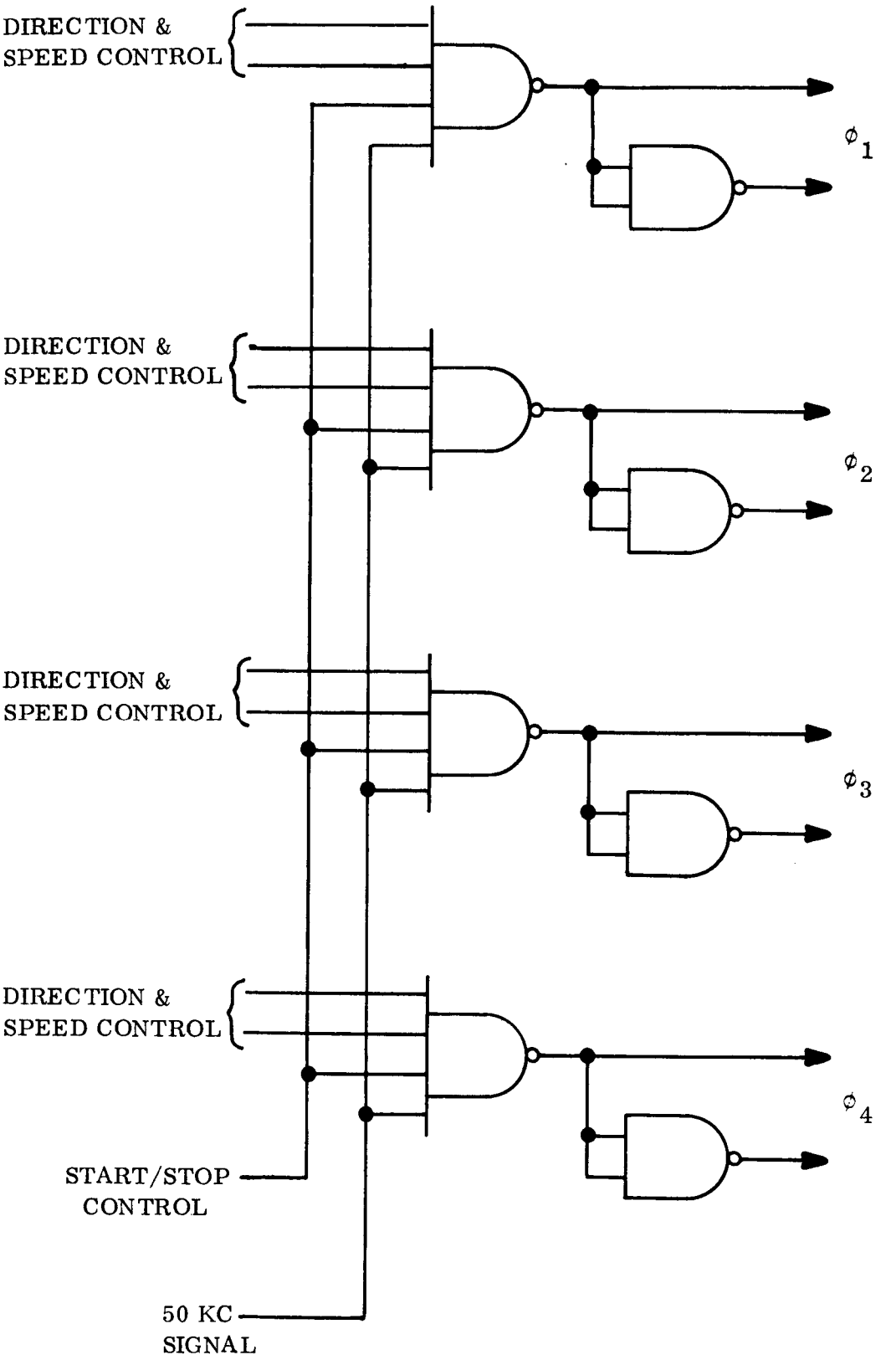

Figure 8-8. Output Stage of Motor Drive Control Logic

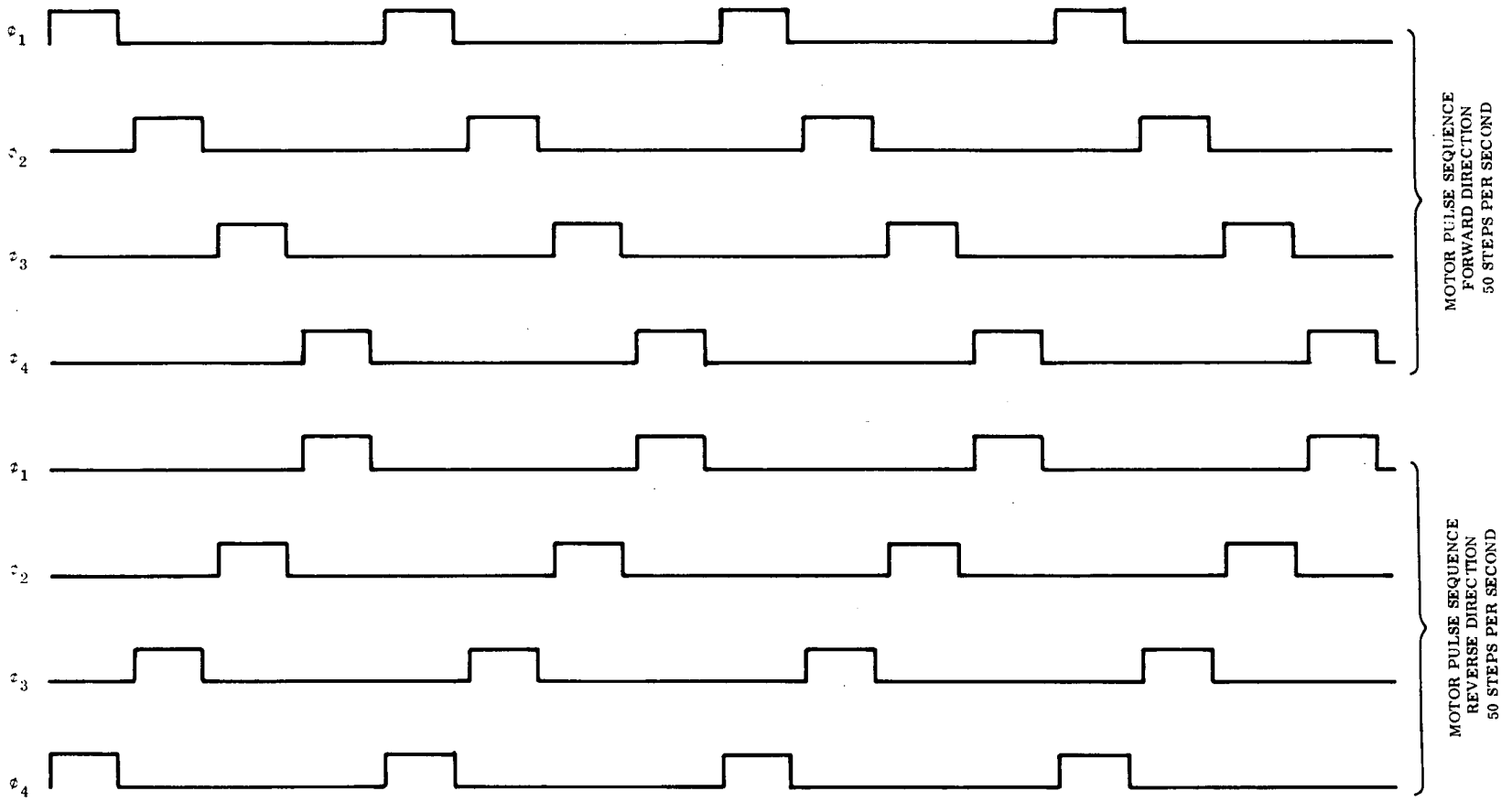

Figure 8-9. Stepper Motor Phase Pulsing Sequence (Forward or Reverse)

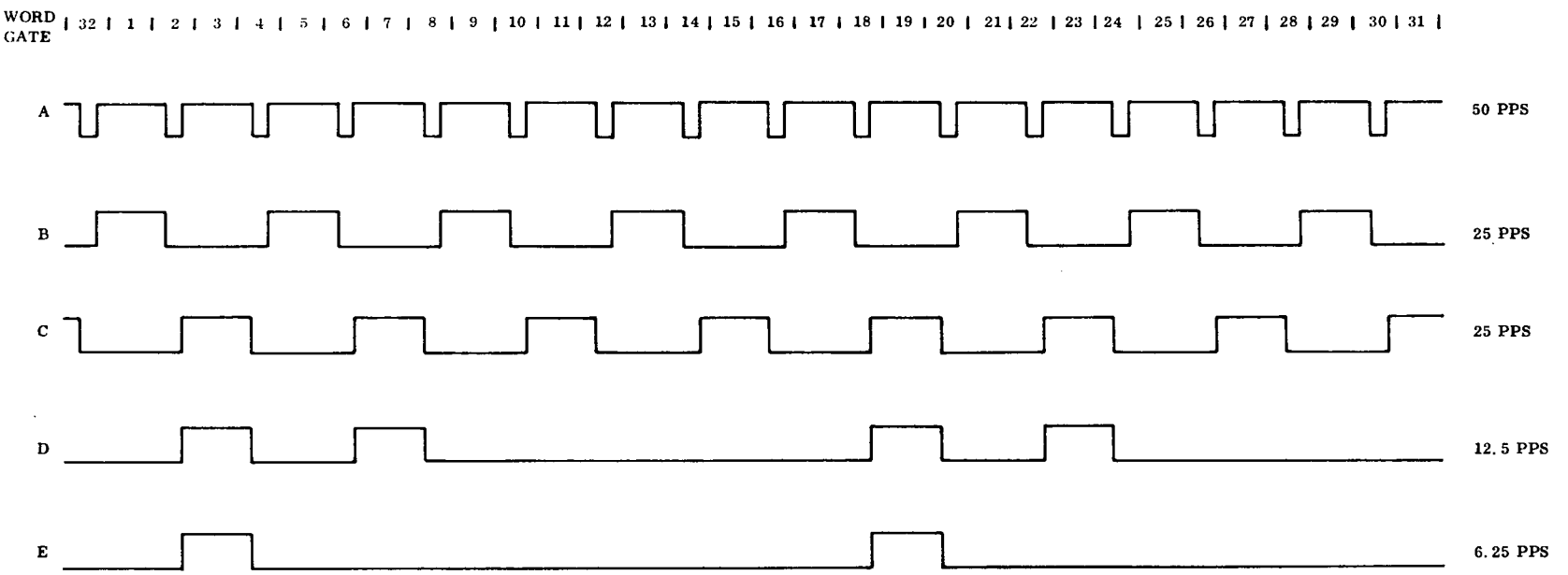

MOTOR	OPERATIONAL MODE	COMMAND	WAVE FORM
EUV MASK	ALL MODES	XN-10 OR XN-61	A
EUV CARRIAGE	SPECT TO SUV	XN-48	A
EUV CARRIAGE	SPECT TO LUV	XN-23	A
EUV CARRIAGE	SPECT FAST SCAN	XN-15	D
EUV CARRIAGE	SPECT SLOW SCAN	XN-56	E
APERTURE WHEEL	APTR TO REF	XN-62	A
APERTURE WHEEL	STEP APTR AUTO	XN-65	E
SHORT X-RAY F.W.	ALL MODES	XN-03, XN-08, XP-68	C
LONG X-RAY F.W.	ALL MODES	XN-03, XN-58, XP-69	B

Figure 8-10. Motor Power Duty Cycle Versus Stepping

SECTION 9

INSTRUMENT ASSEMBLY

9.1 REQUIREMENTS

The spectroheliograph instrument is one of the two main pointed instruments in the OSO-H spacecraft. As such, it is mounted in the elevation frame of the spacecraft so that it is always pointed to the sun during the daylight portion of the orbit. The instrument structure provides the mounting base for the elements of the EUV, H-α, X-ray and polarimeter subsystems as described in Sections 3, 4, 5, 6 and 7. The structure must have adequate strength and stiffness to hold the subsystem elements in precise alignment with each other and to maintain alignment of the optical axis of the EUV subsystem parallel to the axis of the X-ray subsystem within 10 arc-seconds after long term storage and handling environments, after the dynamic test environments, after the dynamic environment of the spacecraft launch, and under the thermal environment of orbital flight.

9.2 STRUCTURE

The instrument structure as shown in Figure 9-1 is an all beryllium box consisting of a heavy base plate (3/4 inches thick) with sides plates, bulk heads, a front plate bonded and screwed to the base plate and a removable cover over the entire box. Beryllium was selected because of its light weight, high stiffness, and high thermal conduction characteristics. Within the original program interface requirements of weight and space, it was the only material that would provide adequate stiffness and low thermal gradients for the structure.

The internal face of the base plate contains the precision-machined surfaces onto which the subsystem elements are mounted. In addition, the provisions for mounting to the spacecraft elevation frame are machined into the external face of the base plate near the center of the base plate. These provisions consist of a precision spherical socket to mate with a spherical boss on the spacecraft and three tapped holes in the base plate for the three interface mounting bolts. Also on the external face of the base plate at the

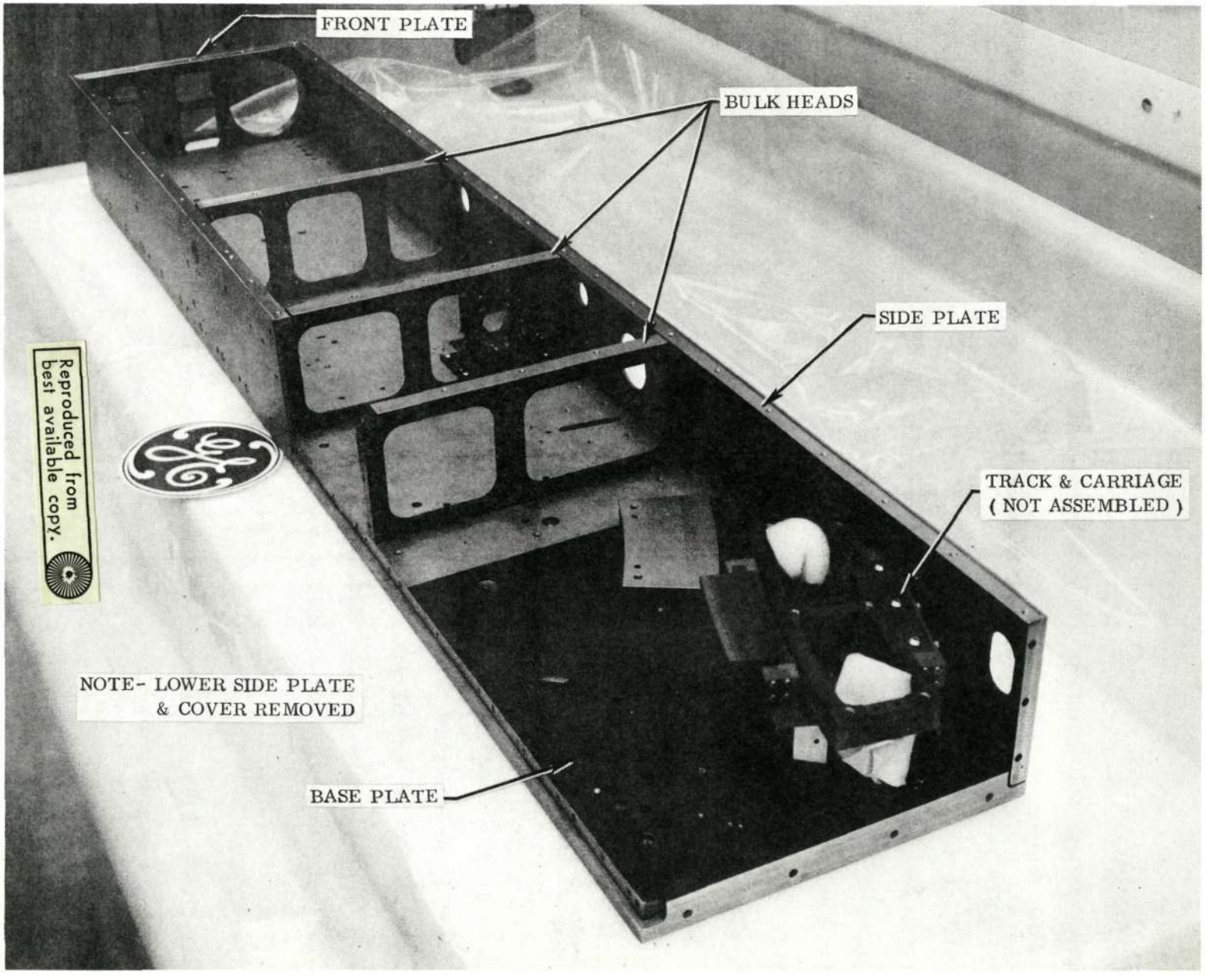

Figure 9-1. Instrument Structure

four corners are provisions for mounting balancing weights. Weights were provided on the final instrument assembly to balance the instrument about the spacecraft elevation axis as required by the interface definition. However, upon installation of the instrument into the spacecraft, changes were made to these weights to compensate for unbalances of the spacecraft elevation frame due to other components mounted on the elevation frame.

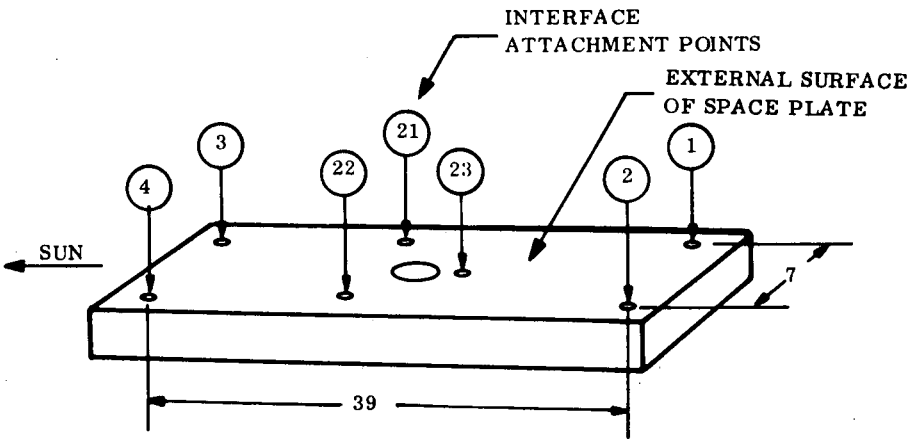

TIME	1	21	3	2	22	4	23
INITIAL FAB (1-15-70)	0.0000	-0.0122	+0.0127	0000	-0.0152	+0.0069	-0.0061
POST PROTO VIBR (7-10-70)	0.0000	-0.0117	+0.0127	0000	-0.0142	+0.0064	-0.0064
REFURBISHMENT (10-13-70)	0.000	-0.0114	+0.0127	0000	-0.0140	+0.0119	-0.0076

NOTE: ALL POINTS ARE RELATIVE
HEIGHT ABOVE SURFACE TABLE IN CENTIMETERS

Figure 9-2. Distortion Measurements

One of the concerns with the beryllium structure was the possibility of micro-creep of the beryllium due to dynamic loads, relief of internal stresses due to machining and assembly, and long-term static loads. Such creep could result in changes in alignment that would degrade the subsystem performance and misalign the optical axes beyond the specified tolerances. To determine the magnitude of distortions of the structure, measurements were taken at seven locations on the external surface of the base plate. Measurements were taken at initial completion of the structure fabrication, after prototype vibration and during the refurbishment cycle. The measurements are shown in Figure 9-2. Note that the external surface of the base plate is not the precision-machined surface, but was used

as the reference since it is always accessable without disassembly of the instrument. All measurements except one agree within less than 0.0025 cm which is within the measurement accuracy and represents adequate stability to meet performance requirements. One measurement varies in refurbishment measurement by 0.005 cm. This point is at one corner of the box and could indicate a slight twist of the open box, which is the least stable mode of stiffness. This measurement could also be an inaccurate reading. In any case, it does not appear to have resulted in degraded performance or alignment.

9.3 LOGIC BOX

The logic box is attached to the aft end of the instrument structure and contains all the control electronics logic. The box is an electron beam welded aluminum structure with two aluminum covers, one on the baseplate side of the instrument and one on the cover side of the instrument. The ten plug-in circuit board assemblies containing the control electronics are removable after removal of the cover on the baseplate side so that boards may be removed and changed with the instrument in the spacecraft. The wiring interconnecting the circuit boards with each other and with the rest of the instrument is accessable by removal of the cover on the cover side of the instrument.

9.4 THERMAL DESIGN

To maintain alignment accuracy and subsystem performance, the thermal distortions and temperature excursions of the instrument must be minimized. During the daylight portion of the orbit, the instrument receives solar energy on its front face and the thermal energy dissipated internally by the electronics. Energy is radiated to space by the instrument surfaces. In addition, there is a conductive flow through the spacecraft interface and a radiative flow with the spacecraft surfaces which are a function of the relative temperatures of the instrument and spacecraft. During the night portion of the orbit, there is no solar energy and the electrical dissipation is minimized.

To maintain an orbital temperature of approximately $20^{o}C$ which is the ambient temperature at which the instrument aligned and calibrated, a thermal coating with an absorbtivity to emissivity ratio (α/e) of 4.0 is required. To achieve this, an aluminized kapton material

is used. The aluminized kapton is bonded in large sheets to all external surfaces of the instrument, except the thermal shield and the forward surface of the logic box facing the left-hand-pointed instrument.

A thermal shield is placed on standoffs in front of the front plate of the instrument to minimize the thermal gradient on the front plate from the solar energy. The thermal shield is finished with D-4-D paint.

The thermal gradients within the instrument are minimized through the use of the beryllium structure which has a high conductivity, thus tending to equalize the temperatures between the thermal inputs and emitting surfaces. The gradients which have the most effect of distorting the alignment of the instrument are the gradients between the base plate and cover. This gradient was calculated at $2.0^{o}F$.

9.4.1 THERMAL GRADIENT TEST

To demonstrate that the change in alignment of the X-ray axis to EUV axis would be less than the maximum allowable change of 10 arc-seconds, a thermal distortion test was run in which the temperature gradients, as predicted by analysis, were generated in the structure and the changes in alignment measured. The test was run in a vacuum. Temperature gradients were generated by controllable strip heaters on the structure and temperatures measured by thermocouples at locations shown in Figure 9-3. The analytically predicted and actual test temperatures are shown in Table 9-1. The X-ray axis was determined by monitoring the X-ray collimator alignment with an autocollimator and the EUV axis was determined by measuring the spatial position of the EUV source required to peak the EUV output. To provide a margin of safety, the thermal gradients were run to approximately twice the predicted values. The distortion results are shown in Table 9-2. Due to bending of the instrument structure caused by the thermal gradients, both the EUV and X-ray axes moved spatially. However, as predicted by analysis, they both moved in the same direction and the differential motion between the X-ray and EUV axes was within the specified limits, even at twice the expected gradients.

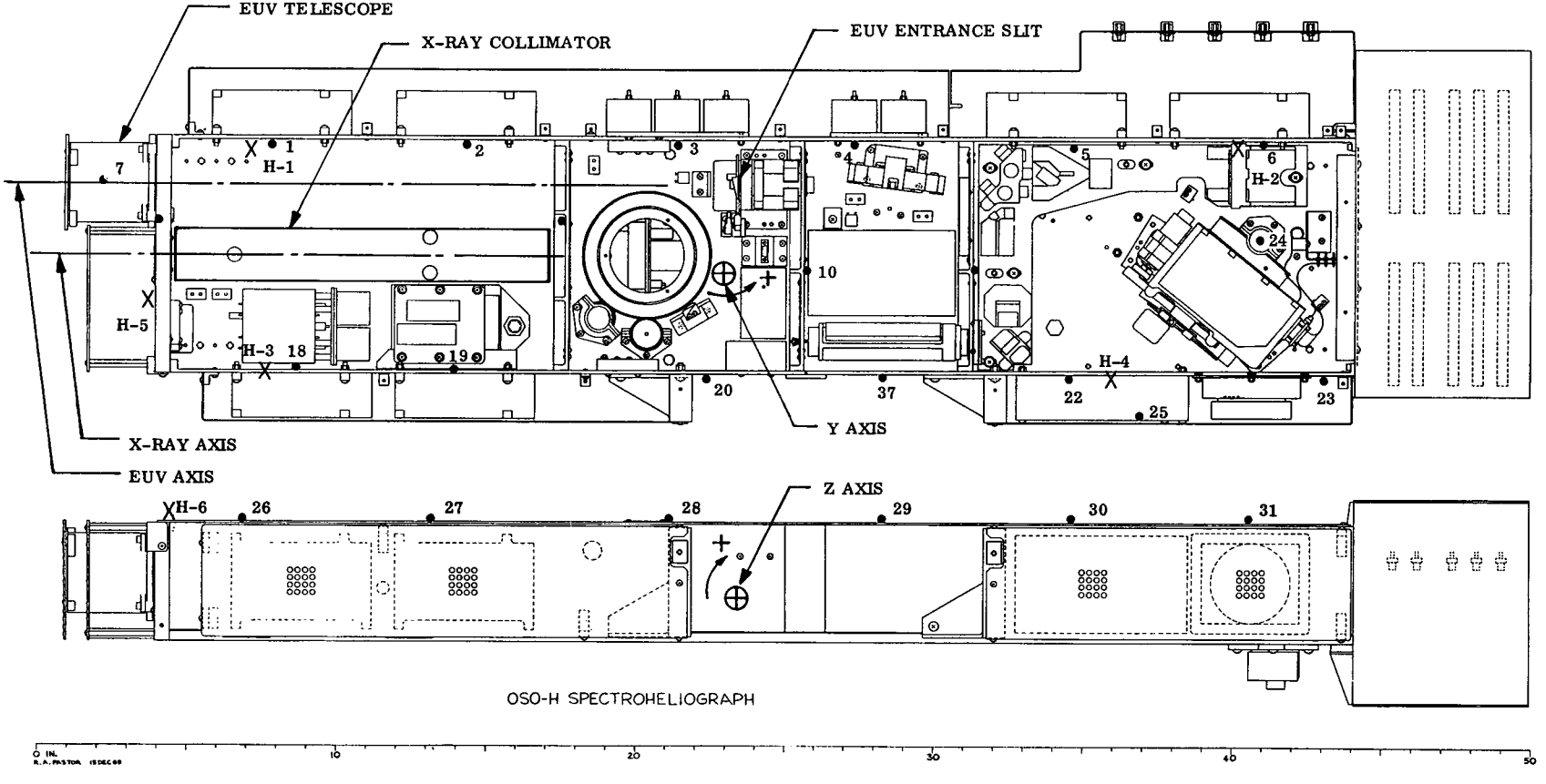

Figure 9-3. Thermocouple and Heater Locations Thermal Distrotion Test (Sheet 1 of 2)

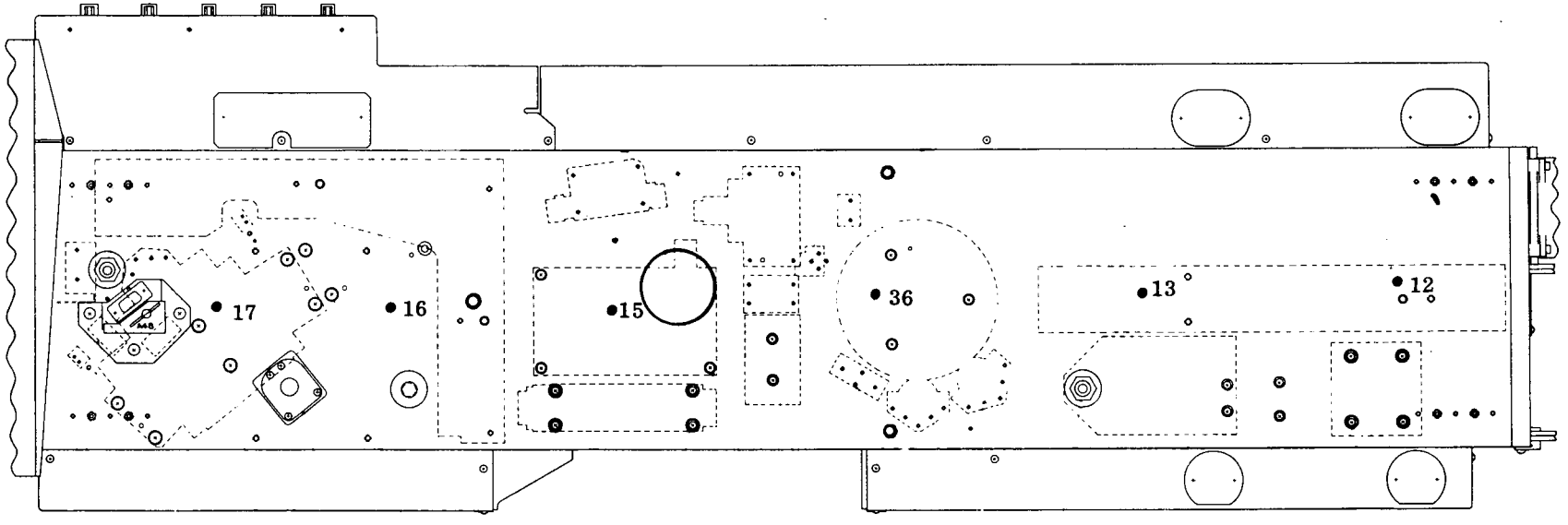

Figure 9-3. Thermocouple and Heater Locations Thermal Distortion Test (Sheet 2 of 2)

Table 9-1. Thermal Gradients

Location	Predicted Average Temperature	1X Gradient Actual Average Temperature	2X Gradient Actual Average Temperature
Upper Side Heaters 1&2 T.C. 1-6	79.4	79.6	81.1
Base Plate Heaters - None T.C. 12-17	76.0	76.0	75.9
Lower Side Heaters - 3&4 T.C. 18-23	77.4	78.0	78.9
Cover Heater 6 T.C. 26-31	78.0	79.0	79.6
Gradient Upper to Lower Sides	2.0	1.6	2.2
Gradient Cover to Base	2.0	3.0	3.5

Table 9-2. Distortion Results

	Y-Axis			Z-Axis		
	Telescope	Collimator	Δ	Telescope	Collimator	Δ
No Gradient	0	0	0	0	0	0
1X Gradient	+14	+11	3	0	0	0
2X Gradient	+18	+13	5	-15	-13	2

Note: All measurements in arc seconds. See Figure 9-3 for sign convention.

9.5 ELECTRONICS PACKAGING

9.5.1 GENERAL PACKAGING SOLUTION

The arrangement of the electronics in the instrument was dictated largely by the sensor characteristics. Electronics were mounted in close proximity to their associated sensors, placed so as to minimize lead lengths. Electronic equipments not closely associated with sensors, such as power supplies and digital logic, were mounted on the external surfaces of the instrument.

In general, the techniques used were: (1) encapsulated welded cordwood and matrix modules, (2) double-sided, plated-through, printed circuit boards, (3) chip-and-wire hybrid microelectronics, and (4) point-to-point soldered interconnections.

Interconnection among components was accomplished by means of laced wire cable bundles, secured to the instrument structure by clamps and conformal coating. Exceptions to the above were the flexible cables interfacing the EUV carriage with the instrument. These cables consisted of laminated Teflon FEP/Copper/Kapton-H approximately 0.05 cm thick configured to minimize torque required to drive the carriage.

In general, parts, materials, and processes used in packaging the electronic equipment were representative of proven space flight hardware built by GE-SSO for recent programs.

9.5.2 WELDED CORDWOOD MODULES

Reliability requirements for OSO-H electronic equipment dictated the use of a well-controlled packaging format. The welded cordwood module, an SSO standard, is a key part of this format. The advantages of this construction are it:

1. Allows high packaging density without over complicating the interconnection system.
2. Provides protection for fragile electronic parts and interconnections from the most severe environments with high reliability.
3. The disciplines of design, manufacture, testing and maintenance are performed in discrete logical steps.

In the standard module, electronic parts are mounted "cordwood style" with their axial leads extending through top and bottom insulating layers of 0.18 cm thick mylar film. Interconnection is accomplished by welding nickel ribbon between leads following the electrical circuit printed on the mylar film. Interconnections between mylar layers are made by nickel riser pins welded to ribbons on top and bottom layers. After interconnections and testing are completed, a freeze coating of epoxy resin is applied to the welded layers and a buffer layer of silicon rubber 0.005 to 0.013 cm thick is applied and cured on the parts, as a cushion against mechanical and thermal shock. A final encapulation using materials ranging from alumina-filled epoxy resins to rigid foam converts the assembly into a solid plastic block with terminal pins protruding from one face, which may be used as the mounting face, if desired.

In order to facilitate manufacture, assembly, tooling and test, a standardization of module dimensions is used. For example, the SSO module specification allows dimensions to vary in 0.635 cm increments, permitting the use of standard tooling. Further, all outgoing terminals are located on a 0.254 cm grid. This interconnection standard is an

important adjunct to the module scheme, for mating modules to printed circuit boards. Many part interconnections can be accomodated inside the module to simplify the interconnection board design and optimize external circuitry.

Parts purchased from vendors are screened and stored in special bonded stock. Inventories and screening test data are maintained by data mechanization methods. Six discrete assembly and fabrication steps are required to produce a finished module. A separate inspection is performed at each step.

9.5.3 WELDED MATRIX MODULES

The necessity for ultimate compaction of the logic circuitry led to the selection of a three-dimensional modular geometry for the packaging of nearly 500 flat packs required. A GE-SSO standard module design, under development since 1963, was adapted for this purpose. The concept is shown in Figure 9-4. The flat packs are stacked "cordwood" style between two parallel boards, with leads welded to provide connections between and among functional parts. The key to the stacked flat pack design was the development of a system that could provide the necessary density and diversity of connections within the limitations of the required form factor. This system evolved as the 0.635 x 0.840 cm welded matrix. Almost any required interconnection scheme may be accommodated by mating one matrix with one integrated circuit package. The "right and left" leads of the matrix are located to mate with the leads on the circuit. The internal connections in the matrix are programmed so that all subsequent connections between circuits are made on the "top" or "bottom" side of the matrix. This technique allows the module wiring to be done in one plane, as indicated in the figure. Other advantages provided by the use of the 0.635 x 0.840 cm matrix are:

1. No bending or twisting of integrated circuit leads is necessary, as all forming is done on the matrix leads. This minimizes the possibility of damage to the seals on the flat package.

2. Of the 300 welds required in a typical module, 200 could be made in plane prior to final assembly, leaving only 100 welds to be made at assembly.

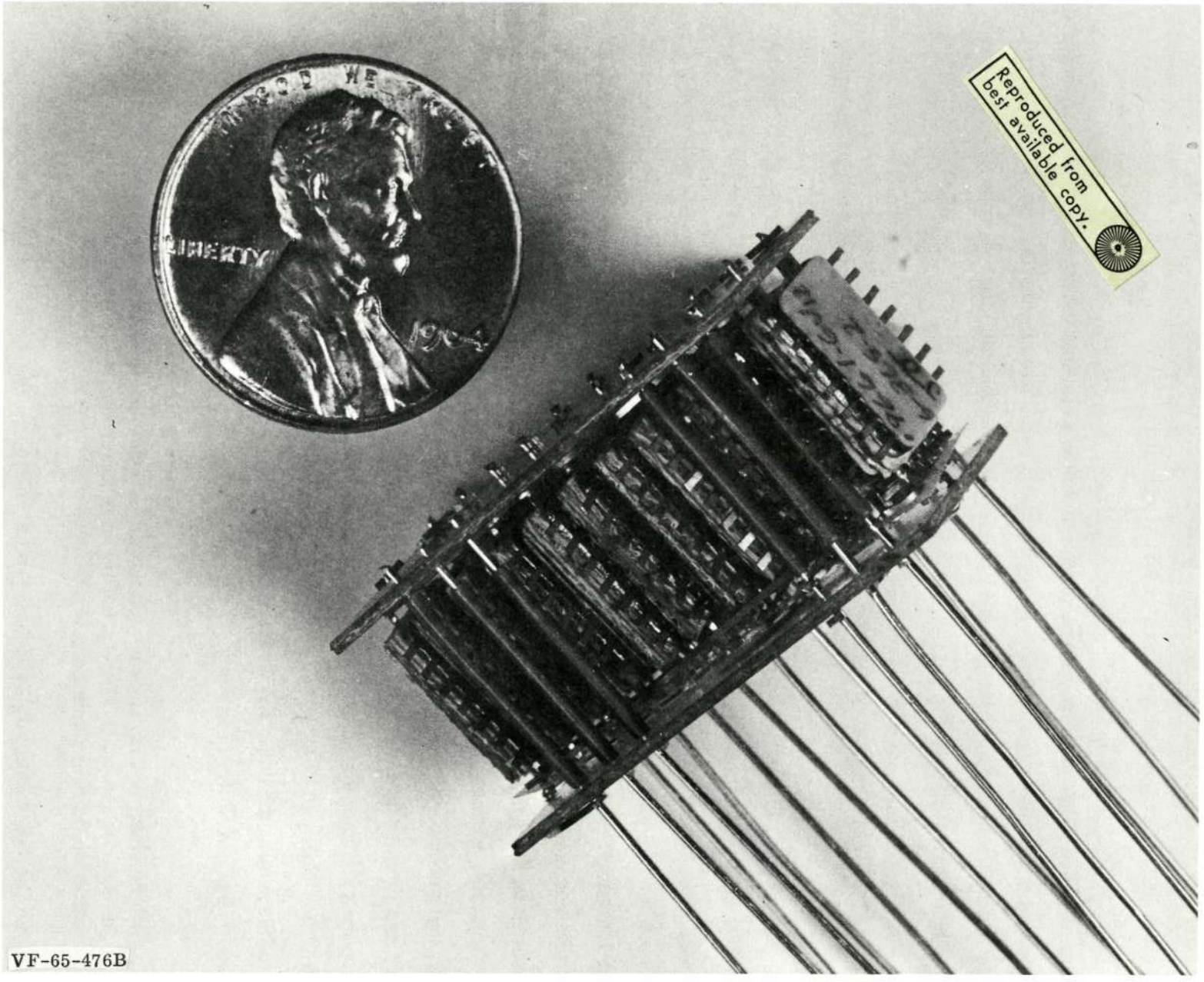

Figure 9-4. Three-Dimensional Modular Packaging Geometry

3. The matrix design is multiple; that is, each laminated assembly contains up to four separate matrices, allowing for separation of signal and power leads and for increased flexibility in design.

4. Repairs and circuit changes can be made by clipping the top leads of the matrix involved and removing matrix and integrated circuit as a unit. The matrix is discarded and a new matrix is mated with an integrated circuit prior to replacement.

5. The 0.635 x 0.840 cm welded matrix is as rugged and easily handled as the flat package itself, and is simple and inexpensive to produce.

The original matrix design called for hand fabrication, using individual 0.013 x 0.038 cm gold plated Kovar ribbons with mylar insulators. A redesign for producibility substituted prefabricated Lexan insulated multilead cable, connected by a "melt-through" welding technique (see Figure 9-5). The result proved to be economical for OSO-H production qualities, but lack of control of melt-thru temperature caused high reject rates in the prototype potted modules. Implementation of tight process controls solved the problem, and no further production difficulties were encountered.

9.5.4 LOGIC ELECTRONICS

The control logic package was required to mount, interconnect and thermally control approximately 500 Texas Instrument 5400 series logic elements, with associated discrete parts. Because of the intermixing of flat packs, relays and discrete parts, both planar and modular arrangements were considered. Preliminary information indicated that the logic would be mounted within the instrument housing. This led to the decision to use a modular approach, in order to use available space between sensors, actuators and ray paths. As the instrument design was developed, the logic was mounted in a separate housing bolted to the rear of the instrument case, in close proximity to the vehicle interface connector panel.

Another decision which affected packaging design was that no separable connector would be required between logic box and instrument. This was a weight-saving decision. It was also decided that no multilayer printed circuit boards be used in the system.

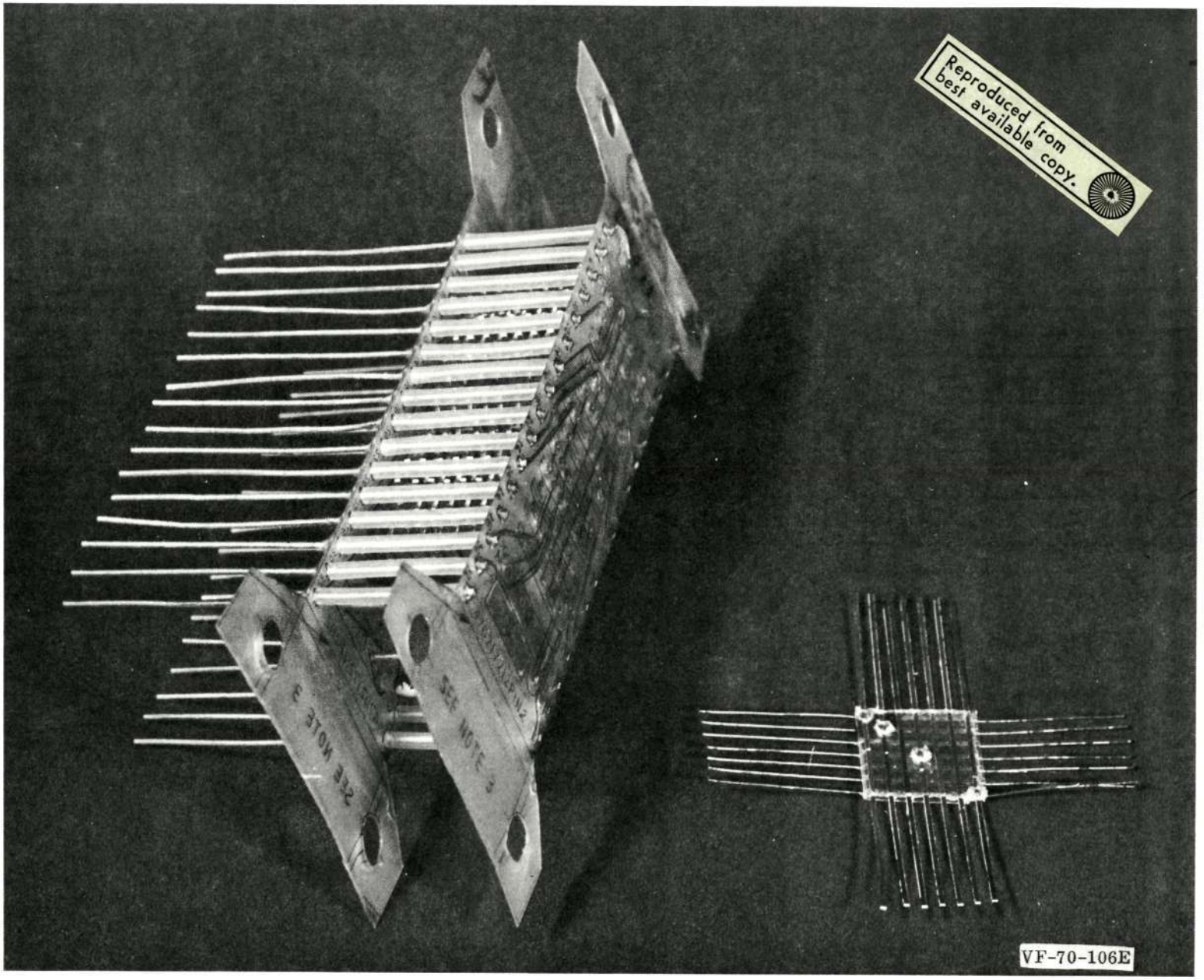

Figure 9-5. Matrix Redesign for Producibility

The logic box development was based on the matrix module concept (see Section 9.5.3) originally planned for packaging the logic inside the instrument. This approach was modified to the mounting of the modules on two-sided printed circuit boards to make plug-in sub-assemblies for installation in an externally mounted logic box.

An electron beam welded "H" frame chassis was designed to hold 10 boards. Two covers allow access to either the harness side or the printed circuit side. The plates making up the box structure are 0.23 cm aluminum, finished with Alodine 1200, a conductive surface conversion coating. Spring-type P/C board retainers Birtcher 15B-8 are riveted to the box side walls. High density two-piece connectors, Amp 1000 series are used to provide plug-in capability.

Circuit boards are epoxy-glass, double-clad, 0.156 cm thick. Circuitry is 2 oz. copper, tin-lead plated and reflowed. Modules are mounted by inserting pins in plated through holes and soldering. A filler bond of polyurethane, PR1538, gives mechanical support to the soldered connections. Removal and replacement of modules has been accomplished using tools and procedures developed at GE-SSO for this purpose.

Interconnecting wiring, terminal boards and ground strips are located in the compartment below the web which supports the printed circuit mating connectors.

The logic box electrical interface wiring is brought out through a grommetted hole in the forward face of the housing, and directly connected through the instrument harness to termination points in the spectroheliograph.

Teflon insulated wire is used in the logic box: 24 gage to connect to printed circuit receptacles and 20 gage for power distribution.

Domed nuts are used wherever possible in the logic box to reduce contamination because of threaded fastner wear.

Polyurethene conformal coating PR1538 is used as required in the harness area to stiffen and dampen wiring against vibration stress. All conductive surfaces, terminals and printed circuitry are coated with this material as well to protect against accidental shorting or contamination damage.

9.5.5 EUV SENSOR ELECTRONICS

The sensor electronics design for the EUV was dictated by the requirement to:

1. Be as close as possible to the magnetic multiplier assembly
2. Provide for high voltage operation without corona or arcing
3. Be as small and light as possible so as not to interfere with carriage motion or lines of sight,
4. Be optically non-reflective.

The functions to be packaged included a pre-amp/amplifier and discriminator circuitry. Amplifiers were prepackaged as hybrid circuits (hermetically sealed flat packages).

The packaging design solution was to encapsulate the circuits in welded cordwood modules mounted inside the carriage top cover (see Figure 9-6). The standard GE-SSO module design was adapted for this application. At a later point in development it was desired to remove high voltage components from the modules to eliminate arcing. These circuits were redesigned on open, shielded terminal boards mounted on the upper side of the carriage cover. At this time, two additional filter modules were developed and mounted on the carriage side cover. Shielding, grounding and wire dress proved critical in this assembly and several iterations were required before a satisfactory design was achieved.

Some development effort was also expended on the selection and application of a black finish compatible with the various shielding and structural materials used.

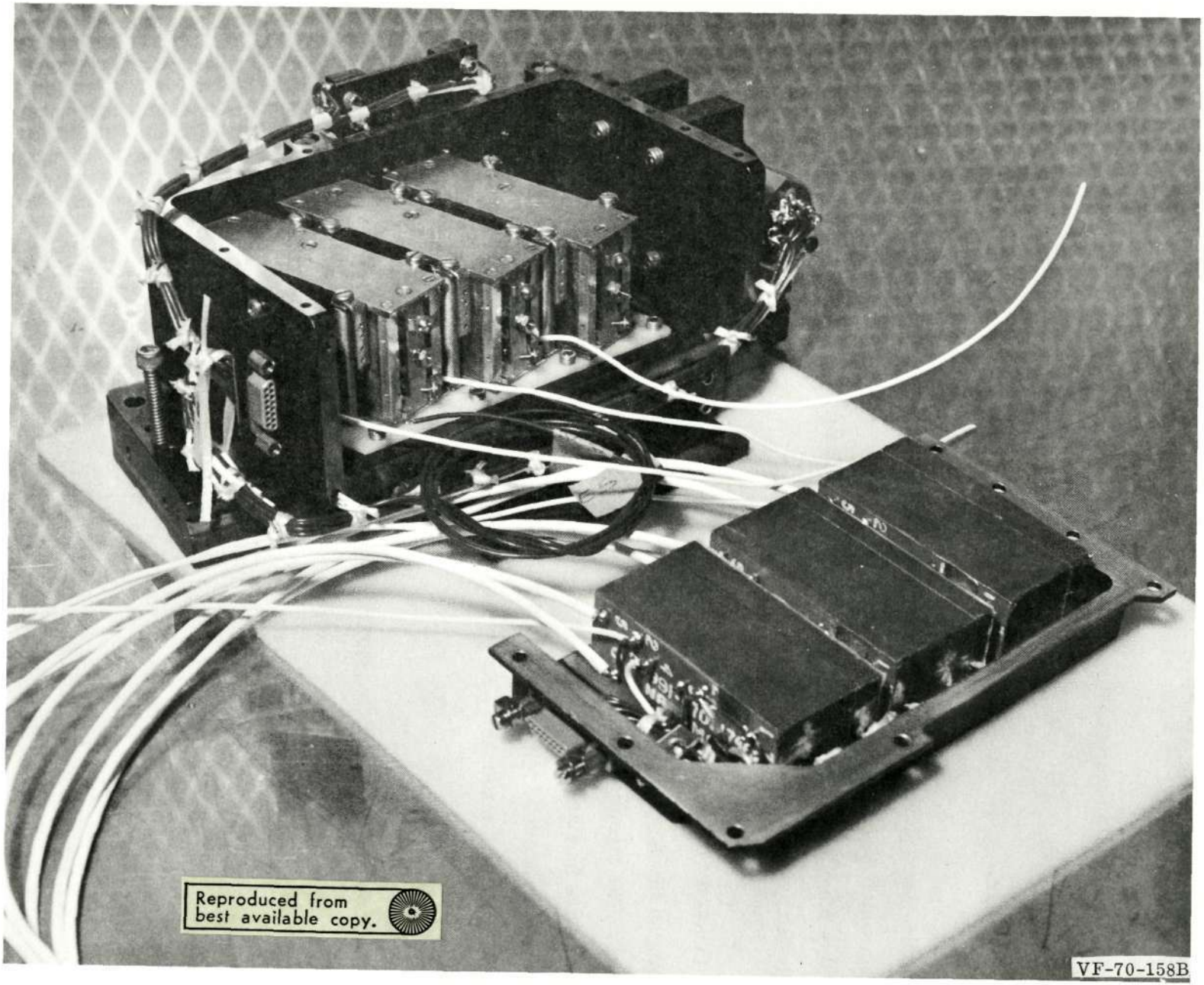

Figure 9-6. Encapsulation of Circuits in Welded Cordwood Modules Mounted Inside the Carriage Top Cover

9.5.6 H-ALPHA ELECTRONICS - PACKAGING

The requirements governing the H-α A to D converter packaging design were:

1. Close proximity to sensor
2. Small size
3. Weight.

The circuits were packaged in a single welded cordwood module approximately 3.81 x 5.08 x 1.905 cm which was mounted to the wall of the instrument housing. Hardwire harness connected this module to the Photomultiplier and to the Timing and Control circuits located in the logic box.

9.5.7 LONG WAVE LENGTH (LW) AND SHORT WAVE LENGTH (SW) X-RAY ELECTRONICS

Packaging of the X-ray sensor electronics was constrained by both internal and external geometry. The circuit elements constituting the pre-amplifier/amplifier and discriminator-functions were themselves packaged in 1.905 x 1.905 cm hermetically sealed flat packages. The desire to keep lead lengths as short as possible between the proportional counters and their preamplifiers made it necessary to package these circuits inside the filter wheel housing.

The initial solution used an adaptation of the standard cordwood module technique, to mount the flat packages "cordwood" style, together with their high voltage decoupling capacitors into two very dense potted assemblies, one each for LW X-ray and SW X-ray, which would fit in the space available. An additional small module was used to house filter components. The discriminator circuits were packaged in a similar manner in a somewhat larger module, containing eight thick film subassemblies.

The amplifier modules and filter were mounted on one glass-epoxy plate, the proportional counters on a similar one. The two subassemblies were mated together and slipped into a groove inside the X-ray filter wheel housing. The original design is shown in Figure 9-7.

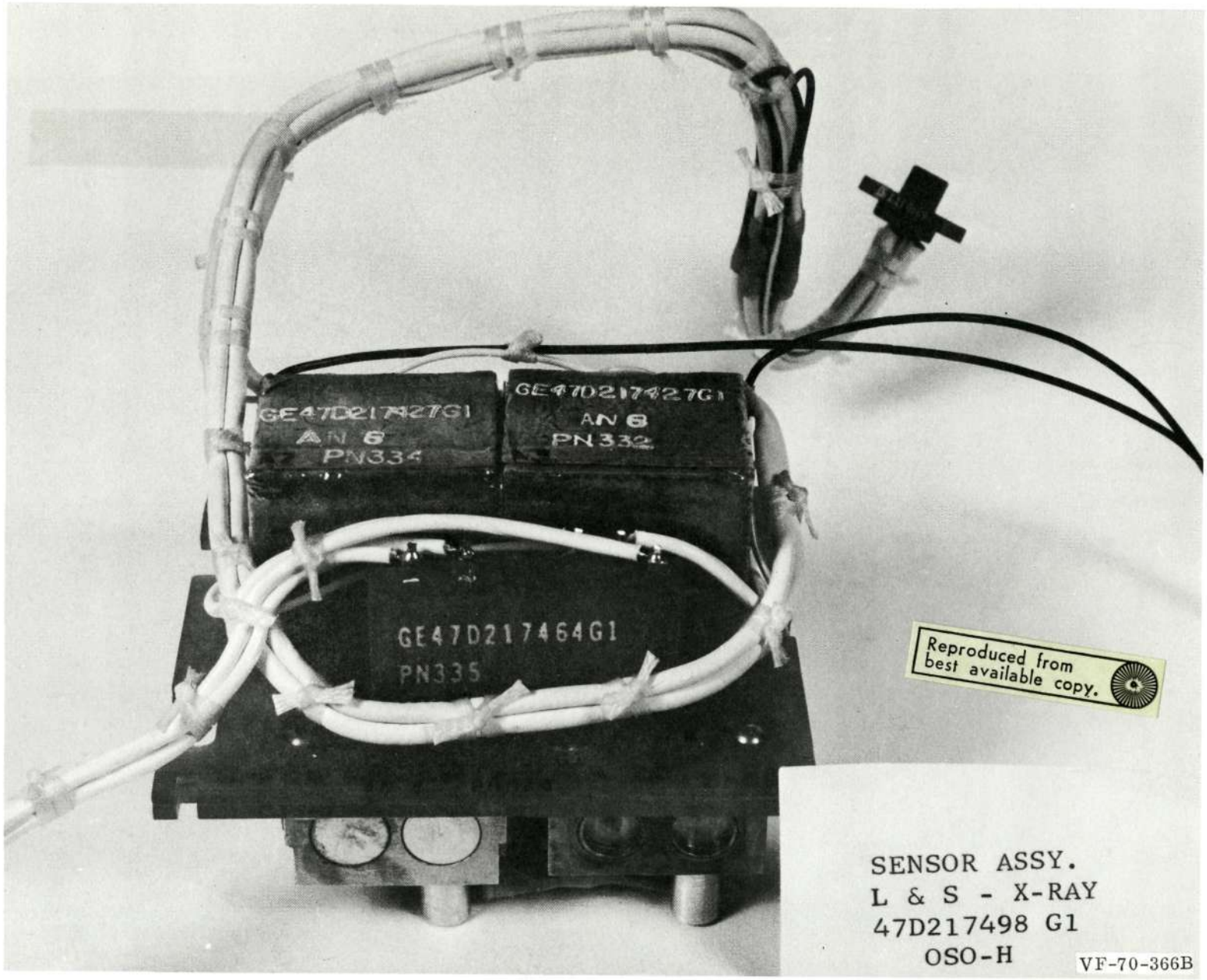

Figure 9-7. X-ray Subassembly

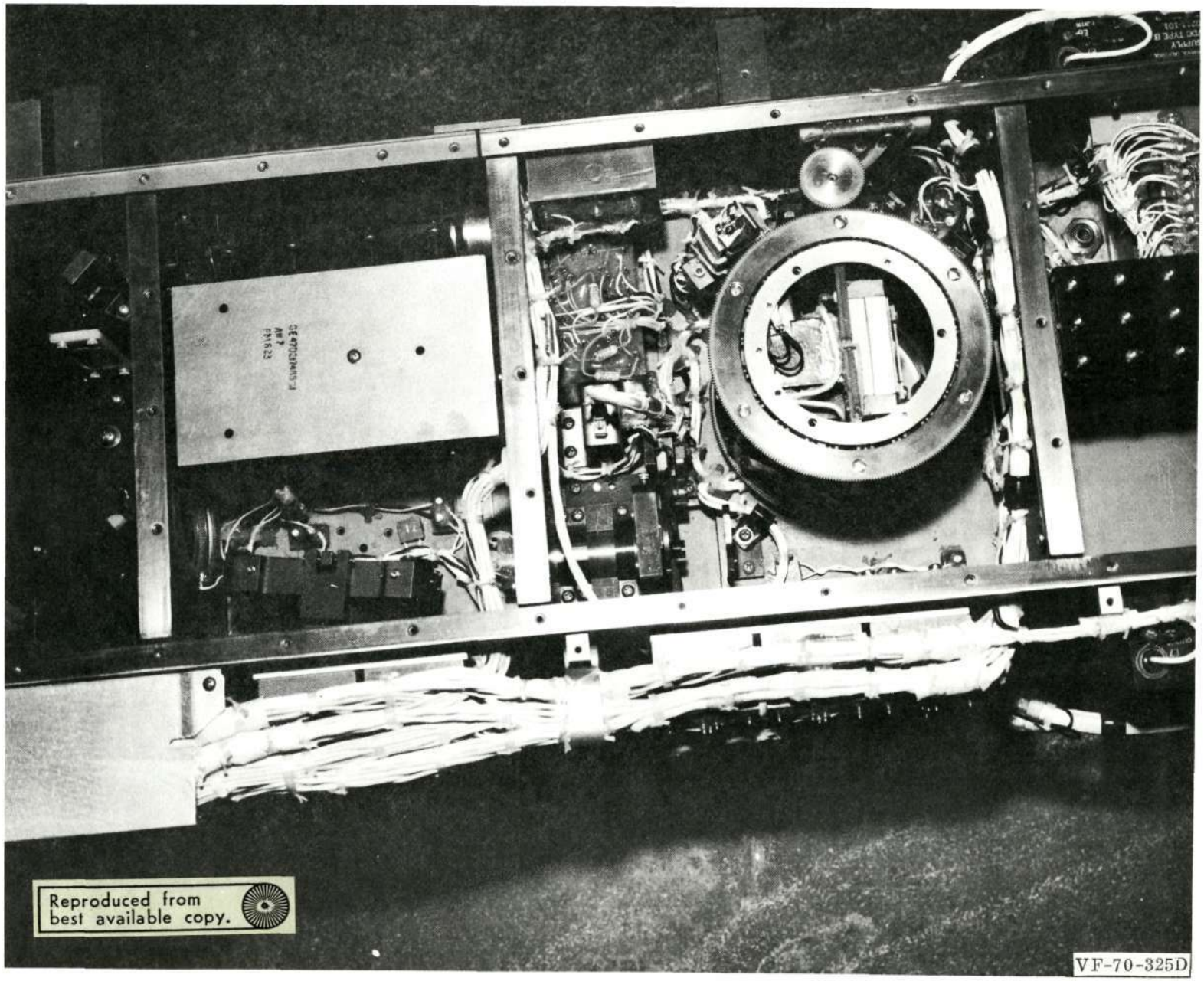

Figure 9-8. Filter Wheel Interconnections

The discriminator module was mounted to the instrument base plate, in the X-Ray compartment.

Interconnections into the filter wheel were passed through a clearance arch at the base of the filter wheel housing (see Figure 9-8).

As a result of high voltage leakage inside amplifier modules experienced during test, it was decided to remove the high voltage blocking capacitors and associated wiring to a separate module whose simpler configuration would allow a complete void-free vacuum encapsulation. This solution proved to be successful, and in the final packaging solution the high voltage module was mounted to the glass-epoxy plate adjacent to the amplifier modules.

9.5.8 POLARIMETER ELECTRONICS

Requirements which determined the packaging approach to the Polarimeter electronics were similar to those specified for the EUV and X-ray subsystems. Short lead lengths between sensor and preamplifier were required because of noise susceptibility. Constrained geometry inside the instrument housing required the use of 1.905 x 1.905 cm flat packages containing thick film circuitry. The circuit packages were divided by function and by channel, the polarimeter being a six-channel device.

The design solution took advantage of the stacked flat pack module technique used in the other sensor electronics. Two modules housed the pre-amplifiers and amplifiers, three channels to a module. Two modules were devoted to discriminator/anti-coincidence circuitry, three channels each. Two modules containing multiplexing logic circuits were mounted on a printed circuit board on top of the sensor electronics module mounting plate. The general arrangement is shown in Figure 9-9.

The amplifier modules were encased in a copper shield at instrument assembly to reduce susceptibility to radiated interference.

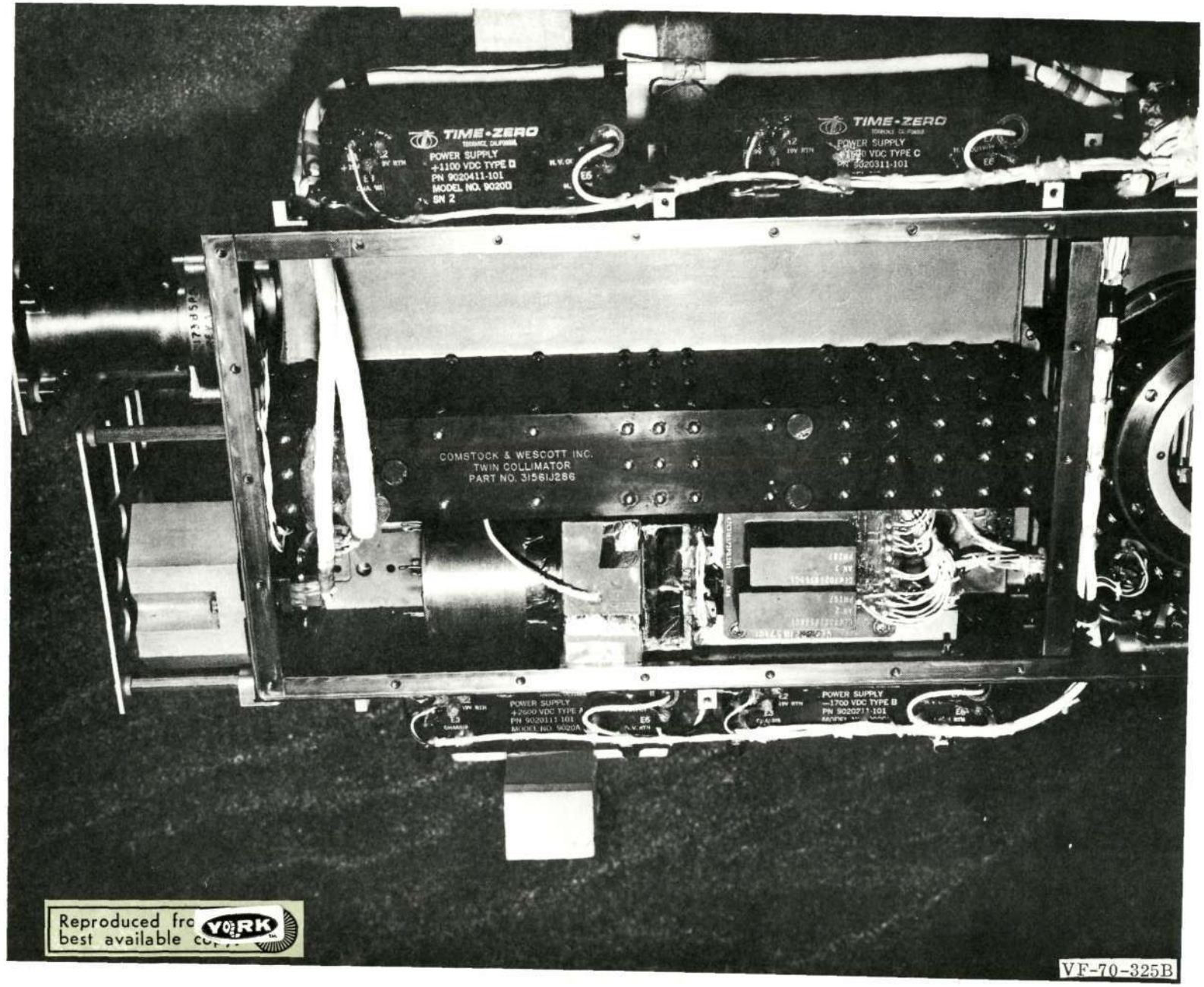

Figure 9-9. General Arrangement of Polarimeter Electronics

9.5.9 LOW VOLTAGE POWER SUPPLY PACKAGING

The low voltage power supply was designed to mount externally in an individual shielded housing. The Regulator/Inverter assembly and Output Filter assembly are encapsulated cordwood modules. The output transformer is also packaged as a potted module (see Figure 9-10).

Wiring is point-to-point inside the housing. Interface connections are made by means of solder terminals extending through the case.

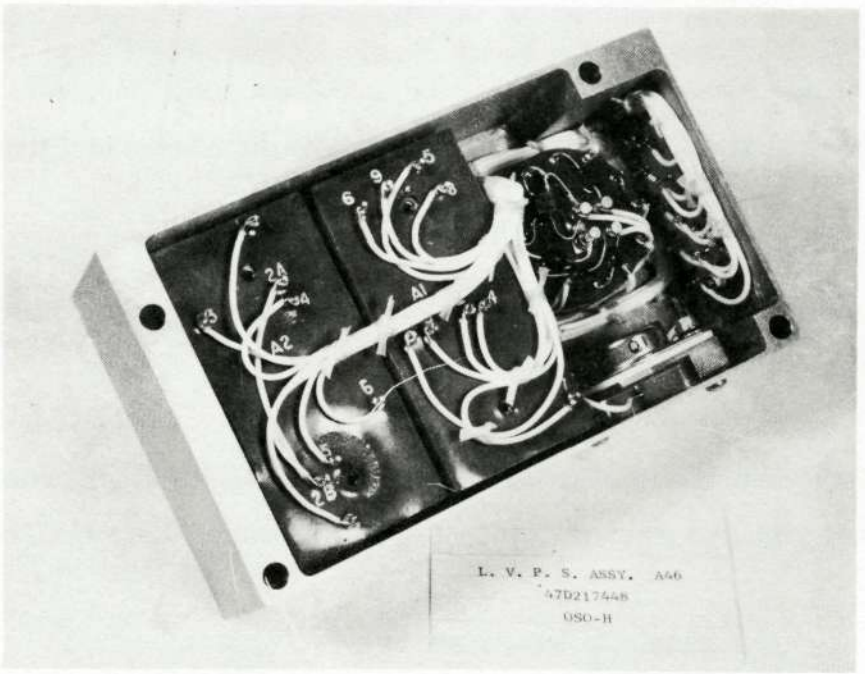

Figure 9-10. Low Voltage Power Supply

The housing is a machined five-sided box which mounts to the Instrument main frame with four No. 6 machine screws.

9.5.10 STEPPING MOTOR DRIVE

There were no special requirements for these packages other than high density and close proximity to motors. The drive electronics for each of the five stepping motors is packaged in an encapsulated cordwood module of 7.62 x 3.81 x 2.79 cm dimensions. The modules are mounted to the outside of the instrument side plate by screws into two threaded inserts cast into each module. Standard cordwood construction techniques are used, welded interconnections, silicon rubber buffer crating, and solid epoxy encapsulation. Interconnections to the instrument harness are made by 0.10 cm-diameter gold-plated nickel pins extending through top face of the potting compound.

The motor drive filter consists of one cordwood module, a potted inductor, two terminal boards containing capacitors, and switching transistor all enclosed in a five-sided machined housing.

The unit mounts open side down, in the H-α compartment, on the instrument baseplate with four No. 6 screws.

Electrical connection into the filter assembly is by means of terminals extending through the case. Internal wiring is point-to-point using teflon insulated stranded hookup wire (see Figure 9-11).

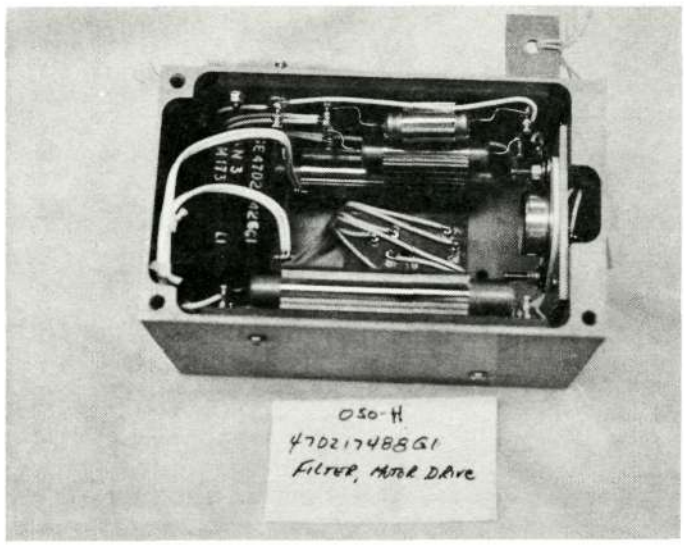

Figure 9-11. Motor Drive Filter

SECTION 10

INSTRUMENT TEST

10.1 INTRODUCTION

This section describes the qualification and flight acceptance tests which are conducted on the instrument. It includes a description of the test programs and summarizes the test results. This section also describes the testing conducted as part of the OSO-H spacecraft test program.

Test data and calibration data for components, subsystems, and the assembled flight instrument are included in the Instrument Log Book (four volumes) which was delivered with the instrument. A listing of the Major Experiment Components appears in Appendix A along with the serial number of the flight item and the component test document number.

10.2 QUALIFICATION TEST

10.2.1 GENERAL

The qualification test was conducted in accordance with the qualification test plan, GE Document No. 70SD4227 and the companion qualification test procedure (Rev B dated 22 July 1970). The procedure was updated as the test progressed to add flexibility to the test sequence and to make additions, deletions, and corrections as identified during the test program. These changes were red-lined into the working copy of the test procedure and were approved by the test director and cognizant NASA/GSFC test representative.

10.2.2 TEST OUTLINE/CHRONOLOGY

The chronology of the Qualification Test is listed in Table 10-1.

10.2.3 QUALIFICATION TEST ENVIRONMENT DEFINITION

During the qualification test, the instrument was subjected to vibration, thermal-vacuum, acceleration, and accoustic environments. These environments are defined in Tables 10-2 through 10-4 and Figure 10-1. respectively. This instrument was also subjected to magnetic moment tests (ref PIR 1450-OSOH-033).

Table 10-1. Prototype Qualification Test Flow

- EUV to X-ray Coalignment (5/11)
- Initial System Functional Test (5/18)
- H-Alpha Subsystem Calibration (6/04)
- EUV Subsystem Calibration (6/12)
- LW X-ray Subsystem Calibration (6/28)
- SW X-ray Subsystem Calibration (6/29)
- Collimator C/O
- Thermal Distortion (6/26)
- Polarimeter Subsystem Calibration (6/28)
- System Functional Test (7/01)
- End-to-End X-ray Test (7/02)
- Vibration (7/07)
- Launch Lock Firing andCheckout (7/07)
- EUV to X-ray Coalignment Recheck (7/09)
- H-Alpha Calibration Recheck (7/09)
- EUV Calibration Recheck (7/14)
- X-ray End-to-End Recheck (7/15)
- EMI Test (7/17)
- Interface Check at Ball Brothers (7/20)
- Weight, C.G., I, Measurement (7/21)
- Magnetic Balance (7/30)
- Thermal-Vacuum Test (8/28)
- Acceleration Test (9/01)
- Acoustic Noise Test (9/02)
- System Functional Test (9/02)

Note:

1. Dates are test completion.
2. Test occurred in 1970.

The vibration test was conducted at GE and the thermal-vacuum, acceleration, magnetic moment and acoustic tests were conducted at NASA/GSFC. The thermal-vacuum magnetic moment and acceleration tests were conducted by GE personnel supported by NASA/GSFC test facility personnel. The acoustic test was conducted by NASA/GSFC personnel.

Table 10-2. Qualification Vibration Levels (Sine Vibration)

Axis	Frequency (Hz)	Level g's Peak-to-Peak	Sweep Rate
Z	5-12	0.45-inch double amplitude (D.A.)	
	12-17	3.5	
	17-40	6.3	
	40-70	18.0	4 octaves per minute, all frequencies
	70-200	4.5	
	200-2000	5.0	
X and Y	5-16	0.45 inch D.A.	
	16-110	6.3	4 octaves per minute
	110-2000	5.0	

Random Vibration	
Frequency Range (Hz)	PSD Level (g^2/cps)
20-300	0.0023 to 0.090, increasing 4dB per octave (12.8 g's rms)
300-2000	0.090

Duration: 2 minutes per axis

Table 10-3. Acceleration Test

Run 1	15.1 G in +Z Axis Combined with 3.0 G in + Y Axis
Run 2	15.1 G in +Z Axis Combined with 3.0 G in + X Axis
Centrifuge Radius	- 798 in.
Centrifuge Speed	- 26.1 rpm

Table 10-4. Qualification Thermal-Vacuum Test Cycle

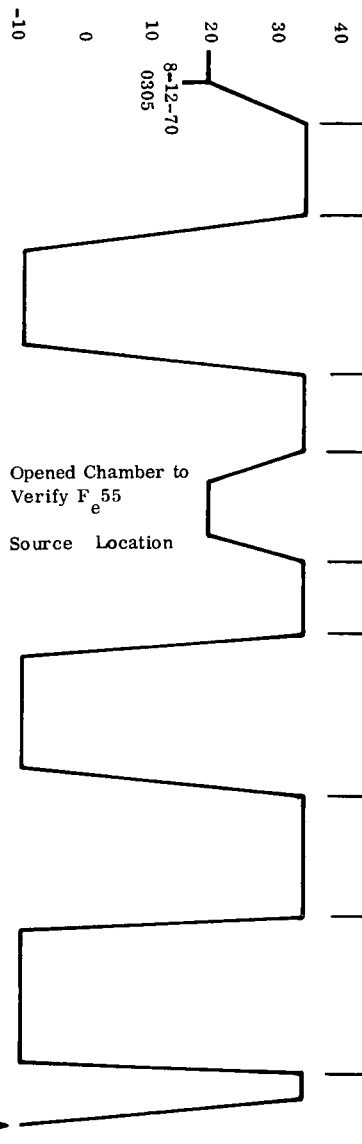

Total Hours	Date	Time
	8-14-70	0810
	System Funct	22V
16:50	System Funct	22V
	Orbit Stability	16V
	8-15-70	0100
	8-17-70	0100
	8-18-70	1130
	System Funct	16V
18:30	System Funct	22V
	Orbit Stability	22V
	8-19-70	1700
	8-24-70	0125
	System Funct	16V
	System Funct	22V
16:05	Orbit Stability	22V
	System Funct	16V
	System Funct	22V
	8-28-70	0130
	8-28-70	1200

Date	Time	Total Hours
8-12-70	1010	
System Funct	22V	
Orbit Stability	22V	26:20
System Funct	16V	
8-13-70	1230	
8-15-70	0800	
System Funct	22V	8:00
8-15-70	1600	
8-17-70	1600	
System Funct	16V	
Orbit Stability	16V	14:00
8-17-70	2000	
8-20-70	0240	
System Funct	22V	
Orbit Stability	22V	78:00
System Funct	16V	
System Funct	22V	
8-23-70	0840	
8-28-70	1130	0:30

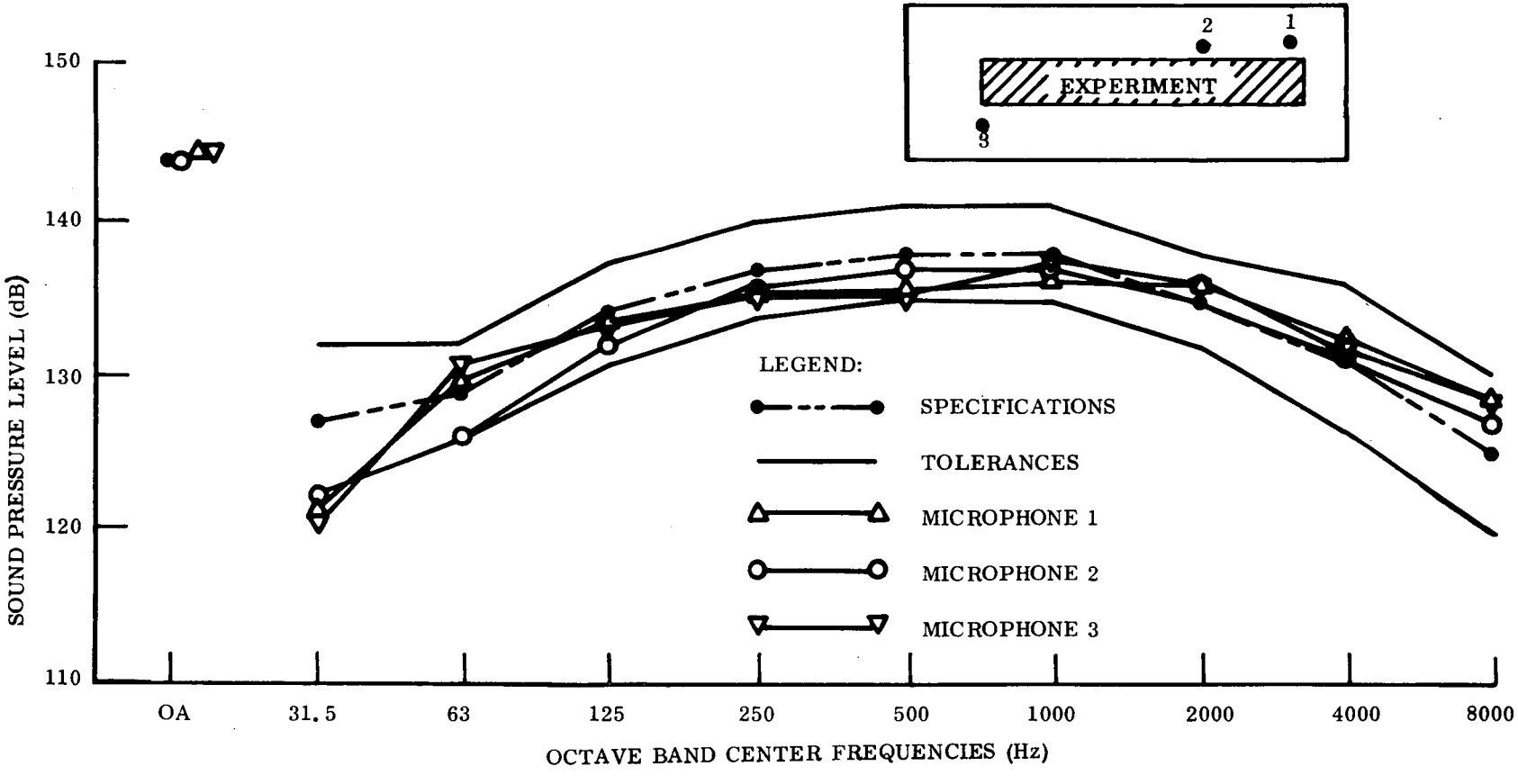

Figure 10-1. OSO-H Acoustic Test - GSFC Spectroheliograph Experiment

Table 10-5. Qualification Test Problem Summary

Problem	Cause	Corrective Action
Structural		
1. Aperture wheel would not stop at reference position. (MR00958).	Reference cam was deformed because of impacting by microswitch actuation arm during vibration. Cam would not actuate microswitch to control aperture wheel.	Recontoured cam to increase bearing area. Implemented operational change to place aperture wheel in position during vibration (launch) which disengages cam and microswitch actuation arm.
2. H-Alpha condensing lens was chipped at one edge (MR00957).	Lens was set in RTV 566 at assembly. Pressures executed by assembly squeezed RTV 566 from interface causing glass to metal contact. Chipping occurred during vibration.	Precoated lens with RTV566 and cured prior to assembly.
3. H-Alpha band pass shifted 1.3 Å (MR00968).	Spherical mirror shifted in mount during vibration.	Redesigned mirror mount.
4. EUV mask did not move upon command (MR00956).	Vibration environment caused brinelling of beryllium "V" groove track in area of the six 1/8 inch diameter balls that support the mask.	Redesigned track to incorporate a hardened stainless steel insert. This insert is similar to the main carriage track insert.
5. EUV mask did not stop at the "A" position when commanded but would pass through the "A" position and return to the "B" position (MR00971).	Improper setting of "A" position microswitch.	Insured both microswitches actuate at angular position of bell crank of 10^0 or greater.
6. Aluminum filter in the Al-Mg filter pair failed (MR00959).	Failure occurred during first axis of random vibration test.	a. Increased filter thickness from 1/8 mil to 1/4 mil. b. Reduced filter panel size by 1/2. c. Added stainless steel mesh for support.
7. EUV telescope resolution degraded (MR00985).	Optical elements shifted during vibration tests.	a. Redesigned optical element supports b. Revised assembly (torquing) procedures.

Table 10-5. Qualification Test Problem Summary (Cont'd)

Problem	Cause	Corrective Action
Electromechanical		
1. Shortwave filter wheel did not respond properly to commands (MR00955).	Motor torque output marginal for application.	a. Removed "O" ring from shafts of LW & SW X-ray filter wheel drive motors to increase effective torque output. b) Change angle of ramp on filter wheel indexing cam to decrease torque requirement.
Electrical		
1. Pulses fed into the H-Alpha counter resulted in out-of-spec readings (MR00947).	Noise pick-up.	Added a buffer stage to reduce noise sensitivity.
2. Polarimeter background measurement was out-of-spec (MR00953/ 61/62).	High voltage leakage in high voltage circuits generated spurious counts.	a. Reconfigured circuits. b. Revised cleaning and test procedures. c. Bonded components with epoxy.
3. EUV background measurement was out-of-spec (MR00965).	Potting voids were found in high voltage areas.	a. Changed design to reduce chance of voids. b. Changed potting method.
4. H-Alpha A/D converter module failed (MR00966).	Transistor Q5 failed. Probable cause due to test operator error which over-powered circuit.	Replaced defective A/D converter module.
5. A 70K impedence between signal and chassis was measured (MR00973).	Temperature sensor failed.	Replaced temperature sensor.
6. Crosstalk was observed between EUV detectors during vacuum thermal test (MR00979).	Electrical crosstalk.	a. Changed layout of electrical conductors. b. Added special crosstalk tests.
7. Continuity existed between signal and chassis grounds (MR00980).	Polarimeter shield (signal ground) was touching collimator (chassis ground) due to assembly tolerance.	a. Insulated polarimeter shield. b. Maintain clearance at assembly.
8. Oscillations in the 0.5 to MHz range were observed under certain grounding conditions (MR00982).	Oscillations were caused by feed back through the high voltage flex print to the EUV detectors.	a. Added filter in each flex print conductor to break feed-back loop.

Table 10-5. Qualification Test Problem Summary (Cont'd)

Problem	Cause	Corrective Action
Electrical (Cont'd)		
9. Measurements for conducted emissions and inrush current were out-of-spec (MR00969).	Insufficient filtering and surge suppression in design to meet stringent interface spec. requirement.	a. Added filters and chokes to the power and ground interface lines. b. Added a surge suppression in each of the power lines.
10. Low voltage power supply became unstable. (MR00983).	Addition of filters described in 9 above caused unstable condition.	a. Modified filter design b. Removed ramping circuit in LVPS.
11. During EMI testing several motors failed to respond correctly to commands (MR00981).	Logic board A6 was removed for investigation. Problem could not be reproduced. Cause is unknown.	a. Replaced logic board A6 for flight. b. Inspected connector for contamination/damage.
Sensor		
1. Polarimeter output not stable with time during thermal-vacuum (MR00975/85).	Leak in polarimeter.	a. Repaired leak
2. Short EUV channel drifted with temperature during thermal-vacuum test. (MR00972).	Detector had relatively poor plateau.	Extended plateau by optimizing voltage distributions on field and dynode strips.
3. H-Alpha output varied during thermal-vacuum test as a function of time and temperature (MR00978).	Component level test have shown that sensor and electronics have some sensitivity to temperature, but are stable with time. Therefore, cause of drift is uncertain.	Replaced the sensor (photomultiplier tube).

Table 10-6. Chronology of Flight Acceptance Test

1. Polarimeter (Subsystem Calibration (1/21/71)
2. X-ray Subsystem Calibration (2/28/71)
3. EUV Subsystem Calibration (3/2/71)
4. H-Alpha Subsystem Calibration (3/5/71)
5. System Functional Test (3/10/71)
6. EMI Test (3/11/71)
7. X-ray End-to-End Test (3/11/71)
8. EUV to X-ray Coalignment Measurement (3/11/71)
9. Vibration Test (3/13/71)
10. EUV to X-ray Coalignment Measurement (3/13/71)
11. System Functional Test (3/14/71)
12. H-Alpha Subsystem Calibration Re-check (3/15/71)
13. EUV Subsystem Calibration Re-check (3/17/71)
14. X-ray End-to-End Test (3/18/71)
15. Thermal-Vacuum Test (4/4/71)
16. Special Tests by NASA/GSFC (4/16/71)
17. Rework Cycle (4/26/71)
18. Vibration (abbreviated to one axis, random, flight level) (4/27/71)
19. System Functional Test (4/28/71)
20. Acoustic Test (4/30/71)

Table 10-7. Flight Acceptance Thermal-Vacuum Cycle

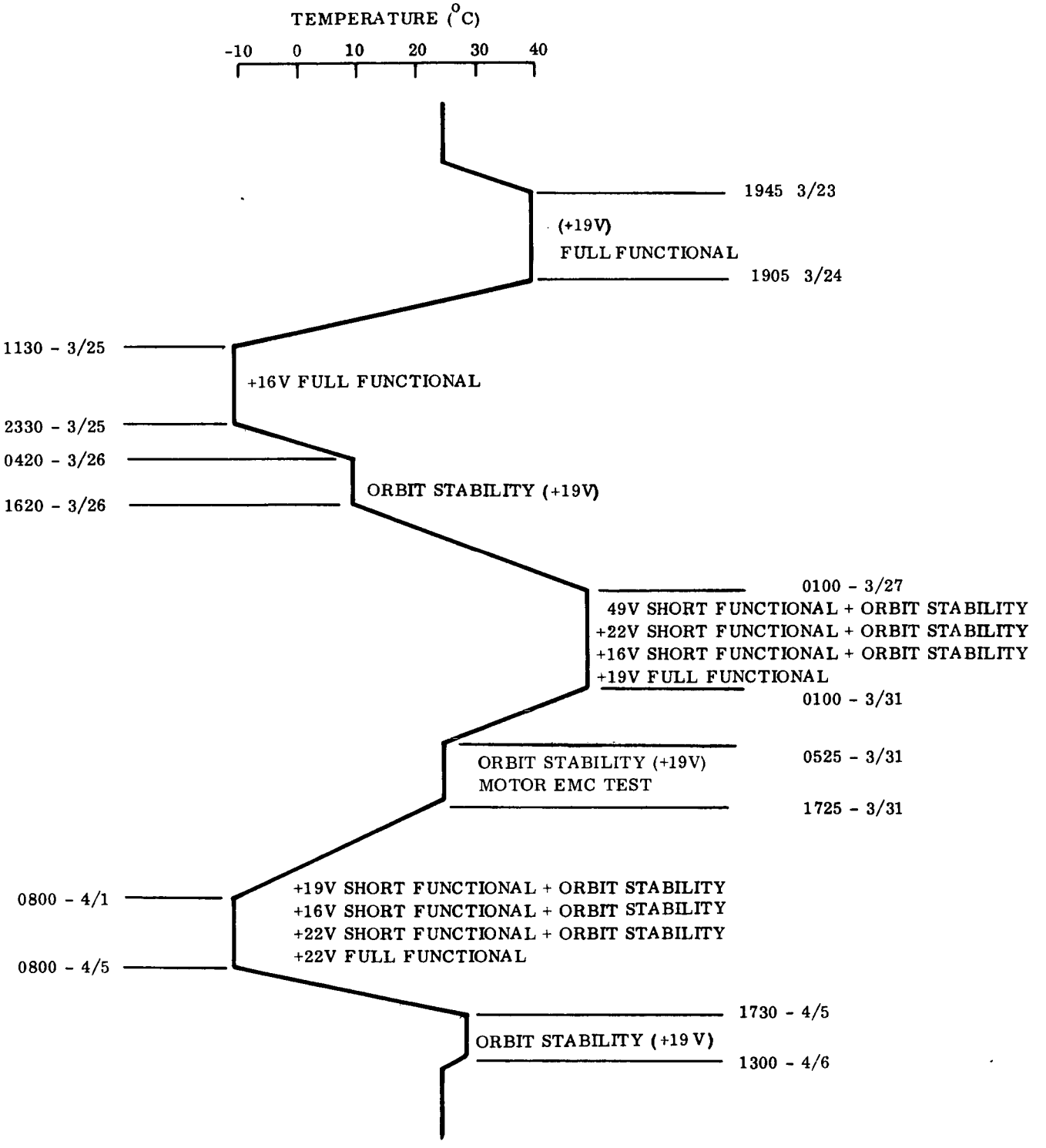

10.2.4 QUALIFICATION TEST RESULT

In general, the instrument passed the qualification test with relatively few problems considering the complexity of the instrument and the fact that the Engineering program was conducted without a model of the complete instrument. The instrument problems which were observed were recorded on NASA/GSFC Malfunction Reports (MR's) as they occurred. The problems, their causes, and the action taken to correct them are summarized in Table 10-5. Problems which were identified with test procedures, equipment, facilities, and/or personnel were also recorded on MR's, but are not included in this report.

10.3 FLIGHT ACCEPTANCE TEST

10.3.1 GENERAL

Following the refurbishment cycle which incorporated the design changes dictated by the qualification test, new sensor electronics, and new logic electronics, the instrument was subjected to a flight acceptance test. This test cycle, as modified by contract, was basically the same as that used for the qualification test, except that an acceleration test was not required and that the upper temperature level for thermal-vacuum testing was increased from $+35^{o}C$ to $+40^{o}C$.

The test procedure followed for the flight acceptance test is documented in PIR 1J86-OSO-H-655 dated March 23, 1971. Again, this procedure was updated as the test progressed to reflect additions, deletions, and corrections as identified during the test program. These changes were red-lined into the working copy of the test procedure and were approved by the test director and the cognizant NASA/GSFC test representative.

10.3.2 TEST OUTLINE/CHRONOLOGY

Table 10-6 lists the chronology of the flight acceptance test.

10.3.3 FLIGHT ACCEPTANCE TEST ENVIRONMENT DEFINITION

During the flight acceptance test cycle, the instrument was subjected to vibration, thermal-vacuum and acoustic environments. The vibration and acoustic environments were the same as used for the qualification test cycle (Ref Table 10-2 and Figure 10-1,respectively). The vibration test was conducted at GE and the thermal-vacuum and acoustic tests were conducted at NASA/GSFC. The thermal-vacuum test was conducted by GE personnel supported by NASA/GSFC test personnel (see Table 10-7). The acoustic test was conducted by NASA/GSFC personnel.

10.3.4 FLIGHT ACCEPTANCE TEST RESULTS

The instrument completed the flight acceptance with minimal problems. The problems which did occur were documented on NASA/GSFC Malfunction Reports (MR's). The instrument problems, their causes, and the action taken to correct them are summarized in Table 10-8.

Table 10-8. Flight Acceptance Test Problem Summary

Problem	Cause	Corrective Action
Structural		
1. X-ray proportional counter mounting screw loosened during vibration (MR01003).	Insufficient locking.	Added requirement to bond screws in place.
2. Cu-Ni X-ray filter failed during thermal-vacuum test (MR01010).	a. Insufficient venting of filter wheel caused excessive pressure gradient across filter, or, b. Thermal stresses.	a. Increased venting area in filter wheel b. Thermal cycled replacement filter prior to assembly.
Sensor		
1. LW X-ray proportional counter degraded during thermal-vacuum test (MR01009).	Leak in proportional counter.	Replaced proportional counter.

Table 10-8. Flight Acceptance Test Problem Summary (Cont'd)

Problem	Cause	Corrective Action
Electrical		
1. Low voltage power supply developed short in 5.4 volt output during vibration (MR01001).	Short in capacitor in output filter	Replace LVPS
2. Surge current and conducted emissions exceeded spec. (MR01008).	--	None - out-of-spec condition acceptable
3. Low voltage power supply (5.4 volt output) out-of-spec at -10°C. (MR01011).	--	None - out-of-spec condition acceptable
4. EUV mask operates intermittently. (MR01015).	Broken conductor in LV flexprint	Replace LV flexprint with modified design and contour.
5. Five logic circuits failed. (MR01015).	High voltage arc-over in test equipment during special tests at GSFC is suspected.	Replace all logic with spare units.
6. Mid-EUV detector output noisy.(MR01017).	Ground wire broken during detector adjustment at GSFC.	Replaced ground wire.

10.4 POST DELIVERY TESTING

10.4.1 GENERAL

The instrument was delivered to the spacecraft contractor's plant on April 30, 1971. Following instrument check-out using the spacecraft simulator, the instrument was installed in the spacecraft and subjected to spacecraft-level test. The spacecraft was delivered to the Eastern Test Range (ETR) on September 15, 1971, where additional testing was performed. Launch occurred on September 29, 1971.

10.4.2 TEST OUTLINE/CHRONOLOGY

Table 10-9 lists a chronology of instrument testing after delivery.

10.4.3 POST DELIVERY TEST RESULTS

During spacecraft level testing at the spacecraft contractors plant, several problems occurred which required correction action. These problems were documented on NASA/GSFC Malfunction Reports (MR's). The problems, their causes, and the action taken to correct them are summarized in Table 10-10.

In addition, two design changes were made to the instrument to incorporate designs which would improve performance. First, a new low voltage flex print was installed to increase the orbital life of the EUV Experiment. Second, the balance between the long wavelength X-ray channels and the short wavelength X-ray channels were improved by blocking approximately 6 and 8 percent of the apertures in front of the respective channels.

Table 10-9. Post Delivery Chronology

1. Weight, Center of Gravity, Magnetic Moment Measurements (5/6/71)
2. Install Instrument, Comprehensive Test (5/13/71)
3. Compatibility Test (5/23/71)
4. Remove Instrument for Long Wavelength X-ray Detector Check (5/30/71)
5. Install Instrument in Spacecraft (6/1/71)
6. Remove Instrument and Replace Flexprint (6/22/71)
7. Comprehensive Test on Simulator (6/22/71)
8. Installed Instrument in Spacecraft, Comprehensive Test (6/23/71)
9. Sun Point Test (6/29/71)
10. Changed H-Alpha High Voltage Setting (7/12/71)
11. Comprehensive (7/13/71)
12. Sun Point Test (7/14/71)
13. Spacecraft Vibration Test (7/19/71)
14. Investigate LVPS noise (220 H Oscillation)
15. Thermal-Vacuum Test (8/11/71)
16. Rework Launch Lock
17. Post Thermal-Vacuum Comprehensive (8/13/71)
18. Remove Instrument from Spacecraft (8/13/71)
19. Replaced LVPS, Logic Board A7, Adjusted H-Alpha Experiment High Voltage. Conducted X-ray Balance Tests (8/16/71).
20. Comprehensive and EMI Test on Simulator (8/17/61)
21. Spacecraft Vibration Test (8/18/71)
22. Comprehensive and Sun Point (8/19/71)
23. Comprehensive (9/4/71)
24. Deliver Spacecraft to ETR (9/16/71)

SECTION 11

NEW TECHNOLOGY

During this contract period of performance, no new technology items were developed.

APPENDIX A

MAJOR COMPONENT IDENTIFICATION

Appendix A lists the major components by serial number which are installed in the flight instrument. Test instructions and test data repositories are also identified. The instrument was assembled in accordance with GE drawing 47R217399G1.

Component	Serial No.	Test Instruction	Test Documentation Repository
EUV Experiment	-	T.I. 016	Instrument Log Book
Telescope	3	SVS 7558 & T.I. 008	Section 3 & Instrument Log Book
Grating	1203	GFE	GFE
Detectors (S)	PR889	T.I.002	Instrument Log Book
Detectors (M)	PR880	T.I.002	Instrument Log Book
Detectors (L)	PR879	T.I.002	Instrument Log Book
HVPS (M)	E3	SVS 7561	Section 8.6 & Instrument Log Book
HVPS (L-S)	E4	SVS 7561	Section 8.6 & Instrument Log Book
H-Alpha Experiment		T.I.015	Instrument Log Book
Photomultiplier	11-9-100	T.I.004	Instrument Log Book
HVPS	B2	SVS 7561	Section 8.6 & Instrument Log Book
LW X-ray Experiment	-	T.I.012	Instrument Log Book
Collimator	1	SVS 7559 & T.I. 006	Instrument Log Book
Proportional Counter	397	GFE	GFE
Filter Ni-Co, Position 1	5L	-	Section 5 & Instrument Log Book
Filter Ge-Zn, Position 2	7L	-	Section 5 & Instrument Log Book
Filter Ni-Co, Position 4	8L	-	Section 5 & Instrument Log Book
Filter Cu-Ni, Position 5	9L	-	Section 5 & Instrument Log Book
Filter A1-Mg, Position 6	4L	-	Section 5 & Instrument Log Book
HVPS	D2	SVS7561	Section 8.6 & Instrument Log Book
SW X-ray Experiment		T.I. 013	Instrument Log Book
Collimator	1	SVS 7559 & T.I. 006	Instrument Log Book
Proportional Counter	2143	T.I. 003	Instrument Log Book
Filter Fe-Mn, Position 1	1S	-	Section 5 & Instrument Log Book
Filter Mn-Cr, Position 2	2S	-	Section 5 & Instrument Log Book
Filter S-A1, Position 3	8S	-	Section 5 & Instrument Log Book
Filter Fe-Mn, Position 4	3S	-	Section 5 & Instrument Log Book
Filter Fe-Cr, Position 5	5S	-	Section 5 & Instrument Log Book
HVPS	C2	SVS 7561	Section 8.6 & Instrument Log Book
Polarimeter Experiment	P0121	T.I. 014	Instrument Log Book
Polarimeter	206	GFE	GFE
HVPS	A3	SVS 7561	Section 8.6 & Instrument Log Book
Low Voltage Power Supply	PN911	PIR 1J86OSOH455	Instrument Log Book